Universitat Autònoma de Barcelona

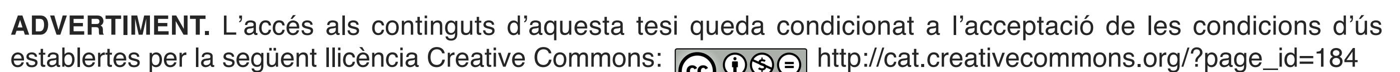

ADVERTIMENT. L’accés als continguts d’aquesta tesi queda condicionat a l’acceptació de les condicions d’ús establertes per la següent llicència Creative Commons: http://cat.creativecommons.org/?page_id=184

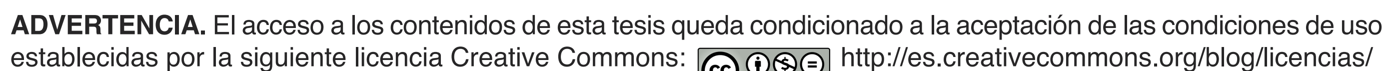

ADVERTENCIA. El acceso a los contenidos de esta tesis queda condicionado a la aceptación de las condiciones de uso establecidas por la siguiente licencia Creative Commons: http://es.creativecommons.org/blog/licencias/

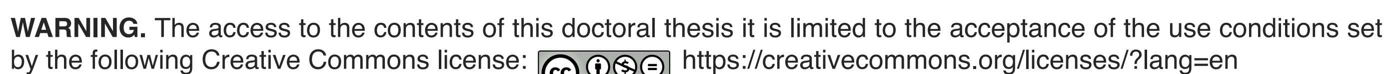

WARNING. The access to the contents of this doctoral thesis it is limited to the acceptance of the use conditions set by the following Creative Commons license: https://creativecommons.org/licenses/?lang=en

DOCTORATE PROGRAM IN MATERIALS SCIENCE

Growth mechanisms and properties of semiconductor nanowires at the atomic scale

From VLS to SAG quantum networks

Sara Martí-Sánchez

Supervisor

Prof. Jordi Arbiol i Cobos

Tutor

Prof. Jordi Sort i Viñas

INSTITUT CATALÀ DE NANOCIÈNCIA I NANOTECNOLOGIA (ICN2), CSIC & BIST

PHYSICS DEPARTMENT, FACULTY OF SCIENCES
UNIVERSITAT AUTÒNOMA DE BARCELONA (UAB)

May 2020

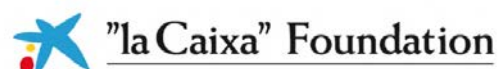

Memòria presentada per aspirar al Grau de Doctor per Sara Martí Sánchez

Jordi Arbiol i Cobos, ICREA Research Professor at Institut Català de Nanociència i Nanotecnologia (ICN2), CSIC and BIST and **Jordi Sort i Viñas**, ICREA Research Professor at the Physics Department of the Universitat Autònoma de Barcelona (UAB)

CERTIFY

that **Sara Martí Sánchez**, MSc in Nanoscience and Nanotechnology, carried out the work entitled 'Growth mechanisms and properties of semiconductor nanowires at the atomic scale. From VLS to SAG quantum networks.' under their direction and qualifies for the degree of Doctor in Materials Science. And for that record, sign this certificate.

Prof. Jordi Arbiol i Cobos   Prof. Jordi Sort i Viñas   Sara Martí Sánchez

Bellaterra, May 2020

Acknowledgements

This PhD thesis could not have been completed without the invaluable help, assistance and guidance of my colleagues and it is difficult to express in words how grateful I feel for their support. First of all, I would like to thank my advisor Prof. Jordi Arbiol, not just for giving me this opportunity, but also for all his support, guidance and advice. His enthusiasm and confidence have made possible to stand up even in the most complicated and stressful periods. I would not be able to imagine a better advisor for entering in such an amazing field of research.

I felt GAe$^-$N was a second home since the beginning, and I could not be happier with all the mates I had during these years for the scientific discussions and the time spent together. It has been a real pleasure to share office and time with all of you: PengYi, María, Aziz, Caroline, Déspina, Albert, Jérémy, Gaël, Christian, Timm, Ana, Meri, Marc, Ting, Xu, Zhifu, Chiara, Ying, Ramon and Ivan. And specially to PengYi, who was with me from the very beginning and I spent uncountable hours of joy with him, and Chiara, who has quickly become a very good supportive friend. Thank you! 谢谢! *ευχαριστώ*! Merci! Danke! Grazie!

The Electron Microscopy Division at ICN2 has been key for the development of the thesis and the knowledge acquisition. Many thanks to Belen Ballesteros, Marcos Rosado and Francisco Belarre for their support, both technical and personal. I want to thank also Rodrigo Fernández-Pacheco and Alfonso Ibarra for helping me whenever needed in the LMA-INA, where most of the experimental data of this work was acquired. In addition, the FIB preparation team formed by Laura Casado and Isabel Rivas have been essential for the specimen preparation of this thesis. Also thanks to Prof. Quentin Ramasse from the SuperSTEM lab with whom I accquired some of the EELS data employed in several chapters of the thesis.

I would like to thank Prof. Anna Fontcuberta i Morral from EPFL and her group for hosting me during a three months internship in Lausanne. All the team made me feel comfortable since the first day. Special thanks to Martin, Lucas, Oscar, Mahdi and Luca for the discussions about the polar driven growth of nanowires. Nada

hubiera sido igual durante estos meses sin los momentos compartidos con mis cordobeses favoritos: Pablo, a quien debo muchos buenos momentos y estoy segura de que es y será un padrazo, y Andrés, a quien ya le he dicho muchas veces que le debo mucho más que una simple pata de jamón ibérico. Tu apoyo académico y personal estos años ha sido esencial para llegar hasta aquí. Muchas gracias a ambos por entrar en mi vida y por seguir en ella, aunque sea a distancia!

I would also like to thank Prof. Peter Krogstrup, Dr. Philippe Caroff and their multidisciplinary teams at the Microsoft Quantum Labs in Copenhagen and Delft for involving us in such an exciting project. Special thanks to Peter Krogstrup and his team for hosting me in his lab during one week that provided me the overall vision of such a big project that I needed. And to Martín, not just for those days, but for all the exciting discussions about TEM during the last couple of years. In addition, I would like to thank Eitan Oksenberg and Prof. Ernesto Joselevich, who were essential for the development of this work, for introducing us into nanowire guided growth and the exciting result discussions.

In addition, I have to thank the valuable support of my friends who have encouraged me during this period, making this experience much easier. A Jony por animarme en los inicios de este proyecto. A les meves amigues des de fa una dècada: Cristina, Marina, Iolanda i sobretot l'Araceli, per donar-me tant de suport sempre que ho he necessitat. A Silvia, Javi y Wendy, por hacerme un huequito en su pequeña familia. A l'Adri i l'Alba pels petits moments que marquen la diferència. I per suposat a l'Adrià, que s'ha convertit en una segona família per mi i un dels majors suports de la meva vida.

Y finalmente quería agradecer el indispensable apoyo en lo académico y extraacadémico de mi familia. A mis abuelos Dolores, Antón, Antonia y Joan. A mis tíos Eudald y Florencio. A mi hermana Marta. Y por supuesto a mis padres, Rosa y Juan, por haberme proporcionado siempre todo lo que he necesitado en la vida. Sin vuestra guía, vuestro apoyo y vuestra confianza en mí jamás habría llegado aquí.

Thank you very much! Gracias a todos! Gràcies a tots!

Abstract

Nanowires based on binary semiconductors and their alloys have a great potential to overcome conventional semiconductor technologies. They present enhanced properties with respect to their bulk counterparts, which goes accompanied with a reduction of materials consumption and higher efficiencies. For this reason, they are outstanding candidates for overcoming conventional electronics and optoelectronics. Recently, they have even been proposed as a basis for shifting computational sciences into the new paradigm of topological quantum computing.

The vapor-liquid-solid (VLS) growth method has been the main technique for growing semiconductor nanowires over the last 50 years. Since it was proposed in 1964, the efforts in understanding the growth mechanisms have led to a deep control of the macroscopic parameters driving nanowire formation. Nonetheless, several factors as spontaneous defect formation and scalability are still limiting their incorporation into functional technologies. With this aim, several new growth strategies have been developed in the last years. Such strategies include reverting the typical growth direction for prevention of spontaneous defect formation and polytypism, enabling single crystal nanowire growth. Likewise, guiding the typical VLS growth in specific substrate directions permits the creation of self-assembled horizontal arrays for parallel nanowire engineering. Last but not least, nanopatterning of the substrates allows the design of predefined nanowire networks in the highly scalable selected area growth approach.

Given the actual technological requirements, the material deposition has to be controlled down to the atomic level, specially when expanding the growth to heterostructured systems. In this regard, (Scanning) Transmission Electron Microscopy and its related spectroscopies are the most suitable techniques to study the growth mechanisms and crystal structure at the atomic scale. With this purpose, the present PhD dissertation provides a (S)TEM-based atomistic investigation of the nanowire

growth mechanisms in such revolutionary growth approaches, all correlating the crystalline structure and local composition of the formed nanostructures with their (opto)electronic and quantum properties.

This dissertation is divided into several chapters. In Chapter 1, a brief introduction of semiconductor physics from macroscopic and microscopic approaches is provided, followed in Chapter 2 by a theoretical and practical description of the methodology employed for these studies (i.e. (S)TEM related techniques). The thesis outcomes are collected in four chapters that chronologically encompass different progresses in nanowire growth for enhanced reproducibility and scalability.

- Chapter 3 deals with the control of polarity in conventional VLS growth as a final step to achieve single crystal nanowires.
- Chapter 4 offers an advance in VLS by switching growth to horizontal directions for the production of self-assembled arrays, enabling parallel nanowire manipulation.
- Chapter 5 turns into direct growth of horizontal nanowire networks by selective area growth on nanopatterned substrates, providing scalable routes for circuit designs and removing the need of catalyst employment.
- In Chapter 6, the nanowires grown through the formerly cited strategies are employed as templates for the epitaxy of ferromagnetic insulators and/or superconductors to form the next generation of hybrid quantum networks.

Finally, the manuscript is concluded in Chapter 7 with a summary of the main results along with a brief outlook.

Contents

Acknowledgements **v**

Abstract **vii**

1 Introduction **3**

1.1 Semiconductor materials: Band theory 3

1.1.1 Types of semiconductors 4

1.1.2 Heterojunctions 6

1.2 An atomistic approach to binary semiconductors 8

1.2.1 Binary III-V and II-VI semiconductors 9

1.2.2 Ternary and quaternary alloys: Vegard's law 14

1.2.3 Defects in semiconductor materials 15

1.3 Epitaxy in heterostructured materials 18

1.4 Nanostructured semiconductors: Nanowires 20

1.4.1 Nanowire growth approaches 22

1.4.2 State of the art and challenges 25

2 Methodology **27**

2.1 Overcoming resolution limits with Transmission Electron Microscopy 27

2.1.1 Aberrations in (S)TEM 29

2.1.2 Aberration correction 32

2.2 (S)TEM imaging techniques 35

2.2.1 Imaging in TEM : BF / DF / HRTEM 35

2.2.2 Imaging in STEM: HAADF/MAADF/ABF 37

2.3 Analytical STEM: EELS and other spectroscopies 40

2.3.1 Electron Energy Loss Spectroscopy, EELS 42

Zero - loss peak (0 eV) - Thickness and energy resolution 43

Low - loss EELS (<100 eV) - Optoelectronic transitions 44

Core - loss EELS (>100 eV) - Elemental composition 45

2.4 Data acquisition and processing 47

2.4.1 Image treatment and Fourier space 48

2.4.2 Strain measurements: Geometric Phase Analysis 49

2.4.3 EELS spectra treatment 51

2.5 3D atomic modelling and image simulation 53

2.6 Strain and electronic properties simulation 54

3 The role of polarity in VLS growth of III-V free-standing nanowires 57

3.1 Introduction 57

3.1.1 VLS polar growth of binary semiconductors 57

3.2 Self-catalyzed A- and B- polar GaAs nanowires 60

3.2.1 Polar-dependent structure of nanowires 62

3.2.2 Optoelectronic response for different NW polarities 66

3.3 Liquid ordering at L-S interfaces in VLS nanowire growth 68

3.3.1 Evidences of liquid ordering at the interface 69

3.3.2 Correlation with polar-dependent crystal structure 73

3.4 Bipolar growth in GaAs nanowires 75

3.4.1 Growth along the <112> direction 76

3.4.2 Engineering vertical growth on (100) Si 78

3.5 Polarity effects on elemental segregation in alloys 82

3.6 Conclusions 87

4 Guided VLS growth of core-shell horizontal nanowire arrays 89

4.1 Introduction 89

4.1.1 Substrate engineering for guided growth 91

4.1.2 VLS guided growth of ZnSe@ZnTe horizontal NW arrays . . . 91

4.2 Crystal structure of core-shell NWs 93

4.2.1 Graphoepitaxial growth 93

4.2.2 Epitaxial growth 95

4.3 Morphology effects in strain minimization 97

4.3.1 The origin of plane bending 100

4.3.2 Dependence of plane bending with core radius 103

4.3.3 Influence of plane bending on electronic band alignment 106

4.4 EELS-based determination of electronic band gap 108

4.4.1 VEELS data treatment in heterostructured systems 110

4.4.2 Results and discussion 115
4.5 Conclusions 117

5 Selective Area Growth of III-V nanostructures 119
5.1 Introduction 119
5.1.1 Models of VS growth mechanisms 121
5.1.2 Selectivity of the grown materials 122
5.1.3 Scalable nanowire networks 123
5.2 Implementation of GaAs nanomembranes onto Si substrates 127
5.2.1 GaAs NM on (111) Si 127
5.2.2 GaAs NM on (001) Si 133
5.3 GaAs NMs as templates for the directional growth of NWs 138
5.4 InAs NW networks: strain engineering towards defect-free systems . . 142
5.4.1 Effects of buffering nanowire networks 143
5.4.2 Addition of ternary $In_xGa_{1-x}As$ intermediate compounds . . . 147
5.4.3 Optimization of In incorporation into the InAs channel 152
5.5 High mobility InSb NW networks 155
5.6 Conclusions 159

6 One-dimensional hybrid heterostructures for quantum applications 163
6.1 Introduction 163
6.1.1 Hybrid tri-crystal configurations 165
6.2 Hybrid tri-crystal VLS nanowires 168
6.3 Interfaces of EuS (FMI) on ZB InAs (SE) configurations 180
6.3.1 EuS planar layers 180
6.3.2 EuS on SAG nanowires 186
6.4 Crystal quality of Al (SU) on SAG nanowires 188
6.4.1 Deposition of Al on InAs SAG nanowires 188
6.4.2 Deposition of Al on InSb SAG nanowires 192
6.4.3 Superconductors beyond aluminum 194
6.5 Conclusions 195

7 General conclusions 197
7.1 General conclusions 197
7.2 Closing remarks and outlook 201

Bibliography **203**

A List of acronyms, symbols & notation **229**

A.1 Acronyms 229

A.2 Symbols 231

A.3 Notation 231

B List of Publications **233**

B.1 Publications 233

B.2 Communications in conferences and workshops 237

C Resum **239**

D Resumen **241**

Chapter 1
Introduction

Silicon-based semiconductor materials are the basis of nowadays technology. The reduction of the size of the components in integrated circuits has been capable of optimizing devices power and speed. However, the low carrier mobility and indirect gap nature of silicon made scientists consider other materials for the creation of electronic components. The reduction of sizes of these materials forming one-dimensional structures allows to exploit their best performance. In this chapter, the basic principles of semiconductor materials are explained from macroscopic and atomistic approaches, basing those concepts in binary and ternary semiconductor materials.

1.1 Semiconductor materials: Band theory

A crystal is composed by an ordered set of atoms presenting relative proximity in a periodic distribution. If the distance between atoms is high enough, the available states of the crystal are just the overlapping of the available states of isolated atoms. However, if the interatomic distance gets reduced, the Coulomb potential of each atomic nuclei overlaps with its neighbour atoms, existing then a coupling between wavefunctions. By Pauli's exclusion principle, states that were degenerated split in energy. The energy difference between the available levels is small, so they are called energy bands. Energy bands can be mathematically derived from the solutions of Schrödinger's equation applied to a system of N atoms and their valence electrons and they are highly dependent on the interatomic distance (lattice constant) and atomic periodicity (crystal symmetry).

Given the different electronic behavior of materials according to their band configuration they are typically classified as conductors, semiconductors and insulators. In the case of conductor materials, the band structure is continuous through energy,

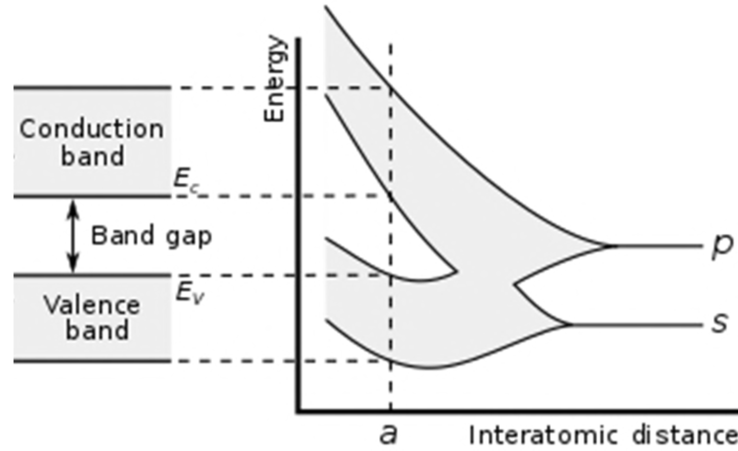

Figure 1.1: Scheme of energetic bands as a function of crystal lattice constant.

while in the case of semiconductors and insulators, the overlapping of bands is broken and a prohibited band (or band gap, E_g) appears, splitting into valence band (E_v) and conduction band (E_c).

The energy of electrons is dependent on its momentum **k**, so band diagrams are typically represented as E(**k**) following different directions in the first Brillouin zone towards high symmetry points (Γ, L, X...). In the diagrams, the maximum of the valence band is located at $\Gamma = (0, 0, 0)$ and it is considered the origin of energy. It is composed by three sub-bands: two of them (heavy holes and light holes) are degenerated in Γ and the third one (spin-off) is energetically displaced from them. Regarding the conduction band, the absolute minimum does not relay in a fixed **k** position. It depends on the type of semiconductor.

1.1.1 Types of semiconductors

Semiconductor materials are classified into two main types according to the position of the minimum of the conduction band with respect to the valence band maximum, or equivalently the nature of their band gap. A semiconductor is said to be direct when the minimum of the conduction band occurs at the same crystal momentum position as the maximum of the valence band (Γ). Contrary, an indirect band gap semiconductor presents the minimum of its conduction band at a different crystal momentum position. This gives rise to different electronic behavior of them. Electrons of the valence band can be excited through thermal excitations or the absorption of radiation, forming an electron - hole pair. Once an electron - hole

pair is created, it can recombine resulting in the emission of a photon. In the case of direct band gap semiconductors this process is a purely radiative recombination. Contrary, in the case of indirect band gap semiconductors phonons are also involved in the transition for momentum conservation. This fact supposes limitations in electronic applicability of semiconductors. Figure 1.2 shows the E(**k**) band diagram of Si (indirect band gap) and GaAs (direct band gap) and schematics of recombination processes with E_g energy.

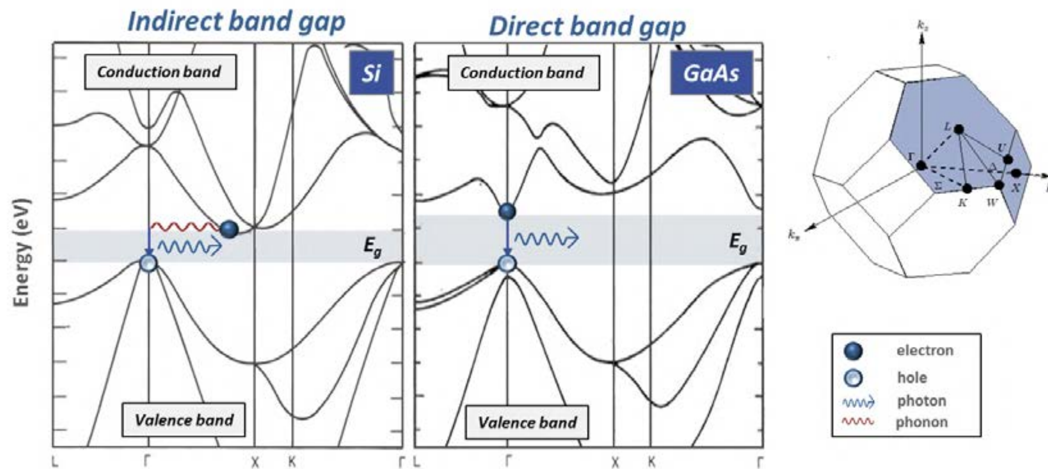

Figure 1.2: Band diagram of indirect (Si) and direct (GaAs) band gap semiconductors with schematics of **k** directions in the Brillouin zone of a face centered cubic lattice.

Another semiconductor classification can be done regarding the nature of their conduction processes. A semiconductor is said to be intrinsic (or i-type) when it is a pure material, without any doping species present. In this case the carrier generation is uniquely produced by the creation of electron-hole pairs. In intrinsic semiconductors the density of electrons (n) and the density of holes (p) are equal. Oppositely, extrinsic semiconductors are materials where doping agents (impurities) are incorporated to the crystal, which tune their electrical properties by providing additional charge carriers and inducing additional states within the band gap.

Depending on the type of impurities added to the material the semiconductor can be n-type or p-type doped. In n-type semiconductors the impurities increase the number of negative carriers (electrons). For this reason, they are called donor impurities, which create additional energy levels close to the conduction band. Therefore, the majority carriers in n-type semiconductors are electrons (n) while holes arise only from electron - hole pair generation. On the other hand, p-type doping accepts electrons from the lattice by creating vacancies or holes and thereby these are called

acceptor impurities. The incorporation of acceptor impurities within a semiconductor results in additional energy levels close to the valence band. This results in holes (p) as majority carriers, being electrons just provided from electron - hole pairs.

The Fermi level can be considered to be a hypothetical energy level of an electron, such that at thermodynamic equilibrium this energy level would have a 50% probability of being occupied at any given time. This value is also affected by the doping concentration: it relays closer to the conduction band in n-type semiconductors and closer to the valence band in p-type semiconductors, where relative position of it with respect to the valence or conduction bands depends on the density of impurities, being closer to the respective bands for higher concentrations. Typical concentration values of dopants are in the range of 10^{13} to 10^{20} cm^{-3}, meaning one doping atom per 10^{10} to 10^{3} lattice atoms. However, for higher concentrations the Fermi level can relay inside the conduction band and the material behaves as a metal. In this situation the semiconductor is said to be degenerated.

1.1.2 Heterojunctions

Electronic systems such as diodes or transistors are based in the stacking of semiconductors presenting different properties. These combinations are named junctions. A homojunction consists in combination of two semiconductors with the same band gap value, but typically presenting different doping. In most cases a p-type material is interfacing an n-type material, forming the called p-n junction. The difference in doping cause band bending and a depletion region at the interface. As a consequence of the charge redistribution electric fields and electrostatic potentials appear.

Nevertheless, most technological devices are based in heterojunctions, or equivalently, interfaces between materials presenting different band structure, including two materials presenting unequal band gaps or semiconductor- metal/insulator interfaces. The performance of the heterojunction relies upon the relative alignment of valence and conduction bands of both materials. This advantage opens a broad branch of possibilities on band engineering for tailoring the device optoelectronic performance according to each desired application.

The relative alignment of the two materials bands is mainly determined by their band gap (E_g), their doping concentrations (N_A/N_D) and the electron affinity (χ) of the materials. Lattice constants of the materials and their spatial variations (strain) may also have effects on band alignment, as it is described in the following sections. From the proper calculation of these parameters the electronic bands of the heterojunction can be predicted, and so the performance of the devices can be engineered. In the case of non-degenerated semiconductor-semiconductor interfaces there are three possible configurations, named as type I, II and III. The band configurations are shown in Figure 1.3.

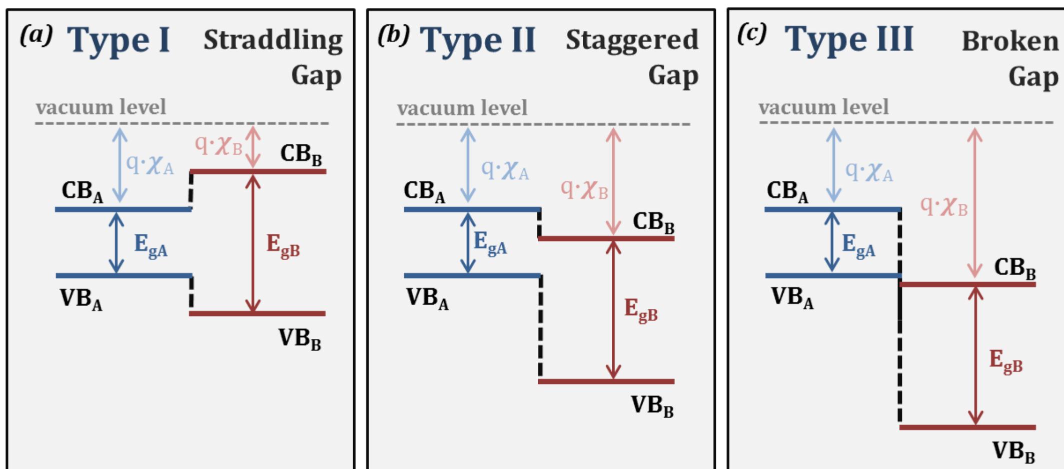

Figure 1.3: Band configurations for semiconductor - semiconductor type I (a), type II (b) and type III (c) heterojunctions.

In type I heterojunctions, or straddling gap junctions (Figure 1.3a), the energy gap of one of the materials (A) lies within the band gap energy range of the second material (B) when taking the vacuum level as a reference energy ($q\chi$). Then, the conduction band of material A is at lower energy than the one of material B ($E(CB_A) < E(CB_B)$) while the valence band of A is at higher energy than valence band of B ($E(VB_A) > E(VB_B)$). In this type of heterojunction electrons and holes get spatially confined in the lower band gap material, so efficient recombination processes can occur. For that reason type I alignment is widely utilized in optical devices such as light emitting diodes (LEDs) and lasers [1]. In addition, multiple heterojunctions formed as a stacking of quantum wells enhance the performance of the devices [2].

Figure 1.3b illustrates the relative band alignment of type II heterojunctions. Also

called staggered gap junctions, this type of junction is created whenever either valence or conduction bands of one constituent lies within the energy gap of the other. This situation is satisfied whenever $E(CB_A) > E(CB_B)$ and $E(VB_A) > E(VB_B)$. These type of junctions are ideal for photovoltaic devices and photodetector systems, so they have been extendedly used [3, 4].

The last possible situation, known as type III heterojunction or broken gap junction, encompasses those interfaces in which there is no overlapping of band gap regions in energy, as shown in Figure 1.3c. Despite this band alignment is the less common when combining typical semiconductors, it can be exploited for tunnel field-effect transistors [5] and multi-junction solar cells [6].

Together with the bulk material properties to be considered when designing optoelectronic devices, the sharpness of the junction is also highly susceptible to variations in composition in the interfaces and strain arising from the material stacking. Actually, fluctuations in composition at interfaces as alloying, for example, present different band gap and band offsets than the primary compounds of the junction. This might even lead to a change in the type of heterojunction [7]. Therefore, it is required to engineer material configurations up to the atomic level in order to achieve a proper device performance, as presented in the following sections.

1.2 An atomistic approach to binary semiconductors

Semiconductor based technology has been mainly composed by crystalline silicon and germanium, which are elemental semiconductors belonging to group IV. The electronic configuration of Si is $1s^2 2s^2 2p^6 3s^2 3p^2$, so the last occupied electron shell is s^2p^2 type, same as for Ge and other group IV materials. sp^3 hybridization occurs in these situations, creating a tetrahedral bonding configuration with bond angles of $\sim 109.5\ ^{\circ}$ (Figure 1.4a). This drives group IV semiconductor materials to crystallize in face centered cubic (FCC) diamond structure belonging to space group FD$\bar{3}$M (Figure 1.4b).

Nonetheless, group IV elemental semiconductors present very narrow band gaps which are at the same time of indirect nature, as stated in Table 1.1. In addition, these elements present low electron mobility in comparison to some binary compounds

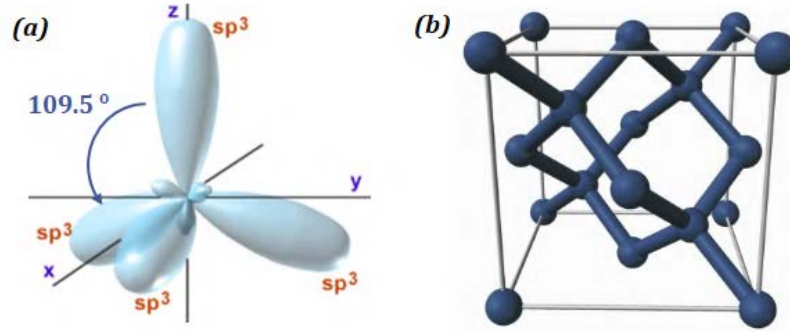

Figure 1.4: (a) Tetrahedral coordination through sp^3 hybridization. (b) Unit cell of cubic diamond-like structures.

combining group II or III species with group IV or V species, respectively. For these reasons, the field of electronics is moving towards the proper combinations of these binary materials rather than elemental semiconductors. The following sections are focused in describing the properties of these binary compounds and their ternary and quaternary alloys.

TABLE 1.1: Properties of group IV elemental semiconductors at 300 K [8, 9].

Material	Crystal phase	Lattice constant (Å)	E_g (eV)	Electron Mobility ($cm^2/V{\cdot}s$)
Diamond	FD$\bar{3}$M (cubic FCC)	a = 3.57	5.47(Indirect)	2200
Silicon	FD$\bar{3}$M (cubic FCC)	a = 5.43	1.12(Indirect)	1400
Germanium	FD$\bar{3}$M (cubic FCC)	a = 5.66	0.66(Indirect)	3900

1.2.1 Binary III-V and II-VI semiconductors

Even though silicon has been widely used for optoelectronics thanks to its robustness, low cost and the ease of processing it, the technological advances have required direct and tunable band gap materials together with a higher carrier mobility for faster operation setups. For this reason, binary combinations of materials are being implemented. These combinations are usually formed by IV-IV, III-V, II-VI or even I-VII elements, and they are highly stoichiometric. Together with the advantages of the intrinsic material properties of these compounds overcoming Si or Ge (Tables 1.2, 1.3), their alloying forming ternary or quaternary compounds allows tailoring materials for precise control over their properties, as it will be stated in section 1.2.2.

TABLE 1.2: Properties of bulk III-V binary semiconductors at 300 K [8, 9].

Material	Crystal phase	Lattice constant (Å)	E_g (eV)	Electron Mobility ($cm^2/V{\cdot}s$)
AlN	$P6_3mc$ (WZ)	a = 3.11, c = 4.98	6.28(Direct)	300
AlP	$F\bar{4}3m$ (ZB)	a = 5.46	2.45(Indirect)	60
AlAs	$F\bar{4}3m$ (ZB)	a = 5.66	2.15(Indirect)	200
AlSb	$F\bar{4}3m$ (ZB)	a = 6.14	1.62(Indirect)	200
GaN	$P6_3mc$ (WZ)	a = 3.19, c = 5.19	3.40(Direct)	1000
GaP	$F\bar{4}3m$ (ZB)	a = 5.45	2.27(Indirect)	250
GaAs	$F\bar{4}3m$ (ZB)	a = 5.65	1.42(Direct)	8500
GaSb	$F\bar{4}3m$ (ZB)	a = 6.09	0.75(Direct)	3000
InN	$P6_3mc$ (WZ)	a = 3.50, c = 5.72	0.70(Direct)	3200
InP	$F\bar{4}3m$ (ZB)	a = 5.86	1.34(Direct)	5400
InAs	$F\bar{4}3m$ (ZB)	a = 6.05	0.36(Direct)	$4.0{\cdot}10^4$
InSb	$F\bar{4}3m$ (ZB)	a = 6.47	0.17(Direct)	$7.7{\cdot}10^4$

TABLE 1.3: Properties of some bulk II-VI binary semiconductors at 300 K [8, 9].

Material	Crystal phase	Lattice constant (Å)	E_g (eV)	Electron Mobility ($cm^2/V{\cdot}s$)
ZnSe	$F\bar{4}3m$ (ZB)	a = 5.67	2.82(Direct)	500
ZnTe	$F\bar{4}3m$ (ZB)	a = 6.10	2.39(Direct)	340
CdS	$P6_3mc$ (WZ)	a = 4.14, c = 6.75	2.50(Direct)	340
CdSe	$P6_3mc$ (WZ)	a = 4.30, c = 7.02	1.71(Direct)	720
CdTe	$F\bar{4}3m$ (ZB)	a = 6.48	1.47(Direct)	1050

Binary compounds of III-V or II-VI groups present high stoichiometry (AB, being A a group III(II) element and B a group V(VI) element) and usually crystallize in cubic zinc blende (ZB) structure (space group F$\bar{4}$3M). This structure is similar to cubic diamond as atomic species occupy the same positions within the unit cell, but in this case two oppositely charged atomic species alternate positions, so every A (B) atom is surrounded by 4 B (A) atoms. The configuration is, in fact, equivalent to two FCC lattices (one containing the cation and a second containing the anion) interconnected and displaced by $(\frac{1}{4}, \frac{1}{4}, \frac{1}{4})$ in the unit cell. Therefore, the bonding acquires a certain ionicity and couples of oppositely charged atomic species are created. These dipole-like atomic couples are called dumbbells and they create internal electric fields that strongly influence the growth and properties of the material [10, 11]. The crystal directions in which the dumbbell pairs create a net electric field are then defined as polar directions, which can be either A - polar (cation - polar) or B - polar (anion - polar).

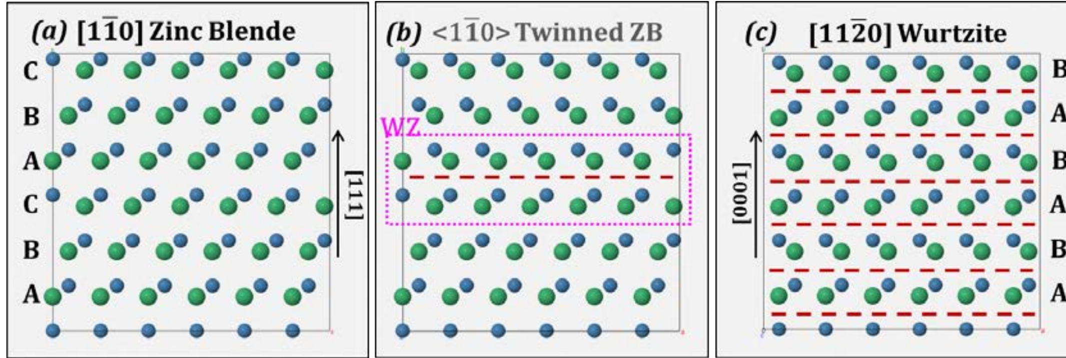

Figure 1.5: (a) The [1$\bar{1}$0] projection of an AB binary compound in zinc blende (ZB) structure with stacking sequence along the [111] direction indicated. (b) Twinning in a {111} plane of ZB structure indicated as a red dashed line. The twin can be considered as a monolayer of the hexagonal wurtzite phase (WZ). (c) [11$\bar{2}$0] projection of an AB binary compound in wurtzite structure with stacking sequence along [0001] direction. The structure can be considered as a ZB structure twinning at each {111} plane, as red dashed lines indicate.

These compounds are very sensitive to the appearance of defects, as detailed in section 1.2.3, and among them twin boundaries are planar defects that occur with very high frequency in {111} planes. Rotational twins or mirror twins occur after a 180 ^{o} rotation around the normal vector of the plane. When twinning occurs in every consecutive {111} ZB plane, a hexagonal symmetry appears in the crystal [12, 13]. This atomic arrangement is known as wurtzite (WZ) structure, belonging to $P6_3mc$ space group, and it is more stable than ZB cubic structure in group III nitrides (III-N) and some II-VI (as ZnS or CdSe) compounds (Tables 1.2, 1.3). Figure 1.5 shows the similarities and differences between ZB, single twinned ZB and multiple twinning in ZB resulting in WZ structure visualized from a <1$\bar{1}$0> zone axis. In that regard, a {111} twin in ZB structure can be considered as an inclusion of a WZ monodomain within the lattice. It is interesting to take into account that a WZ inclusion in ZB or vice-versa may create a homojunction within the material which can affect the band alignment if both phases have a different band structure [12, 14].

It can be noticed then that regardless the spatial symmetry differences of both zinc blende and wurtzite structures, they are indeed quite similar in certain crystal directions. Actually, it is very common to find stacking of both structures in $< 111 >_{ZB}$ grown materials, where the growth direction becomes $< 0001 >_{WZ}$ when phase turns to be wurtzite. It is then straight forward to derive the wurtzite lattice constants from geometrical factors of the equivalent zinc blende when neglecting

any other distortion.

$$a_{WZ} = \frac{1}{\sqrt{2}} a_{ZB} \quad \text{and} \quad c_{WZ} = \frac{2}{\sqrt{3}} a_{ZB} \tag{1.1}$$

The c/a ratio should have a value of $\sqrt{8/3}$ according to Eq. 1.1, but geometric considerations do not consider tetrahedral distortions of hexagonal symmetry and real c/a values slightly deviate from the ideal situation. Notice that these common geometrical distortions in binary systems such as GaN or ZnO might create a decompensation of the dipoles in the tetrahedron, originating the formation of internal electric fields which are responsible of well-know effects as the quantum-confined Stark effect [15] or the presence of piezoelectric properties.

Due to the structural similarities of wurtzite and zinc blende crystal phases, it is important to precisely enhance their main differences when projected along high symmetry directions. Figure 1.5 already highlights that from <110>$_{ZB}$ or <11$\bar{2}$0>$_{WZ}$ projections the main difference between ZB and WZ is a difference in the stacking sequence along <111>$_{ZB}$ or <0001>$_{WZ}$. While the bilayer stacking sequence is $ABCABC$... in ZB, it turns to be $ABABAB$... in WZ. In this case dumbbells are separated $a_{ZB}/4$ apart, corresponding to the $\{004\}$ interplanar distance. It can be noticed that in the vertical direction of this projection (<111>$_{ZB}$ or <0001>$_{WZ}$) there is a net contribution of dipole-induced electric field as all dumbbells are oriented in the same direction. As this is the usual growth direction of nanostructures, the growth is commonly said to be A (cation) or B (anion) polar. However, when looking to the horizontal direction which correspond to <1$\bar{2}$1> in the case of ZB and <1$\bar{1}$00> in the case of WZ, there is a net lateral electric field in the case of ZB, making <1$\bar{2}$1> a polar direction, but the in-plane 180º rotation of dumbbells in wurtzite makes the electric field of dumbbells compensate between them. Therefore <1$\bar{1}$00> direction of WZ is non-polar.

When projecting the structure of Figure 1.6 after a 30º rotation around <111>$_{ZB}$ or <0001>$_{WZ}$, the <1$\bar{2}$1>$_{ZB}$ or <1$\bar{1}$00>$_{WZ}$ projection is reached. It can be observed in Figure 1.6 how both hexagonal and cubic phases are indistinguishable from this direction. Together with this fact, the dumbbell separation observed from this direction is just $a_{ZB}/4\sqrt{3}$, which corresponds to the $\{444\}$ plane distance. This makes

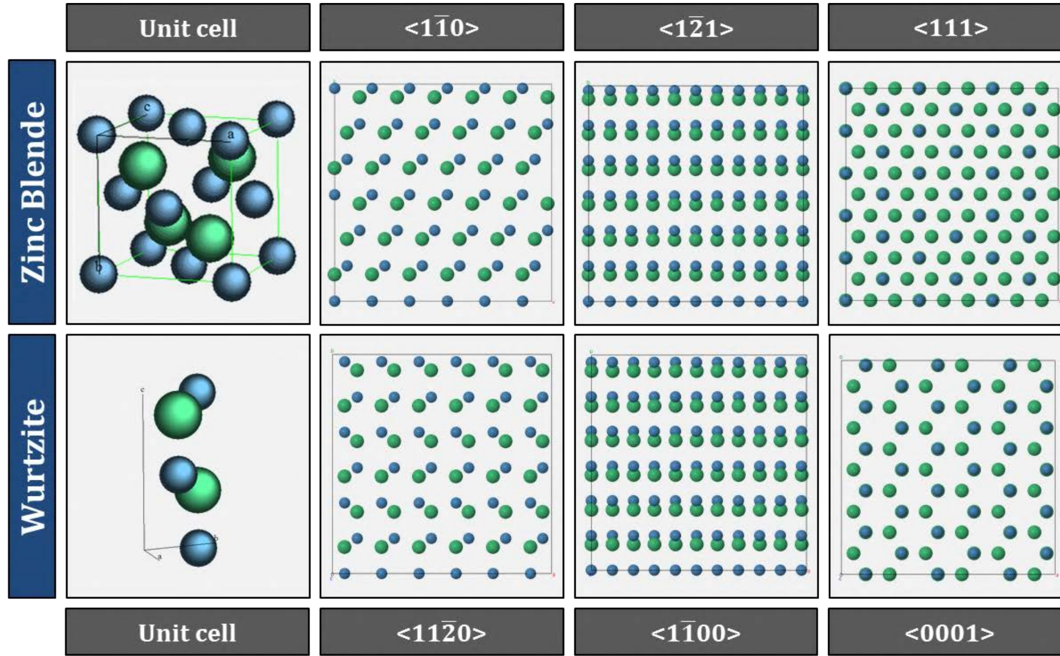

Figure 1.6: Unit cell of an AB binary compound in zinc blende (top) and wurtzite (bottom) structure and projections along some high symmetry crystal directions.

this crystal direction complicated also for vertical polarity determination as ultimate spatial resolution is required (usually the distances relay below 0.1 nm). Regarding the lateral polarity, it is easily observed that lateral $\{110\}_{ZB}$ and $\{11\bar{2}0\}_{WZ}$ are non-polar planes.

Finally, it is interesting to observe the hexagonal symmetry of the structures when projected along the <111>$_{ZB}$ or <0001>$_{WZ}$ directions. It can be noticed how the main difference is the presence of an atomic column in the center of the hexagonal arrangement in the case of ZB, while this position is empty in WZ. These geometries are responsible of a perfect stacking when adding one on top of the other thanks to these similarities, making it very common to have WZ inclusions in ZB grown materials or vice-versa.

Together with the most stable cubic and hexagonal polytypes in which III-V and II-VI materials crystallize, several other polymorphs are stable. The material properties are very susceptible to it, specially electronic conductivity or band gap. The higher the degree of hexagonality of the resulting periodic structure the closer the material properties are to the ones of wurtzite material. Figure 1.7 shows the atomic stacking in some of the polytypes of Si-C like compounds.

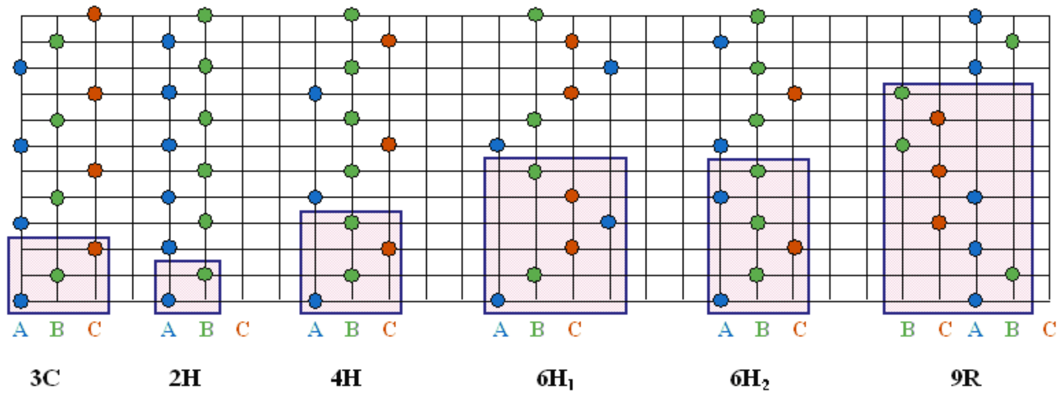

Figure 1.7: Stacking sequence of SiC polytypes labelled according to Ramsdell notation [16]. The unit cell is given by the shortest periodically repeated stacking.

1.2.2 Ternary and quaternary alloys: Vegard's law

The interest in employing binary semiconductors as an alternative to the elemental ones does not rely just in the more suitable characteristics for their electronic performance. The possibility of tuning their properties by alloying different compounds opens a broad branch of combinations for precise band engineering. Assuming two binary compounds AC and BC, a ternary alloy with a stoichiometry $A_xB_{1-x}C$ presents a lattice constant which follows a linear tendency between a_{AC} and a_{BC} as a function of the x fraction. This can be also extended for quaternary alloys like $A_xB_{1-x}C_yD_{1-y}$.

The mathematical expression for this empirical rule is known as *Vegard's law* [17] and it can be expressed as:

$$a_{A_xB_{1-x}C} = x \cdot a_{AC} + (1-x) \cdot a_{BC} \tag{1.2}$$

although some small deviations occur depending on the radii of the covalent bond between the species [18].

As stated previously, the band gap is determined by the structural factors of the lattice, such as the lattice constant. Therefore it is strongly affected by the molar fraction x of the alloy compound. A linear interpolation between the band gap of the two binary compounds predicts the band gap of the alloy as function of x, but a curvature correction characterized by the bowing parameter (b) gives a more accurate

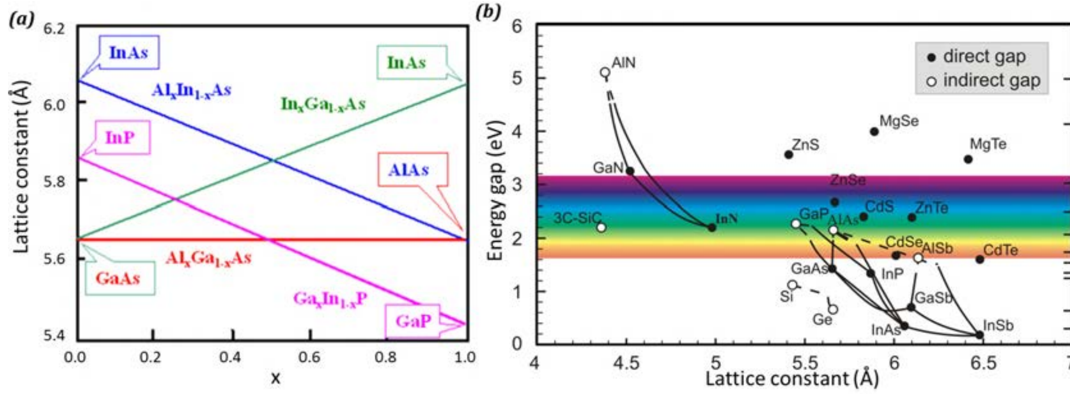

Figure 1.8: (a) Lattice constant of III-V ternary alloys following Vegard's law. (b) Band gap energy as a function of the lattice constant of several binary semiconductors. The nature of the gap of ternary compounds is indicated with continuous (direct) or discontinuous (indirect) lines.

estimation. In that regard, the band gap of a ternary alloy of AC and BC would be expressed as:

$$E_{g,A_xB_{1-x}C} = x \cdot E_{g,AC} + (1-x) \cdot E_{g,BC} - b \cdot x \cdot (1-x) \tag{1.3}$$

Thus, it can be noted that the band gap of alloys can be finely adjusted by tailoring the composition of the compounds. It is of particular interest for optoelectronic applications that all the visible range of the electromagnetic spectrum ($\sim$ 1.65 - 3.10eV) can be obtained in terms of band gap with the appropriate material selection, as reflected in Figure 1.8b. II-VI compounds present band gaps in the visible range, while in most III-V compounds it stands at the infrared or low visible energies (with exceptions on materials such as AlN or GaN which present a wider band gap). This fact allows covering from near ultraviolet (UV) to infrared (IR) photon frequencies with the proper material combinations.

1.2.3 Defects in semiconductor materials

The relevance of atomic structure and composition on material properties has been exposed so far. In this regard, their crystal quality plays also a critical role. Binary semiconductors are susceptible to suffer from structural defects, which are typically characterized according to their dimensionality. Point defects or zero-dimensional

defects as vacancies or dopants have been introduced previously. They are responsible of introducing additional states within the energy gap, modifying then the carrier density and the overall conductivity of the material.

Line-defects or one-dimensional defects, also called dislocations, correspond to misalignments along one crystallographic direction. Dislocations are described by the Burgers vector, which characterizes the magnitude and direction of the lattice distortion. For establishing the Burgers vector, a rectangled circuit where the width and length are integer multiples of the direction plane spacing is drawn. It should close around a non-distorted lattice. However, the circuit fails to close when tracing it around a dislocation. The vector needed to connect start and end points in this situation is named the Burgers vector. The dislocation is named screw dislocation when the vector is parallel to the dislocation line while it is said to be an edge dislocation when they are perpendicular.

Edge dislocations are particularly frequent at the interfaces of semiconductor heterostructures arising from the lattice mismatch between materials (misfit dislocations) [19]. Then, an extra plane perpendicular to the interface is present in the material with lower plane spacing, causing plane bending, compressions and dilatations in the region imminently close to the dislocation (Figure 1.9a). For this reason, they are detrimental for electronic devices as they act as non-radiative recombination centers and introduce extra states in the energy gap that can lead to a complete failure of the device performance [20]. In addition, they can act as carrier trapping centers that deteriorate the conductance of the material.

When considering planar defects (or bi-dimensional defects) the most commonly observed are twin boundaries and stacking faults. Twin boundaries, as explained above, consist in an in-plane rotation around the plane vector axis. However, in heteroatomic semiconductors twin boundaries can be divided in two types: ortho-twins and para-twins. In ortho-twins (or rotational twins) the polarity is preserved across the defect (Figure 1.9b). Actually, it is worth to mention that twinning it is more likely to happen in certain polar $\{111\}$ planes depending on the growth conditions and the material in consideration [21, 22]. Para-twins (or mirror twins) include an extra 180 ^{o} rotation around $\{110\}$, which results in a mirror symmetrical polarity or polarity inversion (Figure 1.9c). However, mirror twinning is far less dominant due

to the high cost in energy to form the homopolar bonding in the case of III-V or II-VI and has been just observed in IV-IV binary semiconductors such as SiC [23].

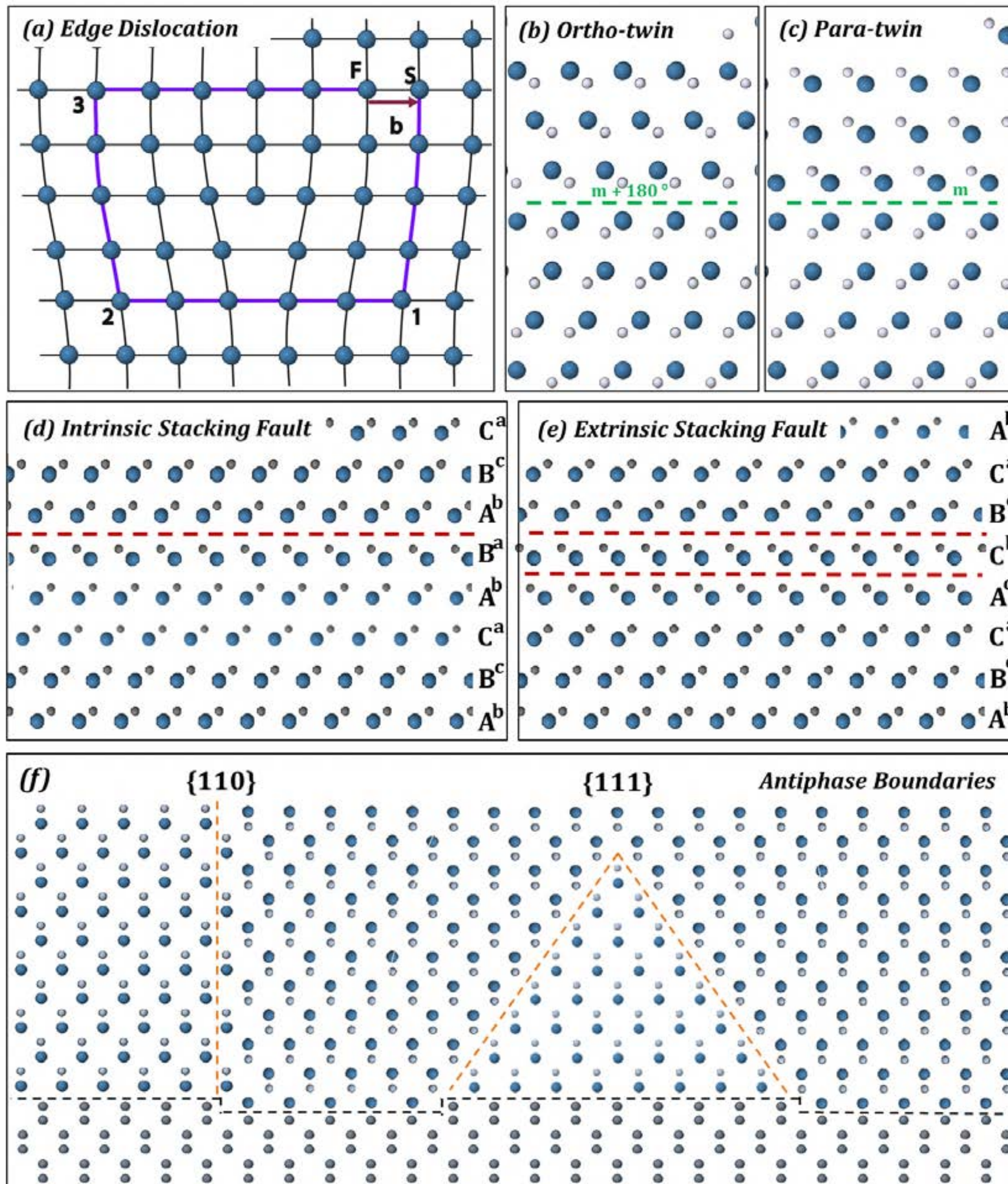

Figure 1.9: Atomic models of defects in binary semiconductors. (a) Edge misfit dislocation and Burgers circuit around it [23]. (b) Ortho-twin and (c) para-twin. (d) Intrinsic and (e) extrinsic stacking faults with their corresponding stacking sequences. (f) {110} and {111} antiphase boundaries arising from a monoatomic step in a {001} non-polar substrate.

It is interesting to mention that periodic twinning is responsible of the different polytypes that can coexist in such materials, as detailed in Section 1.2.1. Therefore, twinning might be responsible of spontaneous multi quantum well structures that dramatically influence material optoelectronics [14, 24–26].

The other common planar defects, stacking faults (SFs), refer to an interruption of the regular stacking sequence at certain atomic planes (usually $\{111\}$ planes), but stacking remains the same manner after the defect. SFs can be either intrinsic when a plane is removed from the perfect stacking or extrinsic when one additional plane is inserted. They are easily formed due to their low formation energy.

Last but not least, Antiphase Boundaries (APBs) are a special case of two dimensional defects in which an inversion of polarity is occurring at each side of the boundary and anti-site bonds (cation - cation or anion - anion) are created. They are mostly produced due to monoatomic steps in non-polar materials (such as group IV semiconductors) employed as substrates. Some APBs propagate through the entire material following $\{110\}$ planes or appear in $\{111\}$ planes, where kinking appears and they self annihilate. Nevertheless, the later are less energetically favorable [27]. It should be noted that the anti-site bonds are responsible of inverting the inner polarization field, which has detrimental effects on device performance [28]. Other more complex defects that sometimes involve polar inversion might appear when propagating defects merge together. It is important to characterize them as they alter the material's optical and electronic behavior.

1.3 Epitaxy in heterostructured materials

Electronic devices are mainly based in the combination of materials presenting different electronic properties to create heterojunctions. In practice, these junctions are achieved by the epitaxial growth of materials, but different phenomena might occur at the interface depending on the crystalline structure of both materials involved. Considering the growth of a material $'m'$ on a substrate $'s'$, both being cubic materials, the lattice mismatch ε between both materials is given by

$$\varepsilon = \frac{a_m - a_s}{a_s} \tag{1.4}$$

where $a_{m/s}$ is the lattice constant of the material/substrate. However, it should be noted that depending on the crystal symmetry and lattice constant different epitaxial relationships are possible. In this second case $a_{m/s}$ should be replaced by $d_{m/s}$, where

$d_{m/s}$ is the interplanar distance of the planes of the material/substrate perpendicular to the interface.

Lattice mismatch is reaching zero when a material is grown on top of itself in a process called homoepitaxy, where the interface is fully coherent and no deformations occur on it. Contrary, when coupling two different phases the material suffers from deformations that influence the efficiency of the junctions. In the case of materials presenting low mismatch ($|\varepsilon| < 1$ %) the first grown epilayer accommodates to the lattice constant of the substrate, with the consequent appearance of strain fields (either tensile if $a_m < a_s$ or compressive if $a_m > a_s$). Elastic energy gets increased with the increase in layer thickness until a critical thickness where the creation of a dislocation is energetically more favorable. In this situation, a plastic deformation event (misfit dislocation) is created to release the amount of accumulated energy. Strain affects the carrier mobility [29] and band structure of materials, including even indirect to direct band gap transitions [30], so the epitaxial relations between materials have to be considered for device fabrication.

When coupling two highly mismatched materials the epitaxy can take place by the creation of crystal domains consisting in m planes of the material for each n planes of the substrate [31, 32]. This mechanism is commonly named domain match epitaxy or coincident lattice epitaxy, and the density of 'dangling' planes at the interface can be easily calculated by taking into account the coincidence of planes between substrate and material. Some residual misadjustment can remain in the lattice after domain formation. In this situation, we talk about the coincidence lattice mismatch δ, which gives some insights on the remaining strain in the heterostructures.

$$\delta = \frac{m \cdot d_m - n \cdot d_s}{n \cdot d_s} \tag{1.5}$$

being m and n the integer number of planes of the substrate and material within the periodic crystal domains. More details on domain match epitaxy are given in Chapter 6.

It has been pointed out before that dislocations act as non-radiative recombination centers, so several strategies as the use of buffer layers are commonly employed to get rid of them when growing heteroepitaxial structures. In the case of

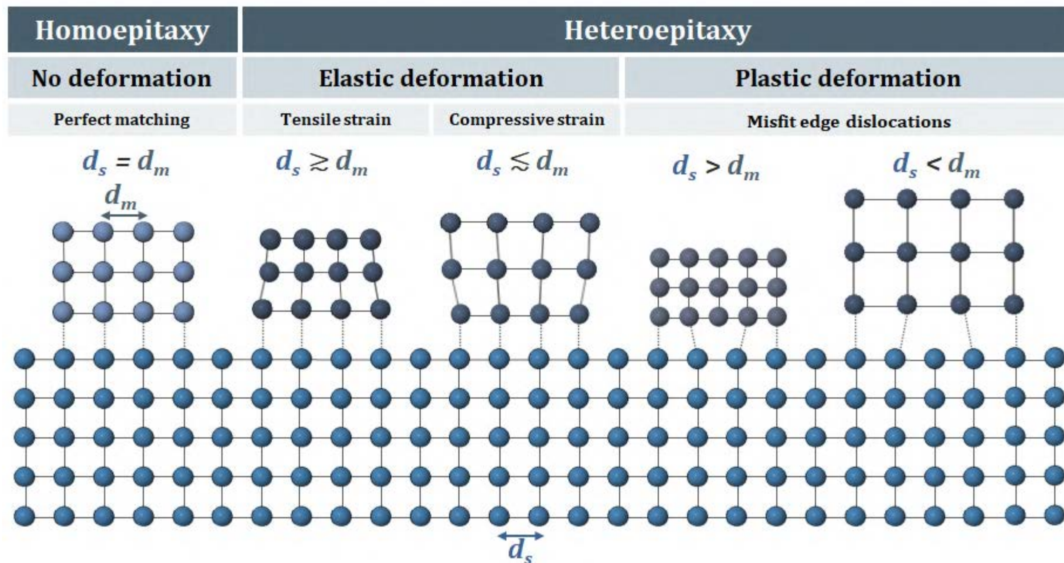

Figure 1.10: Schematics of lattice distortions when matching two different crystal phases for different casuistics in material - substrate plane spacing differences.

nanostructured objects, the limited lateral dimensions are capable of accommodating much more strain by preserving coherent interfaces even when coupling highly mismatched materials. This is just one of the multiple advances that nanostructuring materials have brought to material engineering.

1.4 Nanostructured semiconductors: Nanowires

The visionary lecture "There's plenty of room at the bottom" given by Richard P. Feynman (Nobel prize in Physics, 1965) during the American Physical Society annual meeting in Caltech in 1959 [33] conceptualized the possibility of direct atom manipulation and the benefits it would bring for several technological applications. Within this concept, he proposed some challenges in the framework of scaling down macroscopic items. Even though it took some years to implement those concepts to research and technology, his speech is considered the starting point of the multidisciplinary field baptized as nanotechnology. It was in the 1980s when the technological developments made possible the experimental implementation of the theoretical concepts at the nanoscale by the creation of a broad range of low-dimensional structures.

Nanostructured materials are typically classified according to their dimensionality, where the concept of dimension is defined as zero for sizes below 100 nm, or equally, their dimensionality accounts for the number of dimensions out of the nanometer range. In that regard, 0-D nanostructures are such that all their dimensions remain between 1 and 100 nm (such as nanoparticles [34–36], nanorods [37], quantum dots [38]...), 1-D structures present filamentar-like morphology (nanowires [39], quantum wires [40, 41], nanotubes [42]...), 2-D nanostructures present a planar geometry (thin films [43, 44], monolayers [45]...) and the concept of 3-D nanostructures relays on volumetric structures with nanosized features (nanocomposites [46–48], tetrapods [49], exotic hollow particles [50]...). The increasing interest in nanostructuring materials arises from quantum mechanics effects being relevant under a certain size threshold in such a way that tuning geometry and size of materials allows tailoring their properties. In addition, the increased surface-to-volume ratio enhances the performance of surface phenomena accompanied with a reduced material cost, as for example in the field of catalysis [51].

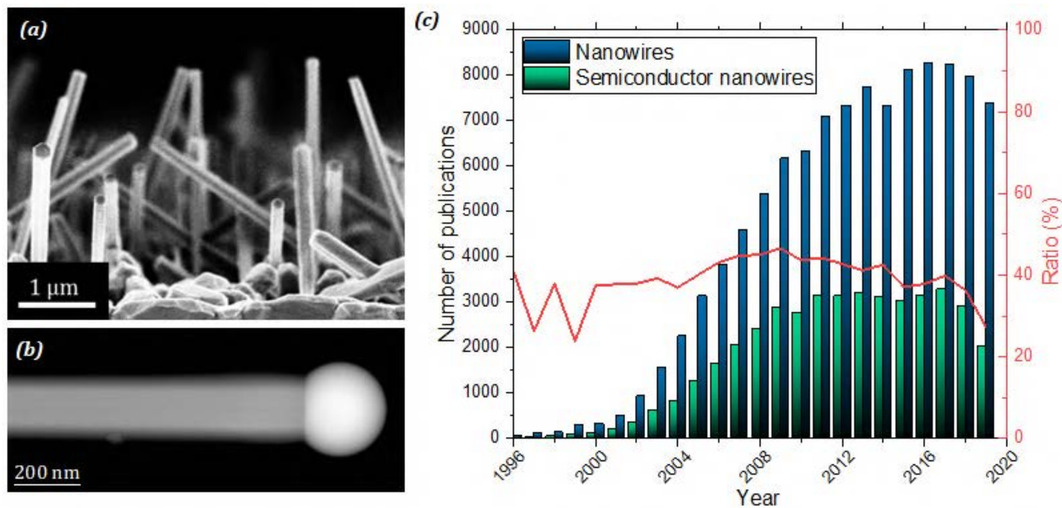

Figure 1.11: (a) Cross-sectional SEM image of GaAs nanowires grown on a GaAs substrate. (b) HAADF-STEM image of a GaAs nanowire. (c) Number of publications per year in the topics of nanowires and semiconductor nanowires. Up to 40 % of the publications regarding nanowires are related to semiconductor nanowires. [52].

This thesis is based in 1-D semiconductor materials, mainly nanowires, which present an enhanced performance than the equivalent bulk materials in electronic and optoelectronic applications. Nanowires (NWs) typically present diameters between 10 and 100 nm, while their length ranges from hundreds of nanometers to few micrometers (Figure 1.11a,b). This geometry provides confinement in two dimensions, but one unconfined direction remains available for conduction of electrons,

holes or photons. In addition, it was introduced before that the amount of strain that can be sustained in an epitaxially grown material depends on the size of the structure. Particularly, nanowire morphologies are able to sustain much more strain preserving higher crystallinity than their equivalent bulk counterparts. This allows combination of materials not possible at the macroscopic scale for the creation of ultimately tailored heterojunctions which allow a precise control and engineering of proper devices. Thanks to these facts, device functionalities such as field-effect transistors [53], logic gates [54] or p-n junction diodes [55, 56] typical in conventional semiconductor technology can be created with an enhanced tunability and performance. More recently, they have been proposed as a basis for developing scalable topological quantum computing devices [57–61]. In addition, several applications can be found in the field of photonics including their use as photodetectors [62], light emitting diodes [63] or solar cells [64]. Their outstanding advantages in comparison to their bulk homologous have produced a great interest in the scientific community during the last decade for a precise control over growth and properties of these nanostructures (Figure 1.11c).

1.4.1 Nanowire growth approaches

The fabrication of nanosized structures can be carried out following many different procedures which have been traditionally classified into top-down or bottom-up approaches. As their name indicates, top-down techniques consist in reducing the initial size of the material until reaching the desired dimensions by cutting, milling or etching them. It can be understood as sculpting the material using either chemical or physical routes. In the case of NWs, they can be obtained in a top down approach by patterning a semiconductor wafer with metals followed by an anisotropic chemical etching, for example. These set of techniques allow the easy production of ordered arrays which facilitates the creation of electrical contacts and their integration into large-scale devices. In addition, these processes are compatible with standard electronics industry which facilitates scaling-up. However, this approach supposes several drawbacks. The first one relays on the impossibility of creating heterostructured wires without the previous compositional modulation of the wafer. In this case, the benefits of nanosized morphologies for sustaining strain when coupling highly mismatched materials are lost. Another option would be employing post-growth atomic

implementation methods, but this supposes additional costs and time consumption.

Due to the poor flexibility in materials design of top-down approaches, bottom-up techniques are the dominant ones in the growth of NWs. In such techniques the structure is built by assembling atoms into the desired morphologies. In this regard, an anisotropic one-dimensional growth has to be achieved for producing nanowires. The most used technique during the last decade is Vapor-Liquid-Solid (VLS) growth, whose name refers to the three phases of matter involved in the growth. A liquid catalyst in a substrate dissolves the gas precursors of the desired NW material until reaching supersaturation. Commonly, the catalyst droplet forms an eutectic solution that melts at lower temperature than the semiconductor material in a way that the material deposits forming a solid crystal and the growth keeps on longitudinally until forming a nanowire. This growth involves a chemical vapor deposition (CVD) system in which the growth parameters such as temperature, pressure and gas fluxes should be adapted to reduce parasitic lateral overgrowth. Traditionally, metallic nanoparticles were used as catalysts, but they can introduce deep traps in the nanowire and this fact makes them incompatible with CMOS technology [65, 66]. For that reason, VLS growth is evolving to a self-catalyzed approach, like employing Ga as catalyst for the growth of GaAs NWs [67–69].

Bottom-up growth provides a deep control of nanowire composition and geometry which enables the production of complex structures with engineered properties. However, the main drawback is the poor applicability of such promising structures without involving further post-processing device fabrication. This fact limits the scalability of the fabricated NWs and their integration into functional devices.

In order to overcome the limitations of both techniques, mixed techniques (namely SAG and TASE) are taking relevance in the top electronic development companies. The objective of such approaches is to provide scalable routes for predefining nanowire networks while keeping a high structural quality by controlling defect formation and allowing multiple material configurations. Template-Assisted Selective Epitaxy (TASE) has been proposed for growing III-V compounds on silicon for integration in CMOS technologies [70, 71]. A first sacrificial layer of amorphous silicon can be deposited on a Si wafer for further selective etching by electron beam lithography

forming the shape of amorphous Si nanowires. Later on, SiO_2 can be further deposited on the patterned Si nanowires. Etching mediated processes can remove the amorphous silicon nanowire by leaving a substrate exposed nanopillar surounded by a tubular SiO_2 template that can be filled with III-V compounds. Further on, the remaining SiO_2 tube can be removed, leaving the III-V nanowire epitaxially grown on the substrate at predefined positions. However, in this thesis we focus on Selected Area Growth (SAG), also named Selected Area Epitaxy, which consists in covering the substrate with a dielectric mask and patterning it using standard lithographic techniques followed by etching of the desired areas. Then, the vaporized precursors can deposit selectively in the mask openings when adjusting properly the growth conditions. This technique is taking relevance in the last years as it provides the feasibility for the creation of large-scale nanowire based devices [72–75].

These methods suppres the need of a catalyst while keeping the flexibility of bottom-up techniques and at the same time provide the scalability and reproducibility of top-down approaches. Figure 1.12 shows schematically the steps for obtaining vertical nanowires through etching methods, vapor-liquid-solid and selected area growth.

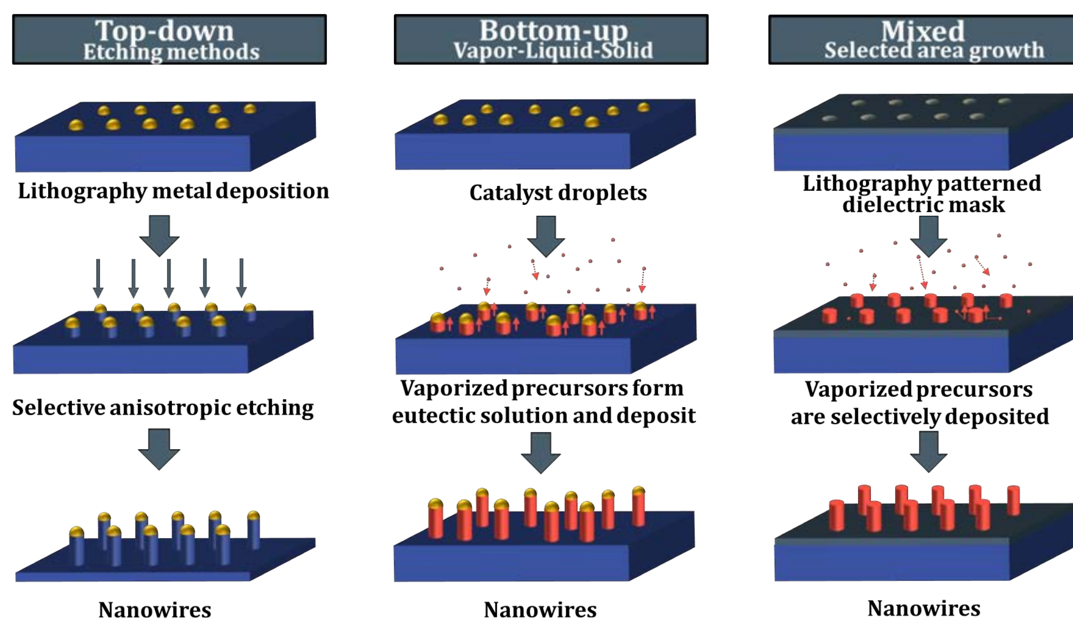

Figure 1.12: Schematics of the steps to produce vertical nanowires through etching methods, vapor-liquid-solid and selected area growth.

1.4.2 State of the art and challenges

Thanks to the deep studies in the VLS growth of nanowires during the last decade, the precise control over their growth conditions has allowed an exceptional tunability of composition, geometry, polarity and growth direction, among others. However, there are some limitations concerning conventional VLS growth in control of defect formation and crystal phase, scalability and integration into functional devices. We will address some solutions from an atomistic point of view in the different chapters of this thesis. Chapter 3 relays in the implications that the polarity has in the growth of nanostructures. Some properties of the NWs are polar-dependent and, in addition, crystal structure, defect generation and elemental segregation have been observed to be influenced by polarity. For that reason, these phenomena are studied by means of Transmission Electron Microscopy from the origin of the crystal in the liquid droplet- solid NW interface.

Nonetheless, even if there is precise control on the growth due to the deep understanding of the different phenomena taking place during it, the difficulties and costs of producing devices, which usually involve single-nanowire manipulation, block the applicability of such structures. One solution to overcome these problems is growing the nanowires into self-assembled arrays by employing VLS guided growth. Core-shell nanowires can be grown and easily manipulated by following this approach, which supposes a deep advance towards the creation of multiple nanowire arrays in a way that enables in-situ device fabrication. However, the creation of such radial junctions might deviate from the expected band alignment due to the epitaxial strain that core and shell exert between each other. In chapter 4, the effects of such strain fields in nanowire performance are analyzed.

Chapter 5 relays in the study of a completely different approach for producing one-dimensional nanostructures in which the scalability of top-down approaches is combined with the compositional control and tunability of bottom-up approaches. This novel technique is known as Selected Area Growth (SAG) and involves substrate prepatterning through lithography as a top-down technique to keep on with the building of longitudinal nanostructures from vapor precursors as a bottom-up technique. In this later case, the growth occurs in a vapor - solid approach in which the need of a catalyst is suppressed, enhancing at the same time the purity of the

grown materials. The potential of this technique is stunning, but the huge area of interaction between the substrate and the material requires deep strain engineering of structures to achieve control over defect formation.

Last but not least, one-dimensional semiconductors are proposed as a basis for topologically protected Majorana quantum devices when coupled to a semiconductor material. Nanowires of high mobility, g-factor and strong spin-orbit coupling are perfect candidates for this purpose when coupled to superconductor materials. As a final study, chapter 6 is based on the epitaxy of aluminum as superconductor coupled to InAs and InSb grown through VLS and SAG and even the possible addition of intermediate ferromagnetic insulator layer for achieving Majorana signatures without needing external magnetic fields. The huge epitaxial mismatch between the compounds together with different crystal symmetries of the involved materials produces complex epitaxy methods that we are discussing with the goal of achieving defect-free materials and perfectly coherent interfaces in hybrid NWs.

All these studies are carried out at the atomic scale by exploiting the multiple imaging and analytical techniques related to (Scanning) Transmission Electron Microscopy. These measurements of the atomic arrangement and chemical composition permit exploring and understanding the mechanisms driving the growth of nanowires for the different considered approaches, all correlating the structure and composition with the (opto)electronic properties of the obtained semiconductor NWs.

Chapter 2
Methodology

Many technological advances have been incorporated in Transmission Electron Microscopes since Ernst Ruska firstly designed an operational device back in 1932. The development of electron optics and exploitation of transmitted and emitted signals arising from electron-specimen interactions have made Transmission Electron Microscopy a very versatile analytical tool with outstanding spatial resolution. In this chapter, a brief summary of the basic principles of Transmission Electron Microscopy and related techniques are presented, emphasizing the state of the art solutions it offers for materials science problems. Micrograph interpretation and spectral analyses require implementation of different computational treatments that are explained. Finally, we present strategies to correlate TEM information with materials properties can be obtained by simulation algorithms thanks to dedicated software.

2.1 Overcoming resolution limits with Transmission Electron Microscopy

When referring to microscopy and imaging sciences the concept of resolution takes a high relevance. Resolution is traditionally defined as the shortest distance between two points where they can be resolved by the observer as separate entities. According to the Rayleigh criterion this distance is given by

$$\delta = \frac{0.61\lambda}{\mu sin\beta} \approx 0.61\lambda \tag{2.1}$$

where λ is the wavelength, μ the refractive index of the viewing medium and β the semi-angle of the lens/aperture. The value $\mu sin\beta$ is known as the numerical aperture of the lens.

Since eyesight is limited to the visible range of the electromagnetic spectrum, our capability to resolve objects is restricted to the range 380 – 700 nm wavelength, meaning the highest resolution achievable with a visible light microscope (VLM) turns to be ∼230 nm. This limits the applicability of VLM into the study of nanomaterials which have by definition some dimension lower than 100 nm.

It was in 1924 when Louis de Broglie described the wave-particle duality of an electron. According to his equation, the wavelength (in nm) associated to an electron accelerated by a voltage V can be defined as

$$\lambda = \frac{h}{\left(2m_0eV\right)^{1/2}} = \frac{1.22}{\left(V\right)^{1/2}} \tag{2.2}$$

which gets modified when considering relativistic effects as

$$\lambda = \frac{h}{\left[2m_0eV\left(1+\frac{eV}{2m_0e^2}\right)\right]^{1/2}} \tag{2.3}$$

According to equations 2.2 and 2.3 sub-atomic resolutions can be obtained when employing voltages even lower than 1 kV, as reflected in Table 2.1.

It didn't take long until the idea of building electron lenses in order to overcome the resolution limits of VLMs. In 1932, Ernst Ruska and Max Knoll built the first prototype of an electron microscope and demonstrated that electron images could be obtained with their instrument, for which the first was awarded with the Nobel Prize in Physics in 1986 [77]. The breaking idea didn't take much to be a revolution

TABLE 2.1: Electron wavelength and theoretical spatial resolution. Adapted from [76].

Accelerating voltage (kV)	Non-relativistic wavelength (nm)	Relativistic wavelength (nm)	Resolution (pm)*
1	0.01734	0.01731	10.589
10	0.01227	0.01221	7.449
50	0.00549	0.00535	3.263
100	0.00386	0.00370	2.257
120	0.00352	0.00335	2.044
200	0.00273	0.00251	1.531
300	0.00223	0.00197	1.202
400	0.00193	0.00164	1.001

**According to Rayleigh criterion and considering perfect lenses.*

in science and only four years later, in 1936, the first commercial TEMs started to be developed. However, resolution limits could not be pushed further because of the imperfections of lenses inducing aberrations in the system. In that regard, the use of aberration correctors, not developed until late 90s, was key for atomic resolution imaging.

2.1.1 Aberrations in (S)TEM

In an ideal optical system any point of the object would be reflected as a point in the image. However, this situation is far from realistic considerations in electron microscopy.

The first origin of image blurring relays directly from the electron beam source, also called electron gun. Historically electron guns exploited thermionic emission of electrons: Tungsten filaments or LaB_6 crystals were heated up to give electrons enough energy to overcome a barrier defined by the materials working function (ϕ). Nonetheless, thermionic electron emission guns present a very high energy spread of 1.5 - 3 eV at 100 kV acceleration voltage. Actual Field Emission Guns (FEG) consist in applying a high voltage in sharp tips so electrons are ejected. This leads to higher brightness compared to thermionic guns as well as reduced energy spread (0.7 eV in Schottky FEG and 0.3 eV in Cold FEG at 100 kV). The energy spread of the incident beam can further be reduced by the use of monochromators, with the compromise of a reduction of brightness, but fully monochromatic beams are unrealistic. The remaining energy spread in the primary beam together with fluctuations in the gun accelerating voltage and energy losses through beam-sample interactions lead to lens chromatic aberration effects.

Electrons presenting different energies focus at different points of the optic axis, as schematized in Figure 2.1a. The chromatic aberration coefficient (C_C) can be defined as a function of the radius of the disc of least confusion r_{chr} and the energy spread ΔE as

$$r_{chr} = C_c \frac{\Delta E}{E_0} \beta \tag{2.4}$$

where β is the collection semi-angle and E_0 is the energy of the primary beam.

Nevertheless, the influence of chromatic aberration is negligible compared to other achromatic aberrations and its effects are just visible when compensating them, although correcting it gets more relevance at low voltages (< 60 kV) when trying to attain atomic resolution. There are five types of monochromatic or achromatic aberrations: spherical aberration, astigmatism, coma, field curvature and distortion, but the three first take much higher relevance than the others. From them, spherical aberration is the main limitation towards atomic resolution. Its origin relays on off-axis rays not focusing at the same point as paraxial rays (Figure 2.1b). The radius of the disk of least confusion r_{sph} depends on the spherical aberration coefficient C_{30} and the collection semi-angle as follows:

$$r_{sph} = C_{30}\beta^3 \tag{2.5}$$

Regarding astigmatism and coma an azimuthal distortion is also added. Astigmatism is caused when the cross-over of the off-axis rays is displaced along the optic axis but the degree of displacement varies with the azimuthal angle of the beam (Figure 2.1c) while coma is related to rays making an angle with the optic axis: rays crossing the centre of the lens focus in the optic axis while rays passing through the peripheral field of the lens are focused in other points (Figure 2.1d).

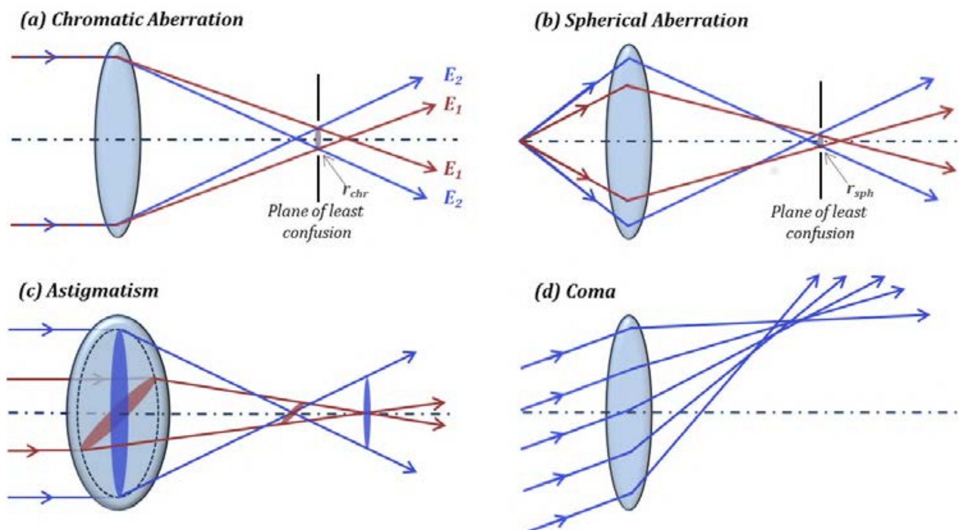

Figure 2.1: Ray diagrams of lenses presenting (a) chromatic aberration, (b) spherical aberration, (c) astigmatism and (d) coma.

A way to mathematically describe aberrations is to introduce the wave aberration function, $\chi(\mathbf{K})$, which describes the difference between a perfect spherical wave and the actual wavefront for a given lens. Eq. 2.6 describes the mathematical expansion up to the fifth order by using the coefficient notation introduced by Krivanek *et al.* [78], in which the coefficient subindexes C_{NS} refer to the radial order (N) and the azimuthal symmetry (S). These coefficients are represented as a graphical glossary up to the fifth order in Figure 2.2.

$$\begin{aligned}\chi(\mathbf{K}) = Re\Big\{\frac{2\pi}{\lambda}\Big\{&C_{01}\lambda\mathbf{K}^{*} + \frac{1}{2}C_{12}\lambda^{2}\mathbf{K}^{*2} + \frac{1}{2}C_{10}\lambda^{2}\mathbf{K}^{*}\mathbf{K} + \frac{1}{3}C_{23}\lambda^{3}\mathbf{K}^{*3} \\ &+\frac{1}{3}C_{21}\lambda^{3}\mathbf{K}^{*2}\mathbf{K} + \frac{1}{4}C_{34}\lambda^{4}\mathbf{K}^{4*} + \frac{1}{4}C_{32}\lambda^{4}\mathbf{K}^{*3}\mathbf{K} + \frac{1}{4}C_{30}\lambda^{4}\mathbf{K}^{*2}\mathbf{K}^{2} \\ &+\frac{1}{5}C_{45}\lambda^{5}\mathbf{K}^{5*} + \frac{1}{4}C_{43}\lambda^{5}\mathbf{K}^{*4}\mathbf{K} + \frac{1}{5}C_{41}\lambda^{5}\mathbf{K}^{*3}\mathbf{K}^{2} + \frac{1}{6}C_{56}\lambda^{6}\mathbf{K}^{*6} \\ &+\frac{1}{6}C_{54}\lambda^{6}\mathbf{K}^{*5}\mathbf{K} + \frac{1}{6}C_{52}\lambda^{6}\mathbf{K}^{*4}\mathbf{K}^{2} + \frac{1}{6}C_{50}\lambda^{6}\mathbf{K}^{*3}\mathbf{K}^{3}\Big\}\Big\}\end{aligned} \tag{2.6}$$

For the particular case of a non-corrected microscope the aberration function is dominated by the effects of spherical aberration (C_{30}) and defocus (C_{10}) so Eq. 2.6 be approximated as follows:

$$\chi(\mathbf{K}) = \Big\{\frac{2\pi}{\lambda}\Big\}\Big\{\frac{1}{2}C_{10}\lambda^{2}\mathbf{K}^{*}\mathbf{K} + \frac{1}{4}C_{30}\lambda^{4}\mathbf{K}^{*2}\mathbf{K}^{2}\Big\} \tag{2.7}$$

In 1949, Scherzer noticed that for a given acceleration voltage (or equally, for a given λ) the effects of spherical aberration can be compensated by introducing a negative defocus [79], which is known as *'Scherzer defocus'* (C_{10}^{sch}) when it gets a value:

$$C_{10}^{sch} = -1.2(C_{30}\lambda)^{1/2} \tag{2.8}$$

The aberration function has a critical effect in image formation. The contrast transfer function, H(**K**), defines how information in **K** space is transferred to the image and it has a dependence with the aberration function as follows:

$$H(\mathbf{K}) = A(\mathbf{K})e^{-i\chi(\mathbf{K})} \tag{2.9}$$

where A(**K**) is the aperture function and describes the the effects of the aperture and the partial coherence of the electron beam.

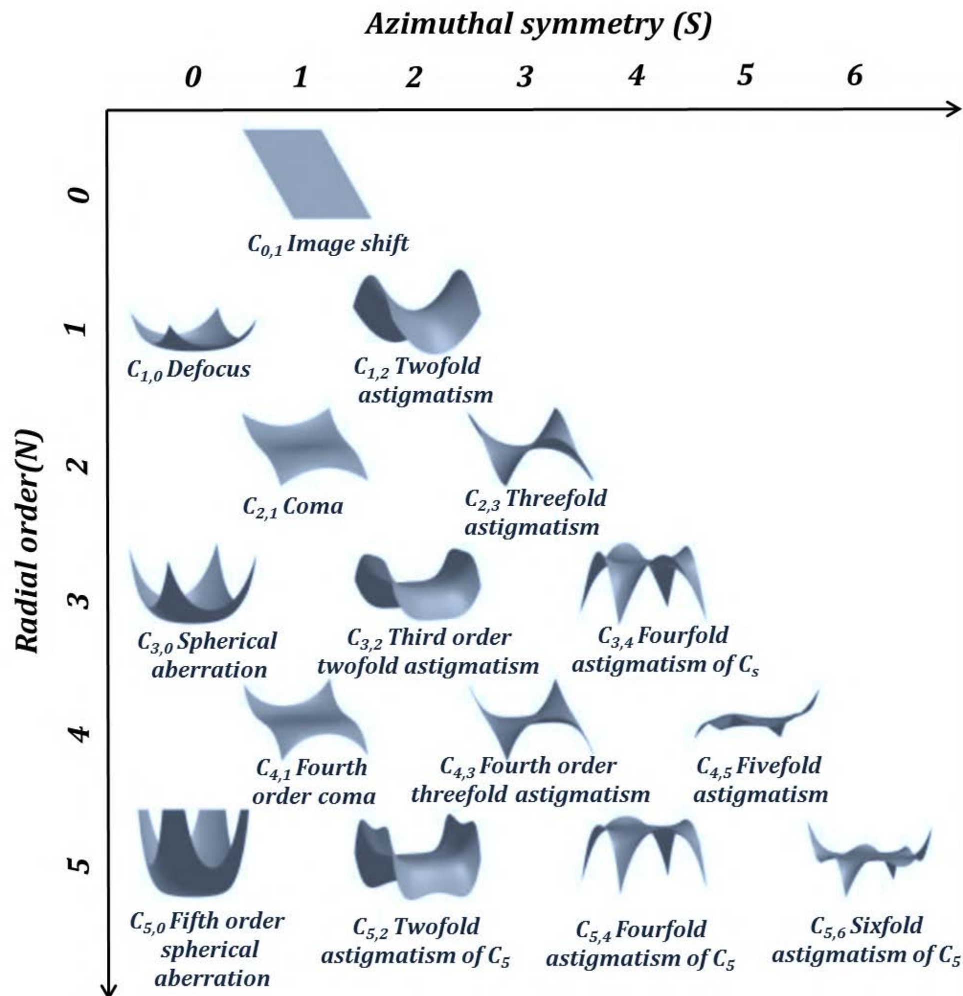

Figure 2.2: Glossary of aberration coefficients C_{NS} with three dimensional representation of the distortions induced in the wavefront by all aberrations up to the fifth order. Adapted from [80].

2.1.2 Aberration correction

Contrary to VLM where best performance systems are practically aberration-free, electromagnetic lenses present very poor quality and several efforts have been performed to overcome their limitations since the first commercial microscopes appeared. The defocus is the lowest order aberration, but can be easily compensated by a proper placement of the sample's height through the optic axis. Other aberrations containing asymmetric elongation can be compensated with the introduction of multipoles which apply magnetic fields perpendicular to the optic axis. For the

case of astigmatism, for example, it can be corrected by the use of two orthogonal quadrupoles which can transform a point to a line. Coma can be adjusted by a dipole altering the alignment of two lenses. Each of these elements should be placed in a way they work independently from others.

Regarding axial aberrations, Scherzer developed his theorem early in 1936 [81] finding that chromatic and spherical aberrations of rotationally symmetric electron lenses are unavoidable when:

i. The optical system is rotationally symmetric.

ii. The system produces a real image of the object.

iii. The fields of the system do not vary with time.

iv. There is no charge present on the electron - optical axis.

Later, in 1947, he proposed to correct spherical an chromatic aberration by breaking any of the constraints of his theorem [82], but in practice the best advances have been performed by breaking the rotational symmetry of the optical system through the incorporation of series of multipoles (dipoles, quadrupoles, hexapoles, octupoles, ...) alternating North and South along the optic axis. However, technological limitations avoided successful implementation into the lens systems and it wasn't until 1998 when M. Haider and H. Rose implemented them in a 200 kV working TEM and reached atomic resolution in [110] oriented GaAs by achieving 1.4 Å point resolution [83]. Since then, aberration correction systems have become more and more sophisticated, being able to correct up to fifth order aberrations.

Recently, in 2018, electron-beam ptychography technique has been incorporated in aberration corrected microscopy through an electron microscope pixel array detector (EMPAD) producing a record-breaking resolution of 0.39 Å at a beam energy of 80 kV, where conventional imaging methods can reach only 0.98 Å [84].

In practice aberration correction relays in a process of aberration diagnosis and measurement followed by aberration compensation using the corrector systems. *Zemlin's tableau* method is usually employed in order to evaluate the aberration function. It consists in imaging diffractograms in HRTEM mode or the electron probe in STEM mode, over and underfocus and for different beam tilts in some amorphous

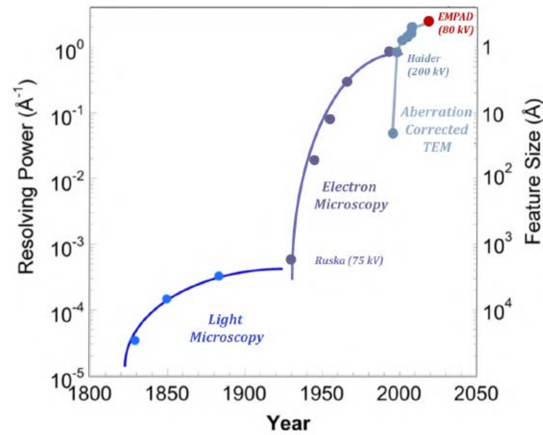

Figure 2.3: Spatial resolving power of instrumentation over history. The actual record of resolution was obtained by Muller's group in 2018 by the incorporation of an EMPAD pixelated detector [84].

material, as their features are dependent on the aberration function χ. From the tilt induced changes in defocus and/or two fold astigmatism the rest of the aberrations can be estimated and compensated.

Another method for aberration diagnosis consists in ronchigram evaluation. The ronchigram can be defined as the shadow image of the sample or as the convolution of the aperture function with the diffraction pattern of the sample. It is highly dependent on lenses aberrations and thus it is a powerful tool for diagnosis. The effects of low order aberrations (spherical, two-fold astigmatism and coma) in the probe, ronchigram and resulting micrographs are shown for in-focus, overfocus and underfocus conditions in Figure 2.4.

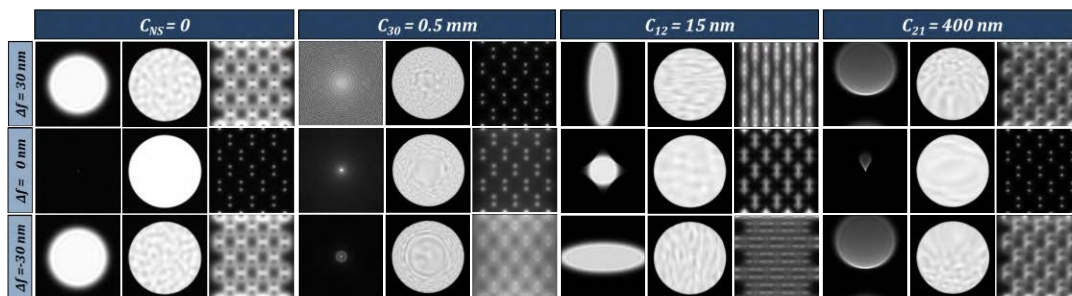

Figure 2.4: Coherent probe intensity, ronchigram and HAADF micrograph of [110]Si simulated at 300 kV acceleration voltage for several defocus values when inducing zero aberrations, spherical aberration, two-fold astigmatism and coma to the condenser lenses.

2.2 (S)TEM imaging techniques

When the primary beam crosses through the sample several events occur. Focusing on the transmitted beam, some electrons keep their trajectory without interaction (direct beam) while some others suffer a series of scattering events (elastic and inelastic, coherent and incoherent) when interacting with the Coulomb potential of the atoms forming the material into study. Consequently, these events modify the amplitude and phase of the incident electron wave.

A variety of imaging techniques have been developed in Transmission Electron Microscopes by exploiting elastically scattered electrons, which are responsible of creating diffraction patterns as well as the major source of contrast in (S)TEM imaging. A general way to classify them is regarding to the illumination employed by adjusting the condenser system: conventional TEM involves a parallel illumination on the sample while Scanning TEM relays on employing a convergent beam scanned across the sample. The main concepts of image formation and different origins of image contrast are described in the next sections for both TEM and STEM modes.

2.2.1 Imaging in TEM : BF / DF / HRTEM

When the incident electron wave passes through the sample both its amplitude and phase get modulated. It is usual to distinguish then between amplitude contrast and phase contrast. Although both of them contribute to image formation, in most situations one of them will dominate depending on the working conditions.

There are two sources of amplitude contrast: mass-thickness contrast and diffraction contrast. Mass-thickness contrast arises from incoherent elastic scattering (Rutherford scattering), which is strongly dependent on the element Z number and the specimen thickness. Meanwhile in diffraction contrast coherent scattering occurs at angles fitting Bragg's condition, being then sensitive to the crystal structure and orientation of the specimen. By placing an aperture in the back focal plane of the objective lens (objective aperture) one can select either the transmitted beam or any of the discrete Bragg reflections, giving rise to the two main operation modes showing amplitude contrast in parallel beam TEM: bright field (BF) and dark field (DF). Other imaging conditions, like two-beam conditions, were used in the past to strengthen

the diffraction contrast arising from a particular *hkl* plane and it was quite useful to enhance the contrast given by certain planar defects. However, nowadays parallel mode TEM usually works exploiting phase contrast in a mode called High Resolution Transmission Electron Microscopy (HRTEM).

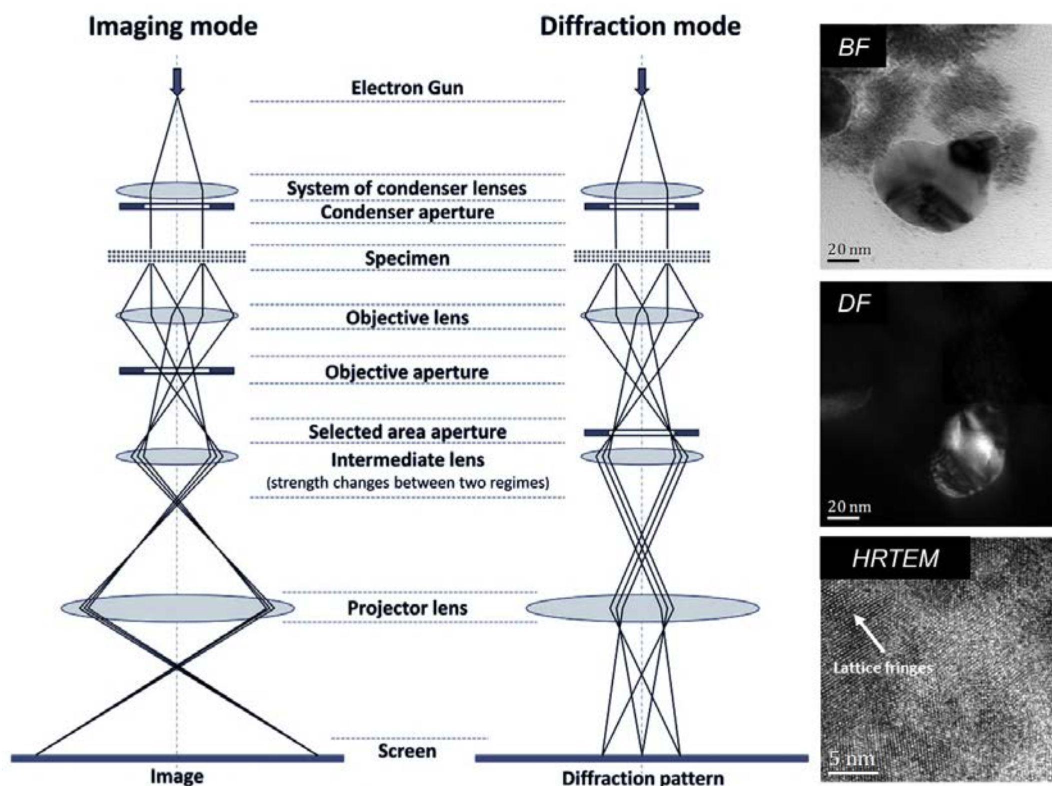

Figure 2.5: Schematic setup of TEM working in parallel mode. On the right, examples of polycrystalline Ag@CeO_2 hybrid nanoparticles imaged in bright field mode (top), dark field mode selecting only some of the Ag planes (middle) and HRTEM mode where lattice fringes of Ag are visible (bottom) .

In HRTEM mode image formation arises from the interference of many different transmitted electron waves in the image plane, including the incident beam and Bragg scattered ones. As a response of the phase difference among the scattered electrons, an interference pattern reflecting the different crystal periodicities (lattice fringes) is obtained. The big sensitivity of this technique can be exploited to obtain information of the atomic structure of the sample, with a spatial resolution that can reach as far as 0.08 nm in a non-corrected microscope, but the contrast is also very sensible to small changes in sample thickness, crystal orientation, defocus and objective astigmatism, so interpretation is not straight forward. Even though the information obtained can allow crystal phase identification or determination of crystal

orientation, atomic identification for a complete structural characterization and image interpretation requires the combination with image simulation.

HRTEM requires selecting more than one beam in order to make them interfere, so usually a bigger objective aperture than in BF/DF is placed in the back focal plane to collect the transmitted and several diffracted beams, as shown in schematic representation of TEM setup in Figure 2.5. An example of imaging in BF, DF and HRTEM is also shown.

2.2.2 Imaging in STEM: HAADF/MAADF/ABF

Scanning Transmission Electron Microscopy (STEM) techniques are based in focusing the electron beam into a small probe that is scanned through the sample without tilting and collecting the electrons elastically scattered by the specimen at different angles. The resolution of the technique relays on the availability of the condenser system to achieve the smallest possible probe. Figure 2.6 shows a schematic setup of a microscope working in STEM mode together with micrographs of a cross-section of GaN@AlN core-shell nanowires obtained employing different detectors.

Since annular detectors were incorporated in 1970 by Crewe [85] they have been commonly employed to collect elastically scattered electrons at different angles at each position of the sample. The angular distribution of the scattered electrons is caused by the different interactions that take place when the primary beam crosses the material, and hence different angular ranges contain distinct sample information. Actually, Crewe's Annular Dark Field (ADF) detector was particularly efficient to image isolated atoms in amorphous substrates, but whenever it got applied to crystalline oriented samples Bragg diffracted electrons and incoherently scattered electrons were both contributing to image formation and image contrast was hardly interpreted. Later on, Howie demonstrated that by enlarging enough the inner angle of the ADF detector, Bragg diffracted electrons could be eliminated from the collected signal, giving rise to High Angular Annular Dark Field (HAADF) detectors [86].

HAADF detectors collect electrons suffering from thermal diffuse scattering (TDS) and Rutherford incoherent scattering when interacting with the Coulomb potential

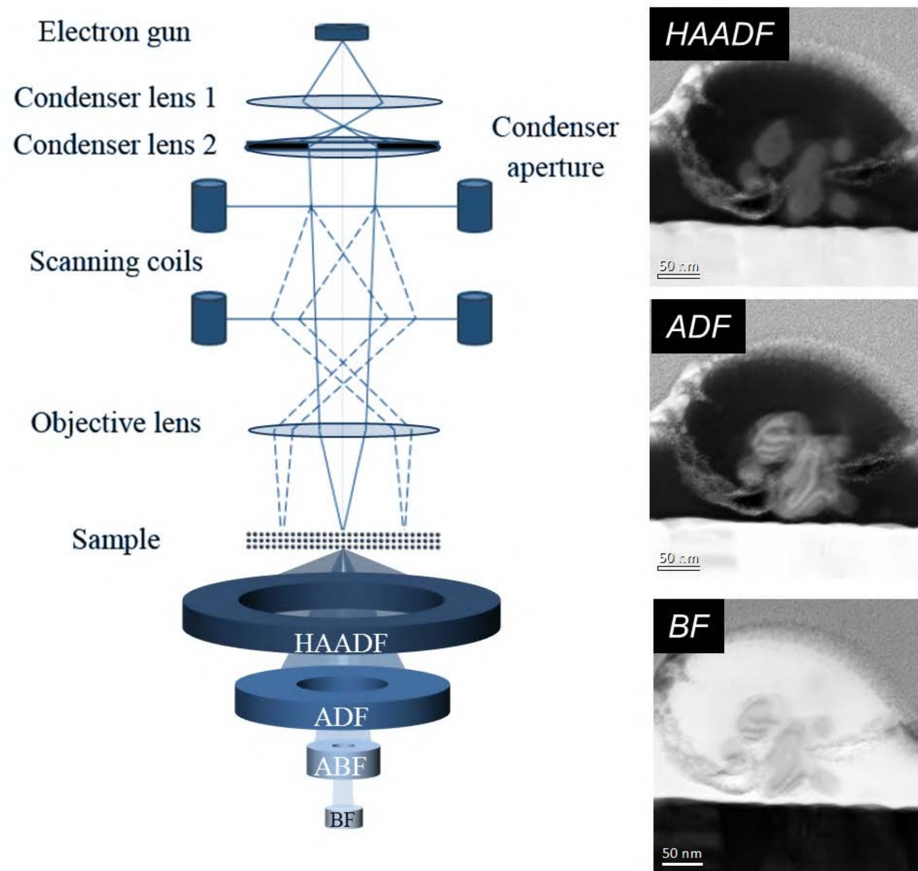

Figure 2.6: Schematic setup of TEM working in scanning mode with different annular detector systems. On the right, cross-section of GaN@AlN core-shell nanowires imaged using HAADF detector (top), ADF detector (middle) and BF detector (bottom).

of the nucleus of the atoms in the specimen, so the contribution of Bragg diffracted beams is negligible. Thus, for inner detector angles larger than a critical value (around 100 mrad for corrected microscopes, Table 2.2) the intensity of the image provides chemical information as the contrast observed scales with Z number with a factor ζ.

$$I \; \alpha \; Z^{\zeta} \tag{2.10}$$

Although for qualitative purposes the value of ζ is considered as 2, the exact exponent ranges between 1.2 and 1.8 as function of the the inner collection angle of the detector [87]. This factor is essential when performing quantitative analyses (Figure 2.7).

Unfortunately, the strong sensitivity to high Z atoms makes the lightest atoms

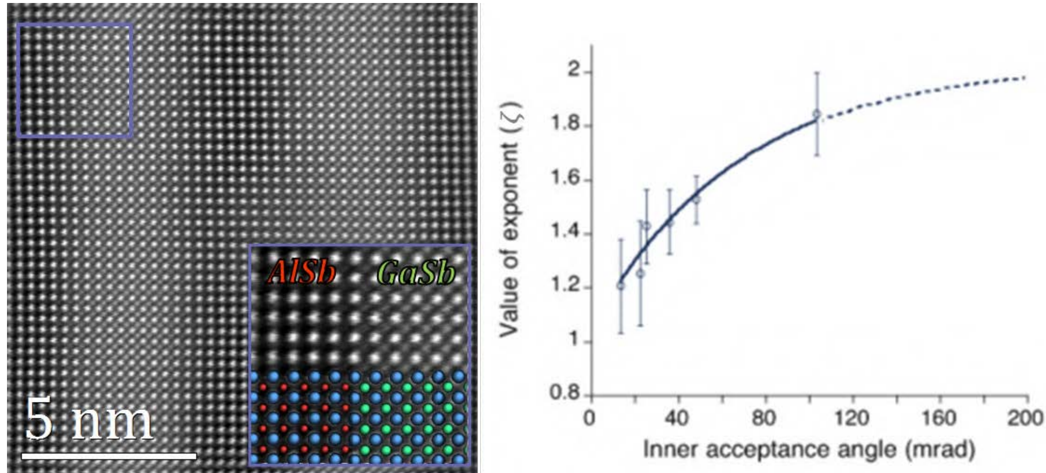

Figure 2.7: On the left, HAADF micrograph of AlSb/GaSb quantum wells. Al atoms appear invisible in presence of heavier Sb. On the right, dependence of ζ exponent with inner acceptance angle [87].

presenting weak scattering power be hardly detectable, specially in the presence of heavier elements. In this way, Figure 2.7 shows an example of [100] oriented AlSb/GaSb quantum wells. The zooming shown as an inset reveals how Al atoms appear invisible in the presence of Sb. In that regard, a detector encompassing a lower angular range is more appropriate for light element visualization. The central region containing unscattered electrons would give rise to a Bright Field (BF) image analogous to BF imaging in TEM mode, but by blanking the central part of the BF detector unscattered electrons are avoided and the resulting signal is dominated by coherent interference of elastically scattered electrons (becoming then a phase contrast imaging). This is the so called Annular Bright Field (ABF) technique and can yield even to the visualization of hydrogen columns [88].

Moreover, other collection angles in between the regimes of BF and HAADF imaging can be considered. They are Low Angle Annular Dark Field (LAADF) and Middle Angle Annular Dark Field (MAADF). In the former both Bragg elastic scattering and diffuse scattering contribute to the image formation. In the second, Bragg scattering contribution is reduced. Electrons scattering in this angular range carry information arising from diffraction so the generated contrast enhances boundaries, phase changes, strain and defects [89, 90].

It has been commented before that pixelated arrays have been introduced recently to microscopy analysis and they substantially improve resolution limits. At the same time, the capability of recording diffractograms at each point of scan gives

TABLE 2.2: Range of collection angles in different STEM annular detectors [91].

Signal collection mode	Collection angle range (mrad)
BF	0 - 20
ABF	10 - 20
LAADF	20 - 60
MAADF	60 - 120
HAADF	>80

a tool to record all angular dispersion in one acquisition. This combination of incoherent Z-contrast imaging and coherent phase contrast provides an outstanding sensitivity for both light and heavy elements at the same time [92]. In addition, the availability of recording shifts in diffraction patterns allows the calculation of local electric field by evaluating the momentum transfer to the STEM probe (Differential Phase Contrast, DPC) [93, 94]. This acquisition setup is often referred as 4D-STEM and it is pushing imaging techniques in STEM together with analytical analyses, breaking spatial resolution limitations of other equivalent techniques.

2.3 Analytical STEM: EELS and other spectroscopies

Up to now it has been exposed how to exploit electrons suffering from elastic scattering events as mechanisms to generate image contrast, but a fraction of the primary beam suffers from different inelastic processes that lead to another branch of techniques: TEM related spectroscopies. The energy loss of transmitted electrons together with energy of emerging X-rays or visible light contain information of the material elemental composition or/and optoelectronic properties. These techniques are usually associated with Scanning TEM mode, meaning that one energy spectrum is collected at each probe position within the specimen. This means that during a single acquisition the signal intensity per each energy value is collected, which can be expanded to include the spatial coordinates and giving rise to spectrum imaging [95, 96]. The set of data collected is commonly known as the data cube, as intensity (or number of counts) is recorded for each energy E at each x - y position.

Figure 2.8 schematizes the main signals emerging from the specimen when the primary electron beam crosses through the sample. From them, the main spectroscopic techniques developed in the framework of Transmission Electron Microscopy

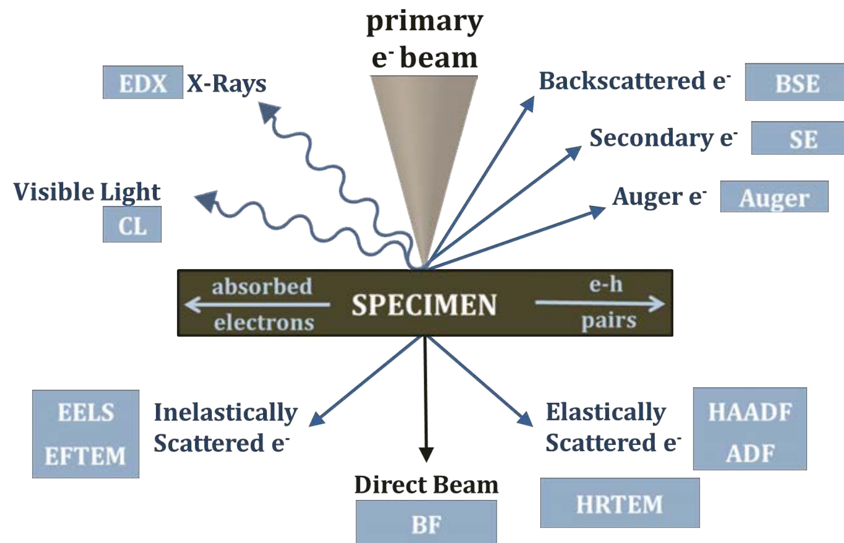

Figure 2.8: Schematics of signals produced during beam - sample interaction .

are related with collection of X-Rays generated in the sample through Energy Dispersive X-Ray Spectroscopy (EDX), collection of emitted photons in the visible range through cathodoluminiscence (CL) and measuring the energy losses of the primary electron beam after interacting with the sample through Electron Energy Loss Spectroscopy (EELS). The working principles of these spectroscopic techniques will be described by taking a deeper insight to EELS principles.

Energy Dispersive X-Ray Spectroscopy, EDX

In order to present the working principles of EDX spectroscopy it is quite common to consider the Bohr atomic model, which takes into account quantization of the electronic orbitals. Given the high energy of the electrons penetrating into the sample it is possible for them to excite one inner-shell electron of the specimen and transfer enough energy to make it escape above the Fermi level. This excitation process creates a hole that gets filled by a lower energy electron from an outer shell to recover the ground state. During this transition either an Auger electron or a X-Ray photon is emitted in order to release the excess of energy. Usually X-Rays are favoured in the case of heavy elements while Auger processes tend to be favoured in low Z elements, which is the main limitation of the technique.

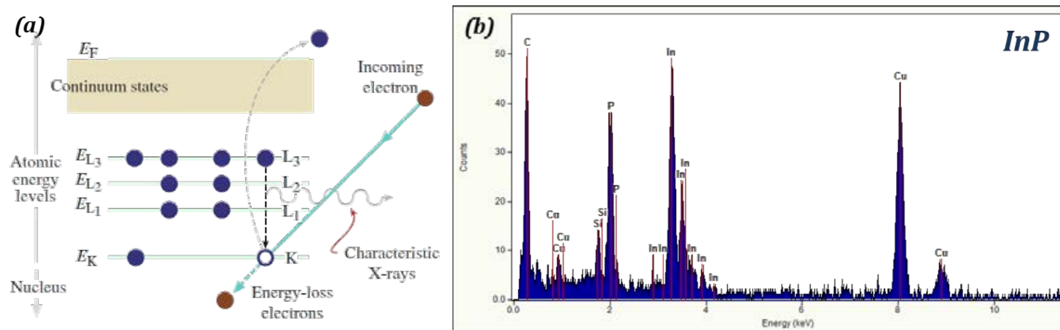

Figure 2.9: (a) Schematics of characteristic X-Rays generation [76]. (b) Example of EDX spectrum obtained on InP. Parasitic signals of C, Cu and Si also appear in the spectrum.

EDX is based in the collection of the emitted X-Ray photons, whose energy is determined by the energy of the electronic levels of the inner ejected electron and the outer refilling electron ($E_{X-Ray} = E_{inner} - E_{outer}$). Due to the discretization of energies of the electronic shells, these energy lines are characteristic for particular elements, so elemental identification is straight forward by a simple energetic analysis. Moreover, line intensity analyses of more than one elemental transition permits relative elemental quantification.

Cathodoluminiscence, CL

Cathodoluminiscence relays on the measurement of visible light photons emitted as a consequence of electronic transitions. The accelerated electrons are able to excite valence electrons towards the conduction band in semiconductor materials, and in this way, electron - hole pairs are created. Recombination processes result in the emission of photons with band gap energy or other interband transitions. This technique is therefore very suitable for optoelectronic properties investigation.

2.3.1 Electron Energy Loss Spectroscopy, EELS

Emitted signals after electron - specimen interaction are leading to the spectroscopic techniques explained above. Nevertheless, an analysis of the spectrum of the energy lost by the primary beam when driving these events leads to a higher sensitivity of inelastic processes. In this regard, EELS has been employed as a preferential analytical technique in this work due to the amount of electronic information that the

transmitted beam carries, so a deeper insight is given to it.

The energy-loss spectrum is usually divided according to post-specimen electron kinetic energy. According to this, the energy losses are classified in three regions. They are the zero-loss peak (ZLP) (0 eV), the low-loss regime (<100 eV) and the core-loss regime (>100 eV), as labelled in Figure 2.10.

Different regimes of EELS spectra carry information of inelastic processes of different nature. In the next sections these regimes are explained in detail.

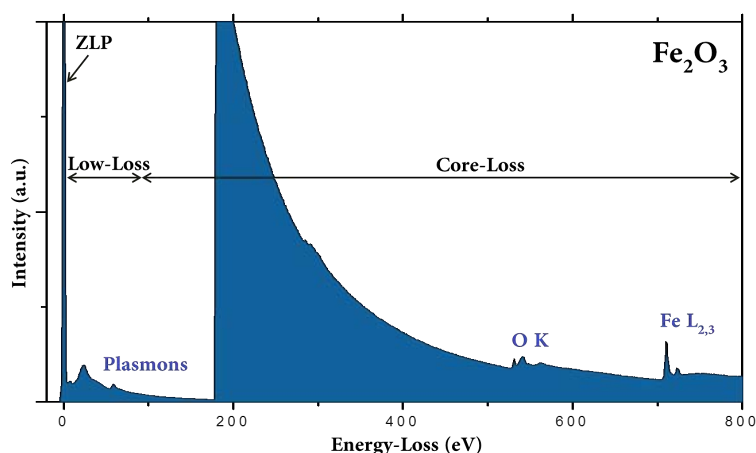

Figure 2.10: EELS spectrum of Fe_2O_3 with labels indicating the zero-loss peak, low-loss regime and core-loss regime. From 180 eV the spectrum has been magnified by a factor of 150.

Zero - loss peak (0 eV) - Thickness and energy resolution

The majority of electrons reaching the EELS spectrometer do not suffer any inelastic collision, so they preserve the primary energy. These electrons form the ZLP, which is the most prominent feature in the spectra. Even though it does not contain any information regarding to electronic transitions it supposes a valuable tool for calibration and experimental resolution determination. It is in fact accepted that the FWHM of the ZLP determines the energy resolution. The incorporation of highly efficient monochromators has allowed to get an energy resolution so far as 4.2 meV in a Nion HERMES operated at 30 kV. Together with an experimental conditions setup, the ZLP can be employed as an analytical technique for sample relative thickness determination. There are several ways to determine sample thickness although

the most standardized is the so-called log-ratio method, so the thickness t can be estimated by Eq. 2.11

$$\frac{t}{\lambda} = ln\frac{I_{ZLP}}{I_{TOT}} \tag{2.11}$$

where I_{ZLP} is the integrated intensity of the ZLP, I_{TOT} is the whole spectrum energy integration and λ is the mean free path.

Low - loss EELS (<100 eV) - Optoelectronic transitions

The low-loss regime comprises the collected electrons presenting energy losses up to 100 eV. Generally this region of the EEL spectrum is dominated by the bulk plasmon excitations, which can be described as a resonant oscillation of the valence electron gas on the solid. The plasmon energy is governed by the valence electron density and hence it is susceptible to alloying and microstructural phase rearrangement. In a free-electron model the expression for bulk plasmon energy E_p is given by

$$E_p = \frac{h}{2\pi}\left[\frac{Ne^2}{m_e\varepsilon_0}\right]^{1/2} \tag{2.12}$$

being N the valence electron density and ε_0 the permittivity of free space.

The plasmon peak position in low-loss EELS can present a shift due to interband transitions (i.e. single electron transitions from the valence band to unoccupied states in the conduction band). For instance, the EEL spectrum is a reflection of the Joint Density of States (JDOS) of semiconductor materials at low energy losses. The lowest energy of these transitions would correspond to the band gap, so band gap information is contained at the onset of intensity rise. Rafferty and Brown (1998) [97] determined in their studies that the shape of this transition can be described differently for the case of direct and indirect band gap transitions. In the case of direct transitions the intensity onset of interband transitions gets a tendency as described in Eq. 2.13:

$$I\alpha(E - E_g)^{1/2} \tag{2.13}$$

meanwhile the momentum transfer in indirect transitions makes the expression be modified as reflected in Eq. 2.14

$$I\alpha(E - E_g)^{3/2}. \tag{2.14}$$

Figure 2.11 reflects the schematic diagrams of direct and indirect transition onset shapes.

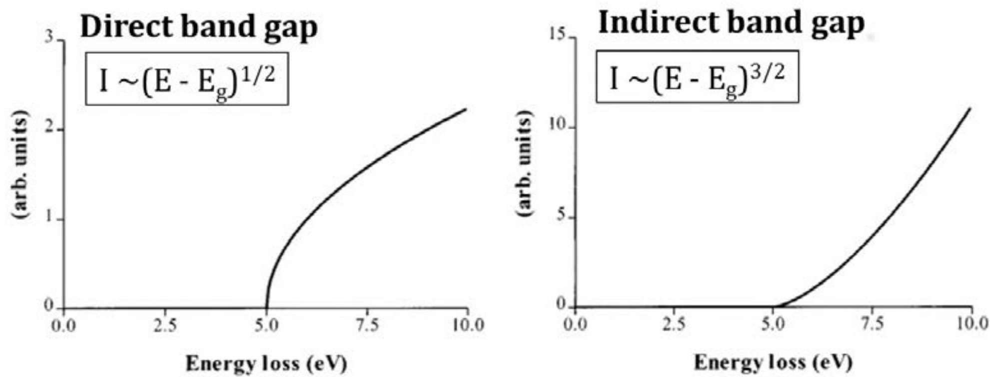

Figure 2.11: VEEL spectrum tendencies for direct and indirect band gap transitions. Adapted from [97].

It might seem straight forward to evaluate band gap with particularly good spatial resolution by VEELS analysis, however the presence of parasitic radiations is in many cases responsible of errors in data interpretation. Special attention is given into Cherenkov radiation, which is emitted when a charged particle (in this case electrons) travel through a dielectric medium with greater velocity that the phase velocity of light in that particular medium. The energy losses due to Cherenkov are usually appearing close to the band gap transition, so in order to minimize them it is convenient to decrease acceleration voltage and sample thickness. Nevertheless, these losses are hardly avoidable in most binary semiconductors due to the high refractive index they present.

Core - loss EELS (>100 eV) - Elemental composition

Core-loss EELS or also called High-loss EELS contains the losses involving inner-shell electrons, which usually occur above 100 eV. Analogously to EDX, the edge threshold is driven by the binding energy of particular electron shells. This acts as

an elemental fingerprint, making the technique suitable for elemental identification by the evaluation with tabulated databases. Relative quantification is possible by intensity integration on different element edges.

Contrary to EDX, EELS is highly sensitive to the chemical bonding. For instance, Energy Loss Near- Edge Structure (ELNES) is based on the study of the fine structure of the different edges. It provides structural and chemical bonding information as it represents the available electronic states above the Fermi level. It has been highly used in oxides for oxidation state determination [98, 99]. These analyses require high energy resolution in monochromated systems, but in the case of non-monochromated microscopes further techniques have been developed relaying on the analysis of integrated intensity of L edges in transition metals [100, 101].

Figure 2.12 shows how by core-loss spectrum imaging in $Mn_3O_4 - Sn$ nanoparticles cation exchange between Mn and Sn is observed in the outer shell of them. An oxidation state map could be obtained from Mn L_3/ Mn L_2 intensity ratio calculation across the area of study when compared to tabulated values.

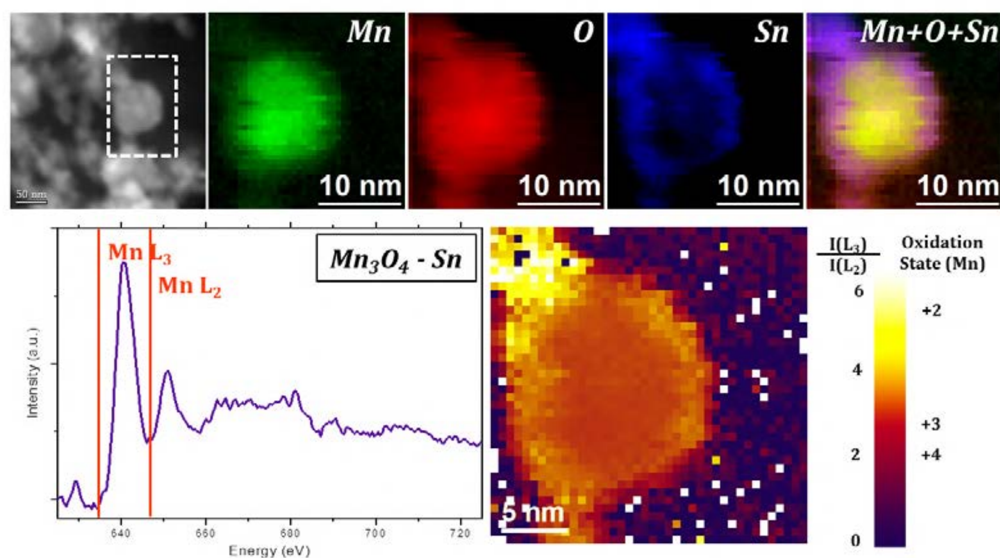

Figure 2.12: Elemental mapping of a Mn_3O_4 - Sn nanoparticle obtained from core-loss EELS spectrum imaging. Spectrum in Mn $L_{2,3}$ edge region is shown. Oxidation state has been calculated from integrated L edge intensity ratio, revealing that in Sn exchange areas Mn is reduced.

2.4 Data acquisition and processing

The samples that have been analyzed in the following chapters have been mainly prepared by two different techniques. In order to analyze longitudinally the vertical nanowires they have been deposited into Lacey Carbon Copper grids with about 3 nm Carbon film thickness by simple mechanical scratching of the substrate. Regarding nanowire transversal cross sections or longitudinal sections of horizontal nanowires, Focused Ion Beam (FIB) preparation has been employed. Lamellae were prepared mainly using a FEI Dual-Beam Helios Nanolab 650 located at *Instituto de Nanociencia de Aragon, Zaragoza*. In horizontally grown samples the lamellae were extracted directly from located positions of the substrate containing the as-grown nanowires. In the case of vertical nanowires cross sections, a first step of nanowire transfer into a substrate was performed, followed by lamellae preparation by cutting several aligned wires.

Different TEM equipment has been employed for obtaining the data analysed in this work.

- A STEM dedicated FEI TITAN (60 – 300 kV) located at the *Laboratorio de Microscopías Avanzadas of the Instituto de Nanociencia de Aragon (LMA-INA, Zaragoza)* has been employed for High Resolution HAADF – STEM imaging. It is equipped with a third order aberration probe corrector (CETCOR C_s-probe, CEOS), a monochromator and a X-Field Emission Gun (X-FEG). The microscope has been operated at 300 kV in which probe sizes of 0.08 nm are obtained. The microscope is further equipped with a Gatan Tridiem 866 ERS spectrometer with energy resolution down to 0.14 eV which has been used with a nominal camera length of 10 mm and 0.7 energy dispersion for core-loss spectra acquisition.

- A FEI TECNAI F20 TEM microscope with a FEG gun operated at 200 kV acceleration voltage has been employed for HRTEM and core-loss EELS analyses. Located at *Institut Català de Nanociència i Nanotecnologia (ICN2, Barcelona)*, it is equipped with a Gatan 2k x 2k US1000P CCD camera for HRTEM images and a Gatan Imaging Filter (GIF) Quantum SE 963 spectrometer for spectra acquisition. The spectrometer reaches about 1 eV energy resolution. The camera

length has been fixed to 30 mm in all the experiments while the energy dispersion, energy acquisition range, integration time and spectrometer collection angle have been suited for each experiment.

- A Nion UltraSTEM^{TM} 100 MC 'HERMES' (40 – 100 kV) located at *SuperSTEM Laboratory (Daresbury, UK)* was employed for VEELS and plasmonic measurements as well as HAADF and MAADF characterization. The microscope has a Cold FEG emitter that has a native energy spread of 0.3 eV and it is equipped with a monochromator able to reach 15 meV energy resolution. It uses a UHV Gatan Enfinium ERS spectrometer, including fast shutter and dual EELS capabilities. In imaging, probe corrector C_5 Nion QO achieves correction up to fifth order $C_{5,6}$.
- Some HRTEM micrographs have been obtained in a FEI Tecnai Osiris from *École Polytechnique Fédérale de Lausanne (CIME – EPFL, Lausanne)* equipped with a XFEG operated at 200 kV and a 4k x 2.6k Gatan Orius CCD camera with large field of view.

2.4.1 Image treatment and Fourier space

The data obtained by aberration corrected HAADF STEM has been treated before proceeding to analysis. HAADF images are believed to be incoherent and they are described as a convolution of an electron probe and a scattering distribution. Therefore the image quality can be improved by the deconvolution of the STEM micrograph with the electron probe function. This procedure is preceded by the application of a Wiener filter to remove environmental noise. In order to proceed, STEM_CELL software package [102] has been used.

Most of the analyses in order to interpret the atomically resolved micrographs have been performed in the reciprocal space. Fourier transform algorithms have been applied to atomically resolved micrographs in order to convert fringe periodicities into the corresponding power spectra consisting of discrete spatial frequency values, which give a more accurate measuring of lattice spacing. This tool allows to proceed with frequency masking, making it particularly useful to locate spatial distribution of periodicities in the real space by performing an inverse Fourier transform. Digital Micrograph software from Gatan allows to perform the algorithms

together with a measurement of the value and orientation of the different plane frequencies in the sample.

Together with it, CaRIne Crystallography software allows to create unit cells from lattice parameters, space symmetries and atomic positions and generate the reciprocal lattice of the crystal. A systematic methodology consisting on combination and comparison of both procedures has been employed for identification of phase and orientation of crystals. Figure 2.13 illustrates a practical case of phase identification and orientation determination on a GaN @ TiO_2 core-shell nanowire cross section.

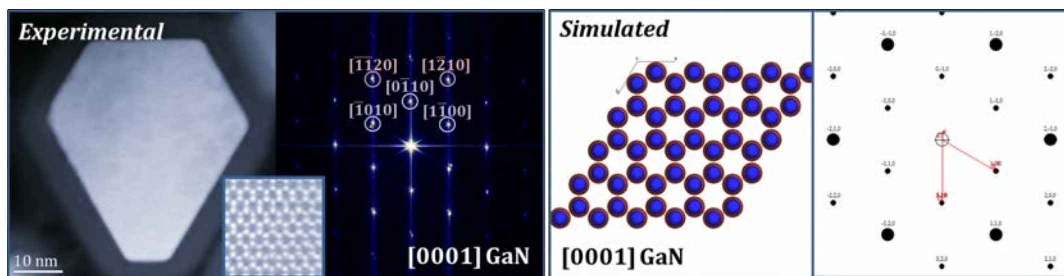

Figure 2.13: On the left, experimental HAADF of the cross section of a GaN@TiO_2 nanowire and the calculated power spectrum. The inset shows zoomed details of the central part of the nanowire. On the right, simulated atomic structure of the GaN wurtzite phase visualized along the [0001] zone axis and the calculated projection of the reciprocal lattice. By measuring theoretical values in reciprocal space and comparing them with experimental values, phase and orientation have been determined.

2.4.2 Strain measurements: Geometric Phase Analysis

Since HRTEM or aberration corrected STEM images might present atomic resolution or lattice fringe information, lattice distortions such as strained lattices, defects or grain boundaries can be locally analyzed. Several algorithms have been developed in order to evaluate strain and other local lattice distortions, working in either real [103] or Fourier space. In particular, Geometric Phase Analysis (GPA) evaluates phase variations of a particular frequency in Fourier space across all the micrograph [104, 105].

Considering a spacial frequency (i.e. lattice fringe) given by a reciprocal lattice vector $\mathbf{g}$, the phase image $P_g(\mathbf{r})$ can be calculated. Thinking in real space the phase image describes fringe position. The phase is directly related with the displacement

field **u** by:

$$P_g(\mathbf{r}) = -2\pi\mathbf{g} \cdot \mathbf{u}\,(\mathbf{r}) \tag{2.15}$$

Then, the displacement field can be calculated for different selected **g** vectors. This can be extended to the calculation of 2D displacement fields when selecting two non-parallel **g** vectors. This is particularly useful for strain evaluation, as the infinitesimal displacement gradient is related with the strain and rotation tensors as

$$\nabla\,\mathbf{u} \; = \boldsymbol{\varepsilon} + \boldsymbol{\omega} \tag{2.16}$$

where the components of strain and rotation tensor are given by

$$\varepsilon_{ij} = \frac{1}{2}\left(\frac{\partial u_i}{\partial x_j} + \frac{\partial u_j}{\partial x_i}\right) \text{ and } \omega_{ij} = \frac{1}{2}\left(\frac{\partial u_j}{\partial x_i} - \frac{\partial u_i}{\partial x_j}\right) \tag{2.17}$$

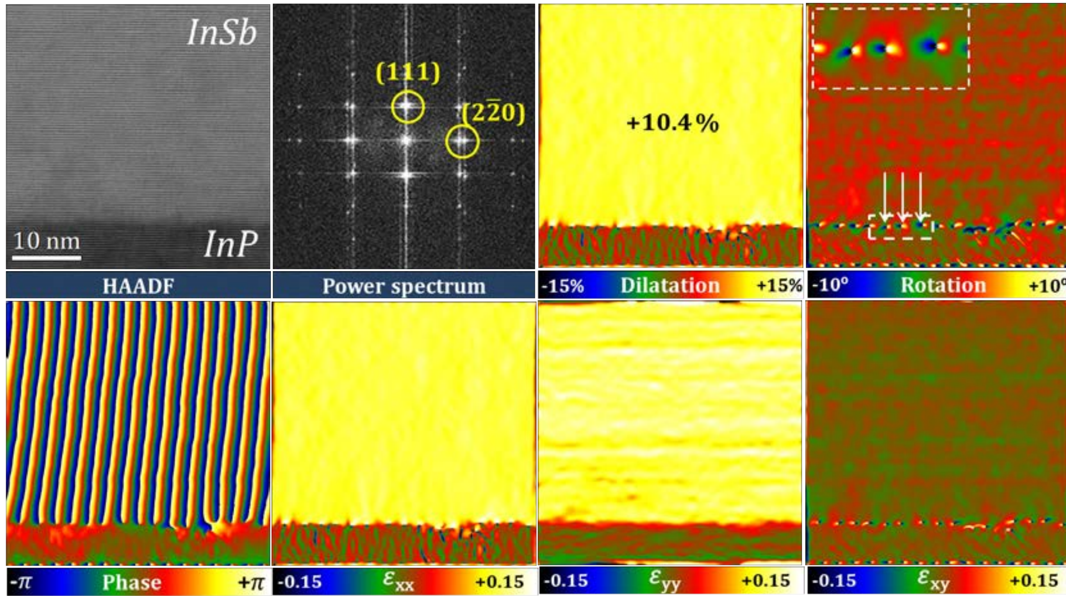

Figure 2.14: Top: Atomic resolution HAADF micrograph of InSb/InP interface and its power spectrum with (111) and (2$\bar{2}$0) planes labelled. Dilatation and rotation maps of (2$\bar{2}$0) planes obtained through GPA. Bottom: Phase map of (2$\bar{2}$0) plane. Maps of the 2D strain matrix coefficients obtained using (111) and (2$\bar{2}$0) planes.

This opens the possibility of mapping dilatation and rotation of planes (in the case of selecting one lattice vector) or mapping strain tensor components (in case of selecting multiple lattice vectors) with reference to an undistorted lattice. This

tool is especially valuable for studying epitaxial strain relaxation mechanisms at heterostructured interfaces [106]. An example of GPA employed for epitaxial strain study is shown in Figure 2.14. InP and InSb present a 10.39 % lattice mismatch, which matches with the 10.4 % dilatation measured by GPA. In that regard, it can be confirmed that the InSb lattice is relaxed. In addition, a set of misfit dislocations can be observed in the rotation map (highlighted with white arrows). From this simple study it can be concluded that strain is fully relaxed by the creation of misfit dislocations at the interface.

2.4.3 EELS spectra treatment

EELS data belonging to different energetic regions have been processed differently depending on the objective of the analysis. However, a systematic procedure for increasing the signal to noise ratio has been applied to most of the spectra. This is the weighted Principal Component Analysis (PCA), an approach of Multivariate Statistical Analysis (MSA), that has been applied through MSA plugin of Digital Micrograph. In PCA the signal is assumed to be a linear combination of orthogonal components (*eigenspectra*, $P_{i,k}$) which contain a weighting factor X_i [107]. Therefore the spectrum at one pixel can be redefined as the sum of all the components.

$$S_i = \sum_k P_{i,k} X_k \tag{2.18}$$

The decomposition can be expanded to spectrum imaging by rearranging the data into a two-dimensional matrix [108]. The decomposed matrix consists then in several elements that get arranged from high to low according to their eigenvalues, so the spectrum image can be reconstructed by discriminating the high order components. This procedure substantially enhances the signal-to-noise ratio. In Figure 2.15, which consists in core-loss spectrum imaging of an InGaN@GaN core-shell nanowire, the improvement of signal-to-noise ratio with five component reconstruction is clearly appreciated.

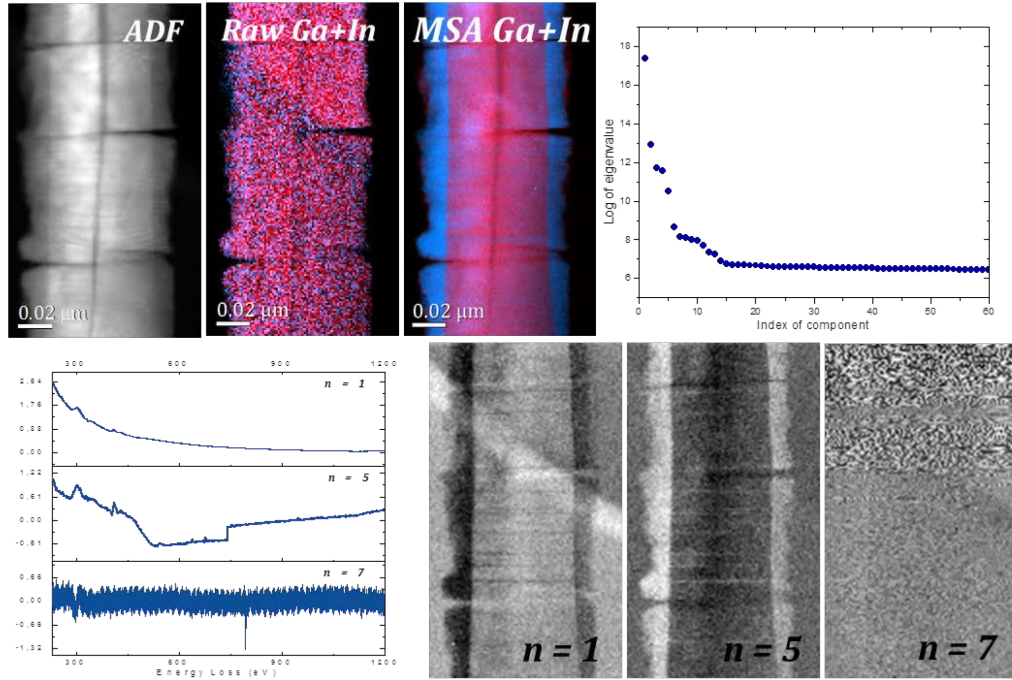

Figure 2.15: Top: ADF micrograph of a InGaN@GaN core-shell nanowire, elemental mapping of In(red) and Ga(blue) of raw EELS spectrum image, elemental mapping after MSA reconstruction using 5 components and scree plot showing the variance of the components. Bottom: Eigenspectra of n = 1, n =5 and n =7 and spatial distribution (score) of 1, 5 and 7 eigenspectra.

In the case core-loss elemental mapping individual signal integration after power-law background removal was applied along every pixel. This process allows to obtain elemental areal density maps. For elemental quantification the following equation is used:

$$\frac{N_A}{N_B} = k_{AB}\frac{I_A}{I_B} \tag{2.19}$$

where the ratio between N_A and N_B refers to the relative atomic fraction of elements A and B, $I_{A/B}$ refers to the integrated edge signal after background subtraction and k_{AB} is an empirical constant dependent of the energy edges. This can be further expanded to include more than two elements, getting a more complex equation, but the process is nowadays highly automatized.

The methodology employed for low-loss analyses was different depending on the goal of the analysis. Most of the analyses have been performed by employing

homemade MATLAB codes, but the exact procedure will be explained for each experiment.

2.5 3D atomic modelling and image simulation

It has been stated before that image interpretation is complicated as many factors contribute to the contrast. It is worth also to consider that the image recorded in HRTEM mode doesn't correspond to atomic columns, but an interference pattern, so simulations are required in order to fully interpret the image. Even though contrast interpretation is much simplified in the case of HAADF-STEM images, the acquired data represents a projection of the finite volume of the sample and therefore features that are not perpendicular to the optical axis modify the contrast in a way that is hardly interpretable in some cases.

In order to solve interpretation problems it is very useful to perform TEM and STEM simulations that recreate experimental conditions from atomic models. Actually, the creation of the crystal model is the first step for performing computational analysis, but it is useful itself as well in order to have a 3D vision of the predicted structures, as conventional (S)TEM just gives a projection. The atomic 3D models were created using an online software from the *Universidad de Cádiz* called Rhodius [109, 110] which includes EjeZ package. The first step for atomic model creation is to define the desired crystal phases involved by defining space group, lattice constants, atomic species and their positions within the primitive cell. Different occupancies can be also specified. Once the different cells are created Rhodius allows to define the 3D structure of the material (i.e. supercell) by defining plane facets. Including crystal rotations or displacing crystals in the space is also possible. Therefore an accurate reproduction of real 3D structures can be achieved.

STEM simulations of the created atomic models rely into two main different methods: the Bloch wave formalism [111] and the multislice routines [112]. Block wave formalism takes into account probe interactions with each atomic column while in multislice routines the sample is mathematically sliced and successive electron beam interactions at each slice get accumulated. In this case the atomic potential at each slice can be approached either by absorptive potential or frozen phonon

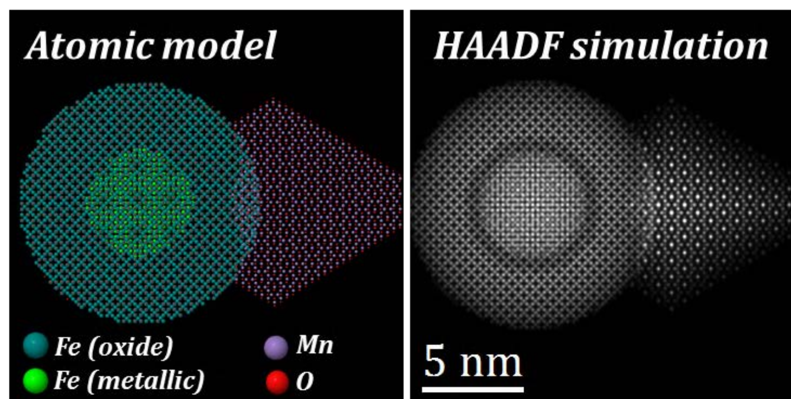

Figure 2.16: 3D atomic model of a Fe@Fe_3O_4-Mn_3O_4 hybrid nanoparticle system and multislice based HAADF simulation for an aberration-free microscope operated at 300 kV obtained using STEM_CELL software.

approach. The latest relies in considering that highly accelerated electrons transit the sample in a much smaller time than the typical period of lattice vibration and thereby each electron will see a lattice where thermal vibrations are frozen in a particular configuration. Multiple multislice calculations can be performed averaging over the different configurations.

STEM_CELL software package [113, 114] was employed for performing image simulations. It is based on the frozen phonon approach of Kirkland multislice routines [112] where thermal diffuse scattering (TDS) can be also included as well as accounting for source size effects. Multislice routines require high computational power and at some cases a linear approximation is more convenient to have a qualitative analysis. STEM_CELL allows to perform this approximation by performing a convolution between the squared probe and the atomic potential. Figure 2.16 shows an example of atomic modelling followed by a simulation by a linear approximation on a hybrid nanoparticle system.

2.6 Strain and electronic properties simulation

The combination of (S)TEM imaging techniques with spectroscopies and computational processing provides precise structural and compositional information even at the atomic scale. The precise knowledge of the material geometry and composition can be employed for performing simulations and calculate (opto)electronic properties of complex nanostructures. A semiconductor dedicated software, nextnano^3

[115, 116] has been employed to calculate them.

nextnano[3] is a semiconductor nanodevice simulator which allows to calculate electronic and optical properties directly from 1D, 2D or 3D structures with realistic geometries. It is based on a reliable treatment of quantum mechanical effects that provides a self-consistent solution of Schrödinger, Poisson and current equations where electronic structure can be outputted as single band or in a multiband $k \cdot p$ envelope function, including strain. It is then very suitable for understanding semiconductors behavior in a mesoscopic regime.

The simulation begins by setting material geometry of the overall heterostructure including crystal orientation. Material parameters such as lattice constants, band gap, valence or conduction parameters, among many others, are contained in an extensive database, although they can be customized if required for the simulation. Material impurities (homogeneous or as a function of position), external stress, electric or magnetic fields can be also included.

Heterostructures of semiconductors presenting different lattice constants are subject to suffer elastic deformations, as it was described in chapter 1, and strain plays a key role as it leads to piezoelectric effects, influences conduction and band edges (as well as their degeneracies) and thus also the band gap. For this reason the flow scheme of the software starts by a minimization of elastic energy, which is calculated from a classical elasticity model. As a consequence the elastic tensor coefficients (Eq. 2.17) that minimize it are calculated.

$$E = \frac{1}{2} \int_V C_{ijkl} \varepsilon_{ij} \varepsilon_{kl} dV \tag{2.20}$$

where C_{ijkl} is the forth-ranked elastic stiffness tensor.

As a consequence of strain piezoelectric polarization appears in the structure, so the next step is to calculate it. In zinc blende structures it can be calculated as

$$\mathbf{P}^{pz}(\mathbf{x}) = e_{14} \begin{pmatrix} 2\varepsilon_{yz} \\ 2\varepsilon_{xz} \\ 2\varepsilon_{xy} \end{pmatrix} \tag{2.21}$$

where e_{14} is the piezoelectric constant. This prior step redefines the band edges of all constituent materials under strain. The resulting multiband structure is further calculated by solving self-consistently Poisson, Schrödinger and/or current equations depending on the input conditions.

Chapter 3

The role of polarity in VLS growth of III-V free-standing nanowires

As the optoelectronic behavior in semiconductor nanowires is directly correlated with the atomic arrangement of their compounds, it is essential to understand and control the parameters that play a critical role on it. Among them, polarity has been shown to be a crucial determinant of the final crystal structure of nanowires [11, 22], and thus, their properties. The aim of this chapter is to study at the atomic scale the polar-driven growth of GaAs, one of the most widely used III-V compounds, and the role that polarity presents in nanowire integration into (001) substrates of both GaAs and Si. In addition, we make a study on the impact of polarity in the generation of core-shell radial heterostructures composed by quaternary alloys by highlighting the polar dependence in spatial elemental segregation.

3.1 Introduction

3.1.1 VLS polar growth of binary semiconductors

During last years, the growth of high quality free-standing nanowires has been mostly carried out in a bottom-up approach following a vapor-liquid-solid (VLS) mechanism through Molecular Beam Epitaxy (MBE) or Metalorganic Vapor Phase Epitaxy (MOVPE). In this method, a liquid metal catalyst (traditionally Au) at high temperature adsorbs the vaporized materials from the precursors until reaching supersaturation. At this stage, the molecules of the precursors precipitate by forming a solid crystal nucleus at the liquid-solid interface with the substrate. This process keeps on in an unidirectional way as the molecules precipitate on top of the formed solid until the gas precursor sources are deactivated. The so-called VLS method arises then from the implication of the three states of matter (gas precursors, liquid

catalyst and solid precipitate) [117]. During the last years, Au catalysts have been progressively replaced by self-catalyzed growth [118, 119], as the metal particles have been demonstrated to generate trapping sites for carriers in the nanowire that can affect the system properties [120].

The VLS method for growing nanowire structures has been widely reported for multiple III-V compounds due to its versatility for creation of heterostructures. For instance, the growth of axial heterostructured nanowires can be achieved by the change of the precursors during the growth [106, 121, 122]. The use of the former strategy allows the creation of complex heterostructures, such as multiple quantum well arrays, which have been shown to act as outstanding candidates for photosensors and optical devices [123, 124]. In addition, it is possible to promote the growth of radial heterostructures by tuning the growth conditions (i.e. increase the temperature) in order to suppress the growth along the axial direction, so the solid deposition occurs on the lateral facets of the nanowire. The versatility of this technique provides then flexibility in the engineering of materials properties.

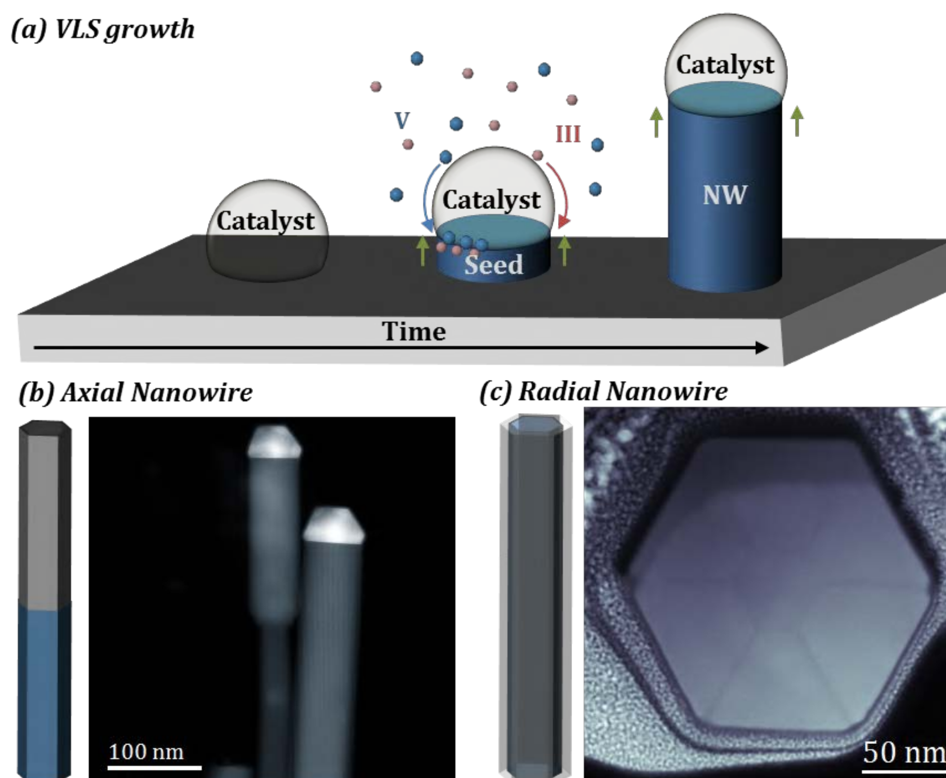

Figure 3.1: (a) Schematics of VLS growth mechanism. (b) Scheme and HAADF micrograph of axial heterostructured InAs-InSb nanowires [106]. (c) Scheme and HAADF cross-sectional micrograph of a radial Ge-GeSn$_x$ heterostructured nanowire.

Most reported III-V nanowires grow following their <111> ZB or <0001> WZ

directions, corresponding to those minimizing the total free energy of the system (although other growth directions have been reported for specific growth conditions [125]). <111> ZB and <0001> WZ are polar directions, as stated in Chapter 1, so their inversion is not thermodynamically equivalent. In that regard, the growth is said to be either A-polar or B-polar driven (III cationic or V anionic driven, respectively). Several studies have reported the latest one as a preferential growth direction for most III-V and II-VI compounds [10, 11] although some exceptions are reported [126]. Given these facts, the growth front orientation with respect to the substrate is well defined by the substrate crystal orientation and its exposed {111} planes. Hence, the available growth directions relative to the substrate crystal can be derived from the study of the 3D structure of an initial octahedral seed formed by the eight {111} planes in a cubic lattice (although other orientations derived from 3D twinning at the initial growth steps are available, as reported for GaAs [127] and InAs [128] nanowires). The employment of polar substrates drives the initial seed into preferential polar orientations that provide certain available {111} planes (Figure 3.2). Considering a material with preferential growth along <111>B direction and the initial seed being B-terminated, the only available <111>B direction allowing growth is the perpendicular to the substrate surface, leading to vertical structural growth. However, in the case of presenting an A-polar seed, three directions separated 120° from each other from the top projection and forming an angle of 19.5 ° with the substrate can lead to growth, which can result in tripod structures [129]. Other complex free-standing nanostructures such as tetrapods can be grown when a truncation of the octahedral seed happens during nucleation [11, 129].

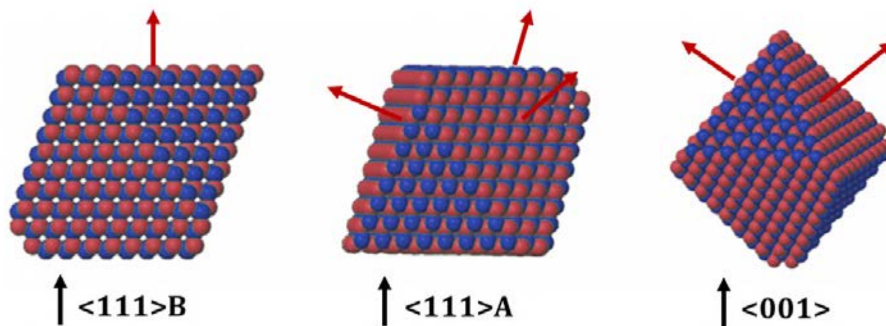

Figure 3.2: B-polar {111} facets available fot the growth in some substrate orientations.

In this chapter, we start focusing in the study of structural and compositional factors affected by the polar driven growth of 1D GaAs nanostructures, mainly in (001) substrates. In this situation, the initial seed presents two {111}B and two

{111}A planes available for the NW directional growth (Figure 3.2). Actually, V-shaped planar membranes can be obtained for conditions with a favorable B-polar growth by a double growth at each side of the seed [130, 131]. However, B-polar direction is also susceptible to a high density of rotational twinning events and polytypism in GaAs structures. For that reason, an effort has been put towards achieving the growth of A-polar GaAs nanowires. They have been successfully grown by Au-assisted VLS growth through the control of the droplet wetting angle [132], but gold-assisted growth is not compatible with the existing semiconductor industry. In this regard, there is a need of tuning of the growth conditions of self-catalyzed VLS GaAs nanowires to achieve high yields of A-polar NWs, which typically present a dramatic reduction in defect formation (and hence, enhanced photoelectric properties) without adding Au-induced trapping sites .

3.2 Self-catalyzed A- and B- polar GaAs nanowires

The first nucleation seed in GaAs [001] substrates presents four exposed {111} facets, two of them being Ga terminated and two of them being As terminated. This provides four discrete possible {111} nanowire growth directions with projections on the substrate separated 90° from each other and forming an angle of 35.2 ^{o} with the substrate, as schematized in Figure 3.3. This configuration makes easy to estimate the polarity of nanowires from direct observation of top or gross sectional projections.

Due to the preferential <111>B growth direction in GaAs, an optimization of Ga and As_4 fluxes was performed in this work for promoting the <111>A growth direction, while growth temperature was kept at 640 ^{o}C. In addition NWs were capped with a AlAs (10 nm)/$Al_{0.33}Ga_{0.66}As$ (100 nm)/GaAs (10 nm) shell heterostructure, as $Al_{0.33}Ga_{0.66}As$ has been reported to self-assemble (Al)GaAs quantum dots (QDs) that enhance the photoelectronic response for quantum photonic technologies [133]. The final AlAs capping acts as oxidation prevention for the inner structure. Figure 3.4 shows the fraction of A nanowires achieved for different V/III ratios and growth rates where a SEM top view or cross-section observation leads to polarity identification. A statistical analysis shows how a reduction of the V/III ratio is the main parameter maximizing the yield of A-polar nanowires (with optimal ratios around

2). The Ga flux itself can also affect the A/B ratio, obtaining an optimal value for 0.21 - 0.24 Å s^{-1} growth rates. In these conditions, the fraction of A-polar nanowires can be turned up to 57 % of the total.

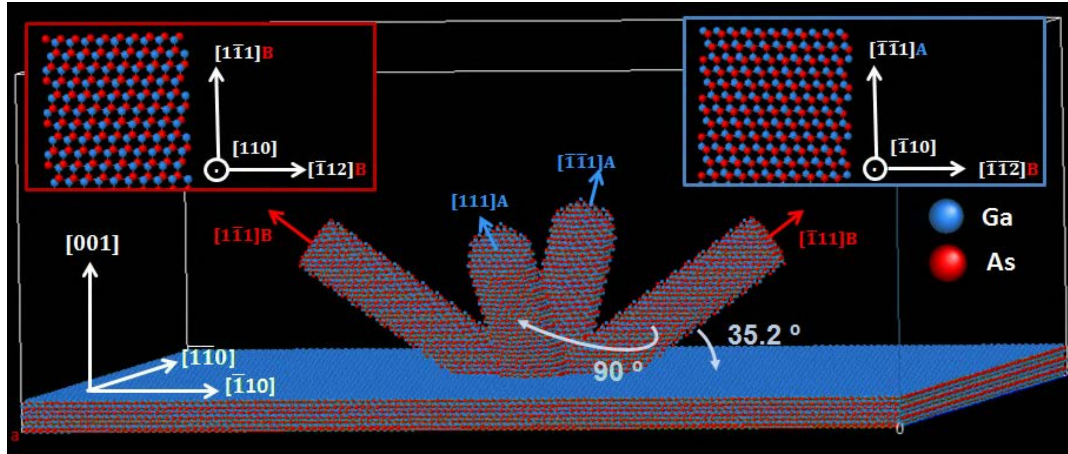

Figure 3.3: Three-dimensional atomic model of GaAs NWs grown along <111> A/B directions on a GaAs [001] substrate. The insets zoom the atomic arrangement of B and A polar NWs from the [110] and $[\bar{1}10]$ directions, respectively.

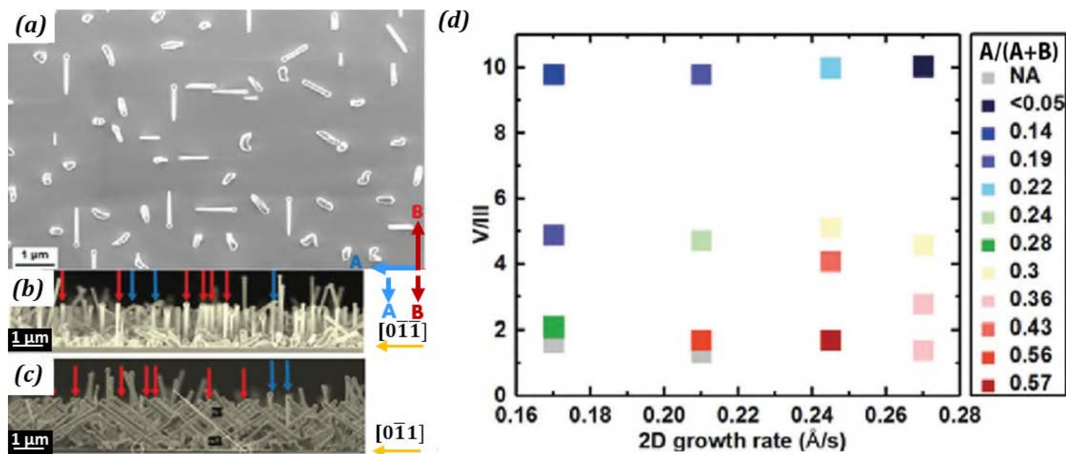

Figure 3.4: (a) SEM top view of nanowires grown with a Ga rate of 0.21 Å s^{-1} and V/III ratio of 1.7. The projections of <111>A and <111>B into the (001) plane can be employed for statistical analyses of NW polarity. (b),(c) Cross-sectional SEM micrographs of nanowires grown with a Ga rate of 0.60 Å s^{-1} and III/V ratio of 2.9. The NW polarity is determined according to the direction of their projections and labelled with blue (A) and red (B) arrows. (d) Fraction of nanowires grown with A polarity as a function of V/III ratio and Ga flux during the growth [134].

The results indicate that there is a competition between nucleation of A and B-polar NWs, getting an enhancement of cation polar NWs when reducing V/III ratios. There is a certain controversy in order to give an explanation of the absence of certain polar facets in the growth front, namely {111}A in the case of GaAs. A higher surface energy could be the cause of suppression of {111}A in favor of {111}B facets.

The {111} surface energy as well as the nucleation probability of GaAs is also affected by kinetic or thermodynamic factors such as chemical potential in the liquid phase. In this regard, it is plausible to believe that the reduction in the As concentration when lowering As_4 fluxes causes the effective energies of A and B surfaces to decrease and increase, respectively [134]. In addition, lowering the As ratio may increase the probability of wetting A-polar surface, resulting in the growth of A-polar NWs.

Based on these results, a further reduction of V/III ratio might seem as the solution for enhancing A-yield. However, further reduction of the fluxes makes them be relatively close to the background pressure in the growth chamber, so there are still some technological limitations in order to verify this hypothesis.

3.2.1 Polar-dependent structure of nanowires

Besides the growth being favored for a certain polarity, polarity also affects other factors such as morphological or structural aspects. For instance, twinning events tend to appear in preferential polar planes. For example, twinning appears in {111}A planes in the case of GaSb VLS NWs [22] while multiple twinning is commonly observed in {111}B planes of B-polar GaAs nanowires [135], leading to highly defective structures or even polytypism. Such defective plane stacking can be responsible of affecting the overall optoelectronic properties of the semiconductor.

Aberration corrected HAADF-STEM has been employed for determining the nanowire crystal structure. In addition, elemental identification in the atomic columns by direct intensity analyses allows to unambiguously determine the polarity of the growth front at each nanowire into study given the chemical contrast of the technique.

Figure 3.5 shows the nanostructural characterization of a B-polar nanowire. From the low magnification micrographs it is possible to observe how the nanowires present a uniform thickness after the first nanometers of growth. Taking a close view at the atomic arrangement, a high density of twin defects appears in $(\bar{1}\bar{1}\bar{1})$B planes (i.e. those perpendicular to the growth direction), which are the only {111}B planes exposed during growth [26]. Wurtzite inclusions are also found at the highest twinning

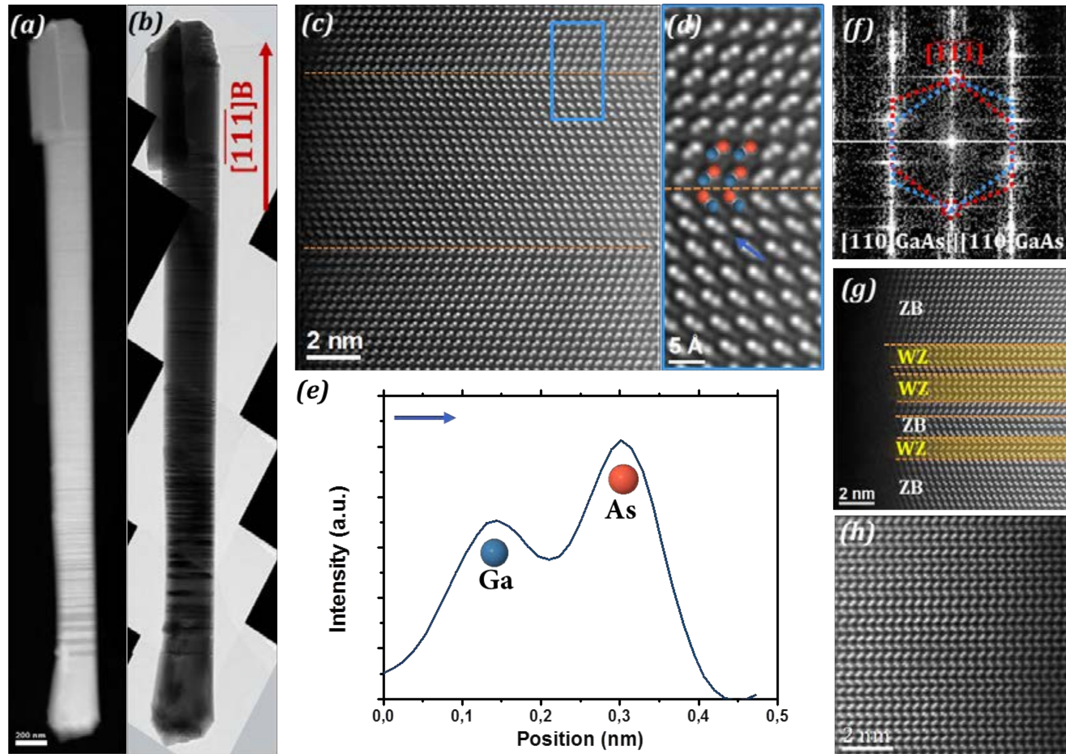

Figure 3.5: Low magnification HAADF (a) and HRTEM (b) micrographs of a B-polar nanowire. (c) High magnification and (d) zooming with atomic identification of the bulk of the nanowire. An intensity profile following the arrow is shown in (e) confirming B-polar growth front. (f) FFT of (c) reflecting twinning events. (g) Highly defective area showing some wurtzite inclusions. (h) Pure wurtzite phase is found close to the nanowire tip. [134]

density areas. Actually, the final section of B-polar nanowires is found to crystallize in WZ structure, as will be further detailed in next sections. This is caused by the final cooling of the growth process taking place under an As flux (and thereby increasing V/III ratio) to prevent GaAs decomposition. It has been reported that under these growth conditions WZ phase is favored [136].

Contrary to B-polar nanowires, A-polar ones show a defect-free pure ZB structure along most of the nanowire length, as displayed in Figure 3.6. Apart from the first stages of the growth that are commented later on, a single twinning event at the tip of the NW is found in most of the A-polar NWs examined so far, which is the only defect present in the bulk of the nanostructure, as observed in Figure 3.6e. This fact is consistent with the polar dependence of twinning events in GaAs that was mentioned previously. The relative orientation of {111}B planes with respect

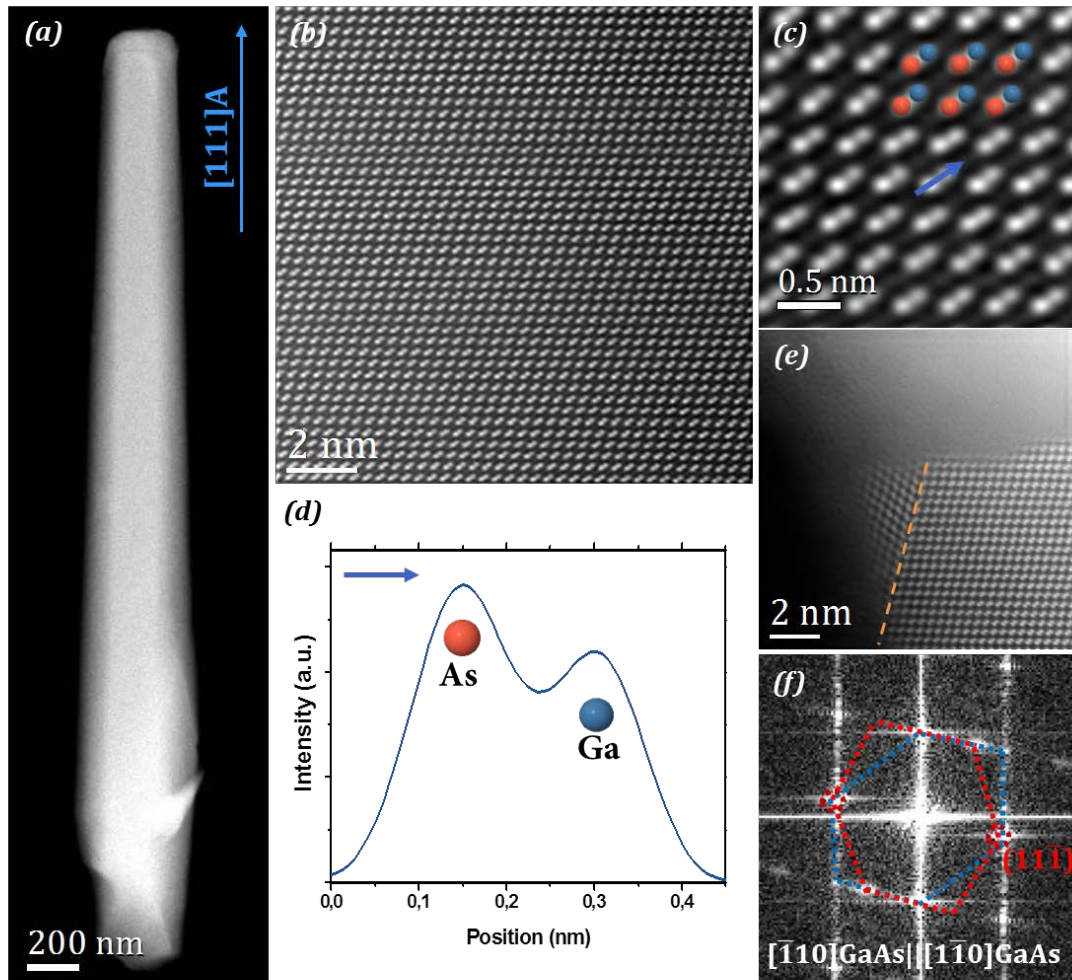

Figure 3.6: (a) Low magnification HAADF micrograph of an A-polar nanowire. (b) HAADF-STEM micrograph reflecting the lack of defects in GaAs ZB structure and (c) zooming of the squared region in (b). (d) HAADF intensity line profile confirming the A-polar nature of the nanowire. (e) HAADF-STEM obtained in the nanowire tip and (f) its corresponding power spectrum showing the presence of a twin boundary appearing in the (11$\bar{1}$)B plane. The two last micrographs are from a different nanowire to the one shown in (a), however the same structure is found in all the A-polar nanowires analyzed so far. [134]

to the {111}A growth front was shown in Figure 3.2. This geometry leaves a three-fold symmetry for {111}B planes that might produce twinning. However, their orientation with respect to the A - growth front makes them extinguish without further propagation within the formed single crystal, creating large pristine crystalline structures [137]. Notice that the orientation of {111}B planes with respect to the growth front allows the presence of two extra twinning plane possibilities that are not perpendicular to the zone axis, and then, they are not observable by HAADF from this specific nanowire orientation. We assume then that despite the high crystal quality observed, the density of these oblique twins is three times higher than observed.

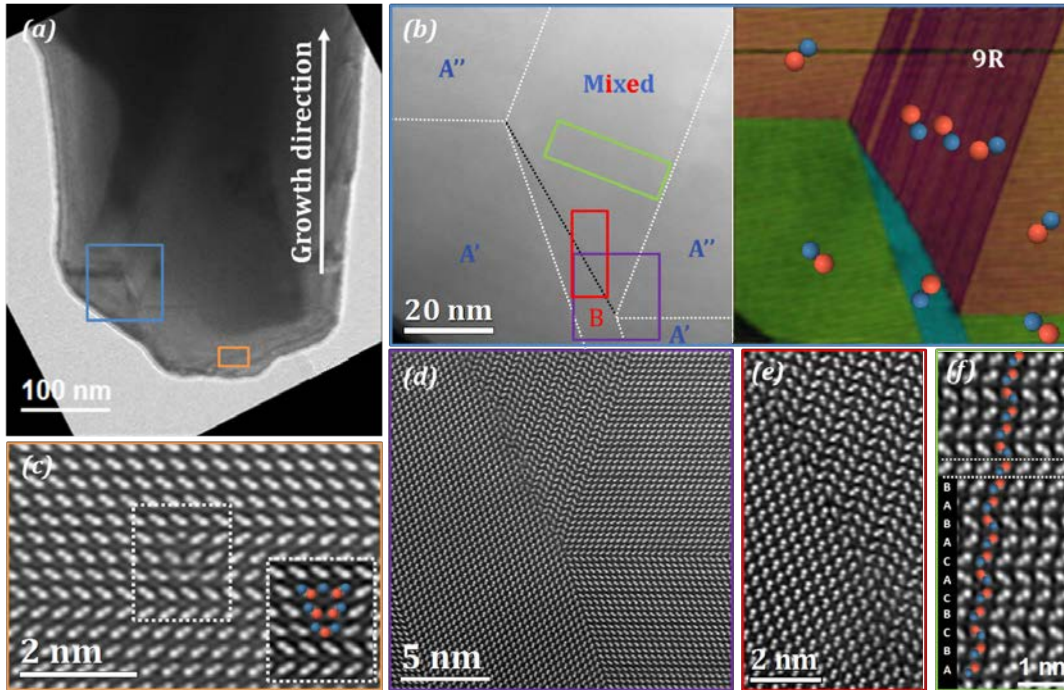

Figure 3.7: (a) Low magnification HRTEM micrograph of the defective base of an A-polar nanowire. (b) Details of dumbbell orientation changes after twinning events at the base of the nanowire. The labelling A′, A″ and B′ reflect the dumbbell orientation with respect to the overall nanowire growth direction. A color map obtained by {111} plane filtering is also shown. (c)-(f) Details of the atomic columns of defective regions including a {112} mirror polar defect when an atomic step occurs in twinning (c) and 9R polytype stacking (f). [134]

Nevertheless, the quasi defect-free structure observed in the bulk of the nanowire develops after several nanometers of nanowire growth. Figure 3.7 shows some of the highly defective features observed at the initial nucleation. When considering A and B polarities strictly referring to NW growth direction, it turns out that several regions with different polar orientations appear at the initial stages of growth as a result of a high twinning density in several directions, including a section presenting different polytypism corresponding to 9R stacking sequence according to Ramsdell notation [16] (Figure 3.7d-f). In addition, Figure 3.7c reveals how a step in a {111} ortho-twin boundary is responsible of forming a polar inversion defect with the height of three {111} planes which presents mirror symmetry at opposite sides of the {112} vertical planes. In this defect, the As-As and As-Ga bonds become 5-fold and 3-fold coordinated at the boundary plane, in a defect configuration resembling those found in (111)B GaAs(P) nanowires [138]. The presence of these kind of defects was deemed to be detrimental to the functional properties of NWs, as they act as non-radiative recombination centers. Notice that the polar preference for twinning events during steady vertical growth is not kept during first stages where A and B

polar growth seem to compete. Nevertheless, all the defective region turns to occur in the first 200 nm of the growth, resulting in the bulk defect-free ZB structure shown previously in Figure 3.6 after them.

3.2.2 Optoelectronic response for different NW polarities

The different nanostructural arrangement of A and B polar nanowires plays a key role on their optoelectronic response, and thus, it is essential to analyze it in order to properly functionalize the NWs. For this purpose, we performed cathodoluminiscence at 20 K to measure the light emission of the nanowires at two spectral ranges: 1.43 - 1.53 eV and 1.77 - 1.94 eV, corresponding to GaAs cores and (Al)GaAs QD emission, respectively.

Figure 3.8 shows the CL emission maps obtained on a region containing nanowires of both polarities. From Figure 3.8b it is already highlighted that nanowires growing in A-polar direction present a much more uniform intensity of emission. Contrary to B-polar NWs, the energy of the emitted photons by GaAs is also uniform across the bulk of the A-polar nanowires when analyzing the three main GaAs emission energies 1.51, 1.48 and 1.45 eV, which correspond to 822, 836 and 854 nm wavelength, respectively (Figure 3.8c). Regarding the QD emission region (1.83- 1.87 eV) in Figure 3.8d, we observe several emission sites along A-polar nanowires while B-polar ones show no trace of it.

In order to understand the different optical behavior of both cases, CL spectra were obtained in different points labelled as A1, A2 and A3 and B1, B2 and B3, where 1 is acquired at the base, 2 at the middle and 3 at the tip of a nanowire presenting A or B polarity, respectively. GaAs core emission range spectra (Figure 3.8e,f) are clearly different in A and B polar nanowires. A-polar nanowires show two emission peaks centered at around 1.51 and 1.48 eV which appear uniformly along all the nanowire length. While the first one corresponds to the free exciton emission of GaAs at 20 K, the second one can be attributed to carbon contamination [26]. Contrary, B-polar nanowire peaks are broader and redshifted with respect to the free exciton emission. This phenomenon can be attributed to the defected microstructure, as WZ/ZB stacking is known to have staggered type II band alignment [26, 139, 140], where electrons are localized in the ZB and holes in the WZ regions (Figure 3.9). Therefore,

multiple transitions from 1.43 to 1.51 eV are available as a signature of polytypism or equivalently, twinning events producing a WZ monodomain. In addition, there is almost no intensity at 1.51 eV, as expected for polytypic structures as the twinning events behave themselves as unitary WZ regions, making the nanowires behave like multiple stacked quantum well structures, which explain both the red-shift and peak broadening in B-polar nanowires with respect to A-polar nanowires.

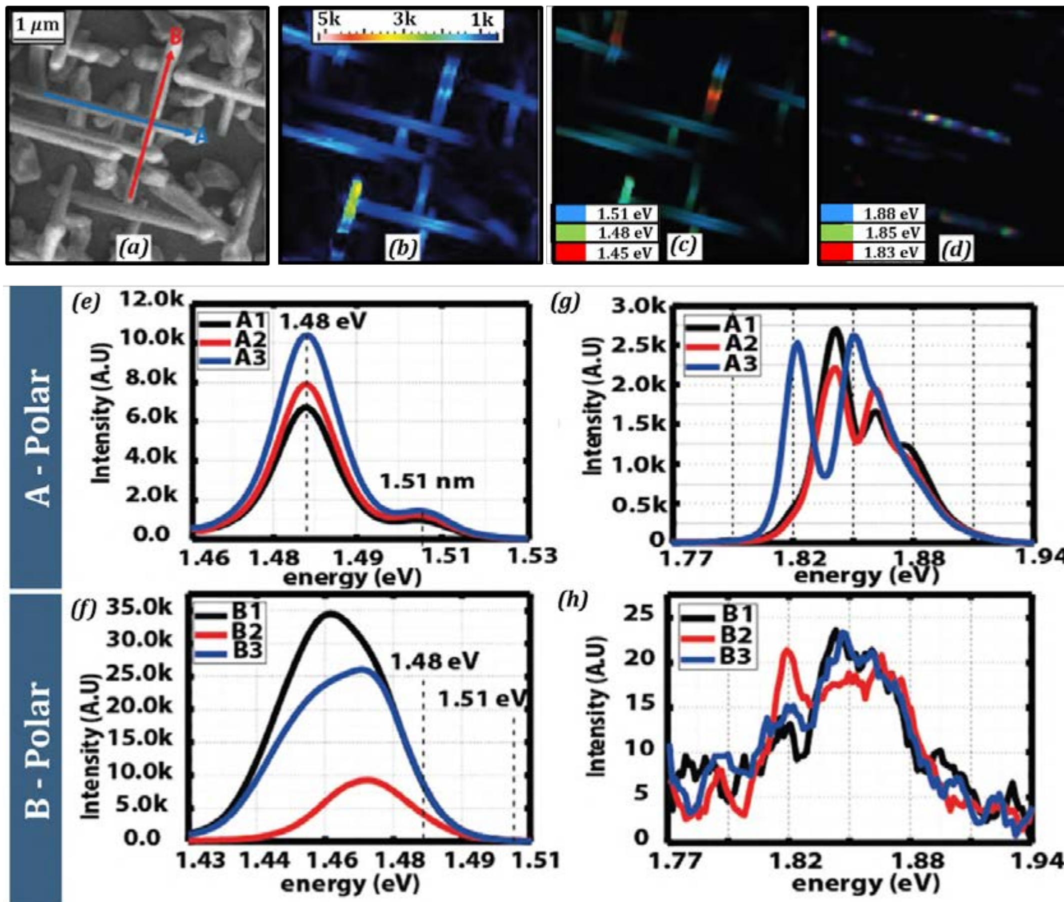

Figure 3.8: CL emission maps showing the optical response of NWs with A and B polarities. (a) Top view SEM image with labels indicating the directions of the two different nanowire polarities. (b) Panchromatic intensity map in the region of study. (c)-(d) Wavelength dependent CL intensity map for the low and high energy ranges of study, respectively. (e)-(h) CL spectra at different points of the nanowire in the GaAs and (Al)GaAs emission ranges, where A(B)1 is acquired at the base, A(B)2 is acquired in the middle and A(B)3 is acquired at the tip of an A(B)-polar NW.

Finally, analyzing the emission range corresponding to the emission of the AlGaAs shell (1.77 - 1.94 eV) several spatially localized emission spots are found in A- polar nanowires while there is no significant emission for B-polar nanowires (Figure 3.8d). When analyzing the emission spectra (Figure 3.8g,h), emission around 1.85 eV is observed for both A and B polar nanowires, being B-polar emission intensity two orders of magnitude lower than the A-polar one. As mentioned before, the emission

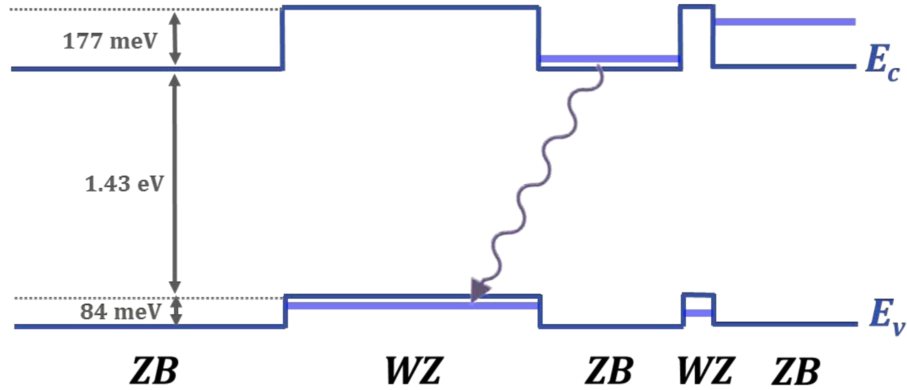

Figure 3.9: Band diagram of stacked ZB and WZ segments showing available transitions from 1.43 eV through the type II staggered band alignment.

lines between 1.77 and 1.94 eV arise from QD self-assembled from AlGaAs compositional fluctuations [133]. The difference in emission brightness can be attributed to the defective structure in B-polar nanowires, where defects act as shortcuts for injecting excitons from shell to core. This migration depletes the QDs from excitons in B-polar NWs.

3.3 Liquid ordering at L-S interfaces in VLS nanowire growth

The key parameter for controlling the nature of VLS growth process is the liquid-solid interface, which involves the whole interface together with the nature of the triple phase line. However, the studies on it developed so far have been carried out in terms of macroscopic parameters such as the contact angle of the liquid droplet, surface energies at the solid-vapor and solid-liquid interfaces and chemical potentials. However few studies take into account the atomistic nature of each of the growth components.

Previous works have shown that the liquid phase can exhibit some degree of order at the interface with the solid [141–143]. Kaplan and Scheu groups demonstrated that ordering of liquid Al at the interface with Al_2O_3 could take place up to four or five layers. The degree and nature of the order depended on the polarity and crystallography of the surface. Their data is also points out to the influence of the solid crystal in the liquid ordering and the possible role of this ordering in crystal growth processes [142]. However, none of such ordering effects in the VLS growth

have been considered so far.

3.3.1 Evidences of liquid ordering at the interface

In order to study the ordering at interfaces and demonstrate its relevance in polar growth, HAADF-STEM micrographs were obtained in nanowires grown on (001) GaAs substrates at As_4 fluxes providing a 50 % ratio between A and B nanowires. As advanced in the previous section, the crystalline structure in the last layers of the nanowire belongs to ZB phase in the case of A-polar nanowires while WZ phase is favored under the increased As fluxes of final growth for B-polar nanowires [136]. Figure 3.10 shows the evidences of liquid ordering at the liquid-solid interface for both A and B polar nanowires. A different arrangement depending on polarity is clearly observable: while certain periodicity is present along $[000\bar{1}]$ GaAs(WZ) direction in B-polar NWs, this behavior occurs following [110] GaAs(ZB) direction in the case of A-polar NWs.

Comparison between ordering at A and B liquid-solid interfaces has been carried out by considering [111]ZB or $[000\bar{1}]$WZ directions, those perpendicular to the interfaces. The ordered section is significantly wider in B-polar nanowires, extending up to 11.1 Å compared to the 8.5 Å length observed for A-polar nanowires. Statistics over several nanowires for each polarity reveal a liquid layer spacing of 2.35 ± 0.05 Å for A-polar NWs vs 2.75 ± 0.15 Å for B - polar nanowires. In addition, the intensity profiles shown in Figure 3.10 reveal a significant decrease in layer spacing after the last solid dumbbell unit, being much more pronounced in the case of A-polar nanowires.

Regarding A- polar nanowires, a first layer where atomic positions are clearly resolved is observed. Actually, considering the position of the last As atom forming a dumbbell and ZB stacking sequence they can be attributed to As atoms just being deposited before completing the dumbbell unit. Immediately inside the droplet the Ga atoms order following [001] direction. This agrees with the direction where next Ga atom should accommodate for preserving a defect-free ZB structure. However, the distance where first intensity maximum is located following an intensity profile along [001] does not match with the Ga position within the dumbbell unit. This is a sign of different bonding properties in this area.

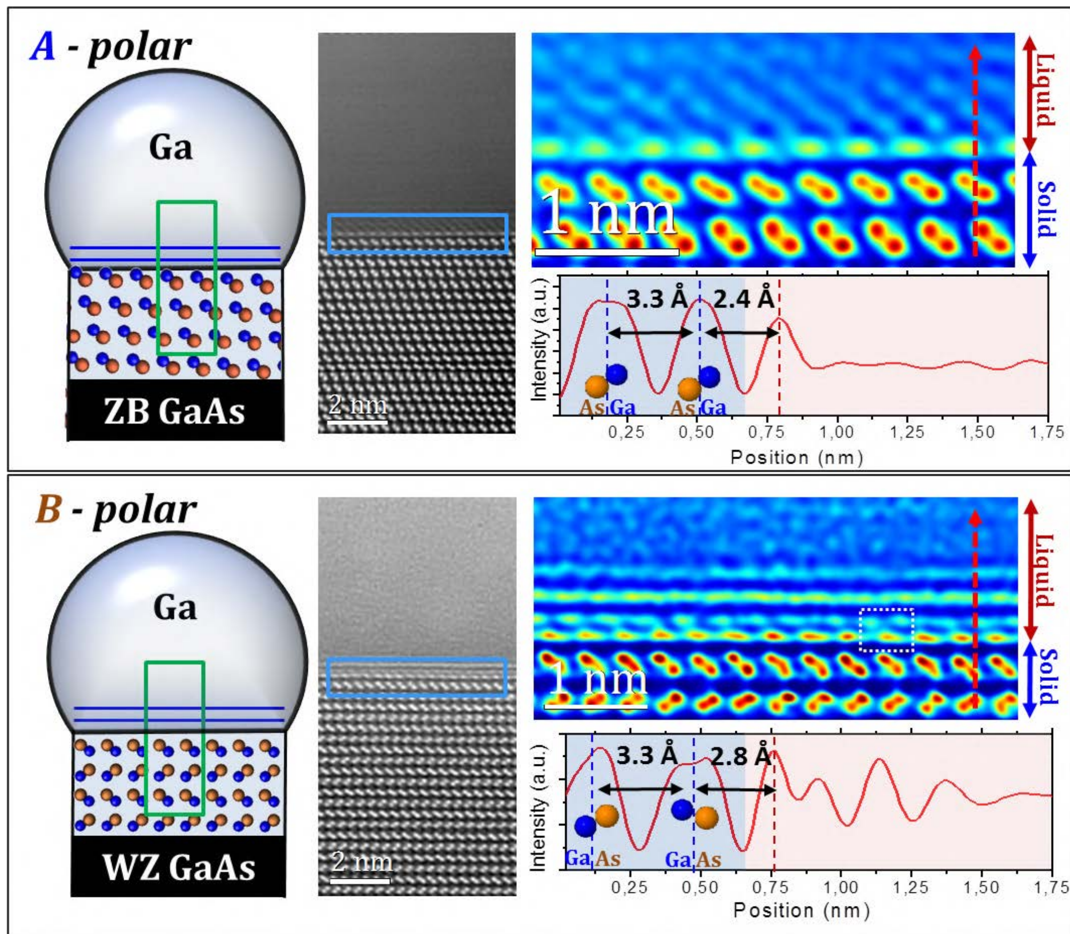

Figure 3.10: Schematics of A and B polar nanowires in contact with liquid Ga droplets, HAADF-STEM micrographs of [111]/[000$\bar{1}$] solid-liquid interfaces with a colored zoom revealing different liquid Ga ordering at interfaces of A and B polar nanowires. Intensity profiles along [111] or [000$\bar{1}$] directions of A and B polar interfaces, respectively, show different interlayer distances at the ordered liquid planes.

The case of B-polar liquid ordering is slightly more complex. The first layer after the last defined dumbbell is attributed to Ga atoms. However, the atomic position in [000$\bar{1}$] WZ direction is decreased with respect to the one in bulk solid. Moreover, the lateral spacing is not constant along this layer, being the intensity maximum positioned in ZB ABCABC stacking configuration in some cases and located closer to a WZ ABABAB stacking configuration in others. Contrary to A-polar NWs, defined positions are also found in a second layer in the liquid. Neither the distance with respect to the last Ga atomic layer or the direction with respect to the Ga positions agree with those of a dumbbell unit. In addition, these positions are not as sharply defined as in the previous layer and a certain lateral elongation suggests that there are several lateral available positions in the depth of the sample. It is important to highlight that in some cases where these positions are defined in a sharper way,

two intensity maxima equidistant with respect to Ga atoms can be observed (yellow squared in Figure 3.10), which is probably related with the availability to rotate 180° the dumbbell orientation (twinning). After this resolved layer, horizontal ordering with reduced interplanar spacing with respect to $(000\bar{1})$WZ is observed without clear lateral ordering.

The differences in the ordering in A and B polar growth explain the different probabilities on defect formation. Ga orders following ZB dumbbell direction in the vicinity of the solid surface, driving atoms to allocate following these positions when depositing into the solid. The lack of defined positions switching this direction indicates the fewer probability of atoms getting linked to form a twin or WZ monodomain. In B- polar NWs, the ordered liquid Ga seems to present two equiprobable positions with respect to the last deposited Ga layer. This fact would allow the structure to twin and form WZ sections or crystallize with ZB stacking.

The presence of ordering at the liquid - solid interface might include a transition region between both phases presenting its own independent properties [143]. In this framework, the transition region (in our case the ordered liquid region of $\approx$1nm thickness) has been named *complexion* [144]. In order to evaluate the presence of an independent electronic behavior at the ordered liquid region, low-loss EELS analysis was performed to obtain information on the bulk plasmon resonance, which is sensitive to the valence electron density (Equation 2.12). This methodology is similar to the one applied by Gandman *et al*. where the bulk plasmon resonance of liquid Al was demonstrated to be dependent on the adjacent faceting [143].

Figure 3.11 shows the main features regarding the bulk plasmon energy loss obtained in the tip of A and B polar nanowires. The liquid bulk plasmon located at 14.1 eV together with the ZLP have been used as calibration references for both cases. Any relevant features distinguishing A and B polar nanowires are observed apart of a different plasmon peak broadening that might originate from differences in nanowire thickness. However, there is a clear transition region from solid GaAs to liquid Ga where the bulk plasmon peak appears at energies between 14.1 eV (liquid Ga) and 16.3 eV (solid GaAs), as observed in the low loss signal display of Figure 3.11. It can be also observed that the intensity maximum shift in energy at the ordered liquid section is accompanied with a decrease in the measured intensity.

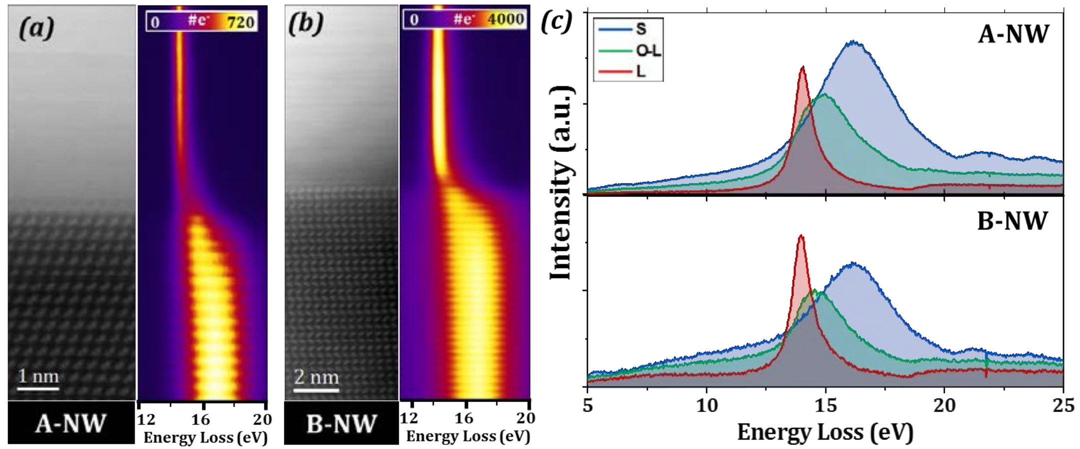

Figure 3.11: HAADF-STEM micrograph and 2D display of cumulative low-loss EELS signal along the horizontal direction displayed from 12 to 20 eV for (a) A-polar and (b) B-polar nanowires. (c) Energy loss signal after zero-loss peak subtraction in solid (S), liquid (L) and ordered liquid interface (O-L) regions for both polarities.

The inherent delocalization of low energy excitations supposes a uncertainty whether to attribute the interface plasmon to the different ordered phase or it is a linear combination of the delocalization of GaAs and Ga plasmon peaks [145, 146]. For that reason, a multiple linear least squares (MLLS) fitting routine has been used to discriminate between these two situations [147]. The spectra displayed in Figure 3.11c were used as reference components for solid (S), liquid (L) and ordered liquid (O-L) losses and the fitting was performed in a range from 10 - 25 eV that encompasses all the main bulk plasmon peaks.

Figure 3.12 shows the representative results of the component MLLS fitting obtained in the A-polar NW. The accuracy of the analysis when considering or not O-L spectrum as an independent component is shown in Figures 3.12c-b, respectively, by a display of the normalized residual signal across the area. Meanwhile the fittings in the liquid and solid parts do not present any relevant discrepancy between both situations, the residual signal obtained at the interface area when performing a two components linear combination indicates that this plasmon peak is not a combination of solid and liquid signals due to delocalization. Thus, it arises independently from the other two parts from the atomic arrangement at the interface. Figure 3.12d displays a RGB map revealing the spatial distribution of the fitting coefficients, and thereby, the total spatial distribution encompassed by each component. This reveals that the O- L plasmon penetrates into the first angstroms of solid and liquid phases, covering a scope of about 3 nm. This fact is clearly observed in 3.12e, where a signal

is obtained in the liquid part at almost 1 nm from the interface. The spectral reconstruction based on the obtained coefficients reveals how the signal at this position arise from a superposition of liquid and ordered liquid regions, even though the ordered range is extinguished at this area. No remarkable differences are found in B-polar nanowires when performing these analyses under the same conditions.

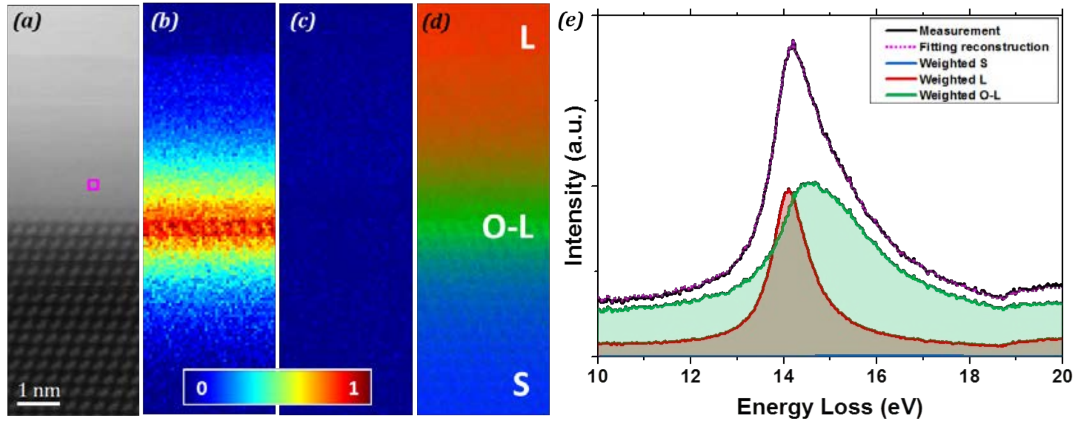

Figure 3.12: (a) HAADF-STEM micrograph of the region of study in an A-polar nanowire. (b),(c) Normalized residual signal from 12-20 eV after MLLS fitting with L and S components and L, S and O-L components, respectively. (d) RGB composition of normalized three fitting coefficients along the studied area for liquid (red), ordered liquid (green) and solid (blue). (d) Intensity of the weighted S, L and O-L components and fitting reconstruction together with the experimental EELS signal in the point close to the interface marked in (a).

This analysis confirms that electronic behavior at the interface acts independently, probably arising from the liquid ordering at Ga droplet. However, we would expect a different electronic response arising from the different ordering in A and B polar nanowires which has not been observed, probably due to the weaker bonding in liquid media not producing remarkable signal differences.

3.3.2 Correlation with polar-dependent crystal structure

Simulations based on machine learning potentials and molecular dynamics were employed to compare with the 3D liquid ordering observed at the interfaces. In order to make the link with the growth process, these simulations are performed at the nanowire growth temperature. Figure 3.13 depicts the ordering of the interface for both polarities where the spatial variation in the Ga atomic density is indicated by blue isosurfaces. Figure 3.13a shows a 3D view of the ensemble for a B-polar WZ solid in contact with liquid Ga. Figure 3.13b provides top and side views for the A and B-polar solids. We find ordering in- and out-of-plane plane for both cases,

with significant differences in the arrangement of Ga atoms as a function of the polarity. These arrangements and their fringe distances are consistent with the stripes measured within the liquid droplet by HAADF.

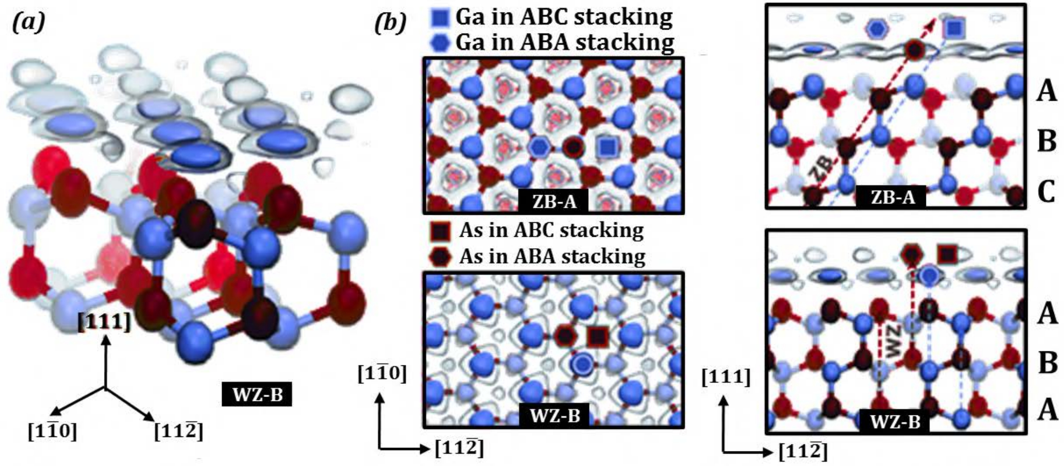

Figure 3.13: Simulations of the Ga(L)-GaAs(S) interfaces at the growth temperature. Isocontours of the Ga atom density, showing ordering at the liquid-Ga/GaAs interface corresponding to densities of ρ =0.11$Bohr^{-3}$(opaque) and ρ=0.06 $Bohr^{-3}$(translucent). Ga and As atoms are drawn in blue and red, respectively. (a) 3D view of B-Polar WZ GaAs. (b) Projections along the $[111]_{ZB}/[000\bar{1}]_{WZ}$ (left) and $[1\bar{1}0]_{ZB}/$ $[11\bar{2}0]_{WZ}$ (right) directions. The positioning of Ga and As atoms required for a new Ga-As bilayer creation are indicated by taking the isocontours and the underlying structure as canvas.

On the B-polar surface, Ga is adsorbed right on top of the terminal As. This is consistent with the large electronegativity difference between As and Ga that is likely to induce strong electrostatic interactions. In-plane ordering is also present at the A-polar surface. Here, instead, Ga atoms in the liquid pair with the terminal Ga atoms in the solid, consistent with the dimerization tendency of Ga.

Moving to the microscopic picture of GaAs growth, any new layer of GaAs forms new Ga-As pairs. Ga and As atoms are shown in blue and red in Figure 3.13, while the positions leading to ZB and WZ configurations are indicated by squares and hexagons, respectively. In the A-polar case, As must displace and occupy the position of ordered Ga in the liquid, with which it may form a dumbbell. The Ga atoms have two choices, as indicated in Figure 3.13b by the square and hexagon. Depending on the position selected, ZB (ABCABC stacking) or a twin (ABA stacking) is formed. These two positions are not equivalent in terms of their first and second nearest neighbours configuration. In the ABC stacking, Ga is found at the middle of a projected hexagon, while in the ABAB it is at a vertex. Further calculations beyond

the scope of this work should corroborate if there is a position that is more energetically favorable. Still, to form a new bi-layer, As atoms should first displace the ordered Ga layer on top of the NW, and this should increase the formation barrier. This is consistent with the difficulty in synthesizing A-polar GaAs NWs [132, 134], suggesting that the slower process may help the growing layer achieve the more thermodynamically stable ABC stacking. The low probability of twinning reduces at the same time the probability of WZ formation, as both are closely connected [12].

During the formation of a new bi-layer for the B-polar surface, the Ga atoms adsorbed on top of the As-terminated surface can stay at their position. The incoming As atoms occupy empty positions in the second row. The fact that the growth can proceed without displacing Ga atoms is consistent with the observation of a more facile growth for this polarity. The higher growth rate can also partly explain the higher propensity to introduce stacking defects and polytypism in B-polar GaAs NWs [132]. These results could explain why in polar semiconductors, growth in certain polarity is preferred and how polarity determines the tendency for polytypism.

3.4 Bipolar growth in GaAs nanowires

It has been stated that there is a preferential <111> growth direction for nanowires where the polarity of the growth front is determined by kinematic and energetic factors. However, a chaotic and highly defected growth takes place at initial stages in conditions where both polarities can coexist until an unidirectional growth is achieved, as seen previously in Figure 3.7. The multiple 3D twinning together with other incoherent defects might lead to different nanowire growth directions [127, 128, 148] which can produce the simultaneous growth of different <111> fronts, making the overall system grow following another crystallographic direction. This mechanism can be employed to tune the growth direction and engineer NWs to grow perpendicular to (100) substrates, making them more suitable for integration in CMOS technologies.

3.4.1 Growth along the <112> direction

The growth of <112> oriented nanowires has been commonly found in elemental group IV semiconductors as a result of multiple {111} twinning during nucleation that creates additional growing sites [13, 149–151]. One particularity of this growth direction is the appearance of axial or lamellar twinning parallel to the growth direction, which leads to large unidimensional defect-free grains [149] that grow as independent vertical fronts [13]. The growth fronts are not parallel to the NW growth direction in this situation.

The <112> growth direction is rarely observed in polar compounds and just few cases have been reported [13]. This is caused because the symmetry of the group IV elements in diamond structure is broken with the appearance of polar bonds in group III-V ZB compounds. The eight equivalent {111} planes of diamond structure are split into four {111}A and four {111}B planes, being two of them more favorable for growth. In that regard, situations where coexistence of A and B polar growth are promoted are required for the growth of <112> NWs.

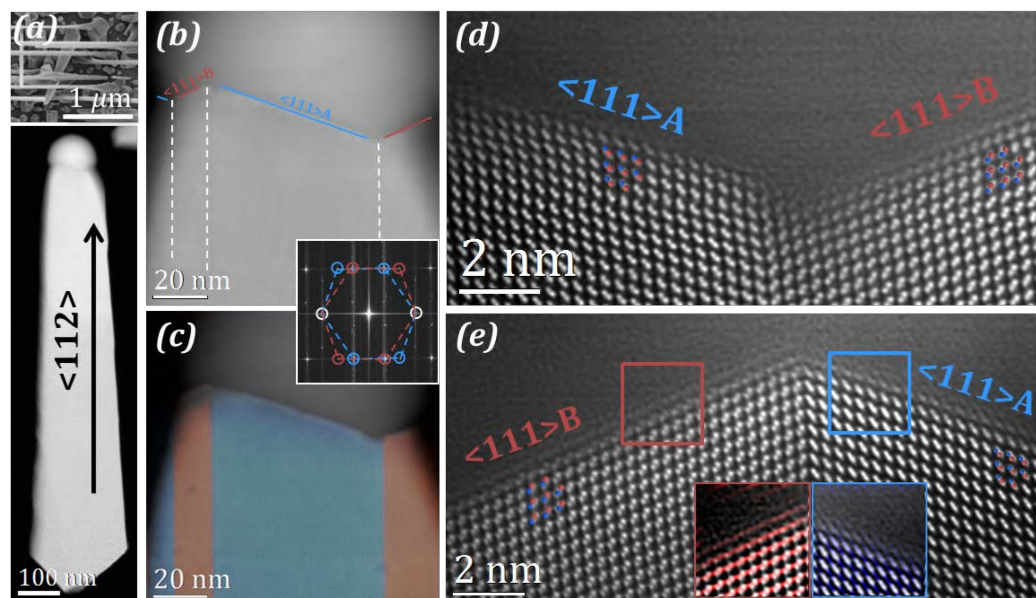

Figure 3.14: (a) SEM micrograph and low magnification HAADF-STEM micrograph of a <112> nanowire. (b) Atomically resolved micrograph labelling the different <111> growth fronts. White dashed lines indicate ortho-twins preserving polarity across nanowire width. (c) Structural map of (b) showing the twinned domains. (d),(e) High magnification micrographs with atomic identification on the two types of kinks in contact with the catalyst. Insets in (e) reveal same polar-dependent liquid ordering in the Ga droplet as in previous <111> NWs.

A 50 % of NWs of each polarity is reached when growing GaAs with the conditions described in previous sections, so growth in cation and anion polar directions can be produced, 'favoring' the creation of these structures. Figure 3.14 shows how the growth of <112> nanowires is possible (even though with a low yield) under these conditions. Four <111> growth fronts (two A-polar and two B-polar) are growing at similar rates creating a planar structure with four defect-free crystals connected by ortho-twin boundaries which preserve the lateral polarity. In addition, Figure 3.14e reveals how the liquid ordering in the Ga droplet preserves the same structure as in the previous analyzed <111> NWs: in the A-polar section liquid ordering mainly appears in [110] direction while in B - polar section the ordering takes place in $[\bar{1}\bar{1}\bar{1}]$ direction.

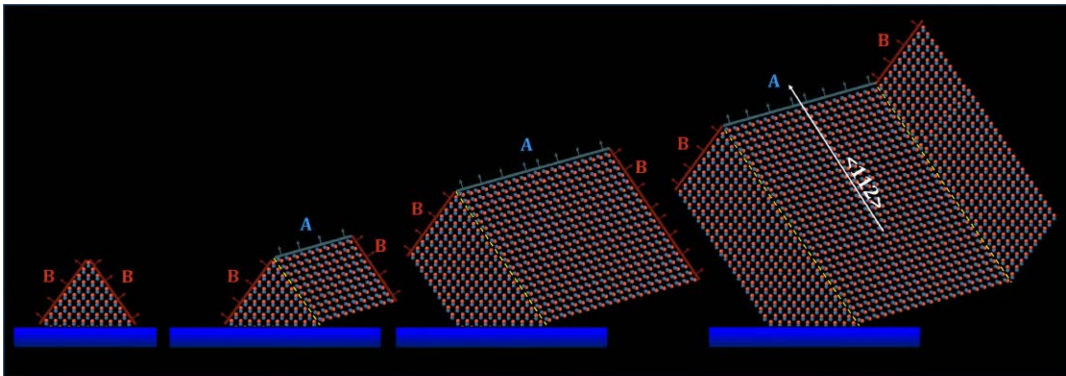

Figure 3.15: Schematics of the formation of the axial twinning that gives rise to <112> nanowires.

The axial twinning observed in <112> nanowires extends until the NW base, meaning it arises from the very first stages of the growth. Figure 3.15 shows the mechanism of formation of <112> nanowires from the initial nucleation seed. At the beginning, a truncated octahedron on the (001) substrate exposes two {111}B and two {111}A facets. The {111}B facets are susceptible of suffering twinning, so spontaneously one twin is produced at one side of the seed while the other {111}B facet keeps expanding. The 180 º rotation along the twinning plane axis inverts the polarity of such octahedron versus the growth front, providing one available {111}A plane for growth. In situations where A and B growth rates are similar, the facets in contact with the droplet can expand regardless of their polarity, so a growth expansion towards the <112> direction starts to be produced as A and B growth fronts advance. At the same time, the nanowire can expand laterally along the <111>B direction and form twins as soon as the droplet still wets the facet. At some point, the

droplet stops wetting the lateral side of the nanowire and the growth is produced unidirectionally in the <112> direction with several simultaneously active growth fronts that create the zig-zag shape observed at the tip of the NW. At the same time, the laterals develop to a more thermodynamically stable faceting configuration. This mechanism also explains the asymmetric shape of the nanowires, which typically present larger lateral expansion in the B-polar side of the nanowire.

The ability of switching the growth direction by twinning at the initial stages of growth opens the possibility of engineering the NW growth to promote the growth of large crystals along vertical directions on (100) substrates, particularly Si.

3.4.2 Engineering vertical growth on (100) Si

Given the special interest in controlling the droplet catalyst interactions for determining the growth of nanostructures in terms of polarity, crystal phase and uniformity, some strategies can be done in order to control the contact angle. Particularly, a top-down approach can be employed for substrate nanopatterning and start afterwards the nanostructure growth through a bottom-up approach [152]. This strategy allows both a control over the nanostructure position and a control over the catalyst contact angle, providing a precise accuracy over the final nanostructure generation.

Figure 3.16 shows the achievement of GaAs vertical growth on Si(100) substrates by the strategy described by Guniat *et al*. [152], which gives rise to planar-like structures baptized as *NanoSpades*. The employment of a non-polar substrate gives two possible non-equivalent orientations for the first nucleation seed, which explain the different nanospade orientation observed in Figure 3.16a,c.

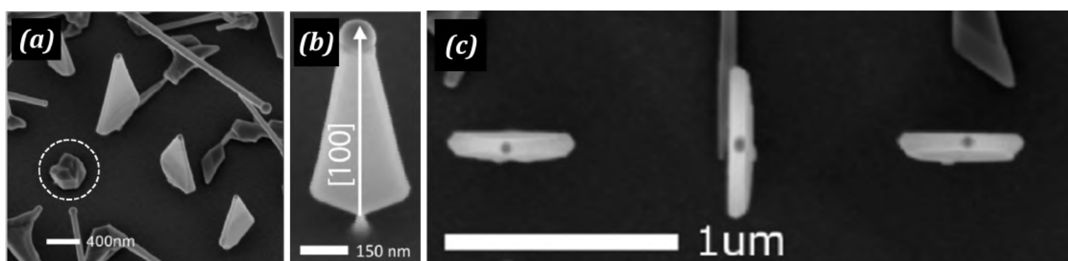

Figure 3.16: SEM images of GaAs nanospades grown on nanopatterned Si pillars [152]. The structures grow vertically along the [100] direction in two possible in-plane orientations. (a) Tilted SEM image showing four aligned nanospades. (b) Details of a nanospade morphology on top of a pillar. (c) Top view showing the two possible in-plane nanospade orientations differing in 90 º between them.

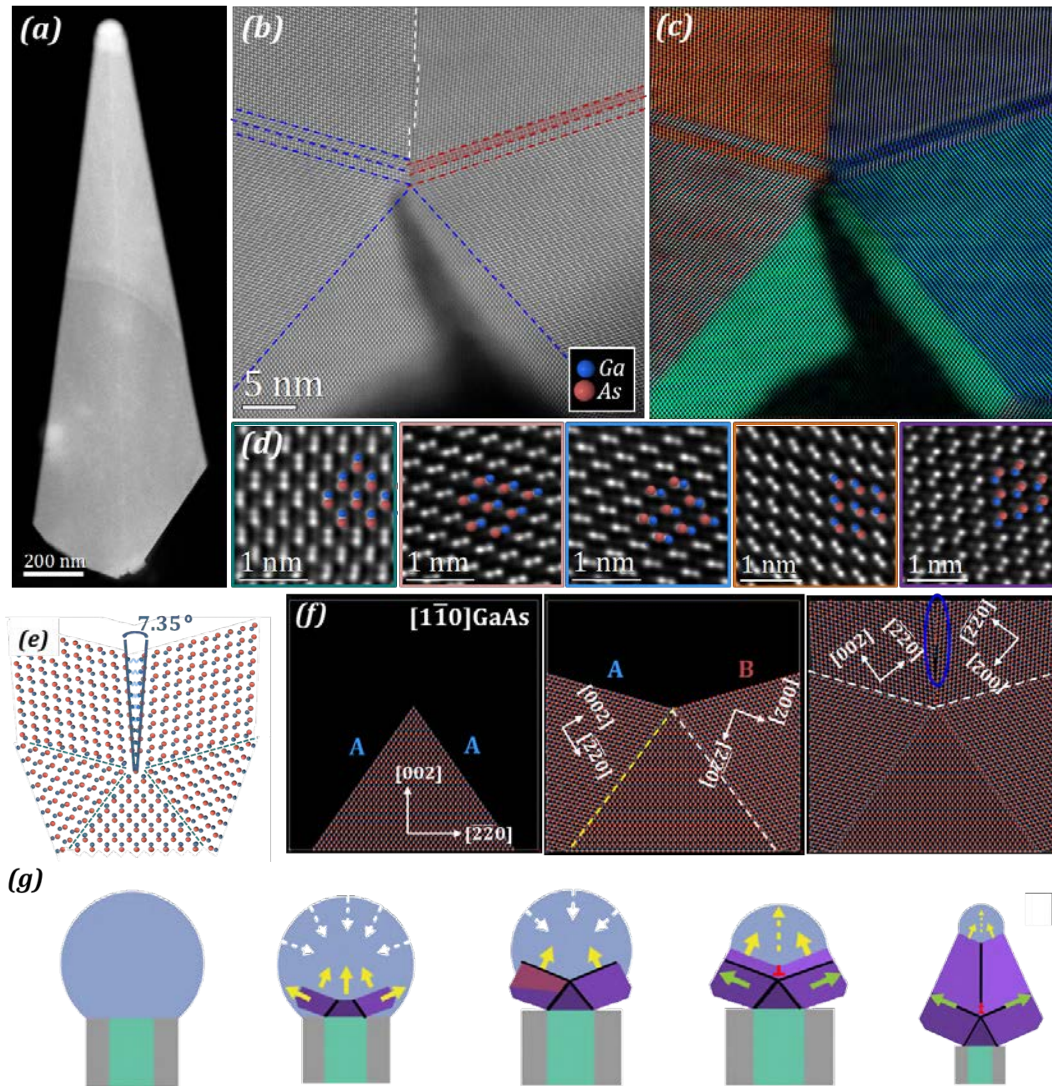

Figure 3.17: (a) Low magnification HAADF - STEM micrograph of a nanospade. (b) Atomically resolved micrograph of the nanospade base and (c) color orientational map obtained through {111} plane filtering. (d) Details of the atomic structure with provided atomic identification on the five different domains. (e) Schematics of atomic structure without polar inversion at the base and simple twinning. In this situation, the structure does not fully enclose and a large high energetic inversion boundary creates. (f) Atomic models revealing the different polarities and spatial directions in the exposed facets during first stages of growth. (g) Schematics of the growth in a microscopic model.

Atomically resolved HAADF micrographs shown in Figure 3.17 reveal the atomic arrangement at the base of the nanostructure being comprised by five different domains united by symmetrical twins at both sides. The initial seed (turquoise) grows epitaxially from Si forming a truncated octahedron that exhibits two different {111}A facets where the growth can continue. However, the growth keeps on laterally in a non-symmetric manner after twinning is produced. While on the right side the polarity is preserved in all the domain, on the left a polarity inversion takes place given

the identified atomic arrangement thanks to the Z-contrast of HAADF. Such polar inversions are rarely observed in semiconductor structures due to their high energetic cost. The low Z-contrast between Ga and As (Z(Ga) =31, Z(As)=33) makes it difficult to confirm the exact position where the inversion is produced, but it can be ensured that it is not immediate at the twin boundary, which is unambiguously identified as an ortho-twin. In contrast, we deduce that the inversion is produced across the (220) planes, in which it supposes a lower energetic cost in comparison with (111) inversions [23, 27]. At this point, twinning in the other available $\{111\}$ direction is produced at both sides and the growth continues in the vertical direction arising from two $\{111\}$ growth fronts which present different polarity. Notice that without a polarity inversion at the first nucleation steps the two vertical fronts would present same vertical polarity, but there would be an inversion across their boundary (Figure 3.17e). This would suppress the vertical growth because of the high energy consumption of building such a long unstable boundary. It is highly probable that this situation took place in many of the available pillars, as the spontaneous polarity inversion is improbable. This would result in residual structures as the ones circled in Figure 3.16a, and explains the low yield of vertical nanospades growth, being 7 % in optimal conditions. However, it is probable that the inversion is produced when reaching the top of the octahedron, where the overall polar fields generated at both sides get more intense so the next atom pair would be located in a reverse way as a more stable position (Figure 3.17g). Notice that the breaking of symmetry in polarity of the two lateral growth fronts also affects the symmetry of the base faceting, and thus, the overall nanostructure is not purely symmetric across its growth axis.

The angle between two adjacent $\{111\}$ planes is 70.53 ^{o}, which creates a certain angular mismatch of 7.35 ^{o} when enclosing a pentatwin structure (which would close with angles of strict 72 ^{o}) (Figure 3.17e). GPA can be employed in order to evaluate how the angular mismatch is released. Figure 3.18b-h shows a structural analysis performed on the first nanometers of growth. The dilatation and rotation maps show the formation of four dislocations when merging both growth fronts to close the structure. This mechanism goes accompanied with a rotation of planes at both sides that permits a better matching of both crystals. It can be observed that such rotation gets released after 30 nm of vertical growth, at a position where no

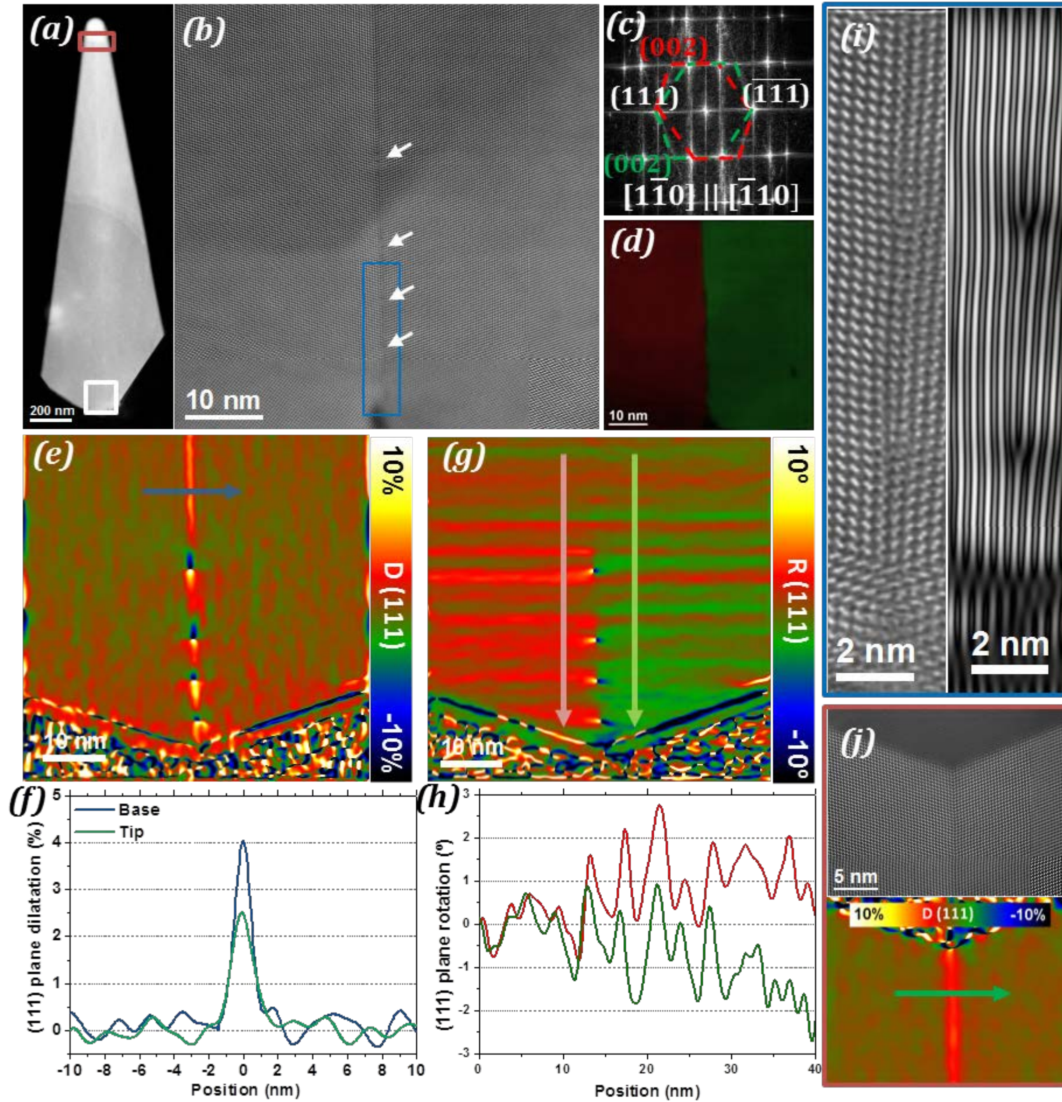

Figure 3.18: (a) Low magnification HAADF-STEM micrograph of a nanospade. (b) Details of the first nanometers of vertical growth with the corresponding domains indicated in the FFT (c) and color mapped after plane filtering in (d). (e) Dilatation and (g) rotation of (111) planes obtained through GPA. (f),(g) Profiles of dilatation and rotation maps along the indicated arrows, respectively. (i) Details on the formation of dislocations when both crystals match and (j) GPA dilatation map of {111} planes obtained at the tip of the nanowire.

more dislocations appear. The mismatch is therefore released by a combination of elastic and plastic deformations during the first 30 nm of vertical growth. After it, a uniform regime is reached that resembles an axial twinning such as the one observed in the previous section with <112> NWs. However, a 4 % dilatation is measured in the junction between both grains. This situation is kept without the presence of any other defects until the tip of the nanospade, where just a 2.5 % dilatation is reached. We assume that this minimization of the dilatation between both grains is reached by a continuous minimal plane rotation along the length of the nanostructure. In that regard, we expect the junction to evolve into a regular ortho-twin at the tip when

growing structures during longer times.

The structural configuration of vertical nanospades make them suitable candidates for lasing and photonic applications due to the two large defect-free crystals that form the main structure. Nevertheless, further studies are required in order to promote a higher yield during growth. Even with the precise control over the catalyst positioning and contact angle, the presence of two exposed B-polar facets in the initial nuclei still favors the creation of B-polar nanowires in front of vertical nanospades under the considered growth conditions. In those cases where A - polar growth starts, a spontaneous inversion of polarity is required in order to grow a stable structure. Otherwise, the energy requirement for creating a large vertical polar boundary prevents growth to continue, resulting in parasitic structures on the substrate as the one circled in Figure 3.16a.

3.5 Polarity effects on elemental segregation in alloys

The possibility of alloying different III-V compounds can be exploited for tuning semiconductor lattice constant and band gap. Particularly, semiconductor nanowires are suitable platforms for growing materials in order to avoid misfit dislocations due to their reduced diameter [106]. With this aim, self-catalyzed GaAs nanowires grown by VLS on Si(111) substrates are employed as templates for the growth of $Al_xGa_{2x}In_{1-3x}As$ quaternary alloys. An outer GaAs shell with 5 nm nominal thickness is employed for preventing oxidation of the inner shell (Figure 3.19b).

It has been highlighted previously that QDs can self-assemble in AlGaAs shells due to the different elemental segregation in the corners of nanowires. Due to the high crystal quality of these QDs, they act as single photon emitters [133, 153]. Moreover, additional segregation effects can occur along different directions of the NWs. For instance, aluminum has been reported to accumulate along the <112> directions [154, 155], presenting some polar dependence [155]. Thus, it is essential to comprehend the mechanisms driving elemental segregation and the local compositional variations because they will intrinsically produce local variations of electronic bands. Figure 3.19a shows a HAADF-STEM micrograph of a cross-section of a NW grown with the configuration described before with a cation fraction of 15 % In.

Figure 3.19: (a) HAADF - STEM micrograph of a cross-section of the nanowire. Polarity in the <112> directions is assigned according to the results obtained by Zheng *et al.* [155]. (b) Schematics of elemental distribution in different NW shells. (c) FFT with labels on the different planes. (d) Intensity profile along the closed circuit shown in (a).

The FFT displayed in Figure 3.19c allows to identify ZB structure and nanowire faceting planes belonging to {110} family in both core and shell. The dark contrast that elongates through the NW corners (<112> crystal direction) is a signal of a local enrichment of a light element, Al in this case. It is appreciated in the HAADF micrograph (and enhanced in the intensity profile) that the thickness of the corner stripes follows a three - fold symmetry that alternates thick (3 nm) and thin (1.7 nm) stripes across the nanowire. In addition, the intensity analysis reveals a lower Al content in A-polar directions. The three-fold symmetry reflects the polar nature of <112> directions originating from the non-centrosymmetric atomic structure of ZB GaAs. The polarity of the different <112> corners has been assigned according to the results on Al segregation obtained by Zheng *et al.* [155], where an additional study through <110> zone axis was performed for polarity identification.

A change to a brighter contrast surrounding the Al-rich (B-polar) corners can be slightly appreciated, reflecting a local increase in heavier atoms, Ga and/or In, with respect to the overall shell composition, as arsenic is assumed to be uniformly distributed to preserve elemental stoichiometry. STEM related spectroscopies (EELS and EDX) were employed for elemental mapping and quantification (Figure 3.20). The presence of Al-rich domains following the corners of the nanowires is evidenced together with a Ga and In depletion at the same positions. The thickness and areal density appreciated through compositional analyses agrees with the three-fold polarity-driven segregation previously discussed.

Indium areal density map (Figure 3.20c) shows In-rich features surrounding the

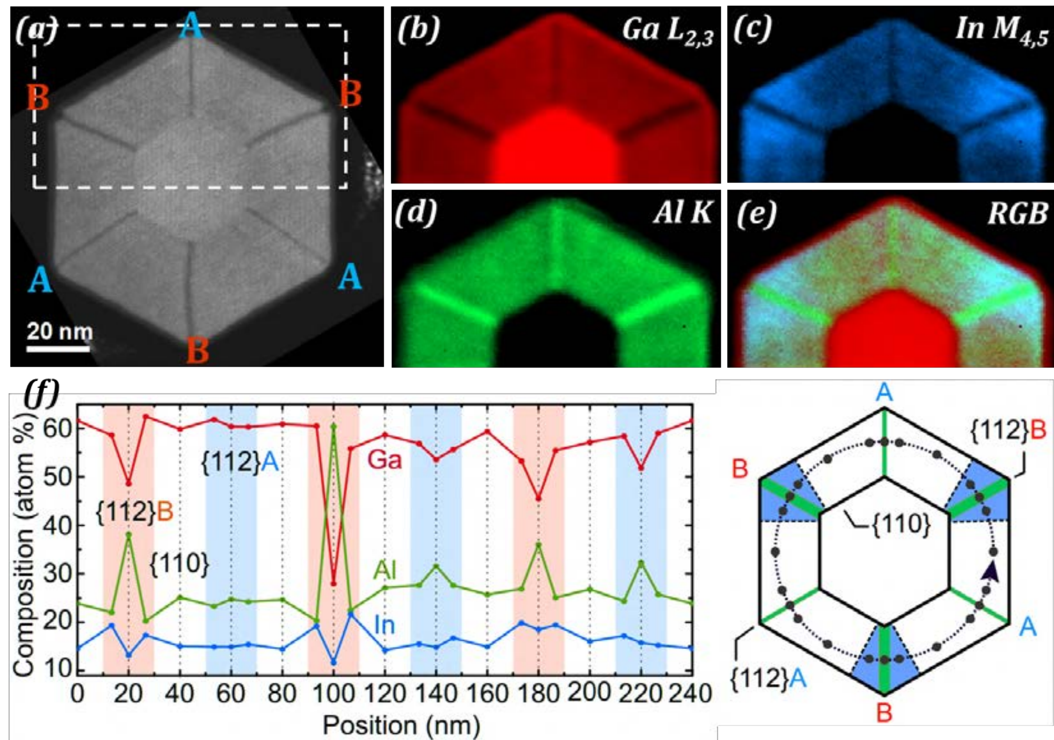

Figure 3.20: (a) HAADF - STEM micrograph with labels indicating the polar nature of the corners. (b)-(d) EELS elemental maps of group III elements and (e) RGB cationic compositional map. (f) Composition profile obtained through EDX quantification in relevant points of the closed circuit indicated in the NW schematics. [156]

Al-rich planes at the <112>B directions, explaining the brighter contrast observed in the HAADF micrographs. Interestingly, the thickness of In-rich regions increases radially, presenting a wedge-like shape at each side of the Al-rich B-polar corners. Contrary, Ga seems to be distributed more uniformly although a slight increase can be appreciated surrounding Al-rich A-polar corners, less pronounced than In and with uniform thickness (Figure 3.20b). All the features revealed in the areal density maps are in agreement with the elemental quantification performed through EDX (Figure 3.20f).

The local variations in alloy concentration have an impact on the lattice constant of the compounds driven by Vegard's law (Eq. 1.2). GPA was applied in order to evaluate possible lattice constant fluctuations across the areas with higher compositional contrast. The GaAs core was employed as reference to compare with the Al-rich corner lattice, where the maximum variations of lattice constant are expected (Figure 3.21b,c). The overall mismatch between GaAs and $Al_{0.285}Ga_{0.565}In_{0.15}As$ is 1.1 %. Taking into account the measured concentrations around the <112>B ridge, Al-rich segments and In-rich wedges surrounding them present a 0.76 % and 1.4%

mismatch with GaAs, respectively. These values are among the limits of accuracy of GPA and no significant features are found when calculating the strain matrix components ε_{xx} and ε_{yy}. Some statistical decrease in ε_{yy} can be observed along the <112> direction, where mismatch with GaAs is minimal, but the average measurement gets a lower value than the standard deviation, meaning the lack of accuracy for these measurements. Nevertheless, these measurements highlight the absence of any misfit dislocation across the structure, where just minimal elastic deformations take place.

A simulation based on elastic energy minimization with the real shell dimensions can give details on how epitaxial strain relaxes radially across the shell. The simulation has been performed with nextnano^3 software considering a uniform shell with composition $Al_{0.285}Ga_{0.565}In_{0.15}As$ and keeping the real system dimensions. Figure 3.21d shows the calculated ε_{hydro}, that is defined as the sum of the diagonal elements of the strain tensor ε_{ij}:

$$\varepsilon_{hydro} = \sum_{i=j} \varepsilon_{ij} \tag{3.1}$$

and reflects the volume variations caused by strain. It is remarkable that, as expected, compressive strain is acting on the shell, mostly accumulated close to the facets separating both phases. However, there is a remarkable anisotropy regarding <110> and <112> directions, and thus presenting a 6-fold symmetry: while a relevant compression is taking place in the middle of the facets, the structure relaxes much better along the corners. Interestingly, these regions presenting smaller strain expand from the corners of the core reproducing the wedge shape of In-accumulation.

The combination of compositional and strain analyses allows to define a model explaining the preferential distribution of cations within the shell (Figure 3.21e). The most prominent feature is the accumulation of Al at the vertices of the hexagonal cross section. Previously reported studies suggest that the radial growth rate of $\{112\}$B facets in AlGaAs is slightly faster than for $\{112\}$ A. The growth rate affects many parameters, such as surface reconstruction or sticking coefficient of adatoms, explaining then the three - fold symmetry of Al concentration in this system.

The wedge shape of In accumulation surrounding Al-rich areas can be explained

in terms of strain. The calculated strain for an homogeneous shell shown in Figure 3.21d indicates a compressive strain at the middle of the {110} facets that gets accommodated in the corners of the hexagon, reproducing the same wedge shape as In accumulation areas. According to Vegard's law (Eq. 1.2), the lattice constant of a compound $Al_xGa_yIn_{1-x-y}As$ is larger as x and y decrease (i.e. the content of In increases). From this consideration, In is expected to be more favorably incorporated in the quasi-relaxed areas around the corners. Indium atoms present high mobilities that allow diffusion to occur allocating them in positions where relaxation occurs more efficiently, reducing this way the overall elastic energy of the shell. In addition, the low miscibility of In within Al-based alloys explains the poor incorporation of In into the Al-rich <112> stripes: there is a clear competition between In and Al to stick on {112} B which clearly favors Al. This mechanism might generate a net flux of indium atoms towards the surroundings of the B - polar nanofacets.

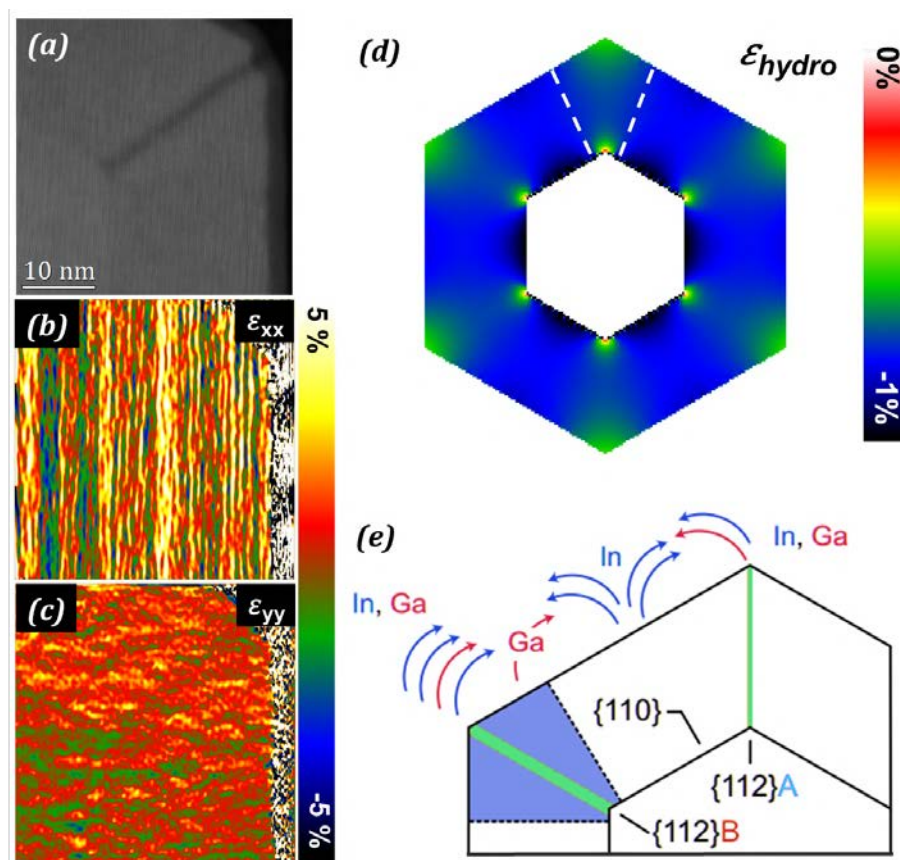

Figure 3.21: (a) HAADF-STEM micrograph of an Al-rich corner. (b),(c) Diagonal components of strain matrix tensor obtained through GPA. (d) AlGaInAs hydrostatic strain simulation of a core-shell nanowire. (e) Sketch of Ga and In diffusion on the NW sidewalls.

3.6 Conclusions

Polarity arising from the different electronegativities in the atomic species of III-V compounds has a strong impact in crystal growth. The lack of inversion symmetry makes polar surfaces behave different when presenting III or V termination. This fact gives preferential growth for certain polar directions, mainly B polarity in the case of GaAs. However, an appropriate control and optimization of the growth conditions can favor the switching of polarity and coexistence of both polar-terminated nanowires. This fact presents a special relevance as it has been demonstrated that structural quality of nanowires is strongly determined by polarity because twinning is shown to be more favorable in {111}B planes.

A study of the interface between the liquid catalyst and the solid nanowire in both polar cases provides insights on the stacking probabilities during growth. A study through EELS of the bulk plasmon resonance of the liquid Ga droplet at the vicinity of the solid nanowire highlights that the interface between solid and liquid presents independent electronic properties, probably arising from the presence of ordering in the liquid Ga. The different nature of the ordering for A and B polar nanowires provides information about probabilities of next atomic species deposition, concluding that the nature of the liquid ordering establishes the probability of twinning perpendicular to the growth direction, which explains the quasi defect-free structure of A - polar nanowires.

However, this behavior is not preserved during the nucleation and the growth of the first NW nanometers, where multiple twinning can appear regardless of polarity until a steady growth regime is reached. Among all the possible casuistics, the simultaneous growth of several {111} planes can take place, driving an overall growth along <112> directions. This fact has been commonly observed in group IV semiconductors by achieving large defect-free crystals connected by axial twinning, but its very rare in binary compounds as it requires bipolar simultaneous growth.

A control over growth conditions can promote the growth of these structures and even push their vertical growth on Si(001) substrates. The achievement of vertical large defect-free crystals is essential for integration in CMOS technologies. We inquire on the need of a spontaneous polar inversion during the multiple twinning at

nucleation as a requirement for stable growth, avoiding large polar boundaries that would preclude further growth. This restriction resides on the need of five - fold twinning to achieve the vertical growth direction, needing a polar reversal to close the structure. The detailed atomic model on structural growth of nanospades opens a field of study in order to promote the polar reversion for enhancing the low yields achieved at the moment.

In addition, the effects of polarity in elemental segregation in core-shell nanowires of quaternary AlGaInAs alloys have been studied. Elemental segregation of Al and In in <112> directions follows a three-fold symmetry, indicating that the polarity of these planes plays a critical role. Moreover, the spatial distribution of In around <112>B corners takes a geometry that minimizes the inhomogeneities of strain. These polar and strain dependent elemental segregation mechanisms produce local changes in the electronic band structure, and thus, it is essential to understand the origin in order to exploit at maximum the outstanding properties of these self-segregated embedded quantum wires.

Chapter 4

Guided VLS growth of core-shell horizontal nanowire arrays

Recent studies on NW growth are devoted to the assembly of horizontally aligned arrays. Even though high quality VLS grown nanowires have been achieved thanks to the effort in understanding the growth mechanisms for further optimization of the techniques, their integration into large scale functional circuit platforms and devices remains as a major challenge. In particular, the employment of core-shell nanowires offers an enlargement of effective junction surfaces, but contacting core and shell in free-standing NWs for exploiting these benefits often requires post processing treatments that involve single nanowire manipulation, and thus, they suppose low scalability. This chapter is devoted to the study of guided grown horizontal core-shell nanowires based on II-VI compounds (particularly ZnSe and ZnTe, presenting both band gaps in the visible range) as an advance in VLS growth towards device fabrication. The NW-substrate interface gets a higher relevance in this situation by affecting crystal structure, morphology and strain release mechanisms. In that regard, we perform a study on the impact of α*-*Al_2O_3 *substrate orientation and/or preparation on the morphology of the NWs, and the consequent influence on the electronic band alignment of the final ZnSe@ZnTe core-shell nanowire arrays by exploring the mechanisms driving strain relaxation and its implication on NW optoelectronic properties.*

4.1 Introduction

The integration of VLS free-standing nanowires into large-scale optoelectronic devices remains being a challenge due to assembly issues or requirement of single-nanowire manipulation [157]. This fact makes integration expensive, time consuming and barely reproducible, not making it useful for parallel device production. Guided growth (GG) strategies have been presented in the last years in order to

produce horizontal arrays of nanowires [158–163]. GG approach exploits the epitaxial or graphoepitaxial relationships of the material with the substrate in order to guide the VLS growth of nanowires through specific substrate directions, creating then self-assembled arrays of perfectly aligned nanowires. During the last decade, VLS guided growth was reported for a limited number of II-VI materials and substrates, such as ZnO [160, 164], CdSe [161] , ZnTe [162] or ZnSe [163]. In this growth approach, the material interactions with the substrate become more relevant, which limits the generalization of the strategy. The high interface area between the substrate and nanowire has an important role into defining the thermodynamic equilibrium and can thus affect the NW faceting.

The study of the ZnSe and ZnTe junction is of special interest as both materials are direct band gap semiconductors with electronic gap values of 2.82 eV and 2.39 eV, respectively, relying both of them in the visible range [165, 166]. The intrinsic impurities present in these materials make ZnSe and ZnTe be n-type and p-type respectively [162, 163] with a type II band alignment when matched together [56, 167, 168]. Then, growing them in core-shell configuration allows to exploit a higher junction surface, maximizing their efficiency in photosensing applications by the presence of radial heterojunctions.

TABLE 4.1: Plane spacing of some of the main planes of ZnSe, ZnTe and α - A_2O_3.

Material	Lattice constant (Å)	hk(i)l	d_{hkl} (Å)
ZnSe(ZB)	5.67	111	3.27
		$1\bar{2}1$	2.32
		$\bar{2}02$	2.01
ZnTe(ZB)	6.09	111	3.52
		$1\bar{2}1$	2.49
		$\bar{2}02$	2.15
α - A_2O_3	a = 4.76 c=12.99	$11\bar{2}0$	2.38
		$1\bar{1}00$	4.12
		0006	2.17
		$1\bar{1}02$	3.48

ZnSe nanowires have been successfully grown horizontally in sapphire substrates prior to this study [162]. For this reason, these horizontally grown NWs might work as suitable templates for the further growth of ZnTe shells on top of them. However, while ZnSe and ZnTe typically crystallize in cubic ZB or hexagonal WZ structures,

α-Al_2O_3 presents a trigonal symmetry belonging to the space group R$\bar{3}$c. Table 4.1 shows the lattice spacing of some of the main crystal planes of these three materials. The difference in crystal symmetry between substrate and nanowire materials opens lots of possibilities for plane interactions depending on substrate orientation.

4.1.1 Substrate engineering for guided growth

Sapphire (α-Al_2O_3) substrates, which crystallize in a trigonal symmetry system (space group R$\bar{3}$c), are employed for guiding the growth of nanowires. The creation of nanosteps on the substrate can be employed to guide the growth along the direction of these nanofacets [169]. Particularly, flat sapphire M-$\{10\bar{1}0\}$ surfaces are thermodynamically unstable and annealing at high temperatures causes surface reconstruction creating nanofacets on the more stable S-$\{10\bar{1}1\}$ and R-$\{1\bar{1}02\}$ planes in a highly periodic symmetry [170], allowing then the growth along the two $\pm$ $[1\bar{2}10]$ directions where the nanogrooves propagate (Figure 4.1). In this growth strategy, referred from now on as graphoepitaxy, the nanowires interact with two different sapphire surfaces and the growth is dominated by the nanoscaled shape of the stepping rather than the epitaxial relationship with the materials grown on top [158, 171].

Contrary, epitaxial relationships can be also exploited to guide the growth in atomically flat substrates (named from now on as epitaxial guided growth). With this aim sapphire substrates were cut in two of the main α-Al_2O_3 orientations: C-plane($\{0001\}$) and A-plane($\{11\bar{2}0\}$). The guided growth on C-plane (0001) is produced along six M $\pm\langle 1\bar{1}00 \rangle$ directions, which reflect the three fold symmetry of the plane and forming 60 º between each growth direction. On A-plane $(11\bar{2}0)$ the growth is produced along two M $\pm[1\bar{1}00]$ directions and four S directions $\pm[1\bar{1}01]$ and $\pm[1\bar{1}0\bar{1}]$. The M and S directions are separated by 61.5 º, and adjacent S directions are separated by 57 º (Figure 4.1).

4.1.2 VLS guided growth of ZnSe@ZnTe horizontal NW arrays

The guided growth of core-shell nanowires is carried out in a multistep process. First, Au catalytic nanoparticles are patterned on the differently treated/oriented substrates by standard photolithography. Then, a ZnSe powder source is vaporized

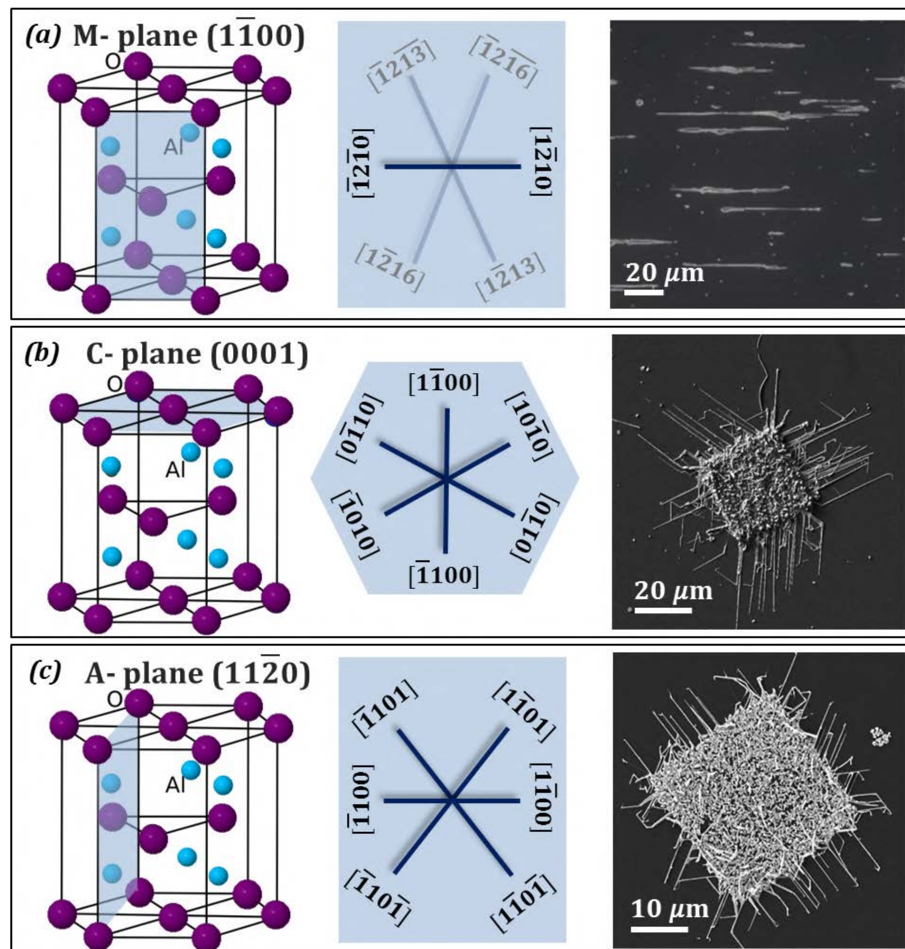

Figure 4.1: Indication of sapphire planes, available growth directions and SEM micrographs of nanowires grown on (a) M-plane after annealing-induced nanogrooving, (b) C-plane and (c) A-plane.

at high temperature and VLS guided growth of ZnSe nanowires is produced at 720-770 ^{o}C. After the cores are grown the source is switched to ZnTe and temperature is decreased to 680 ^{o}C. Under these conditions, ZnTe deposits on top of the ZnSe nanowire templates through a VS approach. This procedure takes place by covering the cores at specific positions by forming ZnTe nanoislands that expand until merging together until the cores are fully covered [56]. The crystal quality of the ZnSe NW cores is key for the proper epitaxial growth of ZnTe shells.

One of the advantages of this growth procedure is the availability of contacting multiple cores and shells without any further nanowire manipulation, something more difficultly accessible in conventional VLS growth methods. This allows to produce multiple devices in parallel by standard lithography and exploiting the large surface area of the multiple radial junctions. Figure 4.2 schematizes the methodology that can be employed for contacting the junction. Once the core nanowires are

grown (a) a part of them can be protected by using a mask (b). The process of ZnTe shell growth can take place then in the non - protected area (c). After the shell is grown, the mask can be removed (d) and the system will present exposed core and shell surfaces where metal contacts can be deposited (e).

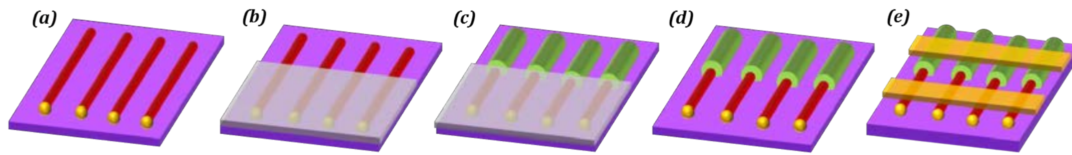

Figure 4.2: Schematics of the process of multiple core-shell contacting. (a) ZnSe cores are grown following specific substrate directions. (b) A protective mask is deposited. (c) ZnTe shell grows before (d) the protective mask is removed. (e) This procedure leaves some part of the cores exposed and allows to contact cores and shells of multiple nanowires in parallel.

It is interesting to remark the importance of the substrate in guided growth. The firstly grown cores present a high area of interaction with the substrate and any crystal deformation arising from this interaction will affect the crystal quality of the shell. The employment of different surfaces as a substrate for the guided growth is then expected to have an overall impact on the structure, and thus, the optoelectronic behavior of nanowires.

4.2 Crystal structure of core-shell NWs

Aberration Corrected High Angular Annular Dark Field (HAADF)-STEM in FIB prepared transversal cross-sections is employed for determination of the crystalline structure and evaluation of the crystal quality of the ZnSe@ ZnTe nanowires grown in nanofaceted M-sapphire surfaces and atomically flat A and C - planes of sapphire.

4.2.1 Graphoepitaxial growth

We start by evaluating the growth of nanowires in the substrates cut along M plane presenting nanogrooves. From the SEM micrograph presented in Figure 4.1a and the atomic resolution images of the substrate of Figure 4.3 it is clearly observed that the guided growth is achieved following the $\pm[1\bar{2}10]$ directions in which the steps elongate through the substrate. However, there is a lack of uniformity regarding

morphology of nanowires and even ZnX (X=Se/Te) crystal growth direction. Actually, the NW morphology appears to be driven by {220} and {111} ZnX faceting planes with respect to the substrate surface. The FFTs shown in the bottom row of Figure 4.3 highlight the position of {220} planes that drive the lateral facets of the nanowires. Then, the top faceting of the nanowire is given by the amount of {111} planes available according to the crystal growth direction. In that regard we observe a flat top when NWs grow following <11$\bar{2}$> direction given by the single available top {111} plane and a triangular top morphology when NWs follow <1$\bar{1}$0> direction given the two available {111} top planes. Additional minor higher order facets appear in some cases, specially in ZnSe cores.

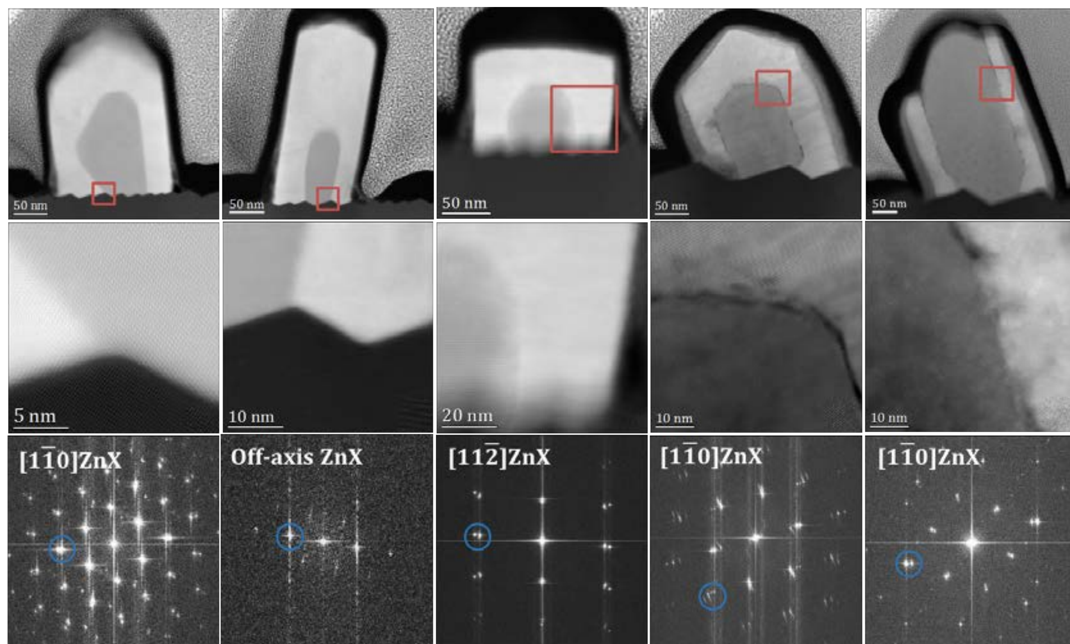

Figure 4.3: General overview, details on the red squared areas and FFT of the ZnX (X=Se/Te) area labelling the crystal zone axis. The blue circles of the FFT are indicating $\{220\}_{ZB}$ planes.

Even though growth in <110> direction is the predominant one, there is not a clear epitaxy between substrate and NW. This fact arises from the difficulties of ZnX {220} planes to adapt simultaneously to two non-equivalent substrate facets due to the differences in crystal phase symmetries. This fact highlights that graphoepitaxial growth is dominant over epitaxial growth and overrules the epitaxial relationships between the sapphire and the nanowire. The lack of uniformity in NW morphology directly driven by the inhomogeneous core templates can even lead into a not fully covered shell on the nanowires. For that reason we study the growth of epitaxial GG NWs, where the epitaxial relationships with the substrate are expected to provide crystal homogeneity in the grown NWs.

4.2.2 Epitaxial growth

Contrary to the case of graphoepitaxial guided growth, atomically flat A and C surfaces of α-Al_2O_3 provide a preferential crystal orientation to the nanowire ruled by the epitaxial relationship between both materials. In both cases, the investigated transversal cross sections reveal that the nanowires are grown following [1$\bar{2}$1]ZnX (X=Se/Te) directions with (111) planes parallel to the substrate and with {$\bar{2}$02} planes perpendicular to the substrate (Figure 4.4c,d). This makes the lateral ZnTe {$\bar{2}$02} facets be strictly perpendicular to the substrate, bringing the arrays a more uniform geometry than in the case of graphoepitaxy. In addition, the EELS based anionic compositional map (Figure 4.4b) reveals no elemental diffusion from core to shell, achieved from the lower temperature of shell growth, which is essential for achieving sharp p-n radial junctions.

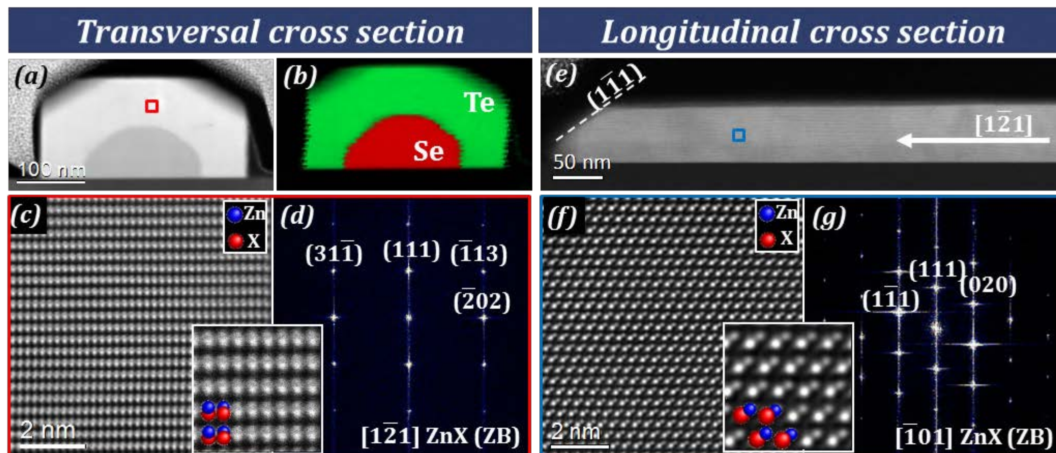

Figure 4.4: Crystal orientation and quality in a nanowire grown in C-Sapphire. (a) HAADF overview of a nanowire cross-section. (b) Te (green) and Se (red) elemental mapping obtained in the same area through STEM-EELS. No diffusion of anionic species is observed. (c) Atomically resolved micrograph and (d) its corresponding power spectrum indicating that the nanowire growth direction is [1$\bar{2}$1]. (e) HAADF overview of a longitudinal cross section. (f) Atomically resolved micrograph with (d) its corresponding FFT highlights the lack of planar defects.

The [1$\bar{2}$1] projection of the ZB structure is insensitive to stacking defects or twinning, as well as discrimination between other possible polytypes. For that reason, a perpendicular cross-section along the length of the nanowire is analyzed along the [$\bar{1}$01] zone axis (Figure 4.4e-g). A defect-free zinc blende structure is unambiguously observed along all the length of the nanowire. The nanowire grows along the [1$\bar{2}$1] direction while the growth front takes place in (1$\bar{1}$1)B planes, as commonly observed for ZnSe and ZnTe compounds [10, 11]. Interestingly, the top (111) facet of

the nanowire is instead Zn - polar, which is assumed to have lower probability to twin [22, 134]. This fact would preclude large horizontal stacking fault formation. In the case of the growth front planes, substrate constricts twinning events or stacking faults, resulting in large defect-free crystals.

The substrate planes interacting with the nanowire in each casuistics should be taken into account for understanding the high crystal quality and uniformity of nanowires. Table 4.2 summarizes the epitaxial relationships between ZnSe and substrates for all the possible nanowire growth directions. As observed, the intrinsic mismatches between ZnSe vertical planes and the corresponding ones of sapphire are relatively high for all the possible interactions. However, when accounting for the creation of crystal domains with n:m plane ratios with Eq. 1.5, the remaining mismatch gets values below 1.3 % in all the studied cases. In this regard, ZnSe nanowires grown along <1$\bar{1}$00> or <1$\bar{1}$01> in both C and A substrates are expected to be relaxed after first few nm of growth, keeping their pristine structure.

TABLE 4.2: Epitaxial relationships and associated mismatches for planes perpendicular to the growth direction.

Substrate orientation	$[hkil]_{\alpha-Al_2O_3}$ || $[hkl]_{ZnSe}$	m : n	Mismatch (%)
C - Sapphire	[11$\bar{2}$0] \|\| [$\bar{2}$20]	1 : 1 5 : 6	15.6 1.3
A - Sapphire	[0006] || [$\bar{2}$02]	1 : 1 12 : 13	7.4 0.3
	[1$\bar{1}$02] \|\| [$\bar{2}$02]	1:1 4 : 7	42.4 1.1

Nevertheless, even presenting relaxed cores as templates for shell growth, the high mismatch of a 7.4 % between ZnSe and ZnTe is capable of generating strain fields that modify the shell band alignment. This fact might modulate the junction effectiveness, so it is worth to evaluate the strain releasing mechanism taking place in the heterostructures.

4.3 Morphology effects in strain minimization

Several nanowires grown on A-sapphire and C-sapphire substrates are considered for determining the strain fields affecting the shell of the heterostructure. Figure 4.5 shows HAADF micrographs obtained in two cross sections at each substrate orientation. Even though crystal orientation is identical for both situations, at a first glance we can observe different core morphologies for each orientation. A-sapphire NWs core morphologies are truncated cylinders in the most extreme cases ranging to truncated elliptic cylinders with different curvatures. The angle between core nanowire faceting and substrate surface is always higher than 90 ^{o}. In the meanwhile, C-sapphire NWs have core morphologies ranging from planar belts to faceted prisms, in all cases with an angle of strict 90 ^{o} between the nanowire lateral facets and the substrate surface.

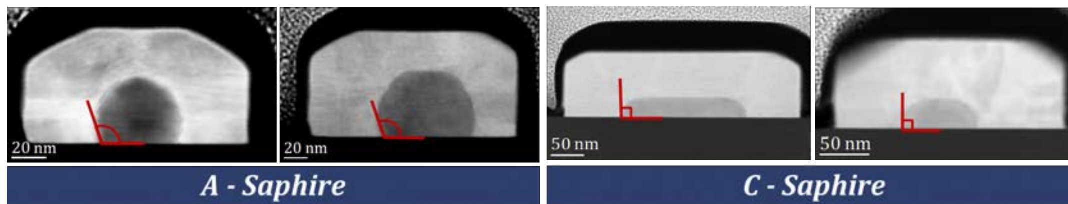

Figure 4.5: Low magnification HAADF micrographs obtained in cross-sections of nanowires grown following $[1\bar{1}00]$ α - Al_2O_3 direction on A surface (left) and C surface (right).

The different morphologies are attributed to a different wetting of the Au catalyst when interacting with different sapphire surfaces before the growth starts. The different interface and surface energies of A - sapphire and C - sapphire give rise to different contact angles of the Au droplets within the substrate, driving the different observed core morphologies.

Geometric Phase Analysis is applied in order to evaluate how the core morphology affects to the matching between ZnSe and ZnTe lattices. For this reason, the study is focused in evaluating the two most extreme cases: a perfect cylindrical core of 20 nm radius grown on A - sapphire substrate and a flat belt core of 30 nm height and 190 nm width grown on C- sapphire substrate. Figure 4.6 shows the main results of performing these analyses on atomically resolved low magnification HAADF-STEM micrographs.

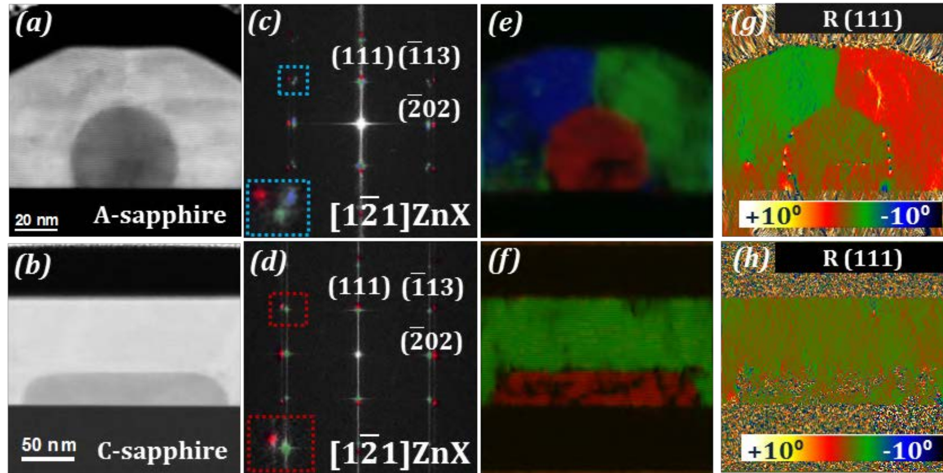

Figure 4.6: On A–sapphire (top) and C-sapphire (bottom): (a),(b) Low magnification HAADF-STEM micrographs of NW cross-sections. (c),(d) Their corresponding power spectra with insets highlighting spot splitting. (e),(f) Color structural map obtained through FFT filtering as color coded in the power spectra. (g),(h) Maps of rotation of (111) planes obtained through GPA.

The disparities between A and C nanowires are already arising by a simple inspection on the power spectra of both micrographs (Figure 4.6c,d). A split of every crystalline plane in two is expected, arising from an epitaxial core-shell structure presenting the same crystal orientation but different lattice constants. This is the situation observed in Figure 4.6d, where inner spots correspond to ZnTe shell planes and outer spots to ZnSe core planes. However, the FFT of the cylindrical core NW (Figure 4.6c) shows a splitting in three spots. Despite the outer spots matching with the expected structure of ZnSe, there are two independent lattices of [1$\bar{2}$1] oriented ZnTe which present a rotation of $\pm$ 2 ^{o} along [1$\bar{2}$1] direction with respect to the ZnSe lattice, which is clearly highlighted in the zooming of (31$\bar{1}$) spots displayed in the inset. When filtering independently these spots and creating a color structural map (Figure 4.6e) it is clearly discernible they arise from regions at both sides of the nanowire intersectioning in the middle. C- nanowire presents, instead, a uniform structure through all the shell (Figure 4.6f).

The existence of these two rotated lattices in the shell of the A - NW (or absence in C - NW) is reflected in (111) plane rotation maps obtained through GPA (Figure 4.6g,h). A $\pm$ 2 ^{o} plane bending is measured for ZnTe at each side of the nanowire with respect to the ZnSe lattice. Contrary, ZnTe lattice is perfectly aligned with ZnSe along all the nanowire when the core of it presents a belt-like morphology.

Same GPA rotation based analyses are carried out in the nanowires presenting cores with intermediate morphologies for both A and C substrates presented in Figure 4.5. Interestingly, a continuous bending across the middle of the nanowire from - 0.5 º to 1.5 º is measured in the A - sapphire NW with flatter top. In this case, however, there is no sharp junction in the middle as in the case of the cylindrical core NW. No bending across both sides is detected in the intermediate C-NW. These results are summarized in Figure 4.7, where it is clearly observed that for nanowires where the contact angle between core and substrate is strictly 90º (C-sapphire) no rotation with respect to the core lattice is measured meanwhile a geometry dependent bending can create a junction that gets up to 4 º difference at both sides of the wire.

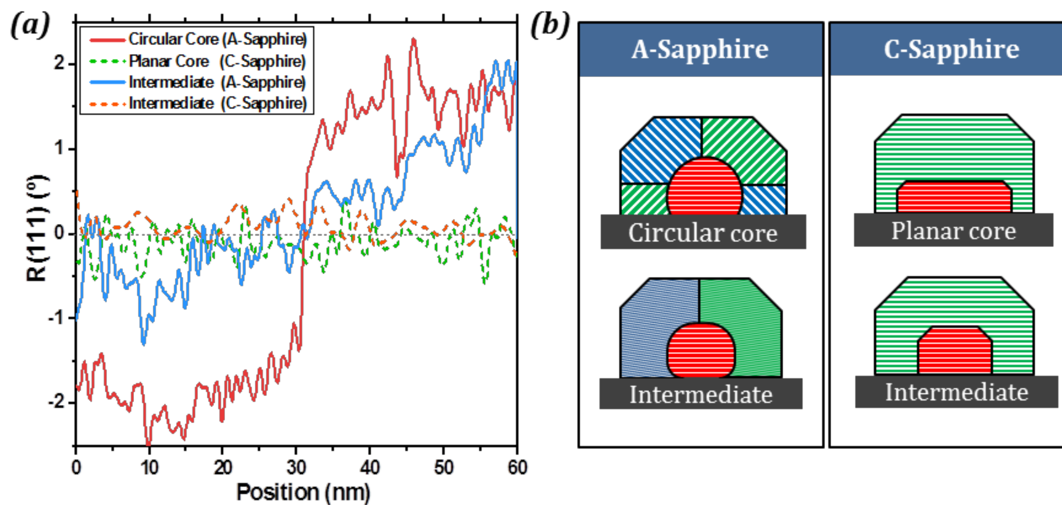

Figure 4.7: (a) Profiles of the measured rotation of ZnTe planes across the nanowire. (b) Schematics of morphology dependent plane bending in cross-sections of A and C nanowires.

Regarding other crystal deformations, strain tensor component mapping has been obtained through GPA. Figure 4.8 reveals a uniform difference in lattice constant of ZnTe with respect to ZnSe through all the nanowire in both substrates, including the junction created by the plane bending effect.

In the case of the cylindrical core nanowire grown on A - sapphire, a main dilatation of 8.8 % is measured in the vertical direction while a 5.9 % is measured for the horizontal direction. The overall dilatation is then found to be of + 7.4 %, which equals the associated mismatch to the structure. This means that the resulting total ZnTe unit cell volume variation (ε_{hydro} = ε_{xx}+ε_{yy}) is negligible. This implies that the ZnTe relaxes with the creation of misfit dislocations (Figure 4.6g) and the residual

strain relaxes within the first 3.5 nm above the interface. However, from the discrepancies in ε_{xx} and ε_{yy} we observe this relaxation does not take place in an isotropical way: ($\bar{2}$02) planes suffer a slight compression (<1.5 %) that gets compensated by a dilatation of the (111) planes.

This anisotropical distortion is also observed in flat C-sapphire nanowires, although it gets more subtle (< 0.3 %). In this case, the total unit cell volume variation ε_{hydro} is also negligible, meaning strain is released by the creation of dislocations. However, the remaining strain relaxes elastically by compressing the first 7 nm near the interface. Shear strain matrix components ε_{xy} are negligible in both cases.

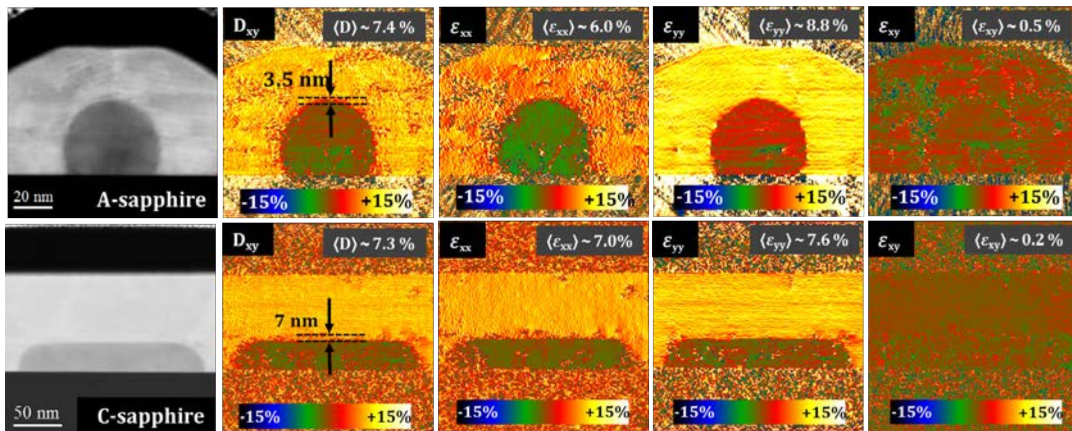

Figure 4.8: Overall dilatation and strain matrix components for A (top) and C (bottom) nanowires.

The differences in shell accommodation to the core templates are, thus, evident: even though both structures are virtually relaxed in terms of unit cell volume from the first nanometers of shell growth, tetragonal distortions appear in cylindrical core NWs grown on A - sapphire. Additionally, the formation of a structural junction arising from $\pm$ 2 ^{o} bending at both sides appears at the center of the nanowire spontaneously when shell adapts to this core morphology.

4.3.1 The origin of plane bending

The appearance of bending when stacking structures decreases the effective mismatch of materials for specific situations. When considering a bending of an angle

β between core and shell, as schematized in Figure 4.9, the effective interplanar distance is defined as

$$d_{shell}^{eff} = \frac{d_{shell}}{cos\beta} \tag{4.1}$$

then, the effective mismatch between materials turns to be

$$\varepsilon^{eff} = \frac{\frac{d_{shell}}{cos\beta} - d_{core}}{d_{core}} \tag{4.2}$$

It turns out from Eq. 4.2 that $\varepsilon^{eff} < \varepsilon$ if $d_{core} > d_{shell}$, which is the opposite situation to this combination of materials. The effective mismatch between ZnSe and ZnTe actually increases with plane bending. Therefore, understanding the mechanism in which bending appears requires a different approach.

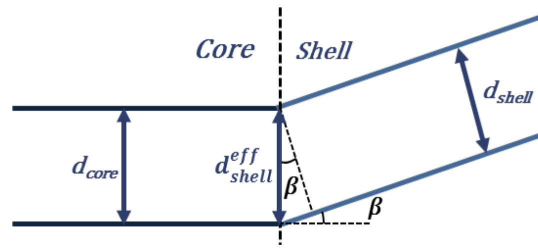

Figure 4.9: Schematics of effective interplanar distance after plane bending.

Atomic models reproducing an A-Sapphire grown nanowire with a cylindrical core were created using *Rhodius* software [109]. Due to symmetries in the structure the top-right quarter of the nanowire was modelled and the results can be extended to the other three quarters. The atomic models include a case where shell planes present no plane bending and a case where 2º bending was introduced in the shell structure. The real measured dimensions of 20 nm core radius were considered. Afterwards, the HAADF-STEM micrographs were simulated using the multislice method based on Kirkland routines [112–114]. This methodology allows to perform GPA in the simulated micrographs and compare with the observed situation of an anomalous 2 º bending with the non-rotated one, which appears virtually as a more favorable situation in terms of elastic energy minimization.

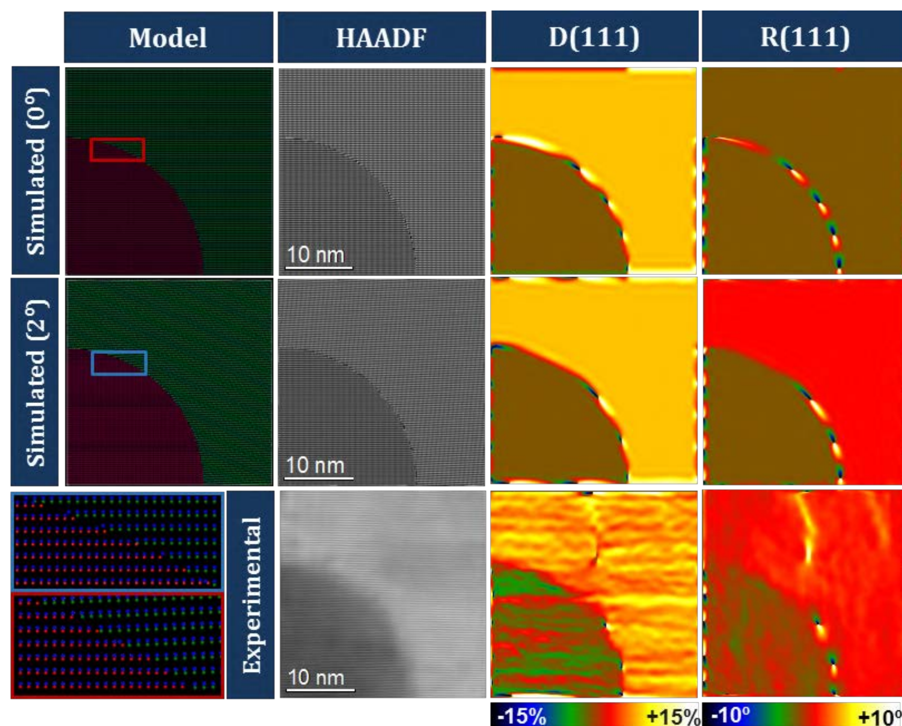

Figure 4.10: HAADF-STEM micrographs, atomic models and dilatation and rotation maps obtained through GPA on a quarter of the nanowire obtained experimentally (bottom), modelling and simulating a 0 º bent shell structure (top) and modelling and simulating a 2 º bent shell structure (middle). A zooming of the interfaces in the atomic models is presented in the bottom-left corner.

Figure 4.10 shows the results of the application of GPA to the simulated structures with 0 º and 2 º plane bending in the ZnTe shell lattice. The simulated dilatation and rotation maps of a 2 º rotated relaxed ZnTe shell reproduce the experimental situation in a quite accurate way and misfit dislocations appear precisely at the same positions as in the experimental measurement. However, an increase in the number of dislocations appearing at the interface, together with a worse plane matching at the top of the nanowire (inset) is observed when no plane rotation is introduced in the model. This behavior arises from the nanometric size of the cores. The small size of the nanowire core makes its surface be atomically stepped, so a better adaptation is reached when changing the effective interplanar distance of ZnTe by a rotation of the basal planes. This fact gets reflected in a decrease in the number of dislocations together with a better matching of the planes with their respective tangent surfaces.

From this morphological origin of plane bending, it turns out that the degree of bending could be relatively predicted in terms of core size by evaluating the matching between core and shell in different situations.

4.3.2 Dependence of plane bending with core radius

i. Nanowire with 20 nm core radius

Following the study suggested in the previous section, different shell rotations (from 0 º to 5 º with steps of 1 º) have been also evaluated for a nanowire with the experimentally observed measurements. Both horizontal (111) planes and vertical ($\bar{2}$02) planes rotation maps are calculated in order to get a detailed study on dislocation formation and plane matching.

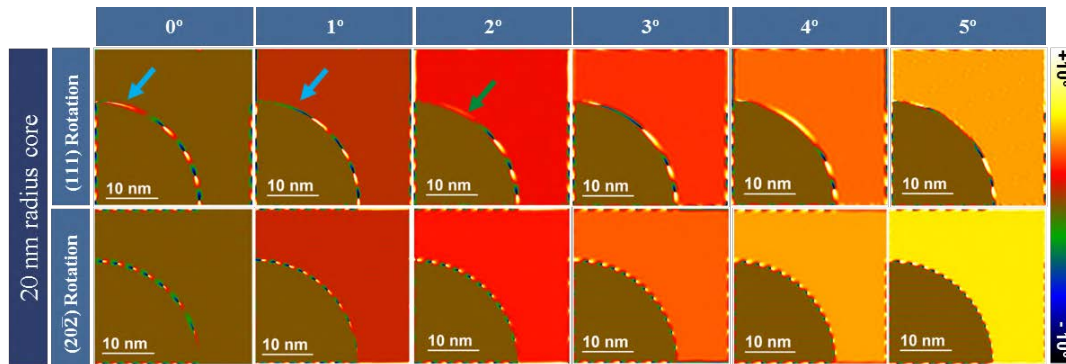

Figure 4.11: Simulated GPA rotation maps of (111) and ($\bar{2}$02) planes for a nanowire with 20 nm core radius.

Rotation maps of Figure 4.11 visually reveal a minimization of elastic energy at the interface for a situation in which the shell crystal is rotated 2 º, as measured experimentally. We can take into account the number of dislocations created by lattice mismatch as a way to quantify lattice accommodation, as an excess of elastic energy leads to dislocation formation (Table 4.3). However, we can observe two different tendencies: for horizontal (111) planes, increasing rotation leads to a decrease in the number of misfit dislocations meanwhile an opposite behavior occurs in the case of vertical planes. Observing the total number of dislocations, we can visualize how for angles higher than 3 º the total number of dislocations (i.e. the effective mismatch) increases substantially. However, this tendency is not that clear for the cases from 0 º to 2 º. Those situations just present one dislocation discrepancy, so other considerations are taken into account.

Observing the planes tangent to the cylinder ((111) in the top part and (20-2) in the right edge), the quality of their matching can be evaluated. While we observe a smooth transition between core and shell in the case of 2 º rotation (highlighted with a green arrow), a lack of adaptation is observed for 0 º and 1 º. This is specially

visible in (111) rotation maps (highlighted with blue arrows). The stepped interface observed in these cases implies an accumulation of elastic energy, but spatial confinement avoids the formation of an extra dislocation. In agreement with our measurements, 2 º bending provide a better plane matching by minimizing the total elastic energy accumulation at the interface.

TABLE 4.3: Number of dislocations in horizontal and vertical planes for angles ranging from 0 º to 5 º in a 20 nm radius nanowire.

Rotation angle	# (111) dislocations	# ($\bar{2}$02) dislocations	Total # dislocations
0 º	4	7	11
1 º	4	8	12
2 º	**3**	**9**	**12**
3 º	4	11	15
4 º	2	13	15
5 º	2	15	17

ii. Nanowire with 10 nm core radius

The same analysis based on atomic modelling and HAADF simulations has been applied to a nanowire with smaller radius (10 nm). Based on the behavior of plane adapting to atomic steps arising from nanowire curvature, we predict higher bending would bring a better matching for smaller radii, as the stepping is more pronounced.

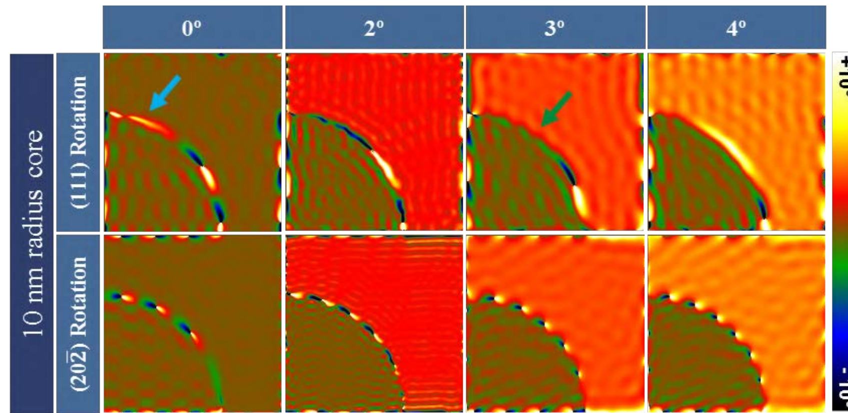

Figure 4.12: Simulated rotation maps of (111) and ($\bar{2}$02) planes for a nanowire with 10 nm core radius.

When analysing the situation presenting a smaller core diameter (i. e. higher curvature) the induced rotation of 2 º does not bring to the most stable situation, but it does shift to higher angles. By taking into account the number of dislocations, as listed in Table 4.4, a minimum is reached in the cases of 0 º and 3 º bending.

However, by focusing in the areas where planes are tangent to the interface (top and bottom) the matching between planes is better with a bending of 3 º, where no distortions remain at the edges (highlighted with blue and green arrows in Figure 4.12).

TABLE 4.4: Number of dislocations in horizontal and vertical planes for angles ranging from 0 º to 4 º in a 10 nm radius nanowire.

Rotation angle	# (111) dislocations	# ($\bar{2}$02) dislocations	Total # dislocations
0 º	2	4	6
2 º	2	5	7
3 º	**1**	**5**	**6**
4 º	1	6	7

Thereby, plane bending for elastic energy minimization in the case of higher curvature shifts to higher angles.

iii. Nanowire with 35 nm core radius

From the conclusions obtained after analyzing situations presenting small cores, we can predict that bending would tend to zero in the case of bigger core diameters. For this reason, same methodology is applied to a core presenting 35 nm radius.

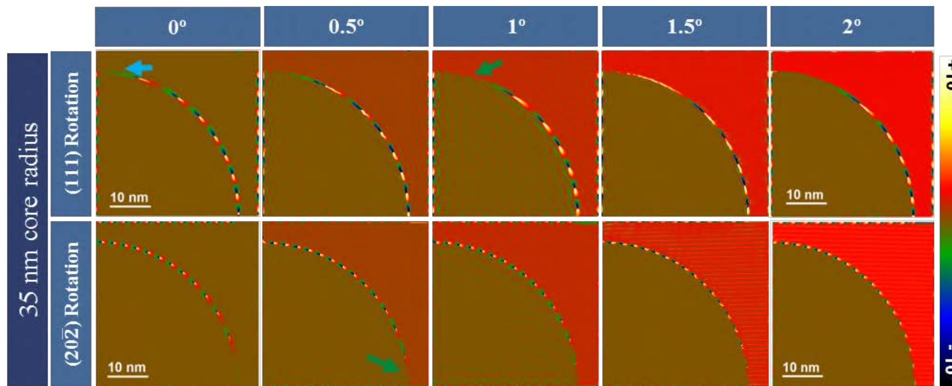

Figure 4.13: Simulated rotation maps of (111) and ($\bar{2}$02) planes for a nanowire with 35 nm core radius.

As predicted, a better lattice accommodation is reached for lower bending angles. When analyzing the total number of dislocations, as displayed in Table 4.5, the minimal number of 20 dislocations is achieved with rotations ranging from 0 º to 1 º. Checking the matching of planes tangential to the core surface we find that 0 º is far from optimal matching, but the matching gets improved for 1 º bending in the case of (111) planes and 0.5 º in the case of ($\bar{2}$02) planes. An optimal situation is thereby

assumed to happen in between 0.5 º and 1 º. At the same time, we assume from this analysis that radius > 50 nm need to be achieved for equalling the flat plane situation of C-sapphire faceted nanowires.

TABLE 4.5: Number of dislocations in horizontal and vertical planes for angles ranging from 0 º to 2 º in a 35 nm radius nanowire.

Rotation angle	# (111) dislocations	# ($\bar{2}$02) dislocations	Total # dislocations
0.0 º	8	12	20
0.5 º	**7**	**13**	**20**
1.0 º	**6**	**14**	**20**
1.5 º	5	16	21
2.0 º	6	17	23

Then, it can be confirmed that plane rotation underlays in the atomic steps caused by the curvature of the nanowire because of its nanometric size. A lower radius of the core would lead to a more abrupt stepping bringing a higher bending angle for minimization of the elastic energy. This behavior explains the lower rotations measured in the intermediate case examined previously, which presents a higher radius together with a top (111) faceting, and thus, a lowering of the overall curvature.

The absence of bending in flat and faceted nanowires grown on C-sapphire, where the core faceting occurs in ($\bar{2}$02) planes, is also relaying on the nanowire morphology. The absence of atomic steps in the lateral facets of the nanowire implies that plane bending would increase the effective mismatch between lattices, bringing an increase in elastic energy accumulation.

4.3.3 Influence of plane bending on electronic band alignment

Due to the polar nature of the bonds in binary semiconductors, polarity gets a key role on their final properties as we were developing in the previous chapter. In addition, the presence of polar defects such as Anti Phase Boundaries (APBs), para-twins or inversion domains has been reported to be detrimental for the electronic behavior of compound semiconductors, as they create local electric fields and potential barriers that critically decrease their conductance [10, 11]. We were observing the rotation mediated strain minimization mechanism in the previous sections for the case of presenting highly atomically stepped cylindrical morphologies.

In the pristine ZnTe structure, (111) planes present polarity due to the dipole direction meanwhile $\{20\bar{2}\}$ planes remain non-polar. However, the presence of a plane bending around the growth axis direction creates a configuration that resembles the one of APBs or paratwins as polar boundaries are appearing at the junction of the rotated ZnTe domains. We could observe in Figure 4.4c,f that the top facets of the NW are driven by (111) planes, which are non-equivalent to $(\bar{1}\bar{1}\bar{1})$ in terms of polarity. This fact implies that the Zn cation is placed on top of the dumbbell unit. In this way, Zn-Zn dipoles are facing each other at the high angle boundary created at the central part of the truncated cylindrical NWs, as schematized in Figure 4.14. This configuration breaks the polar neutrality in the horizontal direction as the $\{20\bar{2}\}$ non-polar planes derive from being vertical.

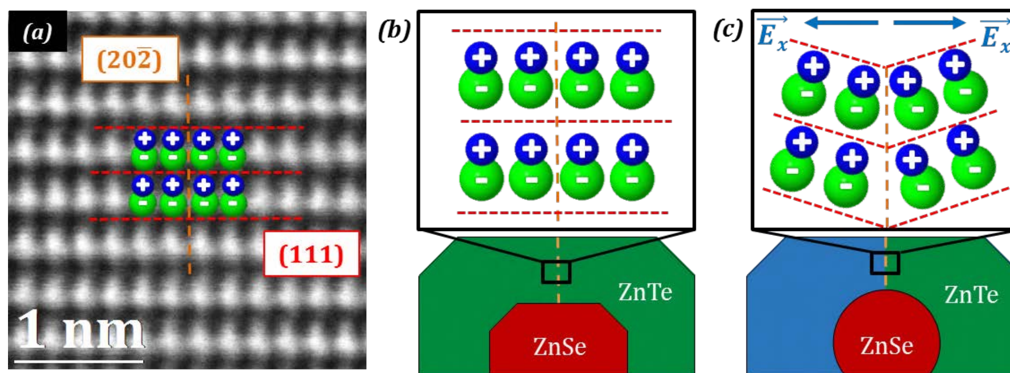

Figure 4.14: (a) Atomically resolved HAADF micrograph with dipole and (111) and $(20\bar{2})$ plane labelling. (b) Schematics of dipole positions in non-bent ZnTe crystals. (c) Schematics of dipole positions in the polar junction of a cylindrical cored NW. A net electric field contribution is appearing at the junction with different direction at its both sides.

The presence of a polar junction in the middle of the nanowire has intrinsic consequences in its optoelectronic behavior. Although the net field contribution along the vertical direction is preserved through the NW, the formation of the polar boundary produces a net horizontal electric field contribution that was strict zero for perfectly vertical $\{20\bar{2}\}$ planes. This generates, at the same time, an inversion of the horizontal component of the electric field at the middle of the junction. The implication is a band bending towards the inner part of the junction, which acts as a potential barrier for carriers and thus modulates the p-n band alignment spatially across the radial junction formed by ZnSe and ZnTe. This fact decreases the accuracy in sensitivity of the system.

Moving towards higher core radii in A-sapphire nanowires would decrease the effects of band bending within the junction, but at the same time it would decrease

the S/V ratio at the junction. For that reason, we considerate the C-sapphire planar core nanowires as a best option for achieving more efficient and highly sensitive photosensing devices.

4.4 EELS-based determination of electronic band gap

Low-loss Electron Energy Loss spectra contain information about optical and electronic transitions of the material, including collective electron excitations like phonons and plasmons and single electronic transitions, with ultimate spatial resolution. The lowest energy losses (Valence EELS or VEELS) reflect the joint density of states (JDOS) with $I \sim (E\text{-}E_g)^{1/2}$ in the case of a direct band gap material and $I\sim(E\text{-}E_g)^{3/2}$ in the case of an indirect band gap material [97]. Thereby, VEELS is a potentially useful technique for band gap evaluation with ultimate spatial resolution and even opens the window for discriminating between the different nature of the materials band gap. However, the complexities of the required data analysis in addition to the presence of parasitic radiations such as Cherenkov, surface states or excitons, among others, have been key issues for limiting the applicability of a methodology for band gap determination in semiconductor materials.

In the particular case of binary semiconductor materials, Cherenkov losses have been the main limitation for exploiting band gap determination. Cherenkov radiation is emitted when charged particles travel in dielectric media with a higher speed than the phase velocity of light in the medium ($\varepsilon_r > c^2/v^2$) [172], and thus they are directly related with the materials refractive index and the electron accelerating voltage. This limits the feasibility of EELS for E_g determination in binary semiconductors, which typically present high refractive indexes. This radiation is present regardless of the chosen collection aperture angle, as it takes place with a very narrow angular width in the 10^{-2} mrad range, although some strategies have been presented using off-axis EELS with ring shaped apertures[173]. Figure 4.15 shows the Cherenkov regime depending on the refractive index of the material and the TEM acceleration voltage. The radiation appears as a parasitic signal in the region of the EELS spectra containing E_g information even for ultrathin specimens [174, 175], and thus, the use of a low accelerating voltage for Valence EELS (VEELS) studies is required. Actually, some recent study claims the benefits of coupling an

EELS spectrometer to a dedicated SEM for getting rid of Cherenkov radiation by lowering the electron energy [176]. We can observe in Figure 4.15 that for the case of study of III-V semiconductors, which typically present 4<n<5, voltages below 10 kV should be employed to ensure working in the non-retarded regime. This issues have limited the applicability of the technique with E_g determination purposes for the case of binary semiconductor materials.

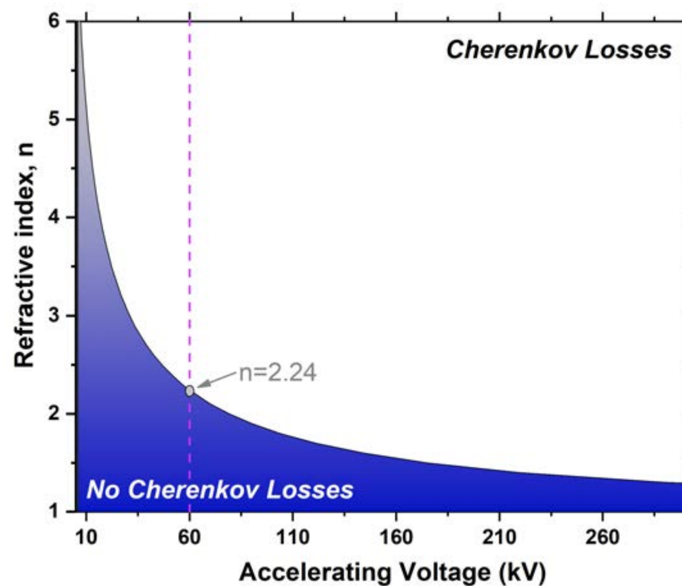

Figure 4.15: Cherenkov losses condition as a function of the material refractive index and the TEM acceleration voltage. The refractive index limiting the zero probability of Cherenkov losses at 60 kV is indicated.

ZnTe and ZnSe present lower refractive indexes than other binary semiconductors (3.06 and 2.61, respectively, compared to 3.95 of GaAs and 4.09 of InAs, for example) [177], together with a wider band gap. In addition, the sapphire substrates employed for the guided growth of these nanowires present such a low refractive index of 1.76 that retardation effects are not present until voltages $\sim$ 100 kV (Figure 4.15). Given the importance of band gap as an electronic property in heterostructured photodetectors and the intrinsic optical parameters of the different compounds of the system (i.e. Cherenkov radiation probability is highly reduced with respect to other binary semiconductors as InAs or GaAs), we have studied VEELS spectra along the NW system including core, shell and substrate for being able to determine the effects of residual epitaxial strain on the junction efficiency.

In order to obtain an EELS based E_g mapping there are several challenges that need to be overcome [178, 179]:

- Achieve a good accuracy in ZLP subtraction as its tail can introduce an error by modulating the measured intensity in low band gap materials.
- Reduce the amount of noise in the VEELS signal.
- Decouple parasitic radiation in the band gap region for being able to proceed with fitting just in the contribution provided by the materials electronic bands.
- Define the fitting energy region and function for each of the materials forming the system.

By taking into account all these considerations, we have computed an heterostructural band gap map based on VEELS spectrum imaging with a homemade Python code in which we deal with all these considerations for overcoming the challenges present in this kind of experiments while processing a multidimensional data set.

4.4.1 VEELS data treatment in heterostructured systems

The data is collected with 50 meV energy dispersion in a monochromated Nion UltraSTEM microscope operated at 60 kV to minimize the effects of Cherenkov radiation in a C-sapphire nanowire, which shows more potential towards photodetection accuracy due to the non-rotated strain relaxation. The microscope is equipped with a C_5 QO corrector, which allows having direct correction up to $C_{5,6}$ and thus the lowering of the accelerating voltage does not compromise the achievement of atomic resolution. The energy resolution of the VEELS spectrum image determined through the ZLP FWHM after a Gaussian fitting is of 59 meV in vacuum (Figure 4.16a). For spectra processing, the ZLP is subtracted by a reflected tail method [180] for removing induced intensity variations close to the band gap, specially in mid-low E_g materials (ZnTe/ZnSe). The spectra are smoothed by a Savitzky-Golay filter with a second order polynomial [181]. Figures 4.16b,c show acquired spectra on ZnSe and sapphire, respectively, after ZLP removal and smoothing filtering applied. In the case of ZnSe, the measured intensity as a function of the energy loss presents a $(E-E_g)^{1/2}$ dependency reflecting the JDOS, in agreement with the expected for direct band gap materials. However, we can observe certain losses measured before the band gap offset energy. These pre-gap measured intensities (arising from Cherenkov effect or the presence of surface effects) extended to the first band transition losses

introduces errors in fitting processing that deviate the measured values from the actual materials band gap. In the case of sapphire, it presents its band gap located at 9.1 eV energy and it presents an indirect nature, so the measured intensity above the band gap value should follow a $(E\text{-}E_g)^{3/2}$ dependency. However, we observe several losses before the band gap offset. As stated before and highlighted in Figure 4.15, α-Al_2O_3 is within the non-retardation regime at 60 kV, but even with that the presence of different surface states within the band gap region and close to it produce parasitic signals that preclude band gap determination.

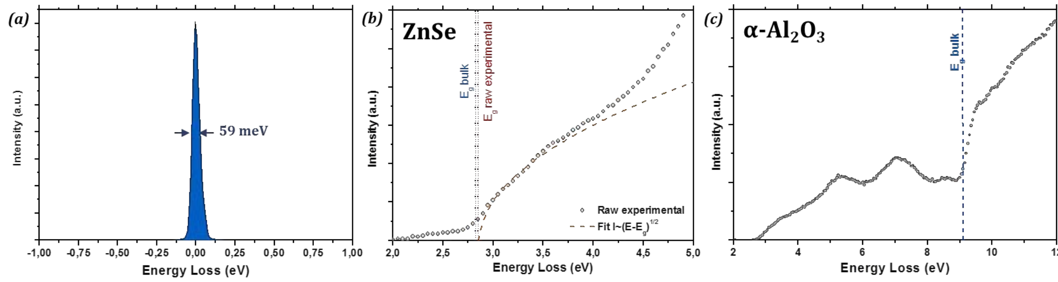

Figure 4.16: (a) Zero Loss Peak in vacuum with indicated FWHM after Gaussian fitting, revealing 59 meV energy resolution. (b) Filtered spectrum of ZnSe after ZLP subtraction together with a $I \sim (E\text{-}E_g)^{1/2}$ direct band gap fitting. (c) Filtered spectrum collected at α-Al_2O_3 substrate after ZLP subtraction. The band gap energy of sapphire is marked.

In order to remove the parasitic radiation from the recorded spectra, dielectric theory is employed for simulating the obtained signal for the different materials and being able to decouple the different contributions forming the recorded spectra. The total energy loss probability has been modelled as a combination between bulk contribution independent of the geometry plus a surface term influenced by the interface positions [182].

Both the exact retarded and the non-retarded solutions (i.e. assuming the velocity of electrons is not comparable to the speed of light) have been computed and compared to extract the probability of emission ratio when electrons interact with bulk material, considered as an infinite single crystal [183, 184]. This way, the exact retarded solution can be computed as:

$$\Gamma_{bulk}(\omega) = \frac{Le^2}{\pi \hbar v^2} Im\left\{ \left(\frac{v^2}{c^2} - \frac{1}{\varepsilon} \right) ln \left(\frac{q_c^2 - k^2\varepsilon}{\left(\frac{\omega}{v}\right)^2 - k^2\varepsilon} \right) \right\} \tag{4.3}$$

where L is the lamella thickness, that is determined to be 50 nm through ZLP analysis, $\varepsilon = \varepsilon(\omega) = \varepsilon_1(\omega) + i\varepsilon_2(\omega)$ is the dielectric function for each material, v is the

velocity of the incoming electron (v = 0.484c at 60 kV) and q_c states the momentum transfer cutoff below which the electrons are collected

$$q_c \approx \frac{1}{\hbar}\sqrt{(mv\varphi_{out})^2 + \left(\frac{\hbar\omega}{v}\right)^2} \tag{4.4}$$

which is determined by the collection semiangle φ_{out}. With this considerations, the final expression for the bulk retarded solution can be written as:

$$\Gamma_{bulk}(\omega) = \frac{Le^2}{\pi\hbar v^2}\left\{\frac{\varepsilon_2}{\varepsilon_1^2+\varepsilon_2^2}\left[ln\left(\sqrt{\left(\left(\frac{q_c c}{\omega}\right)^2 - \varepsilon_1\right)^2 + \varepsilon_2^2}\right) - ln\left(\sqrt{\left(\left(\frac{c}{v}\right)^2 - \varepsilon_1\right)^2 + \varepsilon_2^2}\right)\right]\right.$$
$$\left. + \left(\frac{v^2}{c^2} - \frac{\varepsilon_1}{\varepsilon_1^2+\varepsilon_2^2}\right)\left[arctan\left(\frac{-\varepsilon_2}{\left(\frac{q_c c}{\omega}\right)^2 - \varepsilon_1}\right) - arctan\left(\left(\frac{-\varepsilon_2}{\left(\frac{c}{v}\right)^2 - \varepsilon_1}\right)\right]\right\} \tag{4.5}$$

While the non-retarded contribution can be obtained as:

$$\Gamma_{bulk}^{NR}(\omega) = \frac{2e^2L}{\pi\hbar v^2} Im\left\{-\frac{1}{\varepsilon}\right\} ln\left(\frac{q_c v}{\omega}\right) =$$
$$= \frac{2e^2L}{\pi\hbar v^2}\frac{\varepsilon_2}{\varepsilon_1^2+\varepsilon_2^2} ln\left(\frac{v}{\hbar\omega}\sqrt{(mv\varphi_{out})^2 + \left(\frac{\hbar\omega}{v}\right)^2}\right) \tag{4.6}$$

Additionally, boundary element method (BEM) was used to solve Maxwell's equations to get the energy-loss probability for each energy from 0.5 eV to 10 eV [184, 185]. A translationally invariant system in the direction of the incoming electrons has been considered. Experimental dielectric functions have been employed for ZnSe [186, 187], ZnTe [187, 188], Al_2O_3 [189] and Pt [190], which is contained in the deposited layer for FIB preparation. By using these functions, a representative 84x60 pixels spectrum image has been computed by following geometry and composition of the original 250x166 pixels spectrum image to be able to compute the total contribution of surface terms at each point of the acquisition.

Figure 4.17 shows the simulated total loss probability and the decoupled contributions of the surface term and the Cherenkov-free signal for some representative spectrum image pixels within ZnSe, ZnTe and sapphire.

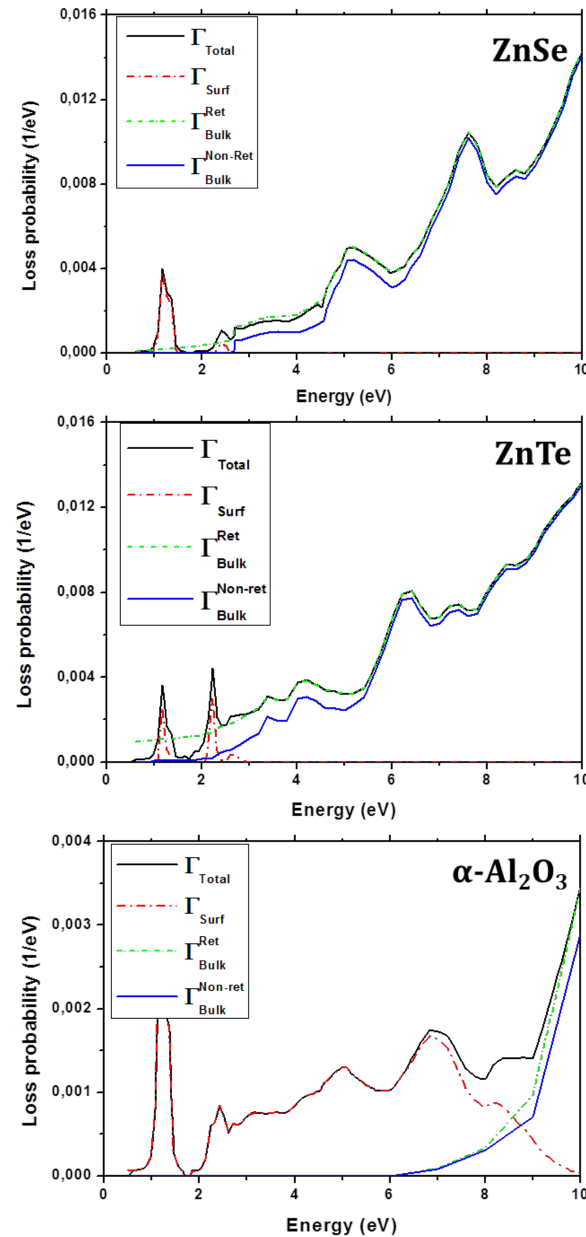

Figure 4.17: Simulated spectra where the surface, retarded bulk and non-retarded bulk contributions are decoupled for regions of the modelled NW in the areas of ZnSe, ZnTe and sapphire, respectively.

By following this procedure, the total energy spectrum at each point of the experimental spectrum image can be simulated by an addition of the bulk and surface contributions. At the same time, the non-retarded solution (i.e. Cherenkov-free) can be subtracted and compared to the total simulated signal. The total simulated spectrum image can be thus employed to correct the experimental data by subtraction of the contributions that do not arise directly from optoelectronic material excitations but from charged particles interacting with the media and interfaces, leaving the JDOS accessible for further function fitting. For doing so, a correction ratio is

defined as:

$$\delta(\mathbf{r}', \omega) = \frac{\Gamma^{NR}_{Bulk}}{\Gamma_{Total}}; \;\; where\, \Gamma_{Total} = \Gamma^{R}_{Bulk} + \Gamma_{surf} \tag{4.7}$$

This correction ratio reflects the ratio of the signal arising purely from the bulk material electronic structure compared to the overall signal at each energy of the collected spectrum. This amount is transferred to the experimental data for applying corrections and reducing the amount of parasitic radiation, to give rise to a corrected experimental spectrum image.

$$\Gamma^{Corrected}_{Exp}(\mathbf{r}, \omega) = \delta(\mathbf{r}', \omega)\Gamma_{Exp}(\mathbf{r}, \omega) \tag{4.8}$$

where **r** is the equivalent position in the experimental spectrum image, given a position of the simulated spectrum defined by **r'**. The settings applied to the corrected image allow to perform intensity fittings with $(E\text{-}E_g)^{1/2}$ for direct band gap and $(E\text{-}E_g)^{3/2}$ for indirect band gap materials coexisting in the sample.

In order to adjust the fitting function and energy range for each of the different materials, principal component analysis (PCA) was employed to create input matrices of the core, the shell and the substrate by using different order components to create 0-1 matrix maps. This mechanism allows to assign the fitting offset and the appropriate fitting function separately for each material, and thus, it provides accuracy to determine small value fluctuations within the material in consideration. Figure 4.18 shows the HAADF image of the nanowire in consideration together with the PCA-based input matrices for each of the materials. After PCA was applied, the component maps were saturated to convert them in 1-0 binary maps. The first order PCA component was employed for calculating the α - A_2O_3 gap, the second order component was employed for ZnTe gap determination and the third order component for ZnSe.

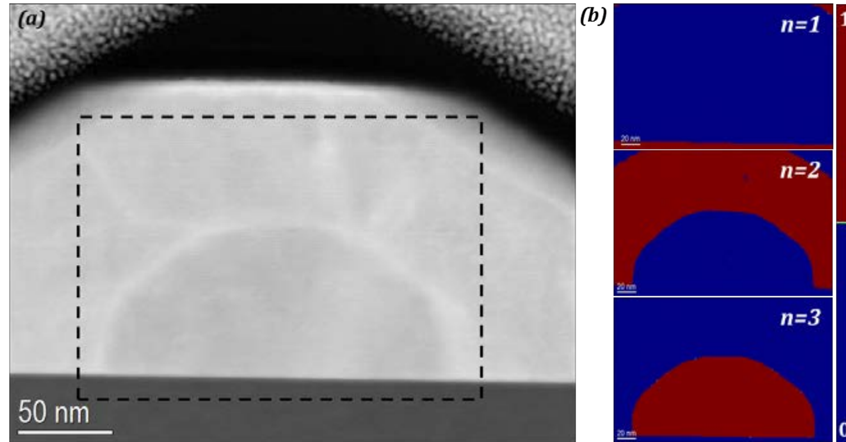

Figure 4.18: (a) HAADF image of the C-NW with indications of the VEELS SI collection area. (b) Saturated PCA components of first, second and third order employed as matrix inputs for material discrimination.

4.4.2 Results and discussion

Following this procedure, the full VEELS band gap map encompassing the whole material system shown in Figure 4.19a was elaborated. For doing so, the Pt-C protective layer is excluded from the calculations, even though it was considered for the simulated spectra used to correct the original spectrum image, as it does affect to the surface term of the probability of energy loss.

We observe a uniform distribution through the entire core as well as in the substrate, as expected if we compare with the lack of strain fields and deformations through the core observed in the previous GPA analyses and lattice constant uniformity through a substrate. However we can observe fluctuations up to 200 meV on the measured values, which demonstrates our energetic accuracy for discriminating different pixels. However, we observe that averaging the obtained data we obtain exactly the 2.8 eV E_g expected for ZnSe. In the case of sapphire, the obtained band gap value is found to be 8.5 eV with indirect nature, indicating a pretty well accuracy of the surface term correction.

The study of ZnSe and sapphire relaxed systems permits to study the effects of interfacial strain in ZnTe shell. We observed in the strain maps obtained through GPA how even given the creation of dislocations, there is a ~ 7 nm compressive ZnTe layer surrounding the core until it reaches elastic relaxation. This is highly reflected in the MAADF micrograph observed in Figure 4.19b, where high bright contrast is

observed in the strained areas near the interface, specially between ZnSe and ZnTe. If we correlate it with the E_g map, we can observe a decrease in the E_g value of 300 meV in the imminent interface area that smoothly reaches within the next 25 nm the average bulk value of 2.35 eV. This is directly correlated with the decrease in the lattice constant of ZnTe caused by the elastic deformation when epitaxing on top of ZnSe [191]. The relaxed ZnTe value is slightly deviated from the 2.39 eV gap from ZnTe at 300 K, but the error observed in the averaged value is then of just 40 meV in energy while preserving higher spatial resolution than with any other technique.

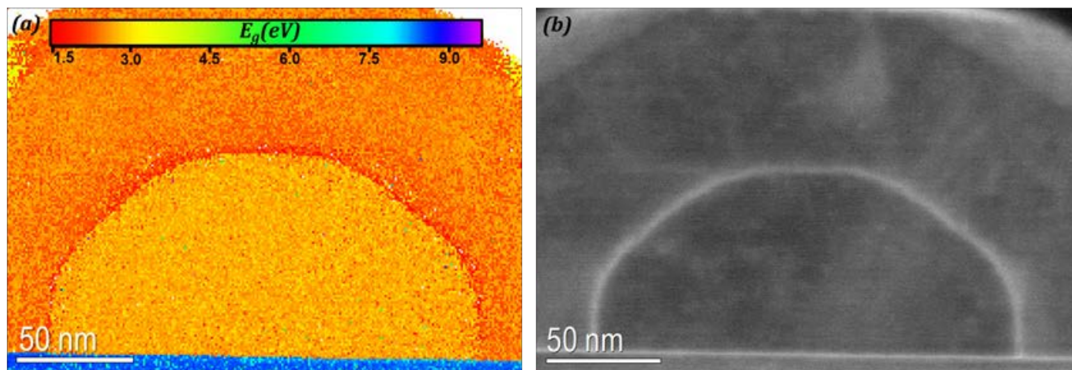

Figure 4.19: (a) Full NW system VEELS E_g map and (b) MAADF micrograph of the same area showing the strained heterointerfaces with a higher brightness.

Related with the spatial resolution of the technique, it is worth commenting about the spatial accuracy we can consider. The pixel size employed for mapping is below the nanometer, exactly 0.9 nm per pixel. However, this value is far away from the actual spatial resolution due to the delocalization of inelastic scattering. The processes driving inelastic scattering (and thus, involving energy loss) occur within a spatial range, which decreases the spatial resolution, specially in low loss measurements [146, 192]. In that regard, the length of confidence is higher than $\sim$5 nm for our experimental measurement.

Given that the junction efficiency is mainly determined at the radial interface between both materials, we are specially interested in the measured decrease of the band gap in that region. Both ZnTe and ZnSe relaxed band gaps present higher offsets than the measured energy. In that regard, we can confirm that the measured intensity before ZnTe offset arises from the compression of the material caused by interfacial strain, as the possible effects of the interfaces were already removed from the raw spectra. However, we observe an elongation up to 25 nm where the band gap of ZnTe is reduced with respect to the bulk gap in strain-free areas. This decrease

is attributed to the delocalization meanwhile the minimum measured at the interface directly arises from a strain mediated band gap reduction.

The versatility of the method proposed to consider complex heterostructured systems is thought to be applicable to materials presenting some alloying that provide local band-gap variations, for example the SAG nanowires that we present in the next chapter. In addition, we propose to expand this strategy with the employment of dual-EELS collection systems to collect simultaneously VEELS and core-loss signals, which would permit to obtain in a straight forward way the 0-1 matrix components by simple and highly standardized elemental mapping.

4.5 Conclusions

In this chapter, we have studied VLS horizontal growth of core-shell NWs through a guided growth approach, which offers a new growth strategy towards scalable radial p-n photodetectors. Guided growth of horizontal arrays presents benefits over conventional vertical VLS regarding its applicability, but the strong interaction with the substrate surface adds an additional influence to the proper crystallization of the NWs. For this reason, ZnSe@ZnTe core-shell nanowires were grown on α-A_2O_3 cut in different orientations to exploit the different directional growth possibilities.

In that regard, annealing M-plane oriented sapphire gives rise to more stable S and R nanoplanes in a periodic symmetry. These spontaneously created nanofacets give rise to two directional A-planes in which nanowires can propagate through graphoepitaxial growth, creating arrays of perfectly aligned NWs. However, given the crystal symmetry differences between the grown material and the substrate, the simultaneous adaptation to the two created substrate nanofacets produces difficulties in defining an epitaxial relationship. This fact makes the VLS grown nanowire morphologies to be highly non-uniform, as the faceting is driven by thermodynamic energy minimization of the available crystal planes.

Better NW uniformity is found when guiding the growth on flat C-plane and A-plane sapphire in an epitaxial guided growth approach. However, the different surface energies of C-sapphire and A-sapphire drive to different catalyst contact angles that result in a clearly differentiated core morphology: cylindrical ZnSe cores

are grown on A-sapphire while faceted prismatic or belt-like ZnSe cores with contact angles of strict 90 ^{o} are grown on C-sapphire. These morphology variations dramatically influence the epitaxial growth of the highly mismatched ZnTe shells. We have observed a ZnTe plane bending phenomena in cylindrical cores that has been demonstrated to improve the epitaxial matching with the atomic steps forming the core. This plane bending, which creates polar boundaries within the ZnTe shell that act as potential barriers, is then influenced by the core curvature in a way that the smaller the core (i. e. higher curvature) the more bending is favoring an elastic energy minimization, while at the same time it detriments the optoelectronic behavior of the formed p-n radial junctions. These effects are not observed in C-sapphire, where the planar shape of the ZnSe cores is translated to a standard shell configuration where most of the strain is released within the first 7 nm of the interface by the creation of dislocations followed by a compressive deformation of ZnTe until reaching elastic relaxation.

In order to test the possible implications of this strained layer on the band gap configuration of the heterostructures, we have developed a strategy to perform a VEELS-based band gap map. We measure that the compressive ZnTe layer is directly translated into a decrease of the band gap value in the ZnTe region close to the interface. This result is matching the theoretical estimation of a decrease of band gap in ZnTe due to elastic compression and opens the possibility to expand this strategy for different systems to be able to determine with exceptional spatial and energetic resolution the band gap in alloys or strained materials with the addition of being able to discriminate between direct and indirect band gap nature.

Chapter 5

Selective Area Growth of III-V nanostructures

The possibility of patterning substrates to grow nanostructures all along desired positions gave rise to the Selective Area Growth (SAG) technique. This technique opens the possibility of suppressing the need of post processing single nanowire manipulation for device production, offering technological advances towards device integration. In this chapter, we investigate the prospects and limitations of growing III-V 1D-like nanostructures for diverse applications: from the integration of GaAs into Si-based technologies to the growth of high mobility InAs/InSb nanowire networks in semi-insulating substrates for the development of quantum devices. Challenges such as achieving single nucleation regime, overcoming selectivity limits and strain engineering towards defect-free structures are faced and their relevance is discussed all comparing crystallographic quality and (opto)electronic performance of the grown nanostructures.

5.1 Introduction

Selective Area Growth (SAG), also named Selective Area Epitaxy (SAE), is a Vapor-Solid (VS) growth approach that permits the local epitaxial growth through the employment of nanopatterned dielectric masks, typically SiO_2. It was presented in 1962 by Joyce *et al.* [193] for silicon integrated circuits. The proper tuning of growth parameters (e.g. employing high temperatures) permits the sticking coefficient of adatoms to be minimized on the mask and maximized within the openings. The growth of SAG nanostructures through MBE or MOCVD allows, then, to leave aside the need of a catalyst. In addition, the control over the nanostructure growth position achieved by nanopatterning with lithography and etching techniques makes this growth strategy appealing for nanostructural functionalization and integration

in existing technologies.

Even though works on SAG of III-V compounds by MBE were reported early in the 1970s [194], there was a very limited knowledge about selectivity, limiting the applicability of the technique. Since then, most reported III-V SAG developments have been devoted to the growth of vertical arrays of nanowires [72, 195–197]. However, although the problems of nanowire localization are overcome with localized growth, the presence of twinning defects in vertical NWs seems to be unavoidable [198]. Instead, defect-free planar-like structures have been achieved through homoepitaxy by the employment of large directional openings [154]. The resulting structures, called nanomembranes (NM), are interesting candidates due to their excellent optical properties because of their pristine crystal quality and high aspect-ratio [154, 199, 200]. However, it is important to mention that the quality of structures, as well as their faceting, are highly dependent on the opening orientations with respect to the substrate crystal directions.

It looks appealing to employ nanopatterning on the mask as a strategy to define nanostructured networks. Nanomembranes can be employed as templates for the growth of NWs on top of them to provide them a larger functionality. In another approach, the growth of networks can be carried out directly in the substrate when patterned in appropriate directions, allowing the connection of nanowires grown on different directions without further manipulation. However, the difference in lattice constants between the substrate and the deposited material might cause strain fields and defects in heteroepitaxial growth.

A special insight has been put recently on the achievement of high crystal quality networks of high mobility 1D semiconductors (mainly InAs and InSb). These horizontal nanowire systems look appealing candidates for the development of a new generation topological quantum computing devices, as it will be further detailed in Chapter 6. However, several challenges still need to be overcome for achieving ideal systems. These challenges include polynucleation, limitations in the directional growth and appearance of defects such as misfit dislocations.

5.1.1 Models of VS growth mechanisms

The VS growth mechanism of a heterostructure in the mask openings is given by the surface energy of the grown layers (γ_F), the substrate(γ_S) and the interface (γ_{SF}), although the substrate- material mismatch also plays a role in the final structure. The three main regimes of epitaxial VS growth are schematized in Figure 5.1.

(a) A layer by layer growth, also known as Frank - van der Merwe growth mechanism [201], takes place when the sum of the surface energy of the deposited layer and the interface is lower than the substrate surface energy ($\gamma_S \geq \gamma_F + \gamma_{SF}$).

(b) Contrary, the growth takes place in islands if the surface energy of the substrate is lower than the sum of the surface energy of the layer and the interface energy ($\gamma_S < \gamma_F + \gamma_{SF}$). The islands grow until they coalesce forming a continuous film. This mechanism is known as Volmer - Weber [202] growth mechanism.

(c) Finally, Stranski - Krastanov regime involves a mixed growth in which a first layered growth takes place. This changes the values γ_{SF} and γ_S in such a way that the growth keeps developing 3D islands that grow until merging together in a continuous film [203].

It is important to notice that growth by independent nucleation of 3D islands might drive to highly defective structures. The appearance of defects in independent islands, together with differences in crystal orientation of the initial nuclei arising from high lattice mismatches are responsible of creating highly defective boundaries when islands merge to form the final nanostructure. Ideally, Frank - van der Merwe growth mechanism leads, instead, to more homogeneous and defect-free materials.

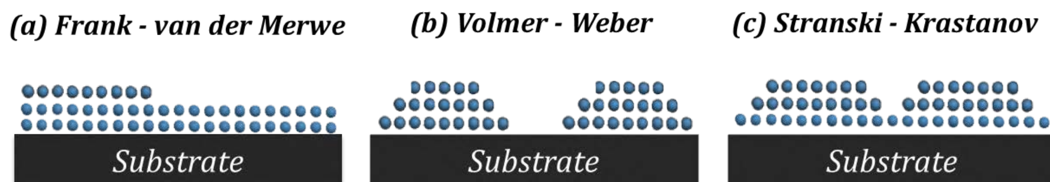

Figure 5.1: Schematics of Growth models in VS growth. (a) Frank - van der Merwe layered growth. (b) Volmer-Weber island growth. (c) Stranski - Krastanov mixed growth.

5.1.2 Selectivity of the grown materials

The growth conditions for growing selectively III-V materials into nanopatterned openings have to be properly adjusted. During MBE, several growing modes can take place, as sketched in Figure 5.2:

(i) Nucleation of randomly oriented III-V crystallites on the mask along with single crystalline III-V growth inside the openings.

(ii) Formation of liquid and partially crystallized III/III-V clusters on the mask along with single crystalline III-V growth inside the openings.

(iii) Selective single-crystalline III-V growth inside the openings.

(iv) No growth on the mask or inside the openings (III-V decomposition regime).

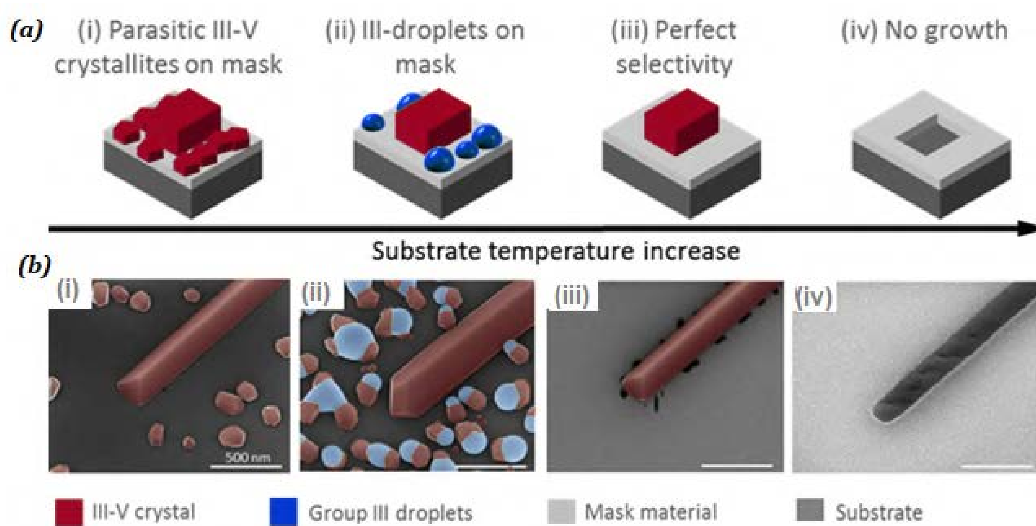

Figure 5.2: For a fixed F_V/F_{III} flux ratio (F_V>F_{III}): (a) Sketch of different growth modes when changing the substrate temperature. (b) Color coded SEM images of homoepitaxial GaAs with fixed III-V fluxes F_{Ga} = 0.26 ML_{GaAs}/s and F_{As} = 0.96 ML_{GaAs}/s at a range of temperatures between 600 °C and 690 ° C [73].

Therefore, it is important to perform selectivity mapping to adjust the growth conditions reducing parasitic growth on the mask for selecting a window in which deposition is just taking place in the opened areas. It is remarkable that the conditions window is different for every material into deposition, as their sticking coefficients to the mask are different. In addition, it can be also susceptible to the substrate composition and orientation. However, by performing selectivity maps for different

compounds, such as InAs and GaAs [73], on different substrates can allow to find conditions for perfect selectivity of ternary compounds such as $In_xGa_{1-x}As$. This fact opens an important factor towards the optimization of devices: strain fields acting from the large area interaction between substrate and the nanowire can be the source of defect generation. The possibility of including intermediate layers with an intermediate composition can allow to reduce the elastic energy accumulation for achieving defect-free 1D structures through strain engineering, as it will be described in section 5.4.

5.1.3 Scalable nanowire networks

The possibility of patterning the desired material configurations is appealing for the in-situ creation of junctions and networks with high scalability. This fact makes SAG the most promising candidate for the next generation of electronic devices and it is of particular interest for the development of new topological quantum computing schemes (more details will be given in Chapter 6). However, there are some limitations, mostly based on material crystal symmetry, for network and junction design. This is intrinsically arising from the final nanowire morphology, which is governed by surface free energy minimization and growth kinetics. In this regard, even though the in - plane shape of the nanowires is mainly guided by the mask pattern, several limitations appear when misaligning patterns from highly symmetric planes, as observed in Figure 5.3a,c. It can be observed how angular in-plane deviations from the high symmetry directions result in NW roughness. The creation of low energy facets which are not anymore parallel to the slit is energetically favored to overcome the excess of energy of the corresponding parallel high order facets.

In this regard, the patterning possibility of the mask is limited to the crystal symmetry of the substrate. For instance, {111} oriented substrates present a 3-fold rotational symmetry which allow uniform faceting in only two direction families, <1$\bar{1}$0> and <11$\bar{2}$>. This allows the fabrication of structurally coherent tri-junctions as shown in the SEM images of Figure 5.3b. It is important to notice that the shape of the junctions is also strongly dependent on the nanowire orientation (see magnified micrographs). <11$\bar{2}$> are polar directions, so junctions formed by <11$\bar{2}$>A and <11$\bar{2}$>B oriented nanowires present different morphologies due to the different growth rates

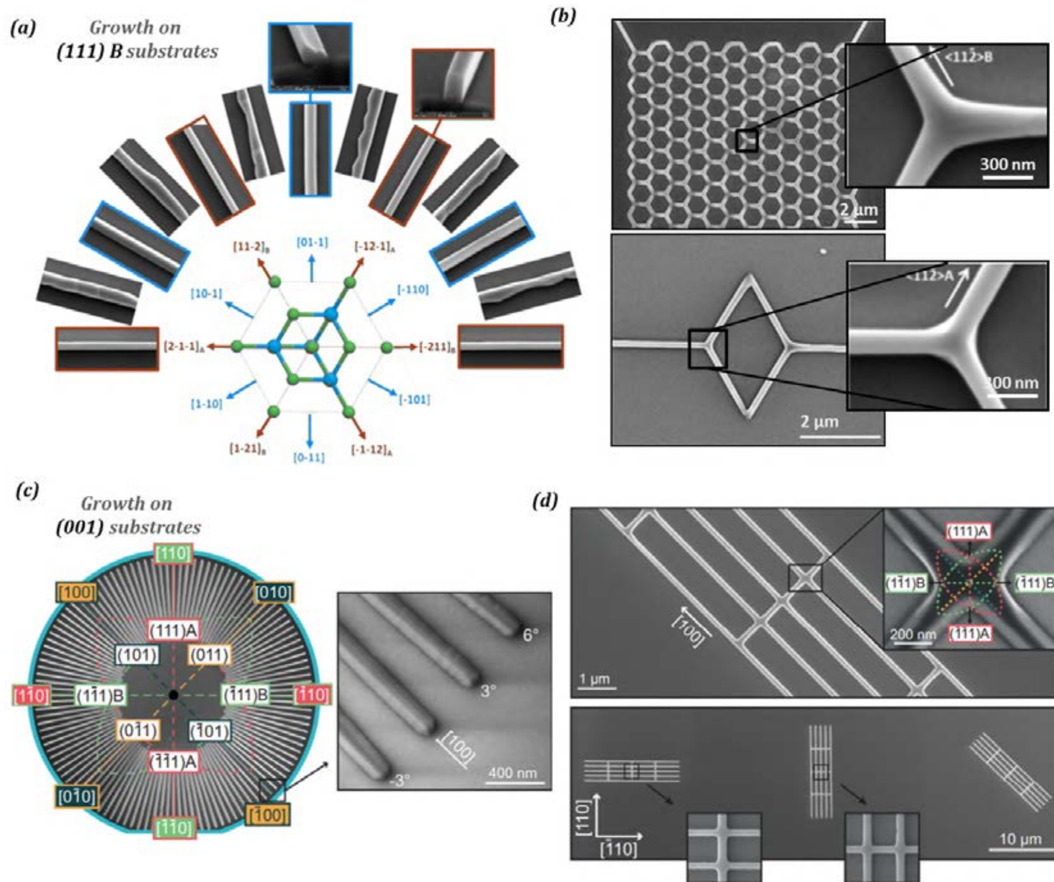

Figure 5.3: SEM micrographs of NWs grown at different in-plane orientations for (a) (111)B substrates and (c) (001) substrates. The high - symmetry orientations are indicated in both cases. (b) and (d) show some possible network and junction configurations in these substrate orientations. [53, 73].

in these directions, being the former one more uniform in shape. In the case of employing (001) substrates, there are eight high-symmetry crystal directions belonging to the <100> and <110> families providing, in principle, a 4-fold symmetry. However, for high growth times, the differences in growth kinetics on polar $\{111\}$ planes turn the structure into a twofold symmetry (see the stereographic projection of $\{111\}$ planes in Figure 5.3d).

As advanced by the SEM images on junction morphologies, the nanostructure morphology is highly dependent on the slit orientation, driven by both growth kinetics and thermodynamic surface energies. Figure 5.4 shows the cross sectional visualization of nanowires grown on the same substrate in differently oriented slits. NWs grown on <112> directions show vertically oriented $\{1\bar{1}0\}$ parallel side-walls, a flat (111)B top facet and small inclusions of $\{021\}$-type facets. This shape symmetry agrees with the lack of polarity of the lateral facets. Contrary, the cross-section of

the <1$\bar{1}$0> NW reveals a highly asymmetrical shape with a clear overgrowth on the right side of the mask opening. The faceting of the nanowire is determined by the lower surface energy of oblique {111} planes with respect to the vertical {112} ones. However, left $(1\bar{1}\bar{1})$ and right $(\bar{1}11)$ planes present different polarities which result in different growth rates and explain the differential lateral overgrowth at both sides. It is interesting to notice that the defect distribution is also dependent on this, as we observe the formation of twin boundaries in the overgrown region while left side of the nanowire preserves the pristine InAs defect-free structure.

One of the major issues of growing nanowires epitaxially on top of the substrate is the formation of interface defects. Substrates and NW materials typically present significant mismatches. In a vertical configuration, the reduced lateral dimensions of the nanowire often permit elastic lattice adaptation. However, the mask is bringing certain confinement into the NW lattice that do not allow the lattice to expand, resulting in plastic relaxation and the inherent creation of misfit dislocations for strain release (Figure 5.4d,g,j). In addition, these defects can be extended through all the nanowire length due to the large area of surface interaction (Figure 5.4j). Misfit dislocations can act as charge trapping centers, which strongly affect the conductivity of the grown nanostructures, as we will analyze further in this chapter. For instance, strain engineering technologies are being developed in order to reduce the high density of misfit dislocations [53].

In this chapter we study several kinds of nanostructures grown by selected area growth. We start addressing the role of nucleation mechanisms on the growth of GaAs nanomembrane structures on non-polar substrates for optical device applications and the drawbacks of polynucleation regimes. Later on, we discuss on the selected area growth of InAs NWs for quantum applications in different strategies. First of all, we investigate the possibility of employing GaAs nanomembranes as templates for the further growth of nanowires. Then we investigate the possibility of growing template-free InAs through engineering different layers for elastic strain release and control on defect formation. Finally, we discuss on the potential of growing InSb NWs as basis for quantum hybrids and the difficulties faced for achieving pristine InSb structures.

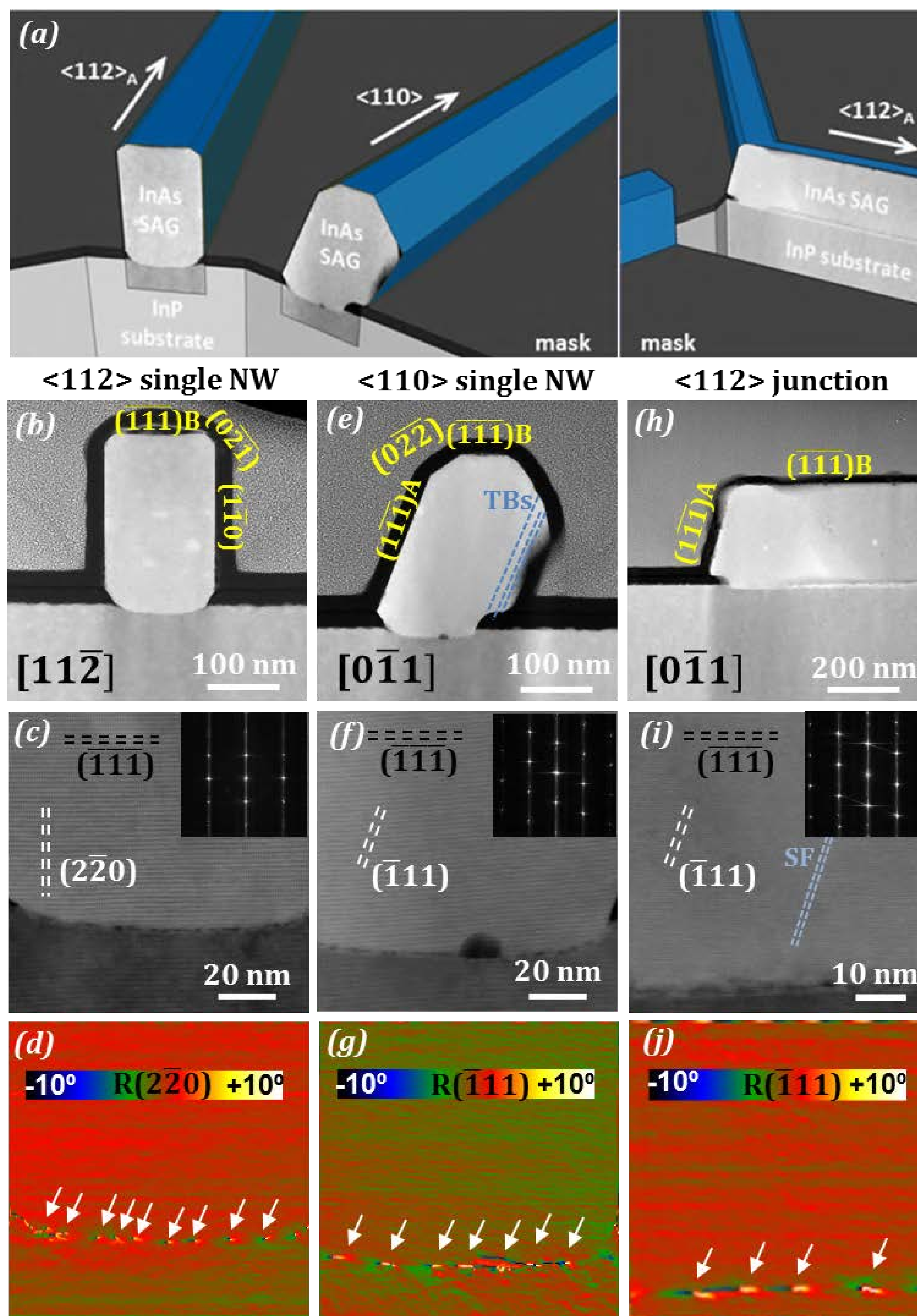

Figure 5.4: Overview of nanowire faceting and crystal structure of InAs SAG nanowires grown along high symmetry directions on InP(111)B substrates. (a) 3D schematics of the nanowire cross-sections. (b) Low-magnification HAADF-STEM micrograph, (c) details on crystal structure at the interface and (d) GPA rotational map of vertical planes highlighting the presence of misfit dislocations at the interface for a nanowire grown along [11$\bar{2}$] direction. (e) Low-magnification HAADF-STEM micrograph, (f) details on crystal structure at the interface and (g) GPA rotational map of oblique ($\bar{1}$11) planes highlighting the presence of misfit dislocations at the interface for a nanowire grown along [0$\bar{1}$1] direction. (h) Low-magnification HAADF-STEM micrograph of a longitudinal cross-section, (i) details on crystal structure at the interface and (g) GPA rotational map of oblique ($\bar{1}$11) planes highlighting the presence of misfit dislocations at the interface on a junction formed by <11$\bar{2}$> NWs.[73].

5.2 Implementation of GaAs nanomembranes onto Si substrates

The growth of defect-free SAG GaAs nanomembranes on GaAs substrates was reported to have excellent optical properties [154, 204]. However, reliable integration of these structures on silicon technologies is still a goal for extending the advantageous properties of III-V compounds onto cheap and ubiquitous Si substrates. The implementation of such elongated nanostructures on silicon is, however, challenging. Two main factors complicate the growth with respect to the homoepitaxial case. The first of them is the 4.2 % lattice mismatch between Si and GaAs, which might create distortions in the nanomembrane lattice. However, a periodic array of misfit dislocations at the Si-GaAs interface can relax plastically the epitaxial strain. The second, and most challenging, is the possibility of formation of antiphase boundaries that would manifest As-As and/or Ga-Ga bonds. When a binary compound is grown on a monoatomic (i. e. non-polar) material, there is no preferential polar orientation for the semiconductor compound. This means, for instance, that A-polar and B-polar nucleated III-V islands are possible. The presence of monoatomic steps in the substrate might lead then to the presence of multiple antiphase domains which would be detrimental for the optoelectronic behavior. Even though this problem can be addressed by a proper substrate engineering towards atomically flat surfaces, polynucleation of multiple islands with opposite polarities also forms APBs when islands coalesce to form the final crystal.

We address the effects of polynucleation on optical behavior by studying the structural features of NM grown on two differently oriented Si substrates, (111) and (001), together with their optical response.

5.2.1 GaAs NM on (111) Si

The nanomembrane growth on Si (111) with mask openings oriented along the $[11\bar{2}]$ direction is investigated. Figure 5.5 shows SEM micrographs obtained on two samples grown under the same conditions but with different opening lengths. It can be

clearly observed that the nanomembranes exhibit a polynucleation regime for aperture lengths greater than 400 nm. High yields of 90% single nucleated nanomembranes are achieved when employing slit sizes below 400 nm.

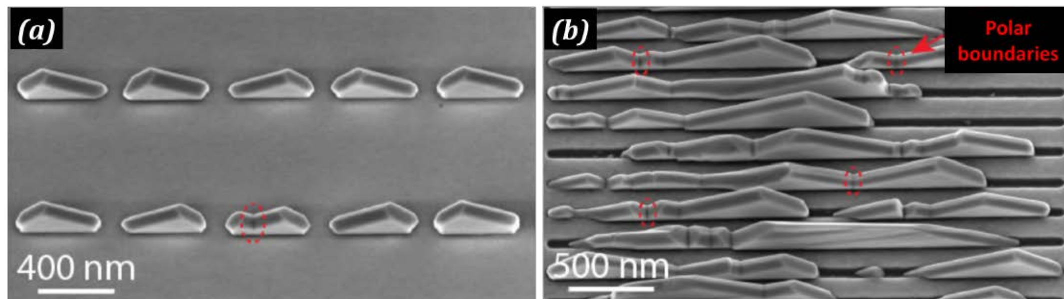

Figure 5.5: Tilted SEM images obtained in samples grown under the same conditions with opening lengths of (a) 370 nm and (b) 3000 nm.

From the SEM micrographs it is clearly appreciated that mononucleated nanomembranes exhibit well defined faceting in the $\{110\}$ planes as a reflect of high crystal quality. However, two different nanomembrane orientations are found depending whether the $<11\bar{2}>$ NM crystal axis is oriented parallel or antiparallel to the $<11\bar{2}>$ Si direction. The nanomembrane morphology can be attributed to a growth mechanism based in thermodynamic factors involving a tetrahedral nuclei formed by three inclined $\{110\}$ planes that present minimum surface energy, consistent with the models of VS growth proposed for VS GaAs NW or homoepitaxial GaAs NM growth [154, 196, 198].

Figure 5.6 schematizes the different phases taking place during single nucleated NM growth. GaAs spontaneously grows along $(\bar{1}\bar{1}\bar{1})$B direction [10, 11], so the nuclei oriented along the $<111>$B direction are expected to dominate the growth. In addition, a Ga predeposition process is taken to guarantee B - oriented nucleation islands. These nuclei form then a tetrahedron with $(\bar{1}0\bar{1})$, $(\bar{1}\bar{1}0)$ and $(0\bar{1}\bar{1})$ exposed facets, that present their long size following the $<\bar{1}\bar{1}2>$ direction. The formed island, starts to grow until reaching the lateral edges of the slit, where two vertical $(1\bar{1}0)$ and $(\bar{1}10)$ side facets start to develop, limiting the lateral growth of the structure. The nanomembrane keeps growing guided by thermodynamics by preserving its shape until the element sources are switched off.

The two oppositely oriented options are a consequence of rotational twins parallel to the substrate - NM interface. A lack of rotational twins in former grown NM - like structures [154] has been attributed to the appearance of large $\{110\}$ vertical

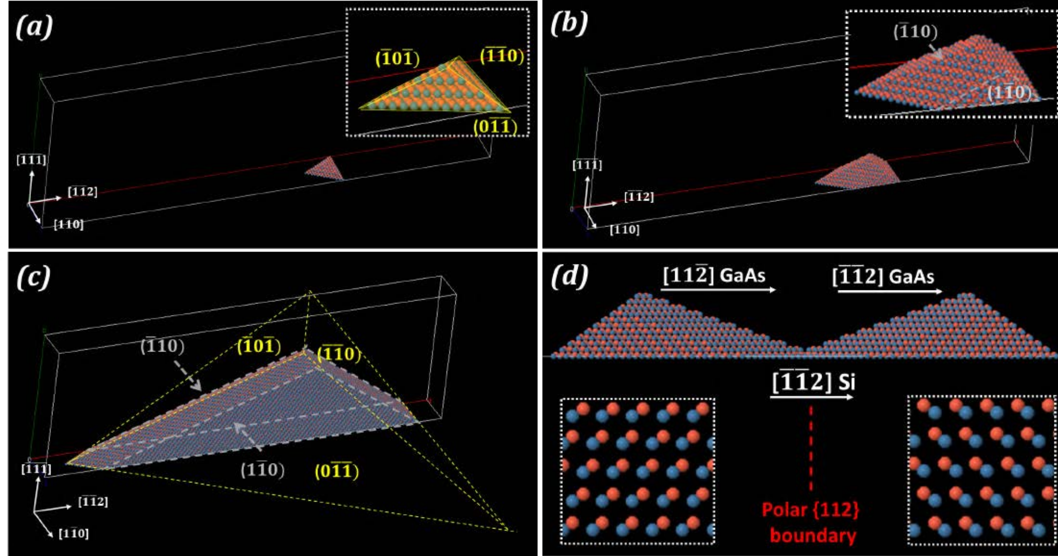

Figure 5.6: Schematics of nanomembrane growth. (a) A first tetrahedral nuclei formed by ($\bar{1}0\bar{1}$), ($\bar{1}\bar{1}0$) and ($0\bar{1}\bar{1}$) facets forms in the openings of the mask. (b) The tetrahedron expands until reaching the edges of the openings, where vertical ($1\bar{1}0$) and ($\bar{1}10$) side facets develop. (c) Nanomembrane keeps growing preserving the $\{110\}$ formed facets until the edge of the aperture. (d) If two nuclei grow with different crystal orientations arising from different parity in twinning, polar inversion domains might form.

facets, which have the lowest energy, as a consequence of the slit orientation. This fact eliminates the need of twin formation to reduce the free energy of the system, explaining as well the high twin density in SAG nanowires [205]. However, twin formation before the vertical facet formation can produce a 180 º in - plane rotation of the whole structure before a defect - free crystal growth regime is reached. In that regard, an even number of in - plane twinning events produces the NM crystal to match the substrate lattice. In contrast, when an odd number of twins are formed, the whole structure is 180 º in - plane rotated.

The two opposite orientations of the nanomembrane preserve the same defect - free single crystal regime, responsible of high optoelectronic response, as soon as there is a single nucleation event in the slit or multiple nuclei present same parity of twins. However, when two nuclei differ in parity within the same slit, a polar $\{112\}$ - like boundary appears (Figure 5.6d), deteriorating the optoelectronic behavior. The probability of having different twin parity nuclei increases exponentially with the number of nuclei per slit, making single nucleation in shorter slits essential for preserving high crystal quality.

Prior to atomic scale investigation of the crystal structure of the nanomembranes, an AlGaAs shell was deposited for passivation of the GaAs surface. The deposition

is carried out below the temperature for mask selectivity, which supposes a full coverage of the surface. Figure 5.7 shows an elemental compositional map where Al can be found on top of the SiO_2 mask. In addition, no elemental diffusion of Al or Si into the NM is appreciated upon the limits of detection. Interestingly, a $(\bar{1}\bar{1}\bar{1})$ top facet appears in the shell together with two small $\{113\}$ facets. These facets are commonly observed in homoepitaxial GaAs nanomembranes [154, 200].

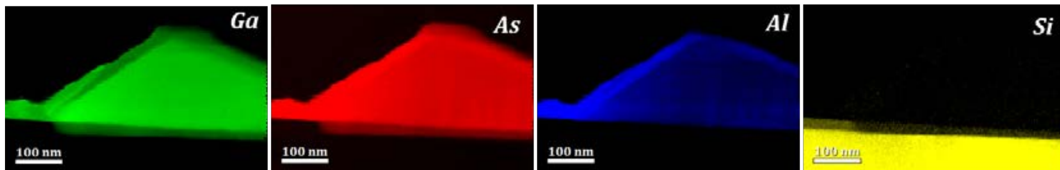

Figure 5.7: EELS elemental maps showing Ga, As, Al and Si areal distribution.

Figure 5.8 reveals the crystalline structure of a membrane with homogeneous morphology, which is attributed to a single nucleation event. The bulk of the nanomembrane is shown to be free of defects with pristine ZB phase. Direct dumbbell intensity analysis unambiguously determines As - polar growth, as expected for GaAs. Interestingly, two regions contain high density of rotational twins parallel to the interface; the first 52 nm of growth close to the substrate interface, and hence responsible of the in - plane final orientation of the nanomembrane according to their parity, and the last 25 nm on top of the membrane, matching with the AlGaAs shell thickness. Additionally, three out-of-plane stacking faults are found at the end of the long edge of the NM, which propagate from the twinned 'buffer' rather than the substrate itself. Thus, they are thought to originate from NM overgrowth rather than polynucleation. Nevertheless, their low density and the symmetry preservation across them makes their effects negligible on the overall nanomembrane behavior.

Another NM showing erratic morphology is studied in detail for crosschecking the effects of polynucleation in crystal structure (Figure 5.9). Several twins along various $\{111\}$ planes are observed, involving in - plane and out - of- plane rotations (which gets highlighted in the FFT). Looking at the structure from the base, it is clearly seen in Figure 5.9b that certain areas do not start with in - plane twinning while others do present a twinning 'buffer' similar to the one found for the mononucleated membrane of Figure 5.8. This change of structure arises from the multiple nuclei growing with different phases that merge forming inclined stacking faults. The different twinning directions in independent grains produce the morphology

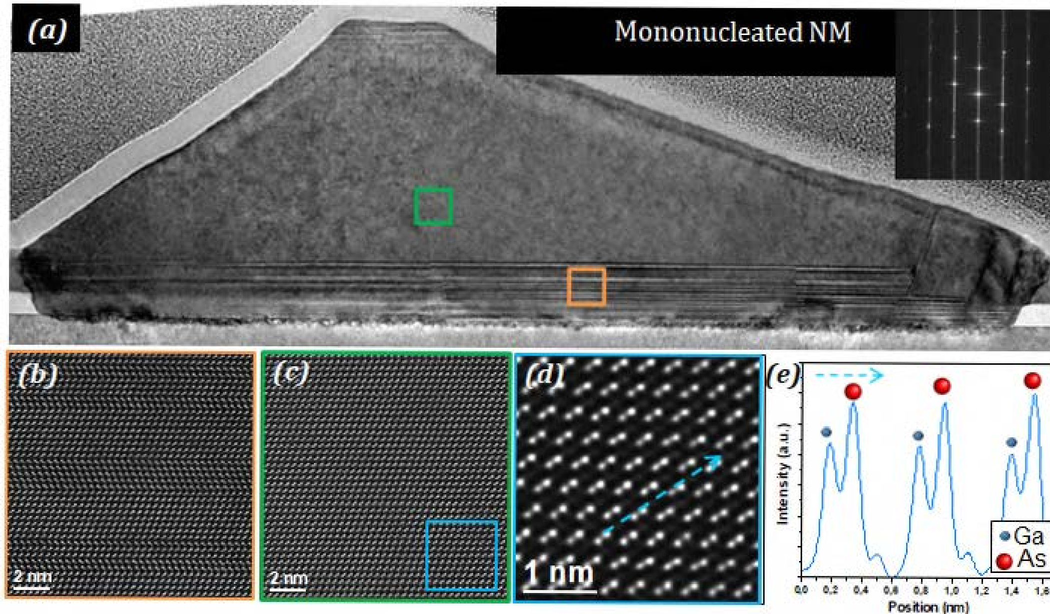

Figure 5.8: On a mononucleated NM: (a) Stacking of several HRTEM low - magnification micrographs revealing the overall defect distribution. The inset shows the FFT of the central NM region. (b) HAADF micrograph of the twinned area. (c) HAADF micrograph of the main defect-free NM body. (d) Zoom of (c) and (e) intensity profile across the arrow in (d) for polarity assignment.

variation observed in the short edge of the nanowire. In addition, the merging of differently twinned grains gives rise to complex defects (Figure 5.9c-e) that involve strain accumulation due to the lack of matching and in-plane polarity inversions. This is specially highlighted in the defect shown in Figure 5.9d, where two grains merge forming a boundary where A′ and A″-polar grains face each other (with ′ and ″ labelling in - plane polarities). This forms Ga - Ga bonds, as confirmed by the atomically resolved EELS mapping of Figure 5.9e.

In order to understand the strain relaxation mechanisms that release the lattice mismatch between Si and GaAs, GPA is applied to the high quality membrane, where a compressive layer of approximately 20 nm with an average GaAs compression of ≈1 % is observed. This value suggests partial strain release through the creation of dislocations, while elastic compression remains in the area surrounded by the 20 nm dielectric mask due to the spatial confinement it creates, precluding the GaAs lattice to fully relax. When the growth overcomes this confined area, the lattice is free to expand and relaxes elastically.

The optoelectronic response of the mononucleated and polynucleated membranes

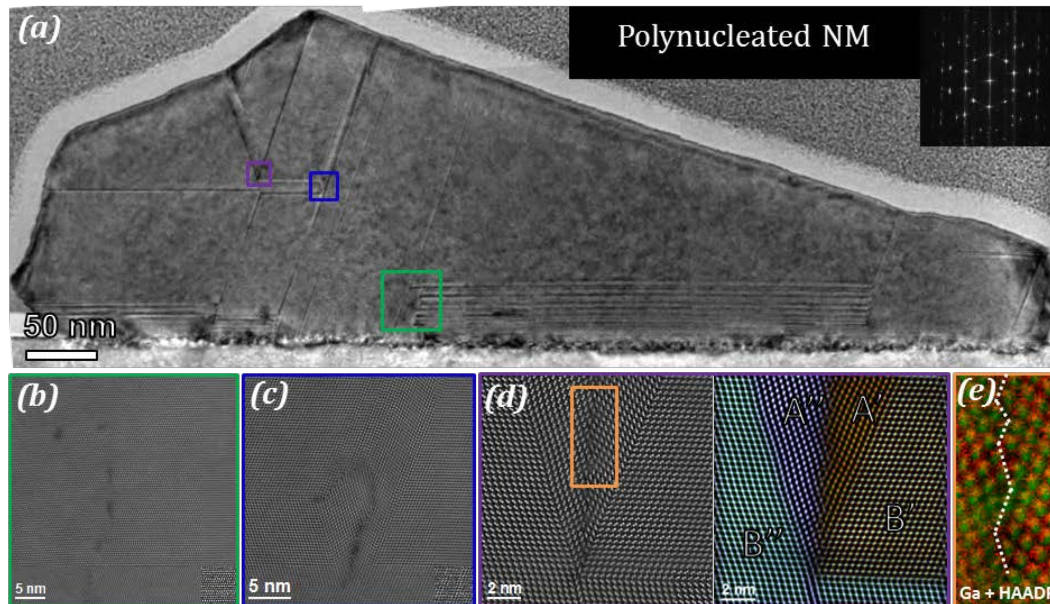

Figure 5.9: On a polynucleated NM: (a) Stacking of several HRTEM low - magnification micrographs revealing the overall defect distribution. The inset shows the FFT of the violet squared region. (b)-(d) HAADF-STEM micrographs of several defective areas, including twin-induced polarity reversals. (e) RGB composition including EELS Ga $L_{2,3}$ edge signal integration (red) and HAADF micrograph (green).

are investigated through CL spectroscopy. Tilted SEM micrographs of both NM, labelled as NM A for the mononucleated one and NM B for the polynucleation case, are shown in Figure 5.11a,b. The CL map obtained on the two NM area shown in Figure 5.11c displays a RGB composition of emission lines at 812(R), 817(G) and 827(B) nm wavelength. The emission of NM A is uniform along the whole structure, with emission centered at 812 nm which is slightly blue shifted compared to the band edge emission of GaAs, most probably caused due to the band filling effects arising from strong electron excitation during CL measurements [206]. In contrast, NM B exhibits two spatially resolved emission regions with lower intensity than NM A. One side of NM B emits at 817 nm and the other at 827 nm, both of them found to be below the band edge of GaAs. This is attributed to defect mediated mechanisms.

From the (S)TEM analyses displayed in Figure 5.9, a polar boundary is found nearby the kinked area of the NM. The right panels on Figure 5.11b show MAADF micrographs obtained in this area, revealing that the reach of the polar boundary covers half of nanomembrane height. Polar boundaries have been reported to act as potential barriers for carriers [10, 11]. Therefore, a polar boundary blocks the diffusion of excitons by creating two separated emission regions. In addition, polar boundaries can act as recombination centers, which results in a decrease in intensity

between the two NM regions [28]. The emission slightly redshifted with respect to GaAs band edge is attributed to the difference in twin defect densities. Twin defects create type II band junctions in the consecutively created WZ monodomains [26], as detailed in Chapter 3.

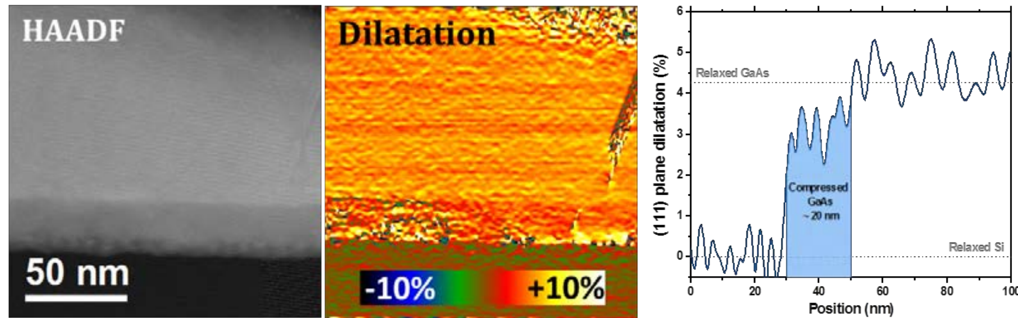

Figure 5.10: HAADF-STEM micrograph, dilatation of $(\bar{1}\bar{1}\bar{1})$ planes obtained through GPA and dilatation profile along the vertical direction.

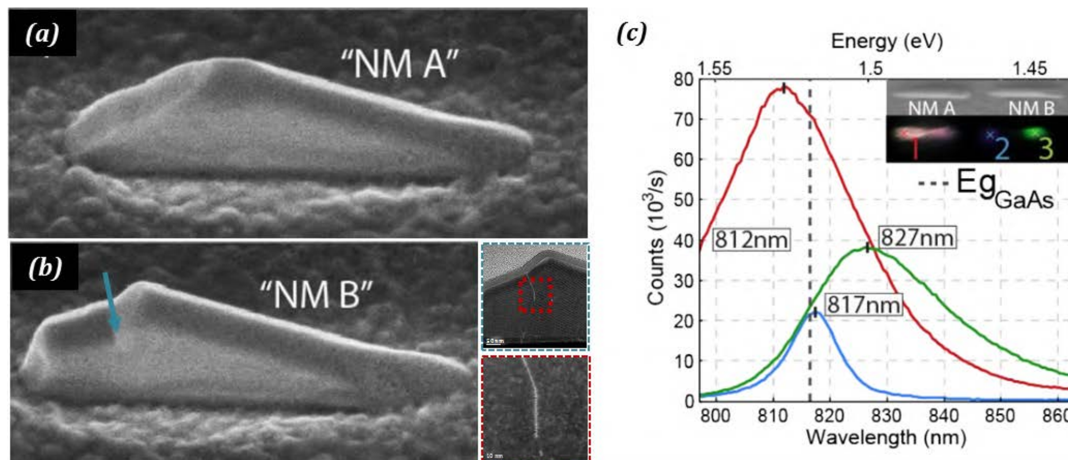

Figure 5.11: (a), (b) SEM tilted images of the area under investigation containing NM A (mononucleated) and NM B (polynucleated). The right panel shows two MAADF micrographs obtained in the kinked area (pointed with a blue arrow), in which the magnitude of the polar boundary is highlighted. (c) CL spectra at different positions of NM A and B. The inset shows a SEM top view together with a RGB color map of emission at 812 nm (R), 817 nm (G) and 827 nm (B).

5.2.2 GaAs NM on (001) Si

Due to the increasing interest of integrating nanosized structures into CMOS technologies, which are based on (001) oriented Si, GaAs nanomembranes are grown on Si(001) substrates. Apertures oriented along Si [110] direction are employed for NM growth following the optimal growth conditions employed in the previous section. In this case, the first nucleus is closed by four {110} - like planes (namely $(0\bar{1}\bar{1})$, $(10\bar{1})$,

$(01\bar{1})$ and $(\bar{1}0\bar{1})$) forming a pyramidal seed, as shown in Figure 5.12a. As material reaches the nucleus, it expands preserving the initial faceting until the edges of the aperture are reached and $(1\bar{1}0)$ and $(\bar{1}10)$ lateral facets are developed (Figure 5.12b) to bring the final highly symmetrical nanomembrane morphology (Figure 5.12c,d).

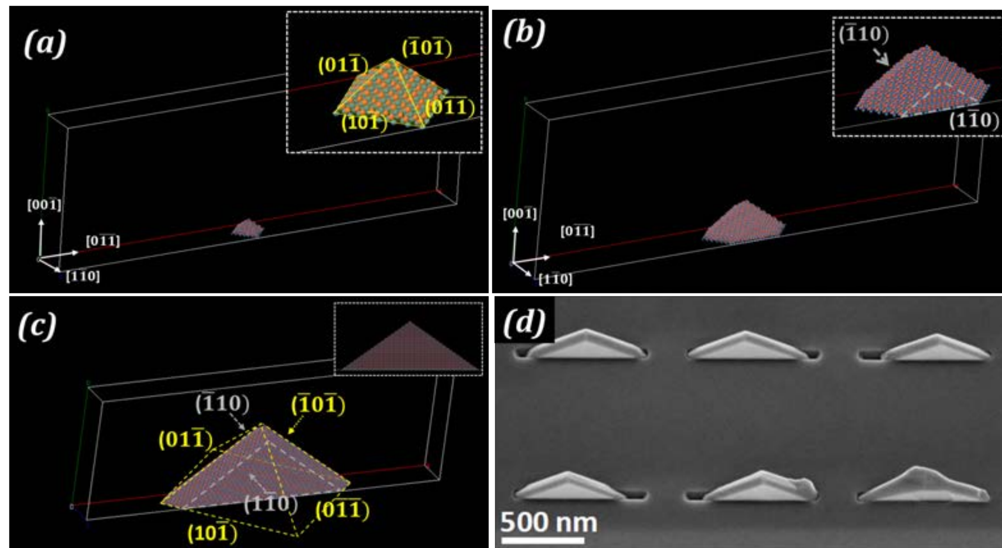

Figure 5.12: Schematics of NM growth on Si(001) substrates. (a) Pyramidal nucleus closed by $(0\bar{1}\bar{1})$, $(10\bar{1})$, $(01\bar{1})$ and $(\bar{1}0\bar{1})$ is formed. (b) The pyramid expands until reaching the lateral aperture sites and $(1\bar{1}0)$ and $(\bar{1}10)$ facets develop. (c) Growth continues by preserving large lateral facets due to the aperture constriction. (d) SEM micrograph showing NM final morphologies.

Figure 5.13 shows the structural arrangement of one standard (001) GaAs NM. A practically defect-free nanomembrane is achieved by this growth approach in what resembles a single nucleated nanomembrane. The buffer twinning observed in the (111) grown NMs is suppressed as no horizontal <111> direction is available. The patterned region observed at the bottom of the structure is instead a Moiré overlap between GaAs and Si lattices, as a pre-deposition etching process was applied and growth starts 50 nm below mask level. The only defect present in the nanomembrane is a stacking fault pointed by a blue arrow, which does not rotate or modify the overall crystalline arrangement at the edge. As discussed before, the appearance of these stacking faults is probably caused by imperfections in substrate surface, as the substrate itself acts as a spatial restriction for them.

In that regard, a lower density of defects is observed when growing on (001) substrates as the main horizontal twins are avoided by employing this crystal orientation and twinning-parity in multinucleated NMs does not suppose a drawback.

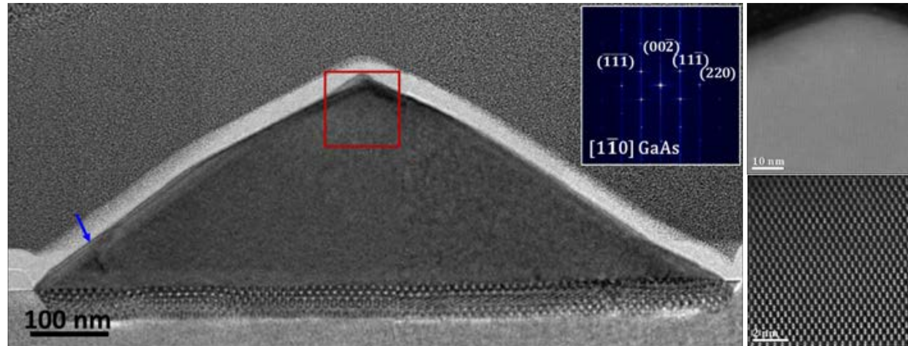

Figure 5.13: Low magnification HAADF micrograph showing a quasi defect-free nanomembrane grown on Si(001). Details on the atomic structure can be found in the right panels. A single SF defect is found at the very edge of the nanomembrane. The Moiré pattern observed at the bottom arises from overlapping of GaAs and Si from a silicon etching process applied in the mask apertures prior to the growth.

In this situation, however, the two-fold symmetry of the substrate is giving two possible orientations to the first pyramidal nuclei: with [110] or with [1$\bar{1}$0] direction of GaAs pointing to the long edge of the aperture. Meanwhile twinning density or parity could be controlled by optimization of the growing parameters to end up suppressing polynucleation problems in (111)NM, control over preferential crystal orientation of GaAs nuclei seems unavoidable in the case of (001)NM. If two nuclei grow in the same aperture presenting [110] and [1$\bar{1}$0] orientations parallel to the long aperture axis, respectively, the formation of an antiphase boundary when both nuclei merge will occur, as schematized in Figure 5.14.

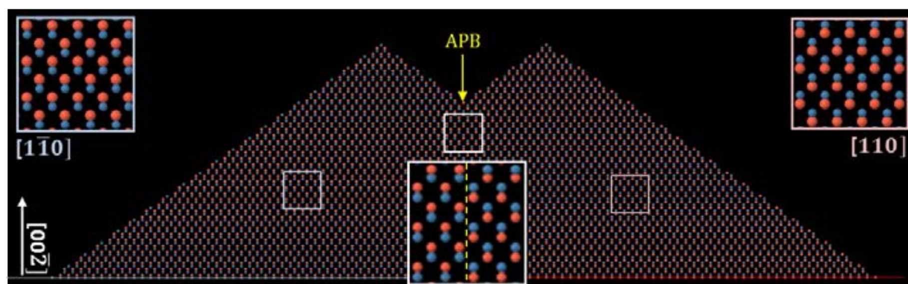

Figure 5.14: Schematics and atomic arrangement of a nanomembrane with two differently oriented nucleation events. A {220} antiphase boundary is formed at the junction between both independently grown NMs within the same slit.

We found experimentally that under properly optimized growth conditions the appearance of nanomembranes containing APBs is minimal, and given the lack of control over seed orientation this is an indicator that the single nucleation event regime is dominating the growth. However, some NMs presenting the characteristic ”*M*” shape of polynucleation are found in coexistence with the defect-free ones. Figure 5.15 shows the structure of one of such NMs.

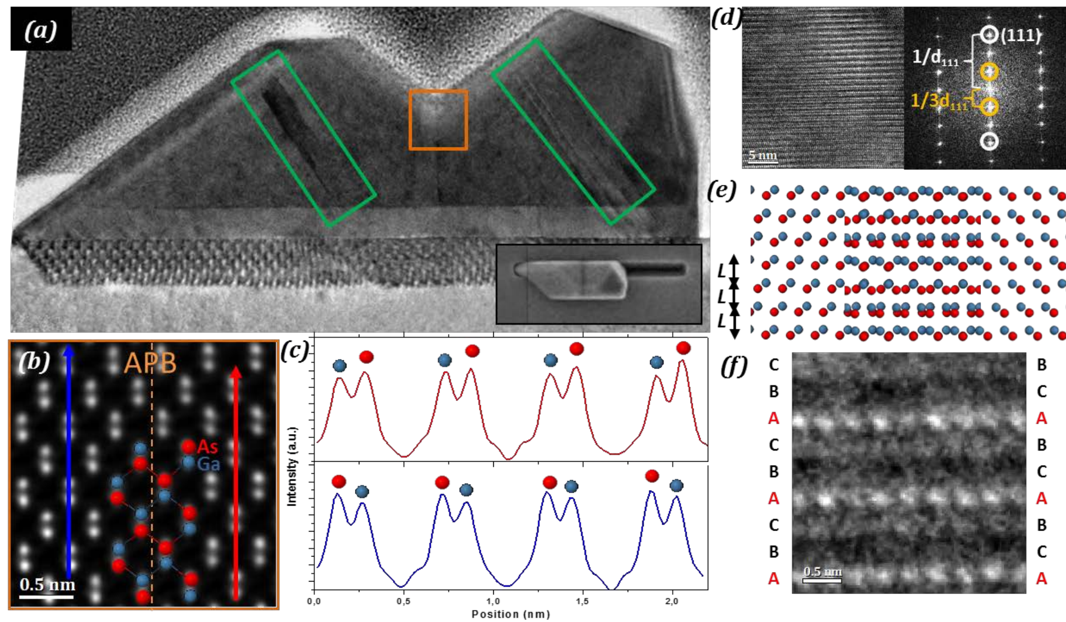

Figure 5.15: (a) Low magnification HRTEM micrograph of a "*M*" shaped (001) GaAs nanomembrane. (b) HAADF micrograph obtained on the orange squared region revealing an APB. Atomic identification has been obtained through an intensity analysis as shown in the profiles in (c). (d) Rotated HRTEM micrograph of the green squared areas and its corresponding power spectrum where a $3d_{111}$ periodicity is observed. (e) Schematics of atomic overlapping of twinned regions. (f) Detailed zooming of (d) with labels on atomic stacking of twinned regions at both sides, which provide matching every 3 (111) planes giving the triple periodicity.

The main features of crystal structure reveal two similarly oriented membranes that get joint forming a vertical defect (Figure 5.15a). When observing in detail the atomic arrangement at the center by aberration corrected HAADF (Figure 5.15b) and performing an intensity analysis for atomic identification (Figure 5.15c), an APB can be found. The high energetic cost of APB formation can explain also the lateral overgrowth of the nanomembrane shown in the inset of Figure 5.15a. As the APB starts to develop, twinning occurs in the inclined $(1\bar{1}\bar{1})$ and $(\bar{1}\bar{1}\bar{1})$ planes for $[1\bar{1}0]$ and [110] oriented nuclei, respectively, and growth direction switches to expand the nanomembrane laterally by decreasing the APB surface of vertical growth. Even though the presence of these twinning events is 'invisible' through this NM projection through TEM (as the twinning planes are not parallel to the electron beam), the effects of the switching of crystal direction can be observed in Figure 5.15d, which shows a higher magnification of the lattice fringes observed in the green squared regions of the HRTEM micrograph (notice that the micrograph is rotated with respect to Figure 5.15a). The appearance of diffraction spots at a triple periodicity than d_{111} planes is a sign of twinning in depth of the studied area, as reported by Kaiser *et*

al. early in 1999 [207]. This effect can be easily explained by the ABCABC stacking of ZB structure. A twinning event changes the stacking to ACBACB, so the overlap of both structures presents a period of $3d_{111}$. This situation is visualized in Figure 5.15e,f.

Due to the low Z contrast of Ga (Z= 31) and As (Z = 33), a deeper analysis of the APB found in the middle of the "*M*" -shaped NM can be performed by means of Geometric Phase Analysis (Figure 5.16). GPA applied to GaAs(002) planes allows to obtain a phase map where a phase shift of π rad is measured across the boundary, as expected for APBs [208]. However, compared with the simulated situation, where the shift takes place sharply at the boundary, we observe a gradual transition shift from 0 to π rad in the experimental case that comprises a spatial region of approximately 1.5 nm. In this region, the contrast in dumbbell intensity is highly reduced. This is an indicator that the APB does not take place at a single {220} plane, but it presents a certain thickness comprising seven atomic planes.

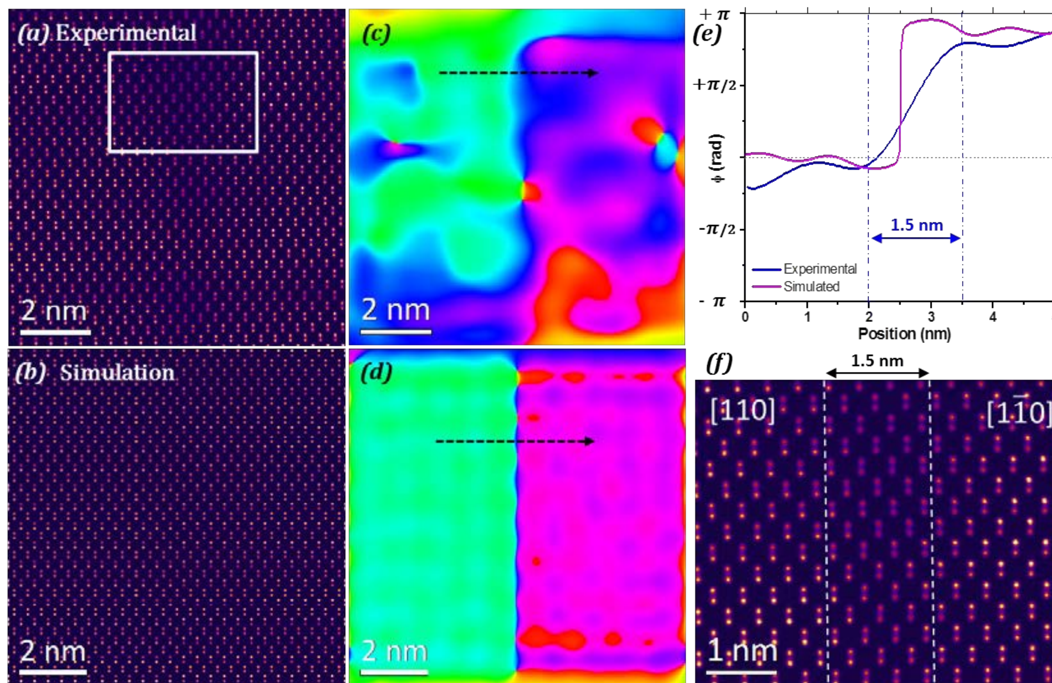

Figure 5.16: (a),(b) Colored HAADF micrograph of the {220} APB for experimental and simulated cases, respectively. (c),(d) Phase maps of (002) planes of (a) and (b), respectively. (e) Phase profile taken along the arrows in (c) and (d) showing a π rad phase shift across the APB. The shift occurs gradually in 1.5 nm for the experimental case. (f) Details of the squared region in (a) indicating the gradual shift in intensity across 1.5 nm.

5.3 GaAs NMs as templates for the directional growth of NWs

One of the main issues regarding nanowire implementation in technologies relies in connecting the 1D - branches of nanowires. This is of special interest for the development of Majorana fermion- based quantum technologies, where defect - free unidimensional branches of high spin - orbit coupling strength and high g-factor semiconductors are needed. This fact makes InAs and InSb nanowires ideal candidates as a basis of topological quantum computing schemes.

For Majorana fermion applications, coherent transport should be kept across the nanowire intersections in the quantum networks. During the last years, these interface-free junctions have been achieved through directioning growth of gold-catalyzed VLS nanowires in two different <111>B directions [209–213] or even tilting growth of VLS nanowires through defect engineering [212]. Even though the in-situ creation of junctions is achieved, the drawbacks in free-standing nanostructure manipulation for device production remain present through this approach, as the junctions should be transferred to separate substrates, limiting scalability and reproducibility. A different growth approach appeals then more suitable for nanowire production.

Due to the exceptional crystal quality of GaAs nanomembranes and the patternability of substrates employed, they are perfect candidates as templates for further nanowire growth in a gold - free VS strategy. As a first approach, homoepitaxy of GaAs NMs on GaAs (111) substrates appeal as better candidates for NM template production, as previous works demonstrated fully twin - free structures [154, 205]. In addition, two {113} GaAs facets appear during first stages of growth in the homoepitaxial case before the nanomembrane evolves to the final shape enclosed by the five {110} planes. The intersection of these {113} facets produces a long edge parallel to the substrate that can be employed to direct the growth of InAs (Figure 5.17a,b). With this aim, patterned Y - shaped mask openings along three-folded <11$\bar{2}$> directions on GaAs ($\bar{1}\bar{1}\bar{1}$)B substrates provide a perfect platform containing triple junctions for further growth of InAs on top, forming horizontal - like nanowires (Figure 5.17c,d).

Figure 5.18 shows an overview of the system crystallography and composition

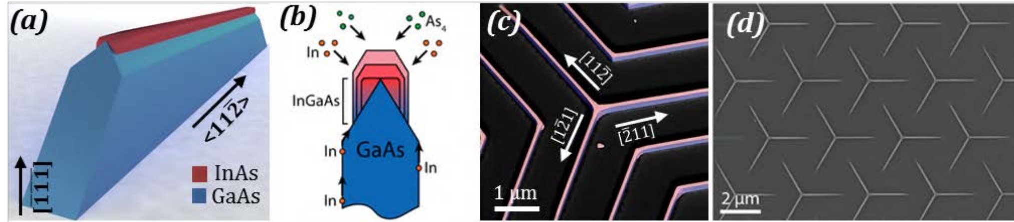

Figure 5.17: Schematics of NWs on NMs. (a) Model of a single NW(InAs)/NM(GaAs) structure. (b) Diagram showing NW growth progression. (c) Colored 30º tilted SEM image taken with an energy-selective back scattered electron detector for Z - contrast. (d) SEM top view of branched NW structures in an array. [200]

observed through transversal [11$\bar{2}$] direction. This projection of the system reveals the GaAs NM template to present (01$\bar{1}$) and (0$\bar{1}$1) facets together with the ($\bar{1}$1$\bar{3}$) and ($\bar{1}\bar{3}$1) inclined facets typically appearing in uncompleted NM growth. This faceting is preserved in the InAs deposition on top of the template where an extra ($\bar{1}\bar{1}\bar{1}$) flat top facet is appearing. The appearance of this facet as major feature instead of the two {113} facets can be explained by the higher As_4 fluxes employed for the InAs growth [214]. Regarding the heterostructure elemental distribution, core - loss EELS mapping was performed to obtain compositional information employing signals of Ga $L_{2,3}$, In $M_{4,5}$ and As $L_{2,3}$ edges. Figure 5.18c reveals the relative elemental composition in atomic percentage of the the whole system. Meanwhile the NM body is composed by pure GaAs, a gradual composition switch is observed in the top NW. InGaAs alloying is found at the lateral sides of the base of the nanowire at the first $\approx$ 20 nm, as confirmed by the presence of Ga until the NM pinch level is reached. After it, pure InAs composition is observed forming a unidimensional InAs nanowire aligned parallel to the substrate at the very top of the structure.

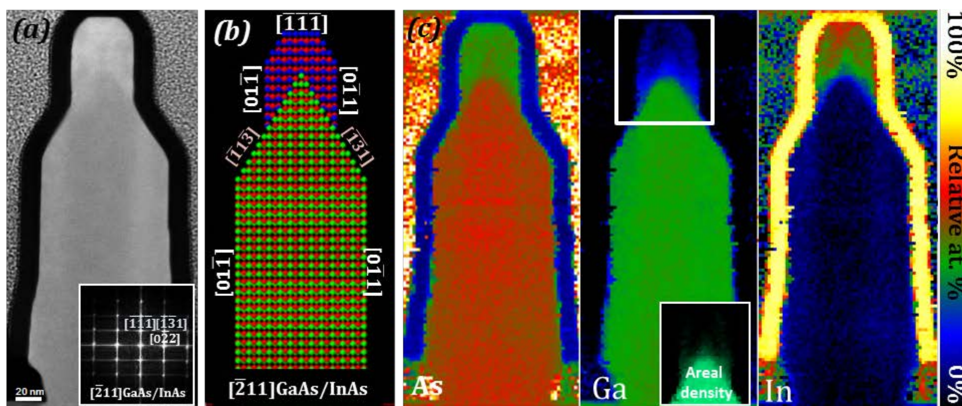

Figure 5.18: On a FIB cross section of a nanomembrane (a) HAADF - STEM image of the NW/NM system. The inset shows the indexed FFT of micrographs obtained on top of the structure. (b) Atomic model with labelling of the system faceting. (c) Relative atomic composition (at. %) obtained through STEM-EELS. The inset in Ga relative at. % shows the areal density of Ga on the NW. [200]

Apart of getting a pure InAs composition on top, the presence of dislocations at the interface or residual strain in the lattice can be detrimental for quantum purposes: in the first case, misfit dislocations act as charge trapping and recombination centers and the second because strain is responsible of electronic band modulation. Geometric Phase Analysis applied to atomically resolved micrographs can be exploited to obtain some insights on these features. The GaAs NM has been employed as a reference known lattice, as bulk GaAs lattice constant is expected after more than 200 nm of homoepitaxial GaAs growth. The relative variation of InAs plane spacing can be therefore calculated from GaAs known values. Figure 5.19a shows the values of the strain matrix tensor components. Dislocations, if present, should be visible in ε_{yy} mapping, as it reflects the distortions of the main planes interacting between the NM and the NW. However, a smooth defect-free transition is observed, confirming the absence of misfit dislocations. This means that the 7.2 % lattice mismatch is relaxed by the introduction of an elastic distortion in the InAs lattice that gradually shifts to InAs bulk lattice value. Actually, this gradual shift is clearly observable to take place isotropically in ε_{xx} and ε_{yy} maps. This is happening due to the reduced dimensions of the InAs NW that do not accumulate enough elastic energy for dislocation formation. In addition, the presence of In(Ga)As at the lateral sides of the NW reduces the lattice misadjustment, favoring elastic relaxation. However, when analyzing InAs compression values (Figure 5.19b) we can observe how InAs does not get fully relaxed. This modifies the overall electronic properties of InAs nanowire such as a decrease of the band gap and conductivity [215].

Simulations on strain relaxation of the system were performed using nextnano^3 software by replicating the system geometry and dimensions and minimizing elastic energy. A GaAs substrate was included at the base of the simulation for relaxing the system. Figures 5.19c,d show the calculated ε_{hydro} and the elastic energy density, respectively, on top of the heterostructure. A -2.4 % compression is found on top of the nanowire, in agreement with the experimental results, confirming that the system geometry does not allow to release all strain elastically and thus, accumulating elastic energy. It is interesting to notice that the major compression and elastic energy accumulation takes place at the edges of the nanowire base. This suggests that the detected Ga in these areas (Figure 5.18c) segregates as the presence of In(Ga)As compound in these areas supposes a lower mismatch, and thus, lower elastic energy

accumulation. This strain - mediated mechanism has been observed in other InGaAs heterostructures [156, 216].

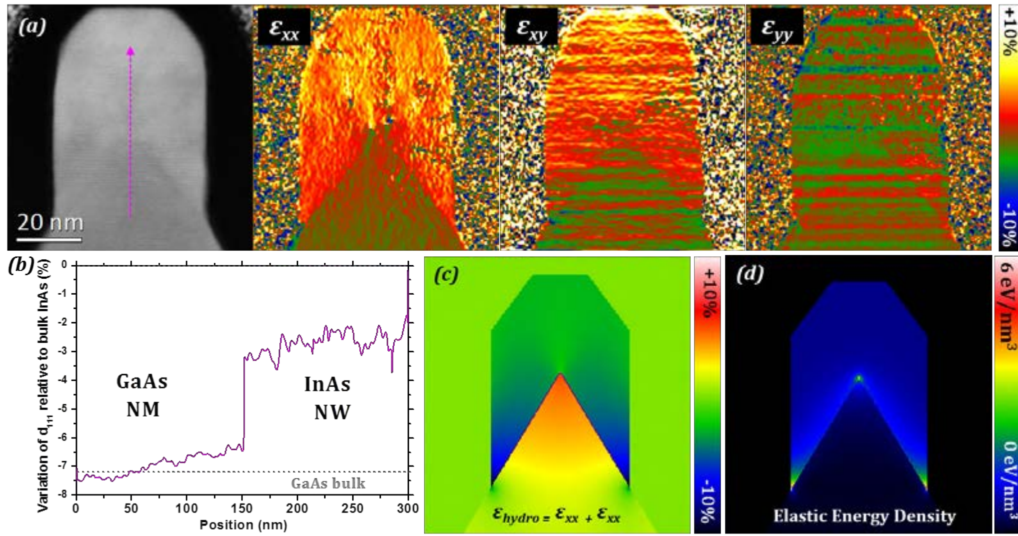

Figure 5.19: (a) HAADF-STEM micrograph of the top of the NW/NM heterostructure and the strain tensor components (ε_{xx}, ε_{yy} and ε_{xy} obtained through GPA employing GaAs as reference lattice. (b) Variation in d_{111} spacing with respect to bulk InAs d_{111} along the line indicated in (a) obtained through GPA. (c) ε_{hydro} calculated with nextnano^3. A - 2.4 % compression is measured on top of the nanowire in agreement with the GPA data. (d) Elastic energy density calculated with nextnano^3.

As [$\bar{2}$11] zone axis is insensitive to twinning defects, a longitudinal lamella was also examined in order to get a deeper detail on defect density. In this regard, examining the lamella longitudinally through the orthogonal [01$\bar{1}$] zone axis allows {111} twinning and stacking fault visualization. Figure 5.20a shows a HAADF micrograph where GaAs NM base and InAs NW top are comprised. In addition, the lateral projection includes an overlapping area between InAs and GaAs lattices, which is produced between the bottom of the nanowire and the nanomembrane pinch. A oblique ($\bar{1}\bar{1}$1) stacking fault originating at the InAs/GaAs interface can be observed in the InAs nanowire while the GaAs nanomembrane remains completely defect - free. The density of these type of defects in InAs NW is, however, quite low (< 10 SF / μm) . Rotational maps of oblique ($\bar{1}\bar{1}$1) planes obtained through GPA applied to this micrograph (Figure 5.20b) reveal as well the presence of misfit dislocations. The reduced lateral dimensions preclude dislocation formation in the transversal section, but the length of the longitudinal direction makes the elastic energy excess relieve with dislocation formation. A dislocation density of 100 dislocations / μm is measured.

In the overall, the high crystalline quality of nanomembranes allows to employ

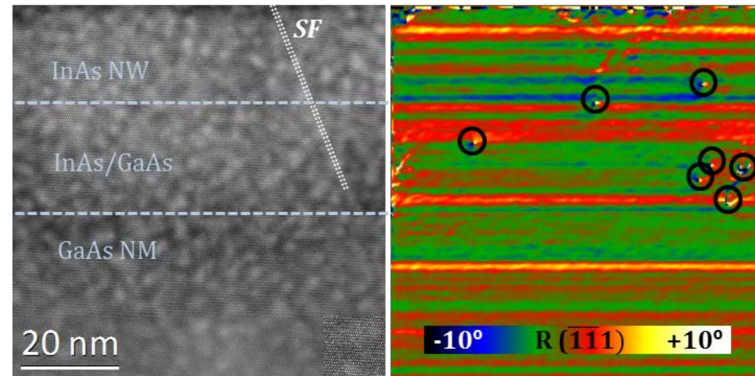

Figure 5.20: HAADF - STEM micrograph obtained on a longitudinal cross-section lamella and the corresponding rotation of $(\bar{1}\bar{1}1)$ planes obtained through GPA. Black circles indicate the presence of a misfit dislocation.

them as templates providing a directional growth of unidimensional InAs, something required for topological quantum computing applications. However, the system geometry still supposes some limitations. Firstly, strain-mediated Ga incorporation into the nanowire modifies the nanowire behavior, so it should be taken into account as the effective InAs NW volume is reduced. Secondly, InAs is shown not to fully relax the strain. Even though the creation of misfit dislocations observed in the longitudinal section partially reduces the energy accumulation, the lattice is not able to fully relax due to geometrical constrictions. Also, these misfit dislocations that ineffectively relax epitaxial strain can be responsible of trapping charge and induce conductance hysteresis, which will be further detailed in the next section. For that reason, other strategies should be considered that allow more freedom in geometry and specially in strain engineering, as the enhanced interface surface in horizontal configurations clearly affects the overall system performance.

5.4 InAs NW networks: strain engineering towards defect-free systems

Due to the limitations in lattice engineering of GaAs NMs as templates for the further growth of nanowires, a different approach consists in growing the NWs directly on top of the substrate. In this configuration, the surface interaction between the template and the nanowire has a strong impact on the morphology of the NW section grown inside the template limits. In addition, the mask confinement affects the relaxation of the top grown material. This is of extreme relevance for the overall material

electronic behavior, as the field effect conductance of the system is highly susceptible to the crystal quality of the material, as we demonstrate in this section. For instance, we already showed in Figure 5.4 that the lattice mismatch between substrate and nanowire gets released by the creation of dislocations along all the nanowire length interface for InAs grown on top of InP (111) substrate, which present a 3.24 % lattice mismatch between them. Other typical substrates include GaAs, which presents an even higher lattice mismatch of 7.24 % with InAs. For that reason, strain engineering by the deposition of different intermediate layers is of extreme importance to reduce lattice mismatch between them, and thus, facilitate strain accomodation to enhance the electrical conductance and carrier mobility of the InAs nanowire channel (Table 5.1).

5.4.1 Effects of buffering nanowire networks

Semi-insulating substrates that become fully insulating at low temperatures are required for as-grown device fabrication. In that regard, InP and GaAs are the most typically employed substrates, which present a 3.24 and 7.25 % lattice mismatch with respect to InAs, respectively. However, even employing InP as substrate the formation of misfit dislocations seems unavoidable due to the lateral confinement imposed by the mask. Even though the defects appearing far from the top NW surface are not so critically affecting the topological regime, getting completely defect-free NWs is of extreme importance for optimal device performance. For that reason, layered structures with different composition could help preventing plastic deformations in the nanowires. We focus on NW devices grown on (001) oriented substrates which allow to obtain more symmetric NW structures in comparison with (111) ones (Figure 5.4).

TABLE 5.1: Lattice constants and associated mismatches of typical semi-insulating substrates employed for SAG InAs NW growth.

	InAs	InP	GaAs	$GaAs_{1-x}Sb_x$	$In_xGa_{1-x}As$
a (Å)	6.06	5.87	5.65	$5.65 + 0.44 \cdot x$	$5.65 + 0.41 \cdot x$
ε (%)	0	3.24	7.25	$-0.49 < \varepsilon < 7.24$	$0 < \varepsilon < 7.24$

As a first approach towards dislocation-free NWs, the implementation of a buffer layer prior to NW growth can help the top NW to relax elastically by providing a

decrease in lattice mismatch at the same time as overcoming the mask confinement, which provides freedom of lateral expansion to the nanowire crystal. The incorporation of Sb into GaAs forming a ternary $GaAs_{1-x}Sb_x$ compound can be used as buffer layer before NW growth due to the surfactant effect of Sb promoting 2D growth. GaSb presents a lattice constant of 6.09 Å, presenting a slight -0.49 % mismatch with InAs (Table 5.1). However, the low energy gap of GaSb (0.75 eV) might add new conduction channels, so very high Sb concentrations might led to the loss of device performance. In this regard, GaAs(Sb) was incorporated as a prior buffer layer to the growth of NWs with low Sb concentrations, as revealed in Figure 5.21a, to exploit the surfactant properties of Sb. In a second step, InAs NW is grown selectively on top of the buffer layer (Figure 5.21b) in high crystal symmetry directions.

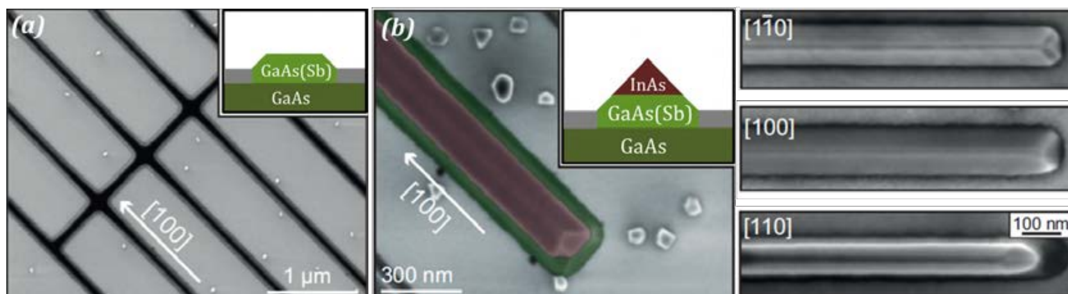

Figure 5.21: (a) SEM top view of selectively grown GaAs(Sb) buffer layer within the mask openings on a GaAs(001) substrate. Surface roughness with a RMS of 3 Å is achieved. (b) Colored top view of InAs NW selectively grown on the buffer. If growth time increases, InAs NW expands laterally. The right micrographs show the final top view morphology of NWs grown in [1$\bar{1}$0], [100] and [110] high symmetry substrate directions.

EELS and EDX measurements show just a 2 at.% Sb incorporation, even though the calibrated flux ratios predict a 7 %. Previous reports agree with the difficulty of Sb incorporation into GaAs [217, 218]. However, even though this small fraction does not have significant effects on mismatch damping (ε ($GaAs_{.98}Sb_{.02}$) = 6.9 %), the low surface energy of Sb makes it act as a surfactant, which promotes a planar 2D growth contrary to vertical nanowire development [219]. This supposes a flat and smooth surface overcoming the mask height with a roughness root mean square (RMS) of just 3 Å. This fact promotes an elastic relaxation allowing NW lattice to expand laterally by suppressing the spatial confinement imposed by the mask, as seen in Figure 5.22.

Transversal FIB lamellae prepared on the three directions of the buffered nanowires are examined for strain relaxation evaluation. Similarly to what is observed in the case of (111) substrates (Figure 5.4), we observe directional dependent faceting mainly

driven by growth kinetics and thermodynamic factors. In that regard, we have a direct observation of the nonequivalent <110> nanowires due to the different growth rates of (111) planes according to their polarity reflected as a different NW morphology. GPA applied to low magnification atomically resolved micrographs is employed for strain evaluation (Figure 5.22a-c). Dilatation maps crosschecked in two independent directions reveal similar behavior in three directions: a + 6.2 % average lattice expansion is measured in the NW bulk when employing the GaAs substrate as reference. Compared with the 7.25 % mismatch between InAs and GaAs, some residual $\approx$ 1 % strain remains in the InAs lattice. For evaluation of the mechanisms relaxing the 6.2 % measured lattice variation, rotational maps applied to oblique planes reveal plane rotations of different sign at both lateral edges of the NWs in the three directions examined, reaching up to $\pm$ 5 º. This rotation is intrinsically appearing as an elastic mechanism for releasing strain accumulation when the nanosized epitaxied structure is able to expand laterally, as sketched in Figure 5.22e. This fact is also reflected in the slight lateral overgrowth observed in the overview cross-sections. In that regard, the observation of rotation is already a sign of elastic relaxation, further confirmed by the simulations shown in Figure 5.22d. This mechanism was not observed in the non-buffered NWs shown in Figure 5.4, where relaxation is fully plastic for lower mismatched InP substrates (ε = 3.24 %).

Even though this strategy enhances the elastic relaxation contribution, some misfit dislocations are still present in the central part of the NW (Figure 5.22f) where the structure is not able to expand. This fact explains the benefits of incorporation of Sb. Despite the release in lattice mismatch is not achieved due to the few Sb incorporation into the buffer, Sb facilitates planar growth of the buffer into a smooth surface that overcomes the mask height. This platform can be then employed for the growth of NWs in highly mismatched substrates (GaAs) due to the increase of the spatial degree of freedom of the top lattice to expand, achieving even better results than in the case of employing low mismatched ones (InP).

Electrical measurements are carried out in a four-probe method in the NWs in order to test the benefits of the addition of the buffer in NW functionalization. The contacts are deposited on top of NWs as shown in the colored SEM micrograph of Figure 5.23a. The conductance (G) of reference non-buffered NWs as a function of

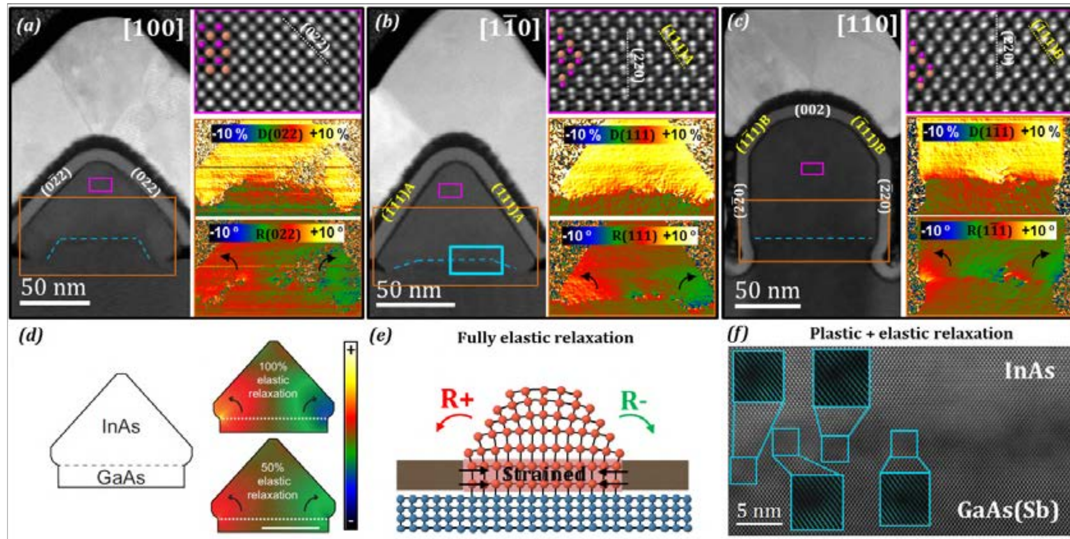

Figure 5.22: (a)-(c) Cross-section HAADF-STEM micrographs with details on faceting, atomic structure and GPA dilatation and rotation maps of buffered InAs NWs oriented along [100] , [1$\bar{1}$0] and [110] directions, respectively, on a GaAs(001) substrate. (d) Simulation of GPA rotational map on a [100]-oriented buffered NW showing rotation as an elastic relaxation mechanism. (e) Atomistic schematics of the origin of rotation as a lattice expansion on top of the constraining mask. (f) Details of the GaAs(Sb) - InAs interface of (b) showing some misfit dislocations in the center of the NW and absence of them close to the nanowire corner.

the gate voltage V_g is shown in Figure 5.23b. There are two characteristic gate voltage regions presenting different conductance slopes. The carriers are firstly depleted in the top part of the NW, while the carrier density moves towards the NW-substrate interface when applying more negative voltage, as schematized in the insets of the plot. This region of more negative V_g provides then qualitative evaluation of the crystal quality of the interfaces. When performing the same measurement on the buffered NWs (Figure 5.23c) a considerably increased conductance is measured. This is attributed to the lower presence of misfit dislocations at the interface. In Figure 5.23d a comparison of NW conductivity in gate voltage sweeps (down and up) is displayed. Highly hysterical behavior is observed due to the charge trapping effect of misfit dislocations at the interface. However, the hysteresis is highly reduced for buffered nanowires due to the enhanced interface quality achieved by the reduction of plastic deformations.

It is essential to achieve high mobilities in InAs transport channels, specially when employing these systems for topological quantum computing devices. The field effect mobility can be extracted from the conductance measurements by fitting

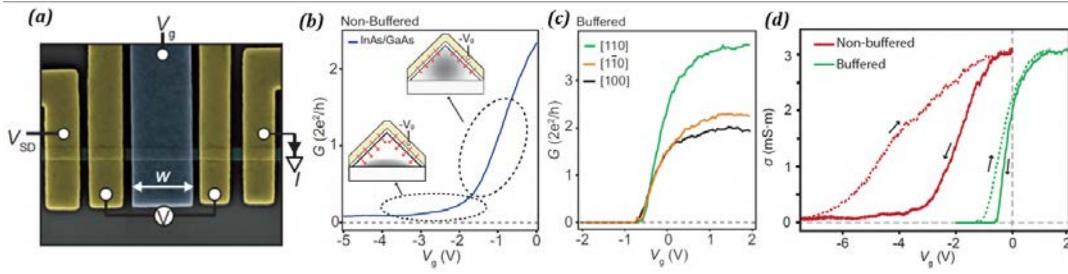

Figure 5.23: Electronic response of NWs. (a) Colored SEM micrograph showing a top-gated device for four-probe measurements on SAG NWs with deposited Au contacts. (b) Conductance (G) as a function of gate voltage (V_g) in non-buffered InAs/GaAs NWs. (c) G as a function of V_g for InAs/GaAs(Sb)/GaAs NWs. (d) Comparison of NW hysteresis in conductivity when sweeping up and down V_g in buffered and non-buffered InAs SAG NWs.

the following equation [220]:

$$G(V_g) = \left(R_s + \frac{L^2}{\mu C(V_g - V_{th})}\right)^{-1} \tag{5.1}$$

where W is the gate width, V_{th} is the gate voltage, R_S is the probe resistance, G is the measured conductance, C is the dielectric capacitance and V_g the applied gate voltage. The employed capacitance is obtained from simulations using the finite element method in the electrostatic module in COMSOL Multiphysics inputting the geometrical parameters extracted from TEM cross-sections and SEM top views. High mobility is measured in buffered NWs, with an average value of $\bar{\mu}\sim$5600 $cm^2/(V \cdot s)$, when measuring several buffered devices. It is clear that the buffer layer improves the transport characteristics of devices, but there are some remaining dislocation events in the interface between GaAs(Sb) buffer and InAs NW that should be overcome.

5.4.2 Addition of ternary $In_xGa_{1-x}As$ intermediate compounds

The next step towards defect-free nanowires and optimization the field effect mobility is adding an intermediate ternary compound with composition $In_xGa_{1-x}As$ between the GaAs(Sb) buffer and the InAs channel. Following Vegard's law (Eq. 1.2), the ternary compound supposes an intermediate lattice constant that can reduce the total amount of accumulated strain, and thus, reduce the presence of misfit dislocations. Figure 5.24 shows NWs grown with the presence of an intermediate ternary compound while preserving a pure InAs channel of about 50 nm thickness.

The areal density map obtained by STEM-EELS shows the elemental distribution of In and Ga cations within the nanostructure. EDX measurements in the ternary compound area reveal an $In_{0.24}Ga_{0.76}As$ average composition, which agrees with the low HAADF contrast observed between the GaAs substrate and this layer. By applying Vegard's law the lattice constant of this compound is calculated to be 5.75 Å, which supposes a much smooth transition from the buffer layer to the SAG grown structure by a reduction of mismatch to 1.81 % (Figure 5.24d).

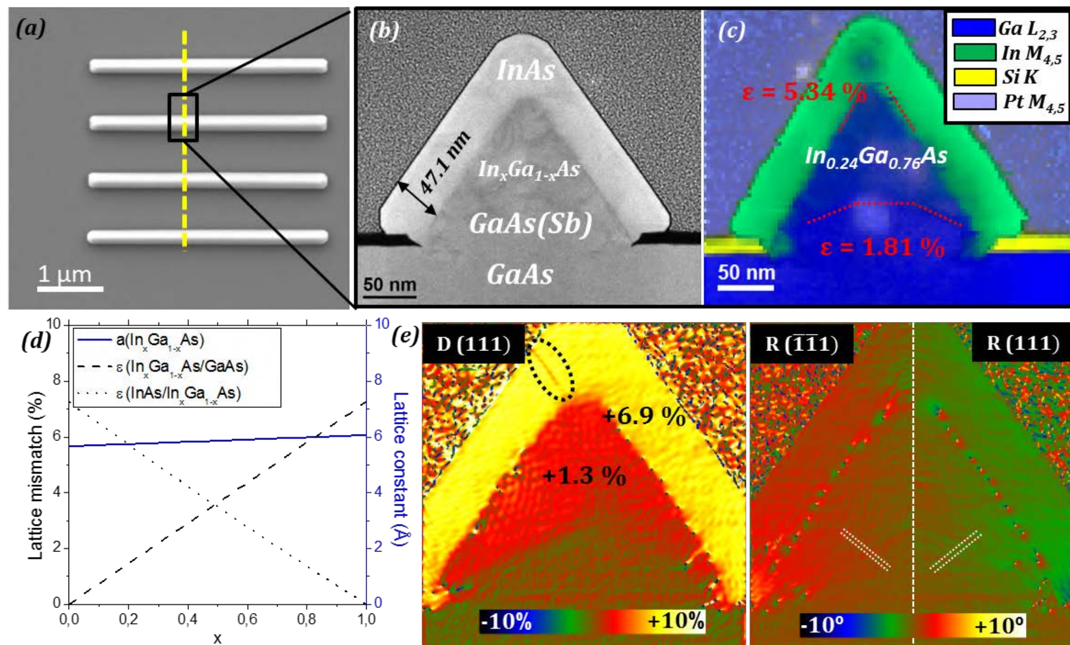

Figure 5.24: (a) SEM top view of [1$\bar{1}$0] NWs with a dashed line indicating the FIB cut direction.(b) HAADF-STEM micrograph and (c) areal density EELS compositional maps of a InAs/InGaAs/GaAs(Sb)/GaAs(001) nanowire grown along [1$\bar{1}$0] direction. (b) Lattice constant and lattice mismatch of $In_xGa_{1-x}As$ with GaAs and InAs interfaces as a function of the In content (x). (e) GPA dilatation and rotation maps applied to {111} planes.

The mismatch between InAs and the InGaAs is also affected by the presence of the intermediate layer. It is calculated to be 5.34 %, which is a great reduction compared with the previous samples into study, in which the lattice expansion between the InAs and the buffer layer is found to be 6.9 %. GPA is applied in order to examine how this intermediate compound affects to the strain relaxation, as in the methodology employed in the former section. The dilatation map shown in Figure 5.24e shows lower average dilatation values than the ones expected according to the measured composition (1.3 vs 1.8 % in the case of the InGaAs and 6.9 % vs 7.2 % in the case of the InAs). This fact suggests that the structures are not fully relaxed and preserve a certain residual compressive strain. In addition, we observe a stacking fault arising from the InGaAs-InAs interface where there is a more abrupt transition

in lattice constant.

More information about defect formation can be extracted from rotational maps. (111) and ($\bar{1}\bar{1}1$) planes are employed for examining left and right sides of the NW, respectively. Whether the transition between the buffer GaAs(Sb) and the InGaAs preserves a smooth transition with no dislocations present in the central part of the NW, improving the crystal quality of simply buffered NWs, there is a set of periodically placed misfit dislocations in the InAs-InGaAs interface due to the abrupt change in composition. In that regard, higher In contents in the intermediate layer are needed to reduce hysteresis and enhance field effect conductivity, which in this case it gets reduced to 4663 $cm^2/ (V \cdot s)$, much lower than that measured for simply buffered nanowires. This fact highlights that the dislocations in contact with the InAs channel are those mainly influencing the electrical performance of the nanowires.

With this purpose the next step is modifying the $In_xGa_{1-x}As$ composition to a x fraction of 0.9 and the nominal thickness of InAs is reduced to approximately 25 nm, which facilitates elastic relaxation of strain, preserving the presence of a buffer GaAs(Sb). However, the composition of the intermediate layer can be influenced by the growth temperature, as higher temperatures might promote In desorption. On the contrary, low growth temperatures are detrimental for the selectivity in the mask windows. The growth temperature of InGaAs has been modified in an interval of 522-538 ^{o}C in order to find optimal conditions guaranteeing low In desorption and high selectivity. Figure 5.25 shows an EELS-based compositional analysis performed on InAs/$In_xGa_{1-x}As$/GaAs(Sb)/GaAs [010] NWs grown at different temperatures. From the SEM micrographs we can see how selectivity gets enhanced when increasing temperature and no mask deposition is taking place at high temperature samples. In comparison, low temperature samples present several deposited clusters on top of the SiO_x mask, specially for samples grown below 529 ^{o}C. Turning out to investigate the In:Ga ratio within the InGaAs transition region, we observe that In incorporation is lower than the nominal 9:1 ratio for all the growth temperatures and pure InAs is just achieved in the outermost 5 nm of the growth. Interestingly, we find elemental segregation taking place for all the growth temperatures in which In incorporation is lower at the corners of the nanowires; following [00$\bar{1}$] top and <1$\bar{1}$0> lateral directions, which is presumably attributed to a strain mediated mechanism as observed in InAs NW/GaAs NM systems (Section 5.3). Profiles obtained

following the lateral edge [$\bar{1}$01] direction allow to have a visual overview of the abruptness of composition variations across the structure. Similar tendency is found for all the samples, however the compositional change is more abrupt for high temperature samples: the x fraction variation changes from 0.55 to 0.78 across the edge of the nanowire. In addition, In incorporation is significantly decreased for higher temperatures. Contrary, despite the poor selectivity of the lowest temperature sample, an average In content of 80 % is achieved together with a high homogeneity in composition across the volume of the nanowire.

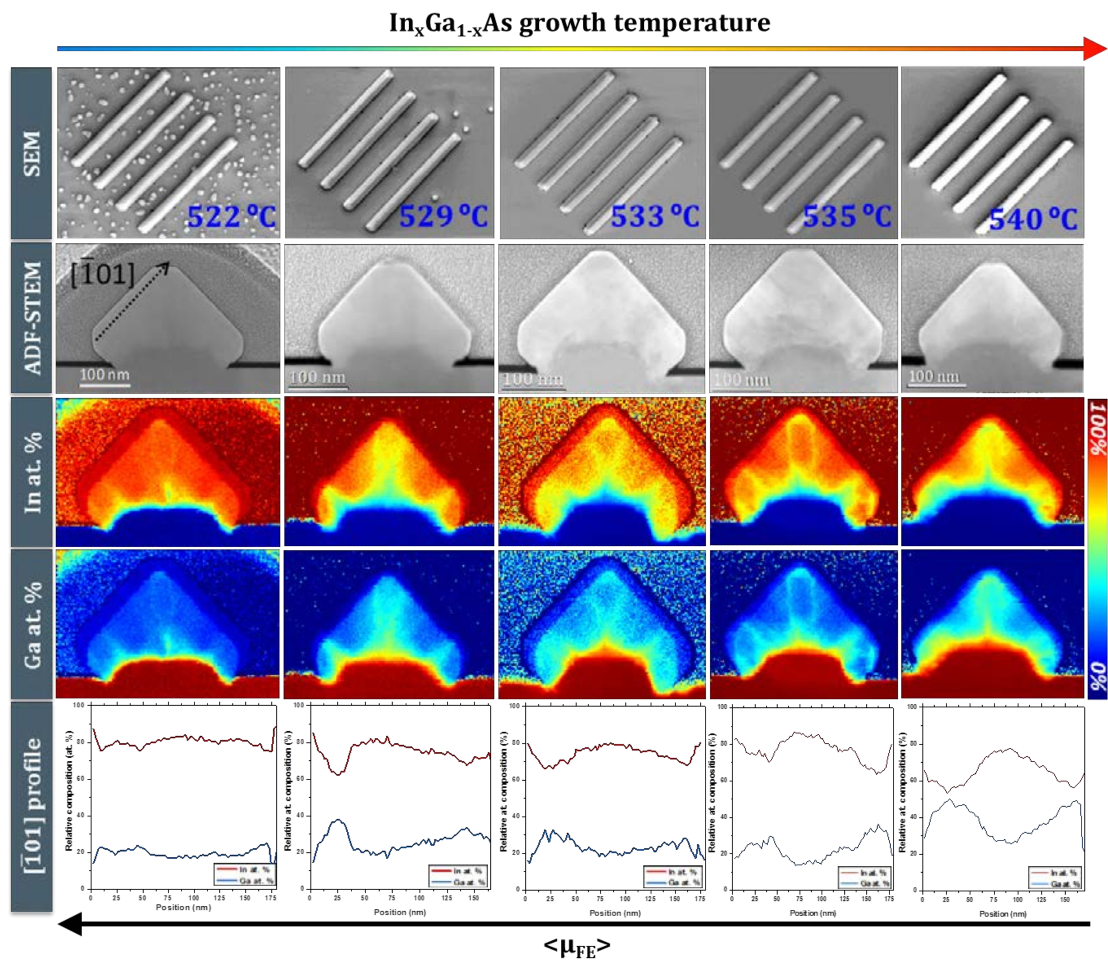

Figure 5.25: SEM top view images, ADF micrographs showing the NW cross sections, EELS-based relative composition of In and Ga (at. %) and composition profiles obtained along [$\bar{1}$01] direction of [010] NW arrays grown at temperatures ranging from 522 to 538 °C.

Transport measurements were performed in the samples with device configurations similar to the ones described for previous designed nanowires. Values on hysteresis in G(V_g) curves, measured saturated currents and fitted field effect mobilities with same approach described through Eq. 5.1 are used as quantification values for testing the device quality. The values of this measurements are displayed in Table

5.2, where the lowest temperature sample is not displayed due to the poor selectivity of the growth. The measured values of hysteresis and FE-mobility for high growth temperatures are similar to the ones obtained for low In content InGaAs buffer shown before. This indicates the low In incorporation at higher temperatures. However, greater enhancement in electric performance is achieved for lower temperatures, with values overcoming those of single buffered NWs where the InAs volume is much higher.

TABLE 5.2: Comparison of electric properties of InAs/InGaAs(T)/GaAs(Sb)/GaAs NWs with the InGaAs second buffer grown at different temperatures.

Temperature (°C)	Hysteresis (V)	Saturated current (μA)	FE-Mobility (cm^2 /V s)
540	1.011	9.1	4666.7
535	0.938	9.6	5488.2
533	0.940	10.9	6015.5
529	0.958	12.4	6899.3

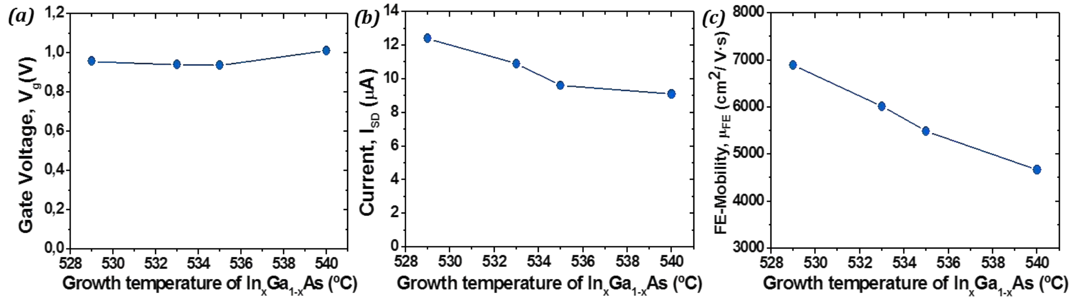

Figure 5.26: Electric transport measurements at different growth temperatures. (a) Measured hysteresis in G(V_g) sweep down-up loops, (b) saturated current and (c) extracted field effect mobility as a function of InGaAs growth temperature.

The tendency of enhancement of electric characteristics when decreasing InGaAs buffer growth temperature is visualized in Figure 5.26. We observe lower hysteresis at low temperature samples, which can be directly related with the presence of charge carrier traps at the InAs/InGaAs interface caused by the abruptness of compositional variation across the $In_xGa_{1-x}As$ layer producing sudden changes of lattice constant that are not able to sustain strain. In order to test this fact, GPA rotational maps are obtained on NWs grown at exactly the same conditions along [110] direction. Figure 5.27 reveals how there is no much change in the number of dislocations created at the interface between the buffer GaAs(Sb) and InGaAs for growth at different temperatures. However, the uniformity in composition achieved at low temperatures provides a strong decrease in dislocations close to the InAs channel. In the case of high temperature grown NWs, several dislocations appear close to

the conduction channel, which is responsible of both an enhanced hysteresis and reduced mobility, deteriorating then the transport properties of the nanowire. In addition, higher saturated currents are achieved for lower temperature samples, which implies lower NW resistance.

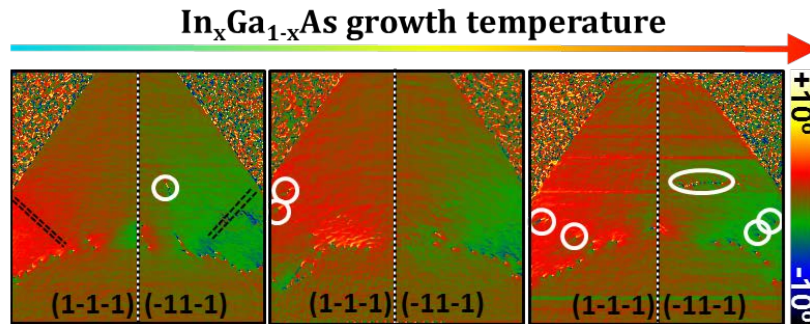

Figure 5.27: Rotation maps of {111} planes obtained at both sides of the NWs with InGaAs grown at increasing temperatures. The presence of misfit dislocations close to the InAs channel is marked with white circles.

The addition of intermediate ternary compounds can be very beneficial for enhancing electronic properties of NWs, but the effectiveness of them clearly relays in an optimization of the growth conditions. Completely defect-free NWs have not been achieved so far, so further strain design must be provided for achieving better results. An option would be combining the two studied types of NWs with intermediate ternary compounds. Nanowires with a ternary compound of $In_{0.24}Ga_{0.76}As$ shown in Figure 5.24 effectively achieve a defect-free interface between GaAs(Sb) and InGaAs, although the quality of InGaAs/InAs interface is very defective. Contrary, NWs with a ternary compound of $In_{0.80}Ga_{0.20}As$ grown at low temperature present a defect-free interface between InGaAs and InAs while a huge concentration of misfit dislocations is found at the GaAs(Sb)/InGaAs interface. A solution might be then growing InAs/$In_{0.80}Ga_{0.20}As$/$In_{0.24}Ga_{0.76}As$/GaAs(Sb)/GaAs NWs combining both strategies.

5.4.3 Optimization of In incorporation into the InAs channel

Keeping on with the previous growth conditions optimization, it could be observed that the composition in the outermost part of the nanowire is not constant. Instead of a purely InAs channel with a nominal thickness of 25 nm, the apparition of two different layers can be observed. Pure InAs could be achieved just at the outermost 5 nm of the NW (which we refer as outer InAs). Contrary, a inner layer of 20 nm

thickness with composition $In_{0.9}Ga_{0.1}As$ (which we refer as inner InAs) acts as a third buffer prior to the InAs channel. The spontaneous formation of these differentiated layers suggests that the InAs growth temperature should be also optimized to reduce the incorporation of Ga on it.

Due to the In desorption phenomena observed previously at high temperatures, the strategy for enhancing In incorporation relays on a decrease on the growth temperature of the channel. For this study, the InGaAs buffer has been grown at 529ºC, which provided the best compromise between homogeneous In incorporation into the buffer and proper selectivity conditions. Figure 5.28 shows similar analyses to those performed for the buffer layer temperature optimization, but for different InAs growth temperatures between 585 ºC and 524 ºC in this case.

Simple visual contrast in In/Ga compositional maps already highlights that the segregation into two different InAs layers is strongly reduced when decreasing the InAs growth temperature. This goes accompanied with the fading of the top (002) facet, while no effects are observed within the InGaAs buffer. Better quantification of the effectiveness of In incorporation can be found in Figure 5.29a, where the measured x fraction of the $In_xGa_{1-x}As$ compound is plotted for three different NW regions: the inner and outer InAs and the InGaAs buffer. Although the elemental segregation is still present in the samples for all temperatures, the averaged composition across this area is independent of the InAs growth temperature. In addition, as in the previously studied samples, the composition in the outer InAs layer is purely InAs within the 1 % error of the measurement, although the averaged measured value is slightly higher for 503 and 485 ºC. The most noticeable difference is found in the inner InAs region. The composition of it is varying from a 90 to a 95 % of In (relative to Ga) when switching from the highest to the lowest growth temperature. This goes accompanied with a more uniform composition where both layers get merged to a gradual compositional transition. This phenomena is, again, arising from lower In desorption at low temperatures, although decreasing more the temperature might lead to poor selectivity.

GPA mean dilatation maps obtained in the NWs allow to calculate the relative lattice constant variation of the inner InAs with respect to the known GaAs reference. We find the average dilatation in this area varies from a 6.2 to a 6.6 % from the

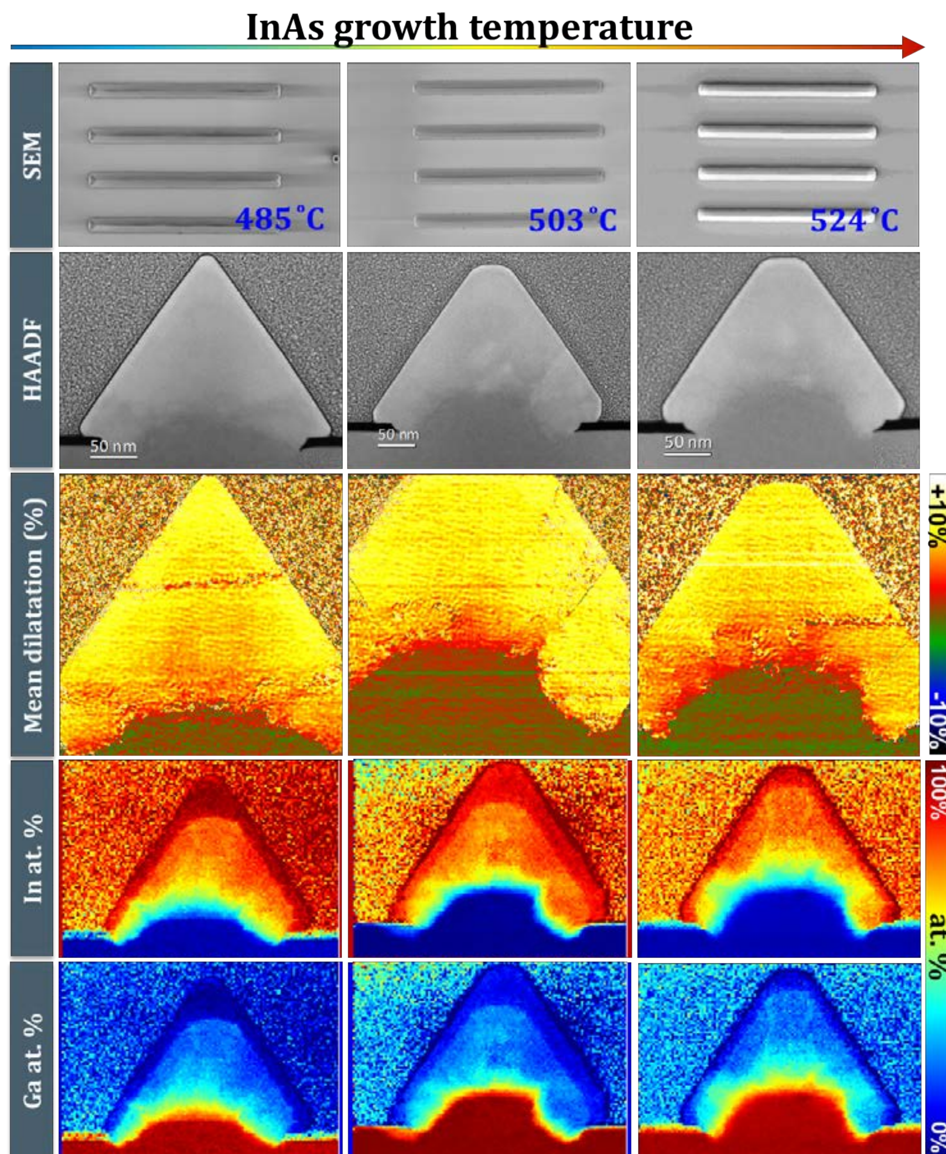

Figure 5.28: Top SEM images, HAADF micrographs, GPA mean dilatation maps with respect to the GaAs(Sb) buffer and EELS-based In and Ga relative at. % maps obtained on NWs with different InAs growth temperatures.

high to the low InAs temperature NW, respectively. This variation is attributed to the higher In content in the low temperature NW. However, when calculated the predicted lattice spacing through Vegard's law we can find that the values overestimate the measured ones for all the cases (Figure 5.29c). This indicates that the InAs lattice does not fully relax, while some compressive strain below 0.5 % remains within the inner InAs channel.

These studies reveal how proper optimization can result in thicker effective InAs channels as the split into two different composition areas gets attenuated when shifted to lower growth temperatures. In addition, the higher In content closer to an

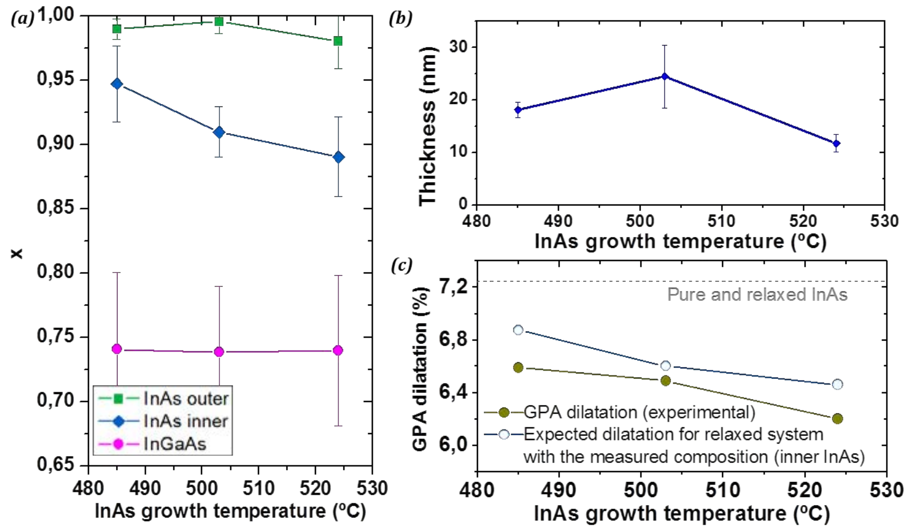

Figure 5.29: Tendency of NW parameters as a function of the InAs growth temperature. (a) x fraction of $In_xGa_{1-x}As$ in the ternary InGaAs buffer, the inner and the outer part of the InAs channel. (b) Thickness of the InAs channel (inner+outer). (c) Measured GPA mean dilatation in the region of the inner InAs together with the expected values derived from the measured composition on this layer.

InAs ideal scenario predicts enhanced electrical performance for NWs whose InAs channel is grown at 485 ºC.

5.5 High mobility InSb NW networks

The growth of InSb NW arrays is of special interest due to its large g-factor, which allows further semiconductor-superconductor 1D coupled systems to enter in the topological regime with relatively small magnetic fields (more details on hybrid epitaxy of semiconductor-superconductor compounds are given in Chapter 6). However, most of the built networks so far relay on single [60] or small scale [213] networks. SAG offers a great alternative to overcome scalability problems, as stated before. Unfortunately, in contrast with InAs and GaAs grown structures, the selectivity conditions for SAG of InSb by MBE do not overlap with preferred nucleation conditions [74, 221]. In order to decouple nucleation and selective growth, Metal-Sown SAG can be employed in a three step process [75] which involves a selective metal sowing (In supply), providing an InSb nucleation layer by supplying only Sb flux to convert In droplets in InSb networks and finally homoepitaxy of InSb on top of the nucleation layer. Figure 5.30 shows SEM tilted view of InSb deposition in conventional SAG, which involves either poor nucleation or poor selectivity depending

on the growth temperature and Metal-Sown SAG InSb.

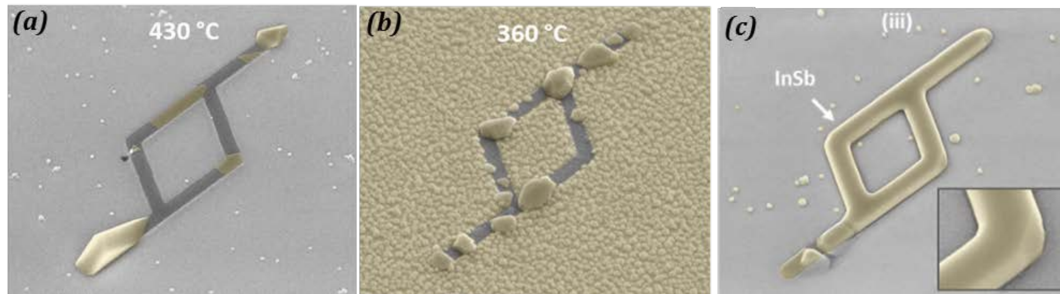

Figure 5.30: Colored SEM tilted images of SAG of InSb on InP(111)B using (a) conventional SAG at T=430 ºC where poor InSb nucleation is observed, (b) conventional SAG at T=360 ºC where no selectivity in the mask opening is achieved and (c) Metal-Sown SAG at T=430ºC where quasi uniform InSb is selectively grown in the mask opening, arising from enhanced nucleation in comparison with (a). [75]

Following the Metal-Sown strategy, InSb NW systems with same configuration as those in Figure 5.30 along either <112> or <110> directions on InP(111) substrates. The lattice mismatch between InP and InSb is +10.4 %, so the presence of a high density of defects at the NW-substrate interface is expected. We start by evaluating the NW system grown along <110> directions as shown in Figure 5.31. By applying geometric phase analysis to oblique planes ($1\bar{1}\bar{1}$), simultaneous evaluation of strain and presence of defects can be obtained. The average measured dilatation of planes with respect to the InP substrate ones is found to be of +10.2 $\pm$ 0.3 %, which is compatible with the expected for a fully relaxed system. The relaxation takes place directly at the interface of the NW by the creation of an array of periodic dislocations with higher density than in the case of InAs/InP case due to the higher lattice constant of InSb compared to InAs. Regarding the apparition of planar defects, we clearly observe in the rotation map the creation of a stacking fault in the left side of the nanowire. When taking a close look into the defect (Figure 5.31d), we observe the presence of twin boundaries parallel to the substrate in the vicinity of the stacking fault, probably appearing from multiple nuclei during first stages of the growth. The effects of these planar defects do not suppose a critical situation in transport properties deterioration. Actually, after performing transport measurements as the ones for strain engineered InAs NWs, the extracted mobilities after fitting Eq. 5.1 range from 10000 to 25000 cm^2 / (V $\cdot$) depending on the nanowires. Despite the high density of defects at the interface, being much higher even than the raw InAs NWs, outstanding electric transport properties of InSb make these bare wires overcome all casuistics of engineered InAs NWs.

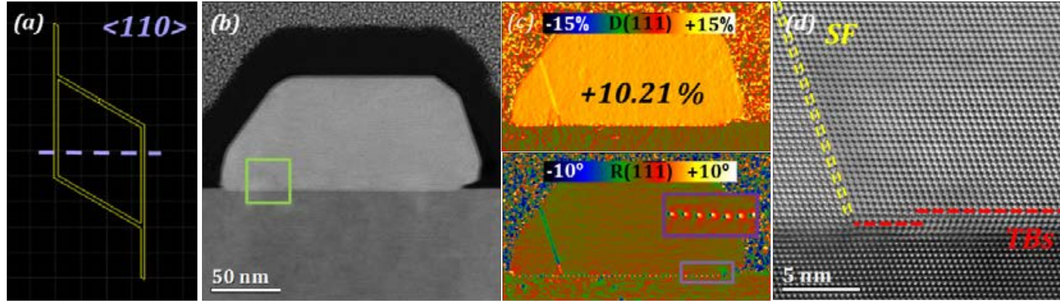

Figure 5.31: (a) Schematics of <110> InSb NW configuration with indication of cross-section position. (b) HAADF overview of NW cross section. (c) Dilatation and rotation of oblique $(1\bar{1}\bar{1})$ planes. (d) Zoom of the squared area in (b) with labels of stacking fault and twin boundary planar defects. [75]

However, the formation of multiple growth fronts can get critical when occurring in the longitudinal direction of the nanowire. Figure 5.32 shows the longitudinal cross section of a similar configuration to that of <110> NWs, this time grown along <112> directions. A 40 nm height step can be observed in the region coincident with the junction of two <112> directions. When taking a close look on it (Figure 5.32c-e), we can observe a complex defect configuration at this area. A single twinning event is taking place in the middle branch of the nanowire and prologues through all its depth. This fact indicates that the growth is not fully layered but at some point layered growth takes place independently in the different branches of the structure to end up merging together to form the final crystal. However, the 180 º rotation produced by the twin in the central branch has detrimental consequences for NW crystal quality. Merging this section with the examined longitudinal wire results in the creation of quasi planar polar boundaries that follow {112} planes. Particularly, the symmetry of the ZB crystal creates a cation polar boundary on the left side of the junction (In-In bonds) and an anion polar boundary (Sb-Sb bonds) on the right side. The dumbbell orientation is indicated in the micrograph by arrows that point the projection of the dipole direction.

The effects of polar boundaries in the electric transport of binary semiconductors were previously studied by de la Mata *et al.* in GaAs [10, 11]. Figure 5.32f shows the conductance of polar (red) and non-polar (blue) twin boundaries in GaAs with respect to pristine GaAs (black) calculated following the Landauer theory. When non-polar defects such as ortho-twins occur, the effect in conductance is quite smooth. However, polar defects as para-twins are detrimental for NW conductance. This is induced by the potential barriers that such configuration creates. Simulations on

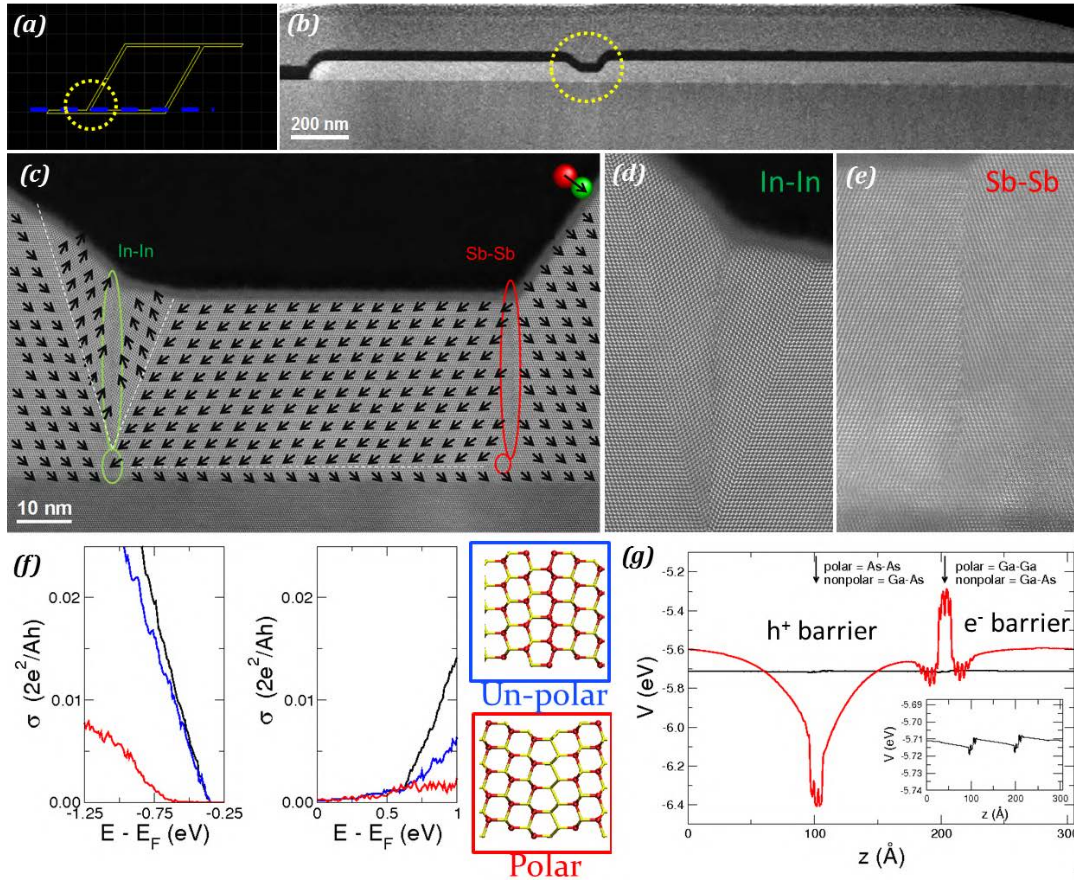

Figure 5.32: (a) Schematics of <112> InSb NW configuration with indication of the cross-section position. (b) HAADF overview of the NW cross-section. (c) Close look into the NW junction circled in (a),(b). Arrows mark Sb→In dumbbell direction and white dashed lines indicate twin boundaries. (d),(e) Details of In-In and Sb-Sb <112> cation and anion boundaries, respectively. (f) DFT calculation of the effects of twinning in conductance of GaAs for an ortho-twin (non-polar) and para-twin (polar) in comparison with pristine GaAs. (g) Potential barriers created in anion-anion and cation-cation polar boundaries in twin-like configurations. [10, 11]

the potential barriers of ZB segments presenting an As-As polar boundary and a Ga-Ga polar boundary are calculated and shown in Figure 5.32g. Even though the strength of the barriers is believed to be different for the {112} polar defects found in InSb NWs due to the lower angle of the boundary and the different ionicity of the compound, similar effects are believed to occur. Further quantification of the barrier strength at atomic scale can be performed by using electron holography or other novel microscopy techniques such as Differential Phase Contrast (DPC), but this study relays beyond the thesis objectives and will be explored in future works.

5.6 Conclusions

In this chapter, we have instigated the benefits of growing nanosized semiconductors in a selective area growth approach. Growing them into predesigned patterns opens the possibility of overcoming the main limitation in exploiting the benefits of nanotechnology: the integration into nowadays technologies. We have studied several strategies to achieve 1D-like semiconductor networks, which have a strong potential to become the basis for the development of topological quantum computing devices. In addition, we have evaluated the difficulties that can arise when following the same strategies on Si substrates for the creation of CMOS compatible devices. Even though SAG was employed as a growth strategy already at the end of the previous century, several physical limitations to achieve high crystal quality and homogeneous systems have slowed down the development of standard procedures for the exploitation of the technique.

The first limitation for the growth of these structures is finding growth conditions that ensure selectivity into the mask apertures with no parasitic deposition. While there is an open window which guarantees both conditions for certain materials such as GaAs or InAs, in the case of InSb other strategies need to be developed. In addition, there is a directional dependence for the growth of nanostructures. Growth rates and surface energies are dependent on the crystallographic planes, so opening slits in the substrate mask out of preferential growth directions (usually low order crystal directions) leads to inhomogeneities in the nanostructure morphology or even to the absence of growth. For this reason, designed networks have some geometrical limitations, contrary to post-grown designed systems. Once upcoming the design limitations and optimal growth condition problems, homogeneous and highly reproducible systems can be obtained. In this situation, the substrate-nanostructure hydrostatic interaction is much stronger than in the case of free-standing nanostructures as the interface area gets strongly enhanced and the ability of low dimensional structures to sustain interface strain is reduced by the mask confinement. The lattice mismatch between substrate and nanostructure is able to create strong strain fields that often get released by the formation of misfit dislocations. These kind of defects are effectively acting as charge trapping centers that strongly deteriorate transport properties of semiconductors. In order to achieve

defect-free structures, some strain-engineering strategies can be followed by the coupling of intermediate layers accommodating strain and reducing the total mismatch between layers. For instance, the addition of a buffer layer with height overcoming the mask thickness effectively provides the structure with freedom to elastically expand laterally, resulting in a reduced number of plastic deformation events. The addition of ternary compounds combining substrate and nanowire composition has been shown to offer benefits on the crystal quality of the system, and thus, on the electronic transport properties. However further optimization of growth conditions and layer composition design should be done for the achievement of fully defect-free NWs.

Last but not least, we have highlighted the importance of layered growth and single nucleation. In the case of GaAs NMs on Si substrates, the lack of polarity in the substrate provides GaAs freedom to nucleate with two non-equivalent preferential orientations. The growth of multiple nuclei within the same slit can give rise to a highly defective structures comprising polar defects such as antiphase boundaries, which are detrimental to their optical performance. In the case of InSb NWs, we could observe the development of other kind of polar defects arising from differential growth on different branches of NW junctions. A single twin formation in one branch of the NW junction creates a 180 º in-plane rotation that results in the creation of polar domains that act as potential barriers for either electrons or holes (depending on the polar nature of the inversion domain junction). Even though the strength and effect of these barriers in InSb conductance have not been tested, they are expected to behave similar to those in GaAs, which introduce a dramatic decrease on quantum conductance. Further studies for barrier quantification will be performed exploiting iDPC technique.

We state the potential of SAG technique for scalable development of nanostructured devices and as future solutions for integration of nanostructures in existing CMOS technologies. The reproducibility and homogeneity of the designed structures together with the possibility of in-situ device fabrication makes SAG NWs outstanding candidates as building blocks for developing hybrid 1D networks with potential in topological quantum computing, specially for high-mobility and low effective mass compounds such as InAs and InSb, as we are detailing in the next chapter. However, further growth engineering and optimization is still needed for

achieving crystal qualities similar to those of VLS-based nanowires.

Chapter 6

One-dimensional hybrid heterostructures for quantum applications

In the last years, the increasing demand of processing power is moving computational sciences into a new paradigm: quantum computing. Among the different approaches to establish the qubit unit, Majorana-based topological quantum computing seems more appealing due to the stability provided against information loss. Stacked composite 1D nanowires based on InAs/InSb - EuS - Al offer the required properties for creation of functional quantum devices due to their intrinsic bulk properties, but sharpness and excellent epitaxy at interfaces are needed to guarantee the functionality of the quantum devices. In this chapter we study, from an atomistic point of view, epitaxies and interfaces in exotic tri-crystal systems in different configurations: from VLS core@shell@shell nanowires to SAG Al-InAs/InSb nanowires.

6.1 Introduction

Back in 1965, Gordon Moore predicted a tendency in which the number of transistors composing integrated systems would duplicate every year. Ten years later, he modified his own law when he corroborated the rhythm would be decreased and the number transistors would duplicate every two years. Moore's law has been accurate during several decades, but it is inevitably reaching saturation arising from physical limits. As technology evolves and the number of transistors gets multiplied, this gets intrinsically accompanied by a reduction of the transistor and chip sizes for achieving higher processing speeds. However, when reaching nanometric scales some unavoidable drawbacks start to appear, as tunneling effects producing charge (and thus, information) losses. This situation has produced a change in paradigm in computational sciences switching classical computing into quantum computing.

In this approach, the basic unit of information turns to be the qubit, which in contrast with the classical bit, can be in any superposition of 0 and 1 states according to quantum mechanics laws. This fact allows to realize several parallel operations depending on the number of qubits, something required for the extremely huge processing power that nowadays technologies demand.

There are several approaches to address the quantum computing problem. Among them, topological quantum computing has emerged as a promising solution to decoherence problems [222, 223]. Quantum states are susceptible to small cumulative perturbations which result in decoherence of quantum states, and thus, loss of information and computational faults. Instead, topological quantum computing employs quasiparticles called anyons whose world lines pass around one another to form braids in a 3D spacetime. In this scenario, small perturbations do not change topological properties of these braids, making the states be topologically protected [61, 222, 224, 225].

Majorana zero modes have emerged as a great promise for topological quantum computing [226]. Majorana fermions are a kind of fermions predicted by Ettore Majorana early in 1937 [227] which are their own antiparticles, contrary to Dirac fermions. They have not been observed as an elementary particle, but they can emerge in condensed matter physics as charge-neutral and zero-energy quasiparticle excitations (called Majorana bound states or Majorana zero modes (MZMs)) governed by non-abelian anyon statistics instead of fermionic ones: interchanging them changes the system in a way that depends only on the order in which the exchange was performed. This non-commutative operation is then topologically protected and may be used for implementation of quantum gates.

A number of platforms have been proposed for hosting MZMs. Among them, a platform consisting in proximity-coupled semiconductor-superconductor (SE-SU) hybrid structures has caught attention of researchers [228] and actually signatures of MZMs have been observed experimentally at the edges of 1D III-V semiconductors coupled to superconductors [229–233]. The needed ingredients for engineering such semiconductor based Majorana platforms were proposed by Lytchyn *et al.* and Oreg *et al.* [223, 234].

The basis of a platform with topologically protected bound states relies on obtaining a conventional superconductor (SU) proximity-coupled to a one-dimensional nanowire of a semiconductor material (SE) [235]. The SE nanowire should present strong spin - orbit coupling, large Landé g-factor, high mobility, low effective mass and withstand high magnetic fields that will lift spin degeneracies in the semiconductor material through Zeeman splitting. Another option for bringing the system into the topological regime without the need of applying large magnetic fields that might weak superconducting pairing is to couple ferromagnetic insulators (FMI) into the system [236]. The carrier quality and tunability of the semiconductor could potentially remain intact while the spin degeneracy is lifted by a ferromagnetic exchange coupling, making the system intrinsically topological.

In addition, tri-junctions are needed for next generation of Majorana experiments, so different growth strategies should be performed for achieving such complex NW-based configurations. In that regard, a top-down lithography process applied to 2D fabricated stacked materials seems as the easiest option, but several imperfections can be introduced in the system that would alter its performance. A VLS approach consisting on substrate and crystal engineering can produce nanowire crossings in an in-situ approach [213, 237]. In addition, the branches can be used themselves for shadowing regions during the superconductor deposition. However, scalability problems and crystal phase control can suppose a limit for employing VLS growth of such configurations. Alternatively, recent developments of SAG nanowire networks provide an outstanding platform for supporting Majorana-based hybrid systems [53, 73, 200, 238].

6.1.1 Hybrid tri-crystal configurations

The intrinsic properties of the materials forming the composite coupled systems are essential for driving the performance of the built devices. In addition, impurities and defects in the structure can introduce additional subgap states that might perturb the system performance [239]. For that reason, it is essential to achieve smooth coherent interfaces between the different materials and structural and crystallographic considerations become also of extreme relevance. Figure 6.1 shows the crystal unit cells of the materials employed in this study.

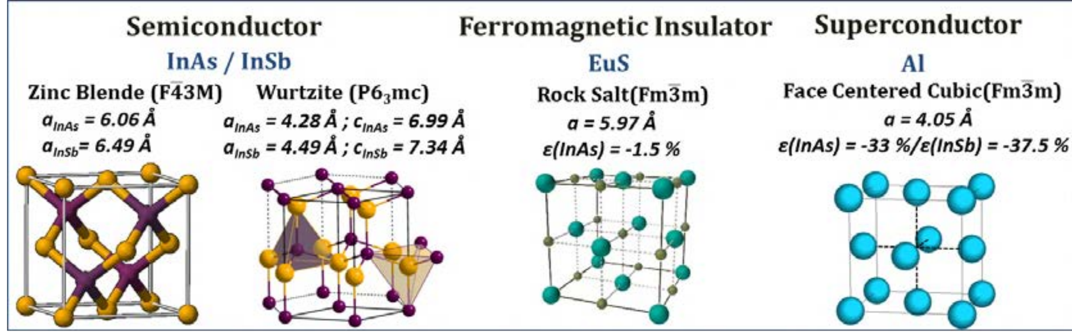

Figure 6.1: Unit cells of the main polytypes of InAs and InSb, EuS and Al with their lattice constants and lattice mismatches with respect to InAs and InSb in ZB structure indicated.

Semiconductor materials

In-based III-V binary compounds are the most suitable candidates for sustaining Majorana platforms due to their outstanding properties involving large g-factor, strong spin orbit coupling, huge mobility and small carrier effective mass. This is the case of InAs and InSb, and particularly InSb has the smallest effective mass and largest g-factor among all binary semiconductor compounds [240, 241]. The physical properties of InAs and InSb are listed in Table 6.1 in comparison with GaAs.

Although InSb seems to overcome the properties of InAs, growing InSb nanowires is much more challenging. The low surface energy of Sb acts as a surfactant and makes the growth initialization complicated. For this reason a heterostructure consisting of an InAs or an InP NW is sometimes used as a platform for further growth of InSb NWs in ZB structure [137, 242, 243]. However, emerging strain fields from the heterostructure formation together with dislocations might affect InSb properties [106]. Contrary, defect-free InAs VLS NWs are relatively easy to produce in wurtzite crystal phase. It is interesting to highlight that both materials are susceptible to polytypism, and given the strong structural differences between ZB and WZ, a precise control on crystal phase is essential to drive epitaxies with further deposited layers.

TABLE 6.1: Bulk properties (300 K) of InAs and InSb in comparison with GaAs [9, 61, 244].

Bulk properties	GaAs	InAs	InSb
g-factor	0.39-0.44	8-15	40-50
Spin-orbit coupling α, eV	0.34	0.41	0.80
Electron mobility m_e, $cm^2\ V^{-1}\ s^{-1}$	≤ 8500	$\leq 4 \cdot 10^4$	$\leq 7.7 \cdot 10^4$
Effective electron mass m*, m_e	0.063	0.023	0.014
Effective hole mass m*, m_{hh}	0.51	0.41	0.43
Effective hole mass m*, m_{lh}	0.082	0.023	0.015

Ferromagnetic insulator

The employment of a ferromagnetic insulator as an intermediate layer has been recently proposed for the development of topological quantum devices that remain operative in the absence of external magnetic fields [236]. Among the possible materials, EuS is an outstanding candidate due to its crystal structure. EuS crystallizes in rock salt (RS) structure with lattice constant of 5.97 Å , which presents just a residual 1.5 % lattice mismatch with InAs, being a guarantee of great epitaxy (Figure 6.1).

The energy band alignment at the SE/FMI interfaces also needs to be evaluated as it plays a critical role on the proximity effects of both materials. It is also of extreme importance to evaluate the possible addition of contributions to the system conductivity, as EuS has been reported to be conducting due to doping and impurities [245]. Figure 6.2 shows the band structure in the first Brillouin zone along Γ-X direction for bare InAs and epitaxially grown planar EuS/InAs. EuS 4f states are located below the maximum of the InAs valence band. The gap between the bottom of EuS conduction band and 4f states is of 1.7 eV, which is much wider than the 0.4 eV band gap of InAs. Therefore, employing EuS as an insulator does not incorporate any contribution to the conductivity of EuS/InAs interface.

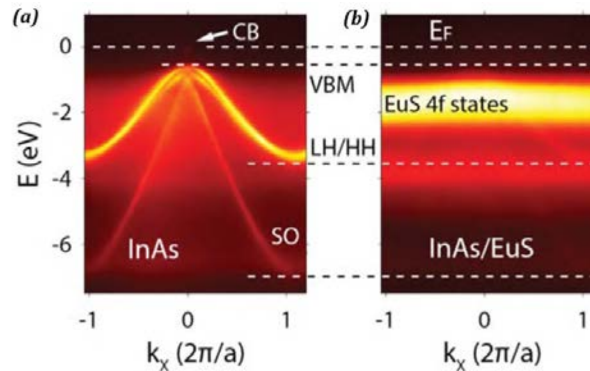

Figure 6.2: SX-ARPES on EuS/InAs(002) hybrid structure along $\Gamma - X$ in-plane direction. (a) Bare InAs(002) (b) EuS/InAs(002) heterostructure. The Fermi level (E_F), valence band maximum (VBM), light and heavy hole band (LL/HH) and split-off band (SO) of InAs and 4f states of EuS are labelled.

Superconductor

Most of the prototypes produced so far have incorporated either NbTiN [233, 246] or Al [58, 60] as a superconductor material. In this chapter we focus on the coupling of Al to several InAs/InSb based systems. Some of the superconducting properties of aluminum are listed in Table 6.2. Requirements for aluminum film

include achieving a uniform morphology along the length of the nanowire to avoid disorder-induced subgap states. Aluminum crystallizes in face centered cubic (FCC) structure with a relatively small lattice constant of 4.05 Å . The large lattice mismatch between Al and InAs/InSb gives rise to complex epitaxial relationships in which interface domains are usually comprised by n_{Al} : m_{SE} planes.

TABLE 6.2: Superconducting properties of aluminum [61].

Critical temperature T_c	Critical field B_c	Superconducting gap Δ	Proximity induced superconducting gap Δ_0	
			InSb/Al	InAs/Al
1.2 K	10 mT	0.2 meV	0.2	0.2

Given the differences in crystal symmetry and lattice constants of the compounds into study, it is essential to understand and control epitaxy on different system configurations, which can be complex. Highly mismatched materials usually form domain epitaxy, also called coincident lattice epitaxy, in which a n:m ratio of planes of the epilayer and the substrate define periodic crystal domains at the interface [31, 32]. In this chapter we study the epitaxy of the materials described above within different configurations by evaluation of the epitaxy mechanisms bringing the most stable configuration. We start by evaluating the crystal quality of VLS InAs–based hybrid tri-crystal composites. Given the limitations of VLS nanowires, we move one step forward to evaluate hybrid compounds from a VS growth approach, including the epitaxy of EuS on planar InAs layers and the deposition of Al on InAs and InSb SAG nanowire networks. The epitaxied layers should adapt simultaneously to both transversal and longitudinal direction of the one-dimensional structures. We will employ then the notation used by Krogstrup *et al.* [57] to define the epitaxial relationships between materials. They will be referred as ($n_{hkl(SU/FMI)}/m_{hkl(SE)}$, $\varepsilon_{\parallel}$)x($n_{hkl(SU/FMI)}/m_{hkl(SE)}$, $\varepsilon_{\perp}$), where m and n correspond to the number of hkl planes of the SU/FMI/SE compound forming the interface domain and $\varepsilon_{\parallel/\perp}$ refers to the residual mismatch along longitudinal/transversal directions.

6.2 Hybrid tri-crystal VLS nanowires

Most of the studies for Majorana-devices have been carried out employing VLS as a growth strategy for the semiconductor. This is due to the precise control over

NW formation achieved during last years. In the particular case of InAs, polytypism (and subsequently electronic behavior) can be precisely controlled by adjusting growth temperature under appropriate V : III ratios [247]. However, ZB phase InAs nanowires seem to be more susceptible to twinning and stacking fault creation. Defect-free ZB nanowires can be achieved by controlling the appropriate growth parameters [248] or doping with Sb [249], but they show a clear tendency to present tapering while WZ structures do not show lateral overgrowth. This is attributed to a lower nucleation probability on the lower energetic WZ $\{1\bar{1}00\}$ facets compared to the ZB $\{112\}$ facets [247]. In the overall, defect-free InAs WZ nanowires can be relatively easier to produce with the lack of any twinning event [250] and at the same time they show absence of tapering, so they are outstanding candidates as a 1D base for tri-crystal hybrid platforms. In addition, high quality epitaxies between InAs(WZ) and Al could be achieved for certain system configurations [57].

Even though a deep effort has been put in the coupling of SE-SU crystals [57], the addition of an intermediate FMI compound had not been reported so far up to our knowledge [236]. High quality interfaces and perfect epitaxial matches are required as they play an important role on the nature of the exchange field lifting spin degeneracies. With this purpose, tri-crystal core@shell@shell SE@FMI@SU nanowires are grown through an Au - catalyzed VLS process [251]. InAs nanowire growth is followed by an in-situ deposition of EuS on two/three side facets and these nanowires get finally capped with an Al layer.

The first nanowire into study is shown in Figure 6.3. InAs crystallizing in WZ structure is faceting in an hexagonal geometry enclosed by six $\{11\bar{2}0\}$ side facets. Three of them ($(2\bar{1}\bar{1}0)$, $(11\bar{2}0)$ and $(\bar{1}2\bar{1}0)$) are covered by EuS with a nominal thickness of 3 nm.

Epitaxy of EuS on WZ InAs

Due to the different crystal symmetries of hexagonal InAs and cubic EuS, the effective mismatch and plane interactions are directional dependent, so longitudinal and transversal nanowire epitaxies and mismatches should be evaluated. We will refer to them as $\varepsilon_{\parallel}$ and $\varepsilon_{\perp}$ for mismatch along longitudinal and transversal directions, respectively. When investigating the nanowire through its longitudinal axis,

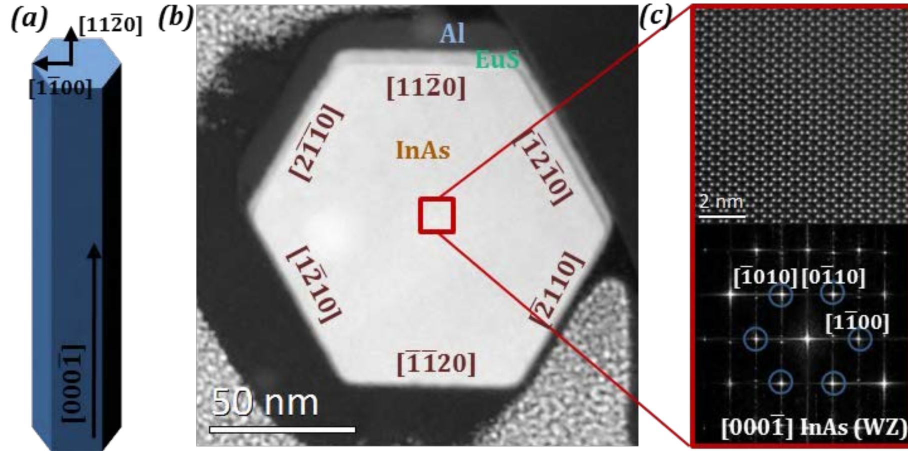

Figure 6.3: (a) Schematics of WZ InAs crystal directions within the nanowire. (b) HAADF overview with labels on elemental distribution of InAs (core) and its faceting, three-fold shell of EuS and two-fold shell of Al. (c) Detailed atomic arrangement of InAs WZ crystal phase obtained in the bulk of the nanowire and its corresponding indexed power spectrum.

the InAs planes interacting with EuS are (000$\bar{2}$), which present an interplanar distance of $d^{000\bar{2}}_{InAs}$ = 3.49 Å. Regarding transversal plane interactions in {11$\bar{2}$0} facets, the epitaxy is driven by InAs {1$\bar{1}$00} planes presenting interplanar spacing of $d^{1\bar{1}00}_{InAs}$ = 3.71 Å.

TABLE 6.3: Mismatch of EuS {hkl} main crystal planes with respect to InAs (000$\bar{2}$), (1$\bar{1}$00) and (11$\bar{2}$0) planes in a $1_{EuS} : 1_{InAs}$ plane ratio.

$EuS_{\{hkl\}}$	d_{hkl} (Å)	$\varepsilon_{\{hkl\}EuS\|\|(000\bar{2})InAs}(\%)$	$\varepsilon_{\{hkl\}EuS\|\|(1\bar{1}00)InAs}(\%)$	$\varepsilon_{\{hkl\}EuS\|\|(11\bar{2}0)InAs}(\%)$
001	5.97	70.69	60.91	178.71
011	5.22	20.65	13.75	97.01
111	3.45	-1.44	-7.09	60.92
002	2.98	-14.65	-19.54	39.35
012	2.67	-23.66	-28.03	24.65
112	2.44	-30.32	-34.31	13.77
022	2.11	-39.64	-43.10	-1.45
122	1.99	-43.10	-46.36	-7.10
103	1.89	-46.02	-49.11	-11.86
113	1.80	-48.53	-51.48	-15.97
123	1.59	-54.37	-56.98	-25.49
223	1.45	-58.60	-60.97	-32.40
133	1.37	-60.83	-63.07	-36.04
233	1.27	-63.60	-65.69	-40.57

HAADF-STEM micrographs obtained on a nanowire transversal cross-section reveal that the EuS shell presents polycrystalline nature (Figure 6.4). EuS grains of approximately 5 nm width appear to show a preferential orientation along [112]EuS zone axis while the planes perpendicular to the nanowire surface are (11$\bar{1}$) ones. However, they show an out-of-plane rotation with respect to the InAs (1$\bar{1}$00) planes

perpendicular to the interface. This rotation around the view axis direction is reflected by the blue arrows shown in Figure 6.4a that point to the EuS [1$\bar{1}$0] crystal direction at each grain. The angle of the grains with respect to InAs (1$\bar{1}$00) planes has been found to achieve up to 22.4 ^{o} in some large grains, while this value gets reduced to approximately 15 ^{o} for smaller grains and at the limits of the grain boundaries. This is reflected in the GPA rotation map shown in Figure 6.4b. The map has been obtained using InAs (1$\bar{1}$00) planes as reference by employing large masks with an angular scope up to $\pm$ 30°. In addition, it is interesting to notice how the breaking of the different grains derives in a quite rough surface that can lead to difficulties in Al deposition, as we will describe in next sections of the chapter.

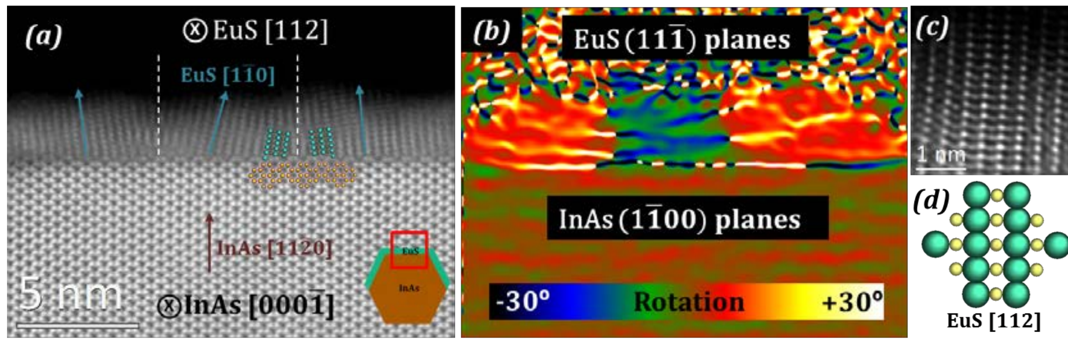

Figure 6.4: (a) HAADF-STEM micrograph obtained on the top (11$\bar{2}$0) InAs facet. EuS grains of approximately 5 nm width are found oriented along the [112] EuS zone axis presenting different out-of-plane rotations around the viewing axis. Blue arrows point to the [1$\bar{1}$0] direction of EuS at each grain. (b) Rotation map of vertical planes ((1$\bar{1}$00)InAs and (11$\bar{1}$)EuS) obtained through GPA. (c) High magnification micrograph of an EuS crystal. (d) EuS unit cell projection through [112] zone axis.

It is interesting to calculate the mismatch between the main EuS crystal planes and InAs (1$\bar{1}$00) planes ($\varepsilon_{\perp}$) for getting some insights on the nature of these tilted epitaxies. Table 6.3 shows the values of mismatch between EuS planes with h,k,l$\leq$3 and InAs main planes in the considered geometry for a 1_{EuS}:1_{InAs} plane ratio. The planes minimizing $\varepsilon_{\perp}$ in this situation are {111}EuS planes, but a -7.09 % mismatch still remains in best scenario due to the highly distinct lattice symmetries. However, if the planes of core and shell structure form an angle β , the effective d - spacing of the shell planes (d_{shell}^{eff}) gets modified as a function of this angle [252] (Figure 6.5a) as follows:

$$d_{shell}^{eff} = \frac{d_{shell}}{cos\beta} \tag{6.1}$$

This fact makes the effective plane mismatch (ε^{eff}) be also a function of β, and it can be written as

$$\varepsilon^{eff} = \frac{d^{eff}_{shell} - d_{core}}{d_{core}} \cdot 100 = \frac{\frac{d_{shell}}{cos\beta} - d_{core}}{d_{core}} \cdot 100 \tag{6.2}$$

Given Eq. 6.2, for $d_{core} > d_{shell}$ the effective plane mismatch ε^{eff} gets reduced when certain β rotations are involved. This is precisely the case in consideration where $d_{InAs(1\bar{1}00)} > d_{EuS(11\bar{1})}$. By plotting the absolute value of ε^{eff} as a function of β (Figure 6.5b) we observe two clear minima at $\beta = \pm 21.7$ º that minimize $\varepsilon_{\perp}$, being [31$\bar{2}$] and [13$\bar{2}$] the closest out-of-plane directions. Due to the lack of preferential rotation directions and the two - fold symmetry of InAs through this direction, both rotations are equally probable, which explains the polycrystalline nature of the EuS layer through a Volmer - Weber island growth model.

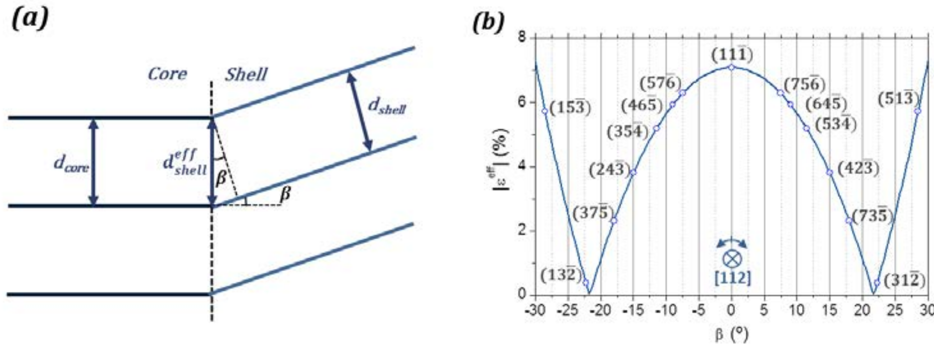

Figure 6.5: (a) Schematics of the effective plane spacing when two planes form an angle β. (b) Effective plane mismatch between InAs (1$\bar{1}$00) and EuS (11$\bar{1}$) as a function of the rotation angle between them around [112]EuS direction (β). EuS planes with hkl $\leq$ 7 forming angles -30 º < β < +30 º with EuS (11$\bar{1}$) are indicated.

The deviation of the measured rotation of EuS grains from the lower mismatch configuration might be attributed to a lower surface energy of the out-of-plane surfaces. However, high index planes usually present higher surface energies. When checking the planes equivalent to the rotation values (Figure 6.5b), we observe that they correspond to high order planes. In that regard, we assume that the lower angles measured are due to lateral tensions between adjacent grains. In this situation, the top surfaces of the grains become irregular arising from a reduction of the top surface energy by the creation of sub-nanometric facets in lower energetic planes.

Now we consider the mismatch along the longitudinal direction ($\varepsilon_{\parallel}$), which is

given by the relationship between InAs($000\bar{2}$) and EuS (hkl). Table 6.3 shows a clear minimum mismatch for EuS$\{111\}$ planes. However, if EuS grains get oriented with $\{111\}$EuS$\|$ ($000\bar{2}$)InAs, there is no possible orientation of transversal planes (which should be perpendicular to EuS$\{111\}$ planes) that implies a low mismatch configuration. Instead, isolated EuS islands nucleate on InAs $\{11\bar{2}0\}$ facets by orienting themselves with [112]EuS | | [$000\bar{2}$]InAs direction. The associated mismatch for such epitaxial relationship is of 30.32 %, but gets reduced to 4.5 % for a $3_{EuS} : 2_{InAs}$ plane ratio. This longitudinal mismatch and EuS crystal direction remain unaffected when crystals rotate along the nanowire axis for minimization of $\varepsilon_{\perp}$.

The overall configuration of EuS crystals on InAs$\{11\bar{2}0\}$ facets can be expressed as ($3_{112}/2_{000\bar{2}}$, 4.5 %) x ($1^{\beta}_{11\bar{1}}/1_{1\bar{1}00}$, < 2 %). As there is no preferential orientation given the two-fold symmetry of the system, β can take either positive or negative values. We have noted the angles to be closer to $\pm 21.7\ ^{o}$ in isolated grains, while the value is highly reduced to $\approx\ \pm\ 15^{o}$ in smaller grains in contact (Figure 6.4b). This could be originated by the adjacent EuS grains creating tensions against grain rotation, which would reduce the final angle inclination with respect to the InAs planes. However, for all EuS crystals observed, the rotation angles bring epitaxial mismatches lower than 2 %.

Interestingly, we noted that in some of the corners of the hexagonal cross section of the InAs nanowire, small $\{1\bar{1}00\}$ nanofacets with a width up to 4 nm were formed. In those, we could find perfectly oriented EuS grains with a uniform orientation (Figure 6.6a). In these facets, EuS is found to be projected along the [332] high order zone axis presenting EuS ($2\bar{2}0$) planes oriented perpendicular to the interface, being then parallel to InAs ($2\bar{1}\bar{1}0$) planes. The mismatch $\varepsilon_{\perp}$ in this configuration gets a value of -1.4 % (Table 6.3), which guarantees an excellent epitaxy between compounds. One of the greatest advantages of employing InAs and EuS as SE and FMI is the low mismatch caused due to the similarities in structure and lattice constant between EuS and InAs ZB. This advantage gets lost whenever switching to InAs WZ structure where most combinations of planes bring large mismatch values. However, the equivalences between ZB $\{112\}$ and WZ $\{1\bar{1}00\}$ planes and ZB $\{111\}$ and WZ $\{000\bar{1}\}$ make these facets be equivalent to the ones in a ZB configuration, which intrinsically makes symmetry drawbacks disappear.

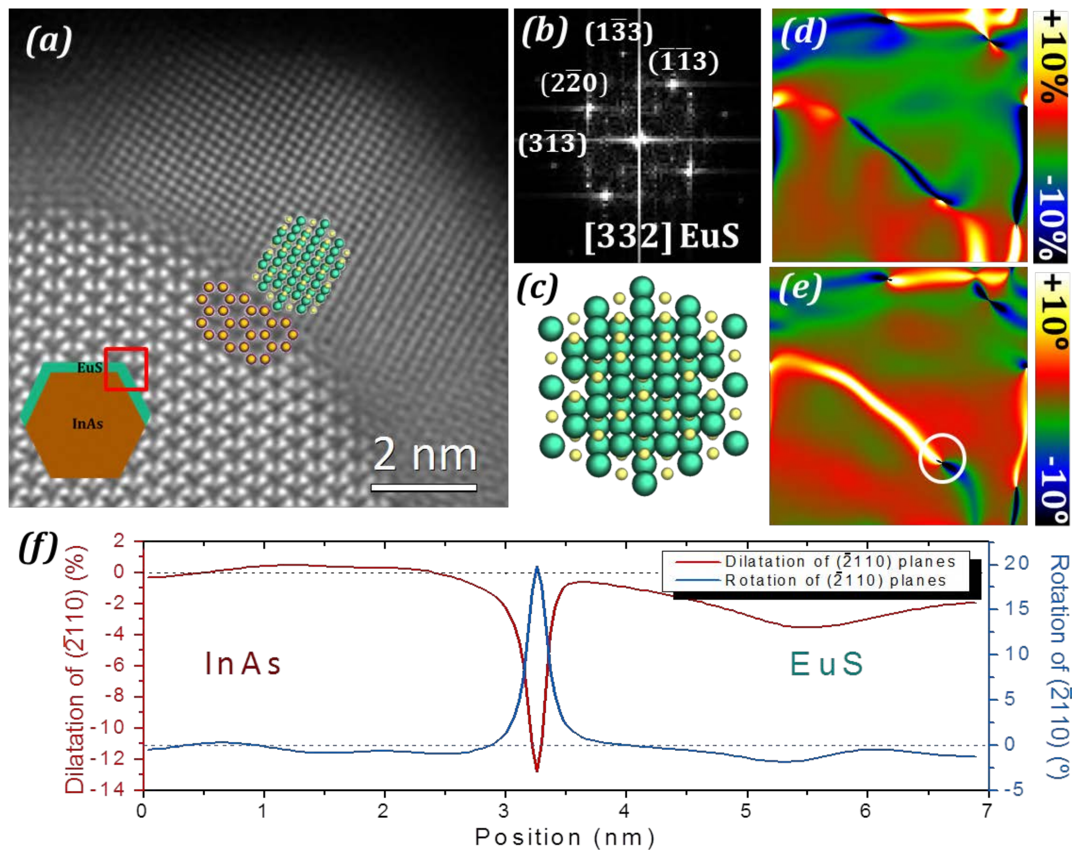

Figure 6.6: Transversal projection of the EuS epitaxy on $\{1\bar{1}00\}$ InAs facets. (a) HAADF-STEM micrograph obtained on a truncated corner of the nanowire showing a small $(1\bar{1}00)$ facet. (b) Indexed FFT obtained on the EuS grain. (c) 2x2 EuS cells projected through [332] zone axis. (d) Dilatation and (e) rotation maps of $(\bar{2}110)$ planes. (f) Profile of GPA dilatation and rotation of $(\bar{2}110)$ planes perpendicular to the interface. [251]

When applying GPA in order to get some clue on lattice adjustment (Figure 6.6d-f) we observe how no dislocation appears in the facet until the end of its length. Then, a single dislocation is formed, which is attributed to the worst matching with the adjacent $\{11\bar{2}0\}$ facet. Interestingly, a compression up to -13 % is measured at the interface between both compounds, which is reflected with the appearance of up to 18 º rotation of planes, even though it has no effects on crystalline arrangement of EuS and do not fully create any defect. This is attributed to a different bonding reducing the interatomic distance between the last InAs and the first EuS monolayers, but a deeper insight on this compression will be highlighted in the following sections.

When checking the matching on $\{1\bar{1}00\}$ InAs facets along the longitudinal NW axis, the nanowire should be imaged though <11$\bar{2}$0> zone axis. Figure 6.7a reveals a continuous film formed by multiple grains of EuS, which might be attributed to a

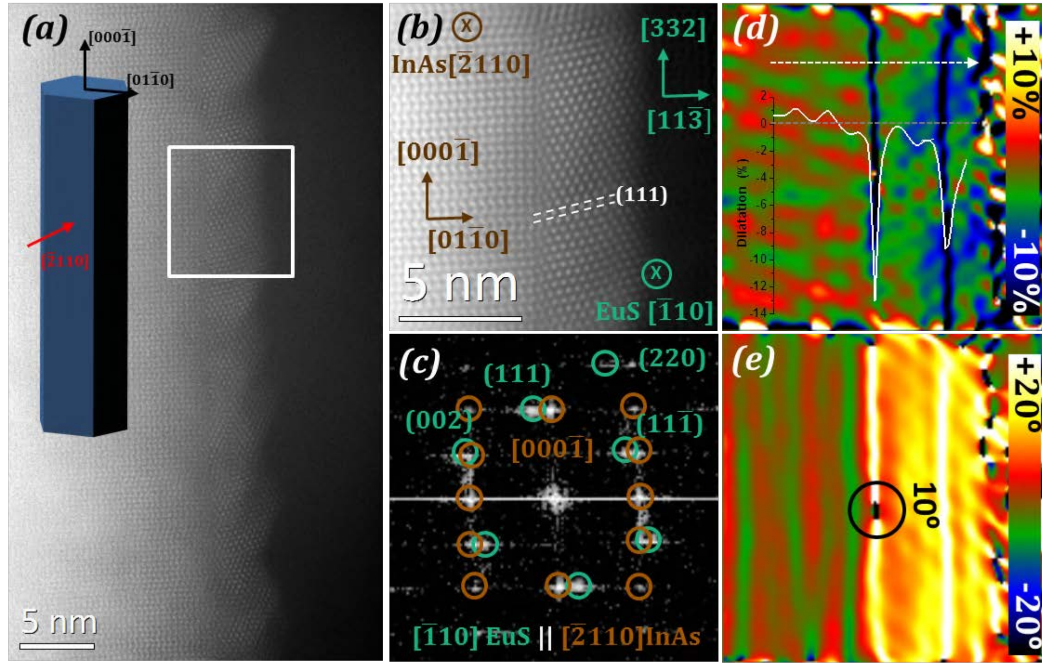

Figure 6.7: Longitudinal projection of EuS epitaxy on $\{1\bar{1}00\}$ InAs facets. (a) HAADF- STEM micrograph showing the atomic arrangement of EuS on a lateral $(1\bar{1}00)$ facet. (b) Details of atomic structure and crystal directions with (c) its corresponding power spectrum. (d) Dilatation and (e) rotation of transversal InAs$(000\bar{1})$ and EuS(111) planes obtained with GPA. The reference area is set in InAs NW. [251]

Volmer - Weber EuS island growth model. The well established epitaxial relationship between EuS and InAs on $\{1\bar{1}00\}$ facets is responsible of the high crystal quality and continuity of the film when merging the different EuS islands during growth. In agreement with observations trough the transversal direction, we observe EuS oriented along its $[\bar{1}10]$ zone axis presenting its [332] direction parallel to the nanowire axis. In this situation, the main planes driving epitaxial match $\varepsilon_{||}$ are InAs$(000\bar{2})$. EuS(111) planes provide a mismatch of 1.4 % with InAs$(000\bar{2})$, but interestingly, the fixed transversal configuration forces $[11\bar{3}]$ to be the out-of-plane EuS direction. This fact leaves [111] direction forming an angle of 10.02 ^{o} with respect to the normal of the nanowire facet. Given Eq. 6.2, the effective mismatch $\varepsilon_{||}^{eff}$ between EuS(111) and InAs$(000\bar{2})$ gets reduced to 0.07 %, which forms a perfect matching between lattices. One single dislocation is found along all the length of the nanowire examined so far, as indicated with a dark circle in Figure 6.6e. An interface compression of -13 % is also measured along this projection.

Therefore the epitaxial relationship between InAs and EuS on $\{1\bar{1}00\}$ InAs facets is well established with $[332]$EuS$(2\bar{2}0)||[000\bar{1}]$InAs$(\bar{2}110)$.

One solution to achieve long-range coherent interfaces would be, then, promoting the creation of $\{1\bar{1}00\}$ InAs facets by adjusting the growth conditions. Figure 6.8 shows one nanowire with growth conditions improved for enhancing $\{1\bar{1}00\}$ facet surface, although $\{11\bar{2}0\}$ facets still represent the major ones. In here, up to 20 nm width $\{1\bar{1}00\}$ facets have been achieved. EuS shells are showing the same epitaxial relationship as in the previously examined NW. Thanks to the minimal mismatch ($\varepsilon_{\parallel}$ and $\varepsilon_{\perp}$) in this 3D lattice configuration, continuous and uniform defect - free 20 nm EuS crystals which form a perfectly coherent interface are achieved. In the $\{11\bar{2}0\}$ facets we observe the same rotated configuration that in the previous case, providing the nanowire with a polycrystalline EuS coverage.

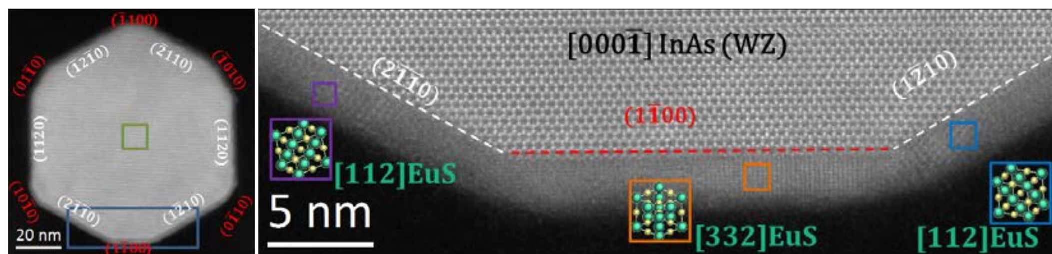

Figure 6.8: On the left, low magnification HAADF-STEM micrograph of an InAs@2f EuS@Al full shell nanowire with major and minor facets labelled. On the right, details of the bottom of the nanowire with 20 nm coherent interface between EuS and InAs at the bottom facet.

Further promotion of these facets can present certain drawbacks. Figure 6.9a shows a nanowire containing three major $\{1\bar{1}00\}$ side facets and six minor $\{11\bar{2}0\}$ side facets. Continuous EuS layers are achieved on the $\{1\bar{1}00\}$ major facets, but the $[000\bar{1}]$ visualization of the InAs lattice reveals features that differ from the pristine WZ lattice (Figure 6.9b). In order to explain the different intensities measured in a micrograph, the HAADF intensities of a model comprised by the stacking of WZ and ZB lattices were simulated (Figure 6.9e-g), which is in agreement with the experimental HAADF. This confirms the coexistence of different polytypes within the same NW through the growth conditions giving rise to major $\{1\bar{1}00\}$ facets, but further optimization needs to be done to avoid polytypism and stacking defects in nanowires presenting this geometry.

Epitaxy of Al on EuS-InAs (WZ) NWs

Aluminum is deposited forming a second shell on InAs@EuS nanowires discussed previously, either covering two nanowire facets or forming a full coverage. So far, controlled Al deposition on top of InAs WZ nanowires has been achieved

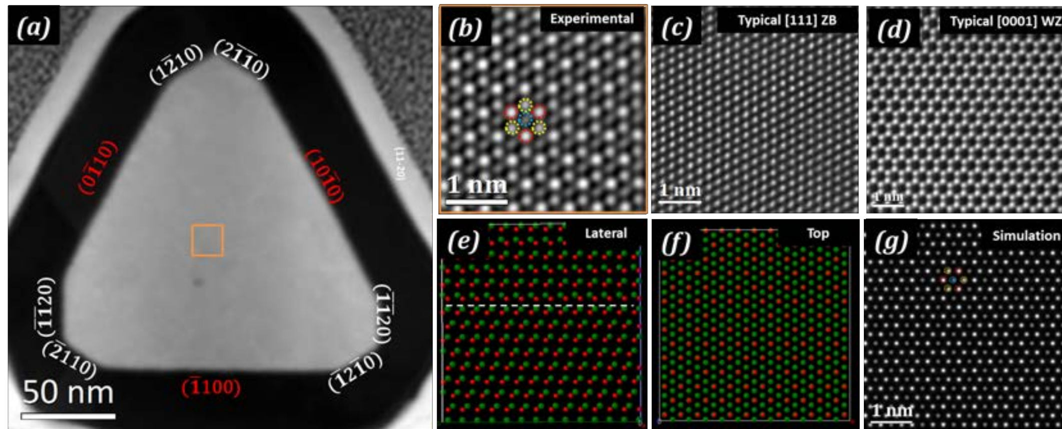

Figure 6.9: (a) Low magnification HAADF-STEM micrograph of a nanowire presenting major $\{1\bar{1}00\}$ facets. (b) Details of InAs structure in the middle of the nanowire. (c),(d) Typical HAADF micrographs of ZB and WZ structures observed along the [111] and [0001] zone axes, respectively. (e) Lateral and (f) top view of an atomic model presenting stacking of ZB and WZ phases. (g) Simulated HAADF-STEM micrograph of the atomic model from top visualization matching experimental HAADF intensities and confirming the presence of polytypism in the nanowire.

with epitaxial relationships depending on the growth dynamics and nanowire configuration [57]. A continuous planar surface could be achieved for thin Al coverage while it evolved to a faceted multigrain structure when increasing the Al thickness. In addition, a structural transition was observed from [112] to [111] out-of-plane direction during growth to thicker structures, suggesting that the structural configuration switches from a thermodynamically driven configuration to a strain-driven one.

The incorporation of an EuS intermediate layer supposes a new challenge towards Al deposition. Firstly, the formation of multiple EuS grains with different crystal orientations produces an inhomogeneity on the surface planes together with surface roughness, which introduce extra small facets on the exposed surfaces. This supposes complications for the simultaneous matching on all available facets. Additionally, the exposed planes differ in direction on InAs and EuS surfaces. As a clear example, Figure 6.7a,b shows how, in addition to the roughness added by the EuS film, the external EuS transversal planes on the right side of the nanowire are inclined 10 ^{o} with respect to the nanowire axis direction, while on the left side of the NW, they keep being parallel. This supposes a complex 3D configuration in which Al grains should adapt to many conditions simultaneously and might derive in some epitaxy problems.

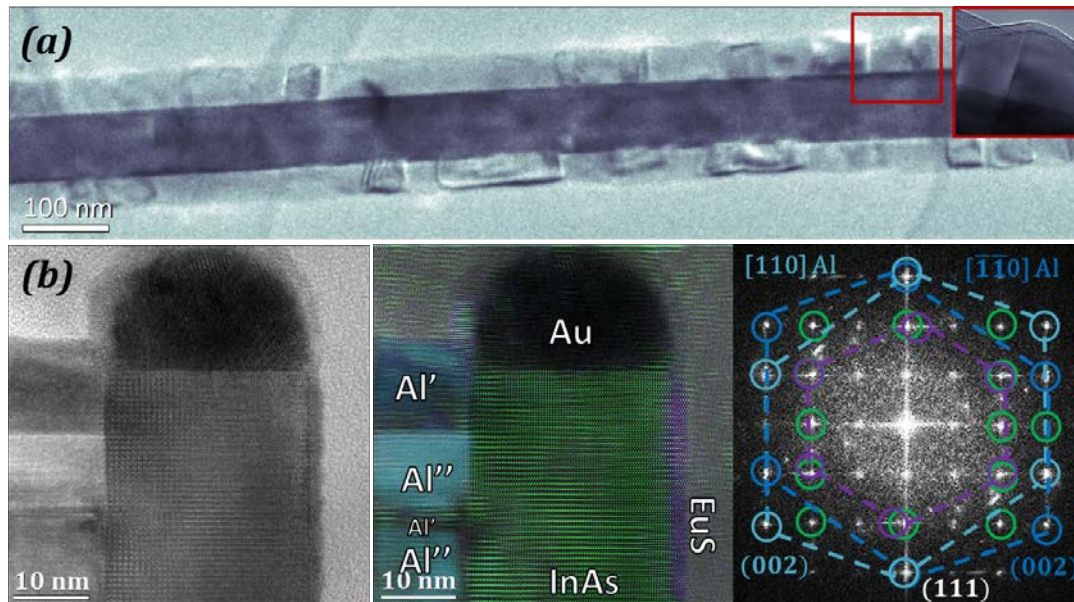

Figure 6.10: (a) Low magnification HRTEM micrograph of a full Al shell covered NW. (b) HRTEM micrograph obtained on the tip of the nanowire, structural phase color map obtained through FFT filtering and FFT with color marks on different compound crystal planes. The non-rounded planes in the center of the FFT correspond to Moiré patterns appearing from the overlapping of Al with InAs crystals. [251]

We start addressing this problem by investigating the nanowire along its longitudinal projection to get an overview of the crystal distribution along a wide nanowire area. Figure 6.10a shows a low - magnification HRTEM micrograph of an InAs@EuS(2f) NW covered with a full shell of Al where the minor $\{1\bar{1}00\}$ facets are partially enhanced and coexist with the $\{11\bar{2}0\}$ ones (growth conditions of the NW shown in Figure 6.8). The enhanced diffraction contrast of this technique in comparison to HAADF allows to visualize multiple grains with up to 100 nm length presenting a well defined crystal orientation with respect to the InAs core. However, the lack of contrast present in many areas along the NW length already predicts problems in epitaxy of the Al shell. A closer look at the NW tip reveals twinned Al oriented through its [110] crystal direction, which is parallel to InAs $[11\bar{2}0]$, with the Al [111] direction aligned with the NW axis (Figure 6.10b). This is the most common Al orientation found along the polycrystalline structure, although it is not kept along the whole nanowire. Checking the nanowire right side where EuS is epitaxied, no evidence of Al atomic planes is found. This is reflecting the disorientation produced by surface inhomogeneities precluding proper matching among the 3D system. The reason for a preferential ordering of Al in the formerly described configuration relies in the mismatch configuration provided in this situation. Checking the mismatch along the nanowire axis $\varepsilon_{\parallel}$ between (111)Al and (0001)InAs, a 33 % epitaxial

mismatch is found. However, this mismatch is reduced to a just residual value of 0.3% for a 3[111]InAs:2[0001]Al plane relationship. The same situation occurs for the transversal mismatch $\varepsilon_\perp$ between (110)Al and (11$\bar{2}$0)InAs, where the 33 % mismatch gets reduced to 0.3 % for a $3_{Al} : 2_{InAs}$ plane relationship. This is highlighted in Figure 6.11 where an Al crystal is perfectly matched with EuS and InAs on a $\{1\bar{1}00\}$ facet. This configuration brings the minimal simultaneous $\varepsilon_\perp$ and $\varepsilon_\parallel$ configuration [57].

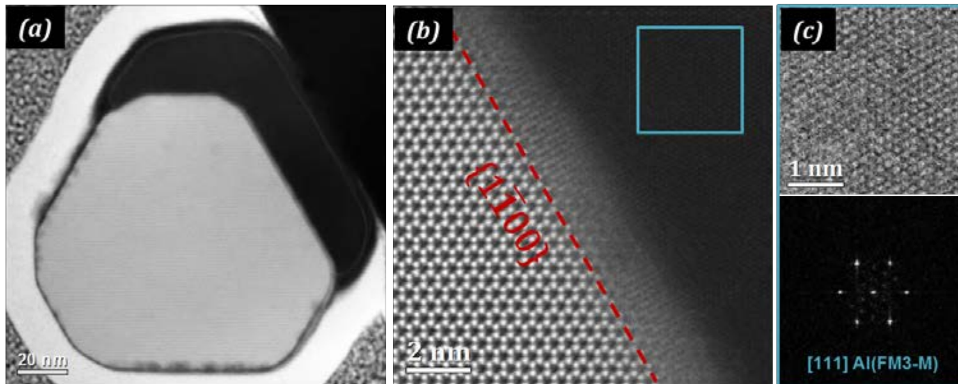

Figure 6.11: Transversal section of a 2f Al shell nanowire. (a) Low magnification HAADF micrograph. (b) Details on InAs-EuS-Al stacking on a $\{1\bar{1}00\}$ facet. (c) Zooming of the blue squared region in (b) and its FFT revealing a [111] oriented Al crystal.

Another interesting interface feature is observed in Figure 6.12. When observing plane spacing in InAs surfaces in direct contact with the Al shell we observe a significant reduction of the lattice constant, which can be clearly observed through plane filtering in Figure 6.12b. GPA was applied to the overall nanowire in order to quantify lattice constant variation (Figure 6.12c). We observe an isotropic compression of a -6.5 % in all the facets contacting Al while no compression is observed in facets contacting EuS. Given this relative variation of lattice constant of InAs in contact with Al, we assume Al is diffusing inside the NW. Applying Vegard's law (Eq. 1.2), an $Al_xIn_{1-x}As$ compound with x =0.98 is found to cover the outermost 2.5 nm of InAs. This self-produced elemental segregation is interesting as AlAs presents a wider band gap than InAs, acting then as a confinement barrier at the interface between Al and InAs. Actually, intermediate tunnel barriers with wider gap had been suggested before to enhance the proximity gap and minimize quasiparticle poisoning [59, 253], being quite advantageous for the overall heterostructure functionalization.

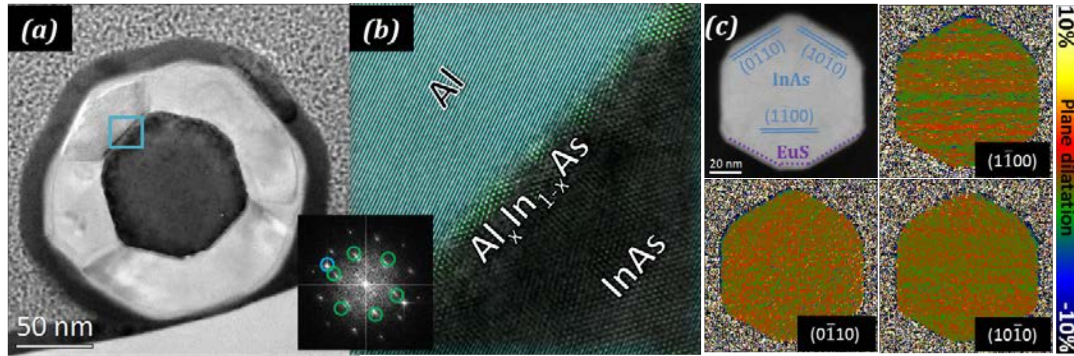

Figure 6.12: Transversal section of a full Al shell nanowire. (a) Low magnification HRTEM micrograph. (b) Filtered color structural map highlighting Al diffusion into the nanowire forming an $Al_xIn_{1-x}As$ compound shell. (c) GPA applied to $\{1\bar{1}00\}$ planes revealing an isotropic lattice constant reduction at the interfaces in contact with Al.

6.3 Interfaces of EuS (FMI) on ZB InAs (SE) configurations

The problems arising from different lattice symmetries of EuS and InAs WZ towards the achievement of large-range coherent interfaces were discussed in the previous section. In addition, several efforts are being done in the development of SAG nanowire networks as they overcome scaling up problems arising from VLS based growth of free-standing NWs. Those SAG nanowires were grown on top of ZB phase substrates and they preserve the cubic crystal symmetry of it. In that regard, even if a huge effort should be done in investigation of optimal growth parameters of SAG NWs together with a strain engineering process, they suppose a quite promising basis for the further development of SU-FMI-SE hybrid compounds for topological quantum computing applications. Thus, a preliminary study of stacking of hybrid compounds in thin film configuration is useful for optimization of the growth conditions and study of the epitaxial quality in such compounds.

6.3.1 EuS planar layers

As a first step, a EuS layer with nominal thickness of 2.5 nm was deposited on top of InAs (002) ZB substrate. A FIB cross-section along [110] direction is examined for obtaining crystallographic information of the interface. Figure 6.13a shows the HAADF – STEM micrograph obtained showing a projection of the bilayer heterostructure through its [110] zone axis. EuS in RS structure is perfectly well epitaxied on InAs substrate with an epitaxial relationship of (002)EuS[110]||(002)InAs[110].

The perfect matching between both structures in this configuration is due to the similarities in crystal structure, both in symmetry and lattice constant, which present an overall mismatch of $\varepsilon_{\perp} = \varepsilon_{\parallel}$ = -1.4 %.

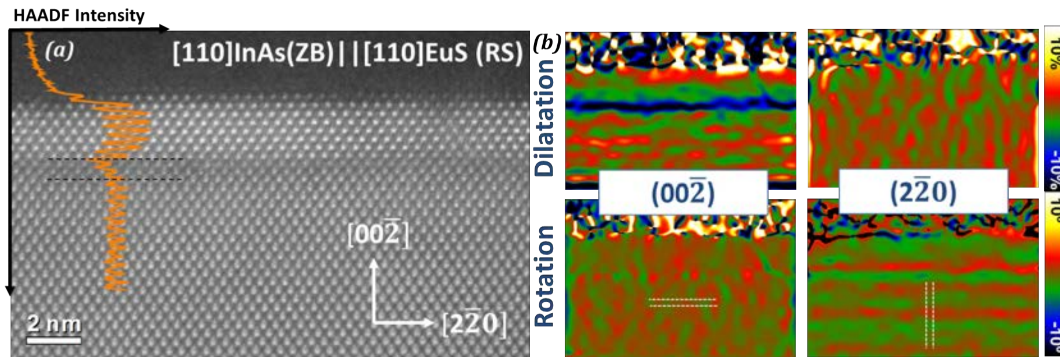

Figure 6.13: (a) HAADF- STEM image of a 2.5 nm EuS film on top of InAs (002). A HAADF intensity profile in a 100 pixel integration width is overlapped with the micrograph. (b) GPA applied to horizontal (002) and vertical (2$\bar{2}$0) planes. InAs substrate is employed as reference lattice.

In order to evaluate the possible presence of dislocations, GPA is applied to the (2$\bar{2}$0) planes perpendicular to the interface (Figure 6.13). No single lattice distortion is observed in any of the areas studied, which supposes a perfect matching between both lattices. In order to finely evaluate the possible tensile strain and overall lattice distortions in EuS, the lattice distortions in the (002) planes parallel to the interface are also studied by means of GPA. The bulk of the EuS layer presents no distortion with respect to the InAs one, as in the case of the perpendicular planes. This means the EuS lattice is tensile strained to adapt to the InAs substrate and the thickness is small enough to hold the residual elastic energy accumulation. However, and interestingly, a compression of about 11.4 % is measured in the (002) planes comprising approximately a bilayer. This compression has been measured to reach up to 23 % in certain interface regions. This compression takes place in a highly anisotropic way, as (2$\bar{2}$0) planes remain unaltered. Small compressions could be arising from a compensation of the lattice dilatations in the transversal planes, but such a high compression must have a different origin.

It is interesting to notice that apart of the compressive layer, there is a significant decrease of Z-contrast intensity at the interface (Figure 6.13a). This decrease matches with the position of the measured (00$\bar{2}$) compression. It is important to understand how atoms distribute at the interface, as the formation of an intermediate compound could introduce additional states in the system electronic band diagram. HAADF

contrast is sensitive to both atomic number and sample thickness, and given the system geometry, thickness variations are not expected. In that regard, intensity profiles were obtained as a first consideration for atomic identification in a closer look at the interface along two non-equivalent $(2\bar{2}0)$ planes (Figure 6.14). Given Z(In) = 49, Z(As) = 33, Z(Eu) = 63 and Z(S) = 16, the associated contrast $I \sim Z^{\zeta}$ to the different species at atomic columns is remarkable different for each element present, allowing then unambiguous elemental identification.

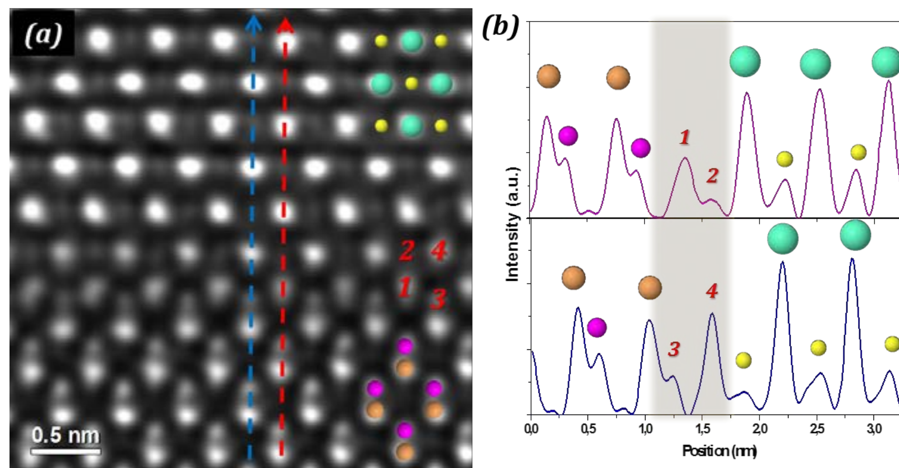

Figure 6.14: (a) High magnification HAADF-STEM micrograph obtained at the interface for Z-contrast analysis. (b) Intensity profiles obtained across the interface following the [002] direction in two non-equivalent positions.

Elemental species are clearly identified far from the interface according to the measured HAADF intensities in Figure 6.14. However, the significant reduction in the bilayer at the interface makes unclear the identification of the elements in four atomic positions (labelled 1-4 in 6.14):

1. There is a decrease in the intensity compared to Eu (-20%) and In (-14%), so simple In-Eu combination within the column given by cation exchange in certain positions would not explain this contrast. In addition, a broadening of this peak with respect to the others associated to cations is observed, including a shoulder prepeak before reaching the intensity maximum.

2. As in the previous case, there is a substantial decrease in column intensity, bringing even a lower Z intensity than S (-6 %), which is the lightest specie present in the sample.

3. Given the position and intensity, As is presented as the more reasonable atomic specie to occupy this position, but the intensity is 13 % lower than the associated for other As columns.

4. The intensity peak resembles the expected In intensity, but its intensity varies along the x direction in equivalent positions: from matching In column HAADF intensity to a decrease up to -18 % with respect to the bulk In columns.

The first hypothesis to explain such an intensity decrease at the interface is the appearance of an intermediate compound caused by atomic segregation. The combination of the lightest species would provide an overall decrease in intensity, but the electronic configurations of As and S make this situation unrealistic. In the case of having some 'InS' species, the valence states (In^{3+} and S^{2-}) do not match up and the doubtful region is not big enough for accommodating a structure with the needed stoichiometry. Additionally, the intensities labelled as '1' and specially '2' can't be explained in such configuration, as '2' presents a lower intensity than the lightest compound (S) in the sample.

HAADF simulations on priory designed atomic models are employed as a tool to investigate the column signal origin. In order to provide an atomic model that would explain the measured HAADF intensities we considered two facts. Firstly, the atomic species at the interface show an intensity peak elongation deviating from a Gaussian decrease from the central intensity maximum. Secondly, the measured compression at the interface could be attributed to different bonding of atomic species of EuS with InAs that decrease the EuS (002) plane spacing in the two first monolayers. Taking into account these considerations, models involving an atomic step at the interface could explain the variations in intensity when including the experimentally measured $d_{(002)}$ reduction that could be attributed to different bonding occurring at the interface. For that reason, here we propose a model containing a 23 % reduction in d_{002}-spacing in a bilayer of EuS at the interface, as marked in the lateral $(1\bar{1}0)$ projection of the supercell in Figure 6.15. We employed the maximum measured compression to enhance the effects of it in our simulated HAADF micrograph.

Figure 6.15 shows a comparison between the experimental high magnification HAADF micrograph close to the interface and the simulated HAADF intensities for the proposed model, which match perfectly. The general observed reduction

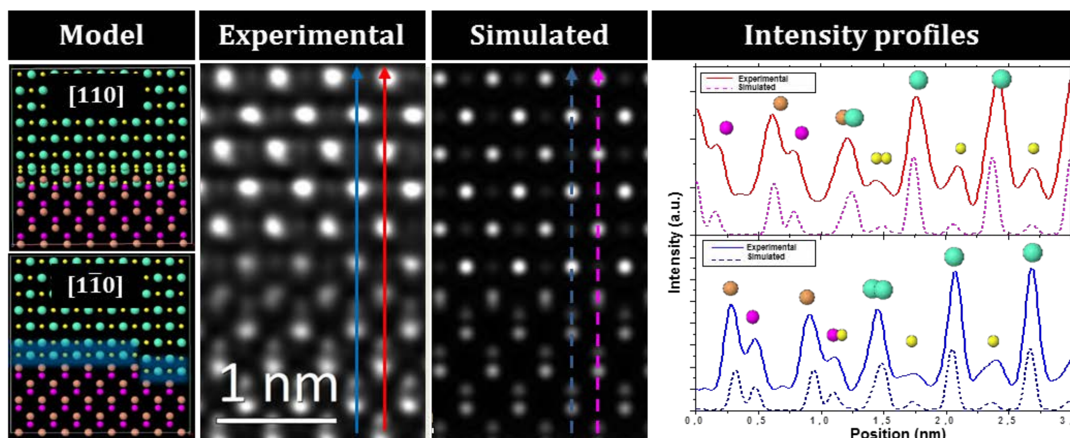

Figure 6.15: Lateral and frontal view of the modelled supercell, comparison of experimental and simulated HAADF intensities and profiles along the arrows with the atomic species assigned from two models containing atomic steps in the case of a monolayer (top) and a bilayer (bottom) compression. The planes where the interplanar distance reduction is applied are marked in blue in the lateral view ([1$\bar{1}$0]) models.

in intensity at the interface arises from the combination of different species without strict overlapping, caused by the sum of the atomic step and the interfacial bilayer compression. In this way, the effective column density gets reduced with respect to those with a full overlapping of the atomic species (bulk InAs/EuS). This is clearly observed in the frontal [110] view of the atomic model in Figure 6.15. This fact also explains the peak broadening or elongation observed specially in positions 1 and 4. It is important to remark that we expect the stepping to occur in both <110> directions and at different stepping height by forming a 3D configuration even if not considered in our model. This fact explains the differences in thickness of the dark layer at the interface in Figure 6.13.

We attribute the anisotropic compression at the interface to the different coordination environment taking place in this region (Figure6.16). Since the substrate is In-terminated at the interface, none of the As atoms experience an alteration of their usual tetrahedral coordination environment in the zinc blende structure of InAs. However, all other elements are exposed at the interface and therefore their bonding there differs from the one in the pure InAs and EuS bulk structures. Both In-As and In-S bond types have a considerable covalent character and, at the interface, In has two of its bonds with As substituted by one with S. Without a compression of this interface plane, the distance between In and S would be about 15 % larger than the In-As bonds, which makes the change from 4 electronegative atoms to 3 in its surroundings even less favorable. Hence both the covalent nature of the In-S

bond, generally related to rather short bonds, and the unbalanced negative charge in comparison with its usual environment for In may be two factors that lead to the interface plane compression.

As for the Eu coordination at the interface, it is not only missing one S that would be located at the interface side, but it is also affected by the considerable repulsion from the In atoms from the same direction, due to the In-termination of InAs. Balancing both the repulsion of the Eu away from the interface and the attraction between In and S as commented earlier may result in the effective compression of both the interface plane and the adjacent plane of the EuS side, as shown in the atomic model. With this configuration, the interface Eu is then brought closer to one of the negative S, while the interface S remains in a similar coordination to its original one, where the distances to both neighboring atoms on the vertical axis of the octahedral coordination is shortened and the bottom Eu is substituted by In.

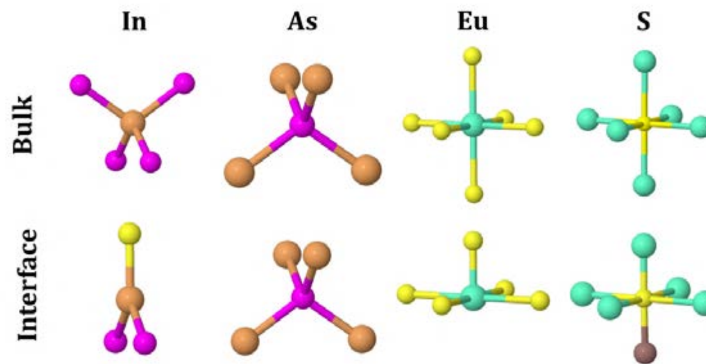

Figure 6.16: Coordination environment of In, As, Eu and S atoms at the bulk and interface.

The proposed model explains then the dark contrast at the interface, confirming that no intermediate compound is created through elemental segregation. The latest, in addition to the successful achievement of dislocation-free interfaces, makes the deposition of EuS on ZB InAs promising for incorporation in one dimensional structures. The only feature observed at the interface is caused by atomic steps that can be easily removed to achieve an atomically flat surface with certain annealing treatments [254, 255].

Increasing the layer thickness is another step to check the amount of strain that the stacked structure can support. Figure 6.17 shows two EuS thin films with thicknesses of 5 nm and 20 nm deposited on InAs(002). We can observe how for 5 nm thick EuS, some dislocations start to appear, as reflected in the $(2\bar{2}0)$ rotation map

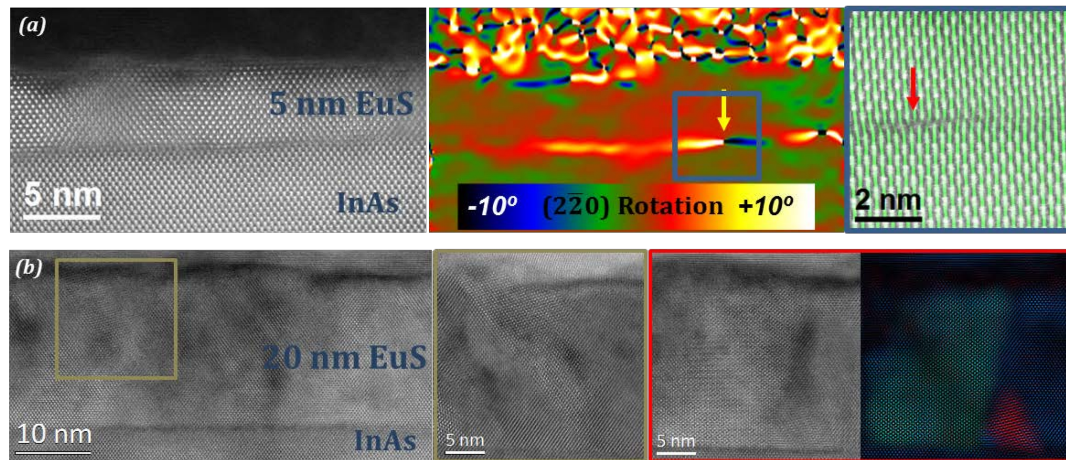

Figure 6.17: Defects appearing in EuS planar films when increasing the nominal thickness to (a) 5 nm and (b) 20 nm.

and plane filtered image. This establishes the critical thickness for dislocation-free interfaces between 2.5 and 5 nm. Even with that, the small mismatch between both structures make the dislocation density be relatively low. More complex issues appear, instead, when the nominal thickness of the layer gets increased to 20 nm. Differently oriented EuS grains appear and the epitaxy problems get reflected in the top surface, where a quite notable surface roughness appears. This might suppose problems for the further deposition of a superconductor on top, as observed previously in the VLS tri-crystal nanowires.

6.3.2 EuS on SAG nanowires

The main goal of epitaxing stacked tri-crystals is to develop one-dimensional heterostructures. With this aim and given the improvement in crystal quality of EuS grown on ZB InAs, EuS was deposited on top of SAG nanowire networks. As it was discussed in the previous chapter, the development of defect-free relaxed InAs nanowires is still a challenge, but testing EuS crystal growth on relaxed InAs NWs is possible by releasing all the strain at the base of the nanowire through misfit dislocations with an abrupt GaAs-InAs transition. Figure 6.18a shows a cross-section of an InAs NW grown on a GaAs (001) substrate. The nanowire presents triangular shaped cross-section with (011) and (0$\bar{1}$1) lateral facets. 20 nm of EuS were deposited selectively on top of the (0$\bar{1}$1) facet. Taking a closer look to the interface between InAs and EuS by means of compositional EELS maps (Figure 6.18d,e) we observe

a slight overlapping of the Eu/In and S/As signals on top of the image, matching where the contrast appears to be darker in the HAADF micrograph of the associated area in Figure 6.18b. Contrary, in the bottom of the maps, there is no elemental overlap at the interface, right where the dark contrast attenuates. This matches with the results observed in planar samples, where atomic steps would create darker contrast and also an overlap of species when projecting the structure into specific directions. Thereby we extend the observations taken in the previous section to epitaxies on (011)InAs surfaces, indicating not atomically flat (011) surface as well as no elemental intermixing. When analysing the HAADF intensity across the interface, we observe how Eu/S atoms arrange forming columns that occupy the As positions of InAs structure, as observed in (002) epitaxy (Figure 6.18c).

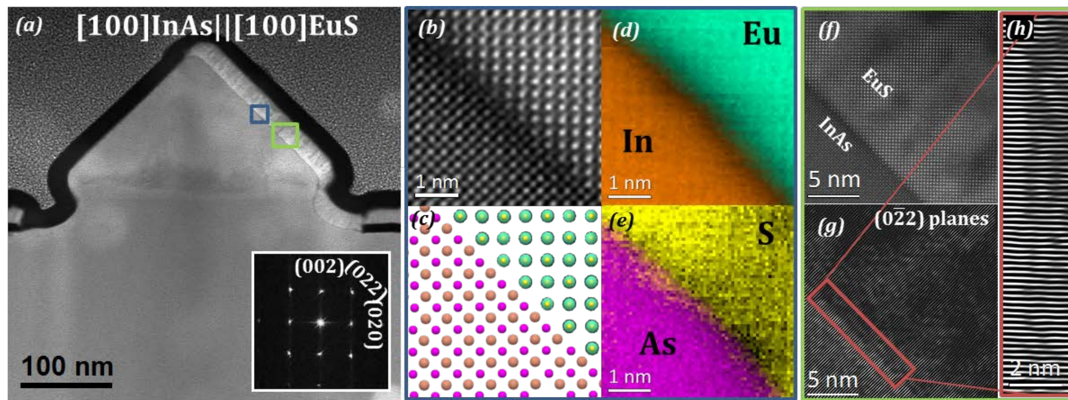

Figure 6.18: (a) HAADF overview of a EuS-InAs(001) SAG nanowire cross-section. (b) Details on atomic arrangement at the interface. (c) Atomic model showing the spatial positions of the atomic species on a sharp interface. (d),(e) EELS mapping of Eu and In and S and As. (f) HAADF micrograph on the interface with (g) filtering of (0$\bar{2}$2) planes perpendicular to the interface. (h) Details of the rectangled region in (g) evidencing the absence of misfit dislocations.

Plane filtering applied to (0$\bar{2}$2) planes perpendicular to the interface allows to evaluate the matching between both lattices and the presence of dislocations. Figure 6.18f-h reveals the absence of dislocations across the interface. EuS lattice perfectly accommodates to the InAs surface through a perfectly coherent matching. In the case of planar layers, we could find a critical EuS thickness below 5 nm for avoiding polycrystallinity and dislocation formation. However, the reduced dimensionality of SAG nanowires allows the structure to finely accommodate forming a defect-free single crystal for higher thicknesses (20 nm in this case).

Last but not least, it is interesting to notice that the EuS layer presents some contrast inhomogeneity (Figure 6.18). This is caused by degradation in contact with

oxygen at the atmosphere. Typically, sulfide compounds tend to oxidize relatively fast. Oxygen penetrates the layer in some channels degrading the EuS crystal quality and properties. This is an issue that should be considered for further superconductor deposition, which highlights the importance of realizing in-situ tri-composite growth without breaking vacuum conditions.

In the overall, the high crystal quality achieved, together with the smooth and homogeneous top surface of the EuS layer makes this bicrystal hybrid a potential candidate for the further deposition of a superconductor. Next section is devoted to study Al epitaxies on SAG InAs and InSb nanowires, but the growth and characterization of a complete SE-FMI-SU in a SAG configuration remains as a goal for future works.

6.4 Crystal quality of Al (SU) on SAG nanowires

The deposition of Al on InAs VLS nanowires was already shown to be challenging due to the high 33 % mismatch between lattice constants. Although the effective mismatch with n : m plane ratios could be highly reduced, imperfections in the surface adding additional reduced nanofacets resulted in polycrystallinity. In the case of InSb nanowires, the lattice mismatch between InSb and Al is even higher, being 37.5 %. In this section, we evaluate the quality of Al epitaxies in both InAs and InSb SAG nanowires. In SAG, both InAs and InSb crystallize in ZB structure, following the crystal symmetries of the employed substrates. In this regard, they preserve cubic structure (such as Al), favoring better control over epitaxy.

6.4.1 Deposition of Al on InAs SAG nanowires

Similar to the analysis performed with EuS in previous sections, the interface in such 3D configuration is defined by the ability of the deposited material on top of the template lattice, in this case InAs, to adapt simultaneously across two perpendicular directions. Thus, it is essential to perform analysis of the nanowire crystallographic configuration in order to get clue on the possible epitaxial relationships. In addition,

when the lattice mismatch between two materials is large, interface domains consisting of n units of epitaxied material and m units of substrate material usually form to reduce the amount of elastic energy accumulation [256].

We start by evaluating InAs NWs grown on InP(111) substrates in such a configuration that the nanowire is forced to be relaxed by the creation of periodic dislocations at the interface with the substrate (Figure 6.19a). This guarantees InAs to present its bulk lattice constant on the top surface of the NW. Given InAs crystal orientation, the matching with epitaxied Al is driven by InAs ($1\bar{1}\bar{2}$) planes in the longitudinal direction ($\varepsilon_{\parallel}$) and InAs ($\bar{1}\bar{1}0$) planes in the transversal direction ($\varepsilon_{\perp}$) .

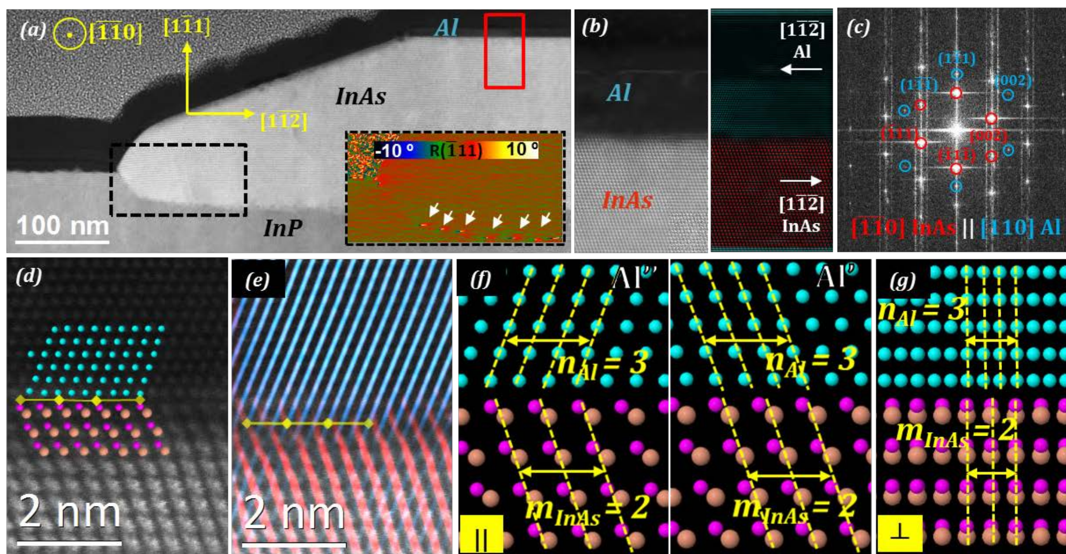

Figure 6.19: (a) Longitudinal overview of an Al/InAs hybrid NW grown along <112> direction of an InP (111) substrate. The inset shows the rotation map obtained through GPA on InAs/InP ($\bar{1}11$) planes with arrows indicating misfit dislocations. (b) Magnified HAADF with details on crystal directions of Al and InAs. (c) FFT of the area in (b) with labels on atomic planes of InAs and Al. (d) Atomic identification on an atomically resolved HAADF micrograph with the 3:2 plane ratio epitaxy indicated with yellow markers. (e) Filtered color map of ($1\bar{1}\bar{1}$) planes of Al and InAs. (f) Atomic model showing the two equivalent configurations of Al (Al′ and Al″) minimizing residual longitudinal mismatch ($\varepsilon_{\parallel}$) with a 3_{Al}:2_{InAs} plane ratio. (f) Transversal projection of both configurations minimizing transversal mismatch ($\varepsilon_{\perp}$) while keeping the 3_{Al}:2_{InAs} ratio.

A perfectly epitaxied Al domain can be observed in Figure 6.19b-e. In this configuration, the crystal directions of both lattices are defined as [110]Al$\|$[$\bar{1}\bar{1}0$]InAs and [$1\bar{1}\bar{2}$]Al$\|$[$\bar{1}12$]InAs. In order to understand this preferential epitaxial relationship, Table 6.4 shows the calculated plane mismatch considering different domain plane ratios for all Al planes with hkl < 2. Due to the high mismatch between both lattices, most of plane combinations bring high associated lattice mismatches even when accounting for different plane ratios. Looking at the longitudinal direction,

$\varepsilon_{\|}$ gets minimized to 0.3 % when orienting {112} Al planes parallel to {112} InAs ones with a ratio 3(Al):2(InAs). This relationship is preserved when considering the transversal direction, where the perpendicular {220} Al planes reduce the mismatch to 0.3 % when interfacing {220} InAs with a ratio 3(Al):2(InAs). The domain match can be referred then as ($3_{\bar{1}12}/2_{1\bar{1}\bar{2}}$, 0.3 %)x($3_{110}/2_{\bar{1}\bar{1}0}$, 0.3 %), which presents a very low residual mismatch and preserves the low energy {111} out-of-plane orientation. In this configuration there are two possible equivalent configurations in terms of energy and mismatch due to the symmetry of the Al unit cell: [1$\bar{1}\bar{2}$]Al ‖ [1$\bar{1}\bar{2}$]InAs or [1$\bar{1}\bar{2}$]Al ‖ [$\bar{1}$12]InAs (Figure 6.19f). This highlights the importance of layered mononucleated growth for getting rid of grain boundaries between such antiparallel domains.

There is only another configuration that brings low remaining lattice mismatch, ($4_{012}/3_{1\bar{1}\bar{2}}$, 1.4 %)x($4_{1\bar{2}1}/3_{110}$, 2.9 %). However, it does not just introduce additional elastic energy to the system but also leaves high energetic Al surfaces exposed, making it unlikely plausible.

TABLE 6.4: Residual mismatch for n_{Al} : m_{InAs} plane ratios in longitudinal ($\varepsilon_{\|} = \varepsilon_{Al\{hkl\}/InAs\{112\}}$) and transversal ($\varepsilon_{\perp} = \varepsilon_{Al\{hkl\}/InAs\{220\}}$) directions for low index (hkl<2) Al families of planes.

	$\varepsilon_{\|}$ ($n_{Al\{hkl\}}$: $m_{InAs\{112\}}$) (%)				$\varepsilon_{\perp}$ ($n_{Al\{hkl\}}$:$m_{InAs\{220\}}$) (%)			
Al_{hkl}	1 : 1	2 : 1	3 : 2	4 : 3	1 : 1	2 : 1	3 : 2	4 : 3
001	63.7	227.5	145.7	118. 4	89.3	278.2	183.9	152.3
011	15.8	131.6	73.7	54.4	33.8	167.7	100.7	78.3
111	-5.5	89.1	41.8	26.1	9.3	118.5	63.9	45.5
002	-18.11	63.7	22.8	9.2	-5.37	89.3	41.9	26.1
012	-23.9	52.1	14.1	1.4	-12.1	75.8	31.8	17.1
112	-33.1	33.7	**0.3**	-10.9	-22.7	54.3	15.8	2.9
022	-42.1	15.8	-13.1	-22.8	-33.1	33.8	**0.3**	-10.9
122	-45.41	9.2	-18.1	-27.2	-36.9	26.2	-5.4	-16.0

Whenever epitaxing Al on top of InAs(001) nanowires, the 3D plane configuration is different. In this geometry, longitudinal InAs planes driving epitaxy are (1$\bar{1}$0) and transversal ones are (110). This leaves the minimum mismatch configuration to be ($3_{110}/2_{110}$, 0.3 %)x($3_{110}/2_{110}$, 0.3 %). However, when checking a nanowire overview in Figure 6.20a, a rough nanowire surface with up to 35 nm thickness variations is observed. The appearance of this geometry is consequence of the appearance of new inclined minor facets. In that regard, Al needs to adapt simultaneously

to more InAs crystal planes, which supposes a difficulty for the formation of single crystal Al layers.

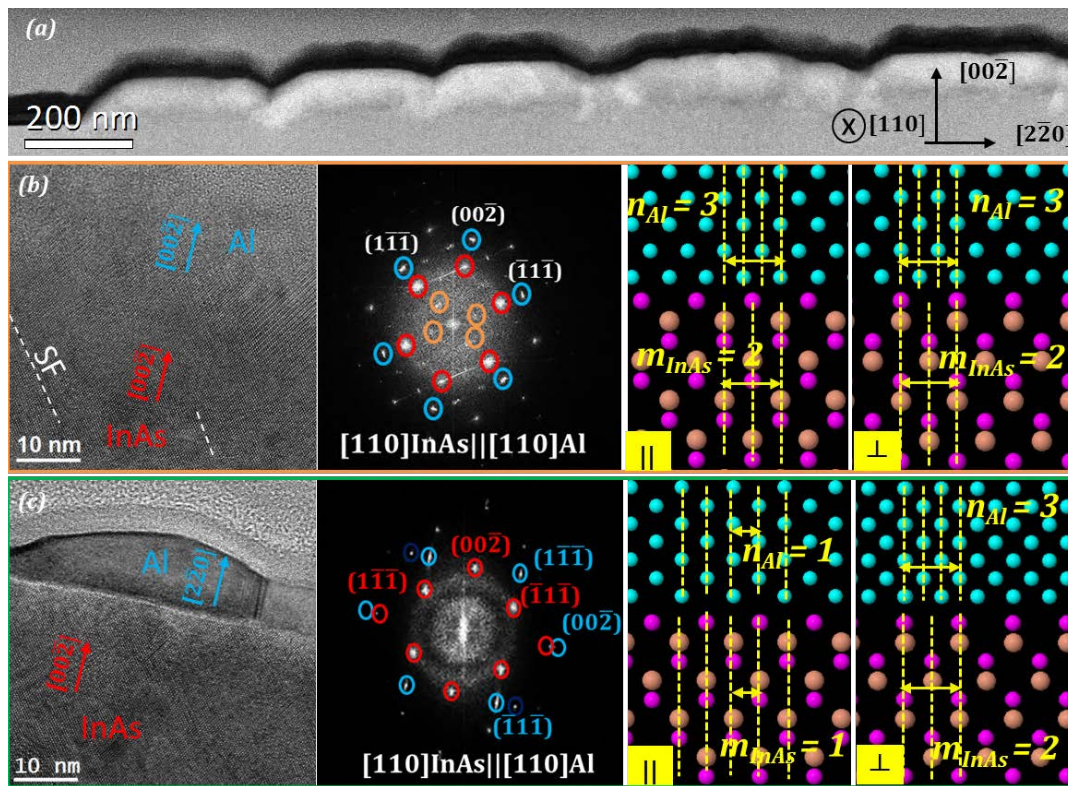

Figure 6.20: (a) Longitudinal overview of Al-InAs hybrid NW grown along <110> direction of GaAs (001) substrate. (b),(c) HRTEM micrograph, indexed power spectrum and atomic models showing epitaxial domains of Al-InAs in longitudinal and transversal directions for observed grain configurations. The orange circled reflections in the FFT correspond to Moiré fringes arising from overlapping of InAs and Al lattices.

Figure 6.20b,c shows two Al grains epitaxing with different orientations. In the first case, the preferential minimum mismatched configuration forms long range Al crystals. However, in the vicinity of kinks in the NW, several Al grains with lengths < 40 nm turn to present different orientations. In Figure 6.20c a grain presenting 90° rotation around the zone axis with respect to the low energy configuration is observed. In this configuration, domains are defined as $(1_{00\bar{2}}/1_{2\bar{2}0}$, 5.5 %)x$(3_{110}/2_{110}$, 0.3 %). Even though the transversal direction preserves the low elastic energy 2_{Al}:3_{InAs} configuration, the plane relationship of 1_{Al}:1_{InAs} observed in the longitudinal direction presents a 5.5 % mismatch, which precludes large grain formation. Thin grains would suffer from elastic lattice distortions that can modify aluminum conduction properties. For thicker grains, instead, misfit dislocations are predicted to appear at a distance of 7.2 nm from each other to release the accumulation of elastic energy.

Controlling nanowire morphology is thus essential for favoring the minimal mismatched configurations which would give rise to larger pristine Al domains.

6.4.2 Deposition of Al on InSb SAG nanowires

We turn to analyze crystal quality of Al deposited on InSb(111) nanowires. Taking a close view on the top facet where Al is deposited, several grains of ≈ 50 nm length showing different crystal orientations can be observed (Figure 6.21b,c). There is a preferential Al orientation by preserving the $[\bar{1}\bar{1}\bar{1}]$ out-of-plane direction, but we observe different in-plane orientations.

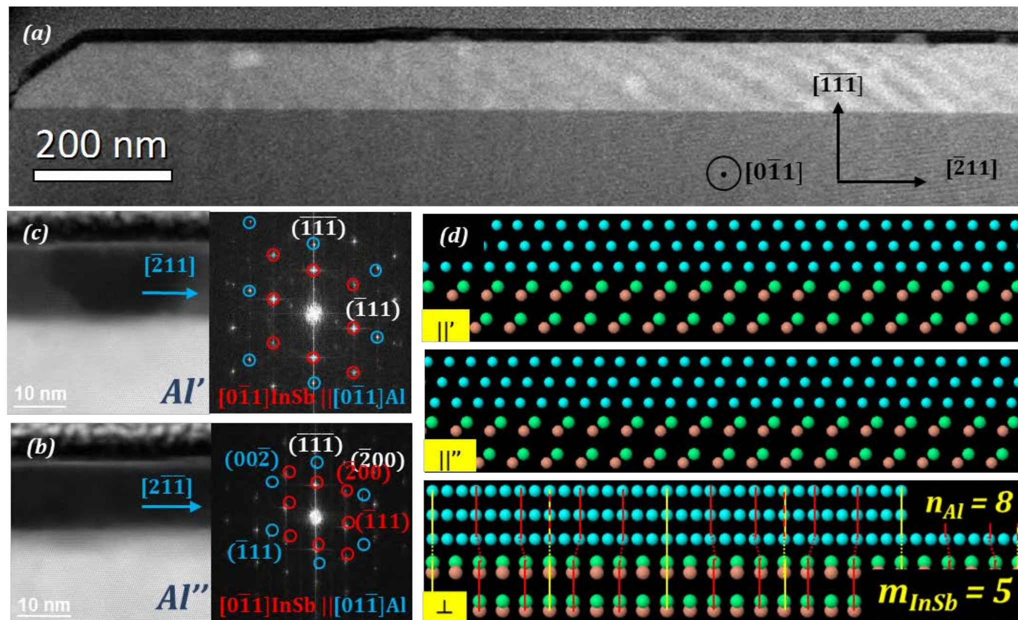

Figure 6.21: (a) Longitudinal overview of Al/InSb hybrid NW grown along the <211> direction on an InP <111> substrate. (b)-(c) HAADF micrographs showing different grain orientations and their corresponding FFTs. (d) Atomic models showing longitudinal and transversal views of the observed Al orientations. Color lines in the transversal direction indicate the lattice coincident sites and plane domain formation.

The lattice mismatch between InSb(ZB) and Al(fcc) is 37.5 %, higher than the mismatch with InAs in which domains consisting of n_{Al}:m_{InAs} planes were more stable. We perform thus a similar domain analysis to the one performed for InAs NW epitaxy. Given a NW grown along $[\bar{2}11]$ direction on an InP(111) substrate, the planes driving epitaxial relationships with Al are $(\bar{2}11)$ for the longitudinal direction and $(1\bar{1}0)$ for the transversal direction (Figure 6.21a). Table 6.5 contains the values of $\varepsilon_{||} = \varepsilon_{nAl\{hkl\}/mInSb\{112\}}$ and $\varepsilon_{\perp} = \varepsilon_{nAl\{hkl\}/mInSb\{110\}}$ for Al families of planes with hkl < 2 for different n_{Al} : m_{InAs} ratios.

TABLE 6.5: Residual mismatch for n_{Al} : m_{InSb} plane ratios in longitudinal ($\varepsilon_{\parallel} = \varepsilon_{nAl\{hkl\}/mInSb\{112\}}$) and transversal ($\varepsilon_{\perp} = \varepsilon_{nAl\{hkl\}/mInSb\{110\}}$) directions for low index (hkl<2) Al families of planes where n = m+1.

	$\varepsilon_{\parallel}$ ($n_{Al\{hkl\}}$: $m_{InSb\{112\}}$) (%)				$\varepsilon_{\perp}$ ($n_{Al\{hkl\}}$:$m_{InSb\{110\}}$) (%)			
Al_{hkl}	1 : 1	2 : 1	3 : 2	4 : 3	1 : 1	2 : 1	3 : 2	4 : 3
001	53.1	206.2	129.6	104.1	76.8	253.5	165.1	135.7
011	8.2	116.5	62.4	44.3	25.0	150.0	87.5	66.6
111	-11.6	76.7	32.5	17.8	2.1	104.1	53.0	36.1
002	-23.4	53.1	14.8	2.1	-11.6	76.7	32.5	17.8
012	-28.8	42.2	6.6	-5.1	-17.8	64.2	23.1	9.4
112	-37.5	24.9	**-6.2**	-16.6	-27.8	44.3	8.2	-3.8
022	-45.8	8.2	-18.7	-27.8	-37.4	25.0	**-6.2**	-16.6
122	-48.9	2.1	-23.4	-31.9	-41.1	17.8	-11.6	-21.4

We observe that there is a preferential orientation when <112> Al direction gets parallel to InSb <112>. In this configuration, domains defined by ($3_{112}/2_{112}$, 6.2 %)x($3_{110}/2_{110}$, 6.2 %) show the minimal mismatched configuration for n = m+1, although a remaining 6.2 % mismatch cannot be retained at large range. In addition, this configuration presents two equiprobable possibilities: Al [$\bar{2}$11] oriented parallel or antiparallel to InSb [$\bar{2}$11] direction.

The atomic models shown in Figure 6.21d are created in order to explain these two grain configurations, labelled as Al' for the parallel configuration and Al'' for the antiparallel one. As we can see in the transversal ($\perp$) projection, which can be extended to the longitudinal one, there is plane coincidence every 8_{Al}:5_{InSb} planes (yellow labels). This relationship can be decomposed by the 3_{Al}:2_{InSb} ratio mentioned before where the remaining lattice misfit of 6.2 % is accommodated by a secondary kind of domain with a larger periodicity [32]. In this case, 8_{Al}:5_{InSb} = 3_{Al}:2_{InSb} + 1_{Al}:10_{InSb}, which means there are domains formed by 3 planes of Al and 2 planes of InSb where there is the appearance of one extra plane of Al every 10 planes of InSb (red labels). This would be equivalent to an array of misfit dislocations accommodating the misfit spaced every 10 InSb planes. The overall domain configuration could then be rewritten as ($8_{112}/5_{112}$, 0.01 %)x($8_{110}/5_{110}$, 0.01 %). In this configuration, the deviation from perfect coincidence in the established periodicities gets reduced to a residual 0.01 %, which is easily sustained by the lattice, and thus, explains the great epitaxy even in such mismatched materials, achieving greater single crystalline grains than in the case of epitaxy on top of InAs where the lattice mismatch is lower.

6.4.3 Superconductors beyond aluminum

Achieving smooth and clean interfaces is essential as it is considered to provide the hard gap superconductivity in the semiconductor given by the proximity effect and the topological protection provided [58]. Even though epitaxial aluminum has been shown to be a promising component for quantum devices and most reported studies are employing it as superconductor constituent of hybrid heterostructures, the observed difficulties in achieving clean interfaces in a controlled and reproducible way highlights the importance of exploring other material combinations. Krogstrup *et al.* proposed several other semiconductor-superconductor combinations that might lead to better epitaxies [57]. Recently Bjergfelt *et al.* succeed in epitaxing vanadium to InSb [257].

The possibility of having materials with larger superconducting critical temperatures T_c and critical magnetic fields H_c can lead to an enhancement of the superconducting gap and therefore achieving a stronger protection of subgap states and higher operating temperatures. For this reason, further studies will be carried out on the deposition of several hybrid combinations and their crystal epitaxial relationships.

TABLE 6.6: Superconducting properties and crystal structure of some single element superconductors as candidates for hybrid systems [258, 259].

Material	Crystal symmetry	Lattice constant (Å)	T_c (K)	H_c (T)
Al	$Fm\bar{3}m$	4.05	1.2	0.01
La	$Fm\bar{3}m$	5.29	6.3	-
Pb	$Fm\bar{3}m$	4.95	7.2	0.08
Sn	$I4_1/amd$	a=5.83, c=3.18	3.72	0.03
Bi	$R\bar{3}m$	a=4.55, c=11.84	$5.3 \cdot 10^{-4}$	$5.2 \cdot 10^{-6}$
In	$I4/mmm$	a=3.25, c= 4.95	3.4	0.03
V	$Im\bar{3}m$	a=3.03	5.4	0.1

6.5 Conclusions

In this chapter, we focused on the study of promising 1D hybrid compounds as candidates for quantum devices. Despite the outstanding physical properties of Al-EuS-InAs/InSb heterostructures for hosting Majorana fermions, the sharpness of interfaces is a critical condition as impurities might end up introducing system faults. In such conditions, structural factors of the different crystals are key for driving epitaxial growth through strain minimization configurations. For this reason, the epitaxial match of several hybrid compounds in different structural configurations has been studied from an atomistic point of view.

The simplest achievable one-dimensional systems through nowadays growth technologies are VLS free-standing InAs nanowires. InAs crystallizing in WZ structure presents different faceting planes depending on the growth environment. We observed a poor EuS crystal quality on InAs $\{11\bar{2}0\}$ facets due to the high associated mismatch given by the difference in crystal cell geometry. High mismatch is partially released by a strain-induced plane rotation, known as tilted epitaxy, but this at the same time creates multicrystal non-continuous coverage where the coherence is lost across their boundaries. Contrary, deposition of EuS on $\{1\bar{1}00\}$ InAs facets results in perfectly coherent interfaces with monocrystalline EuS. However, promotion of InAs $\{1\bar{1}00\}$ facets in front of $\{11\bar{2}0\}$ in VLS environment might lead to twinning in the structure, so further VLS optimization remains as a challenge to overcome these problems. In addition, the further deposition of Al on InAs-EuS nanowires remains challenging. Al presents a preferential orientation when depositing on InAs that decreases the effective mismatch to 0.3 % through domain epitaxy. However, any irregularity in the surface of EuS creates nanofacets where adapting such complex configurations is complicated. This precludes the proper Al crystallization by creating a polycrystalline shell.

One smart solution to overcome the intrinsic problems of VLS based devices is employing SAG NW networks as semiconductor unidimensional systems. By doing so, InAs structure keeps the well defined ZB crystal lattice driven by the substrate. In addition, the reproducibility in growing homogeneous nanostructures together with the possibility of in-situ device production makes this technique quite more promising. EuS sharp interfaces without any elemental segregation are obtained

through this approach due to the preserved crystal similarities between EuS and InAs. We also observe more uniform Al crystallinity on InAs compared to the VLS approach. Remarkably, larger monocrystalline aluminum domains are obtained in InSb nanowire-based architectures even though the intrinsic mismatch between both structures is higher. This is caused by a secondary epitaxial domain formation that provides the overall configuration just a 0.01 % residual mismatch. Again, the crystal quality of Al deposition is observed to be determined by the NW surface smoothness, so a better control of NW growth needs to be obtained for achieving continuous and smooth NW surfaces. In addition, the lack of polarity in Al compound makes several grain orientations equally probable. This highlights the need of achieving layered growth versus the observed island growth for obtaining monocrystalline structures along all the length of the nanowire instead of multiple grains with semi-coherent interfaces between them.

Chapter 7

General conclusions

7.1 General conclusions

Employing electrons as a source for imaging and exciting materials have brought an overcoming of the physical limits of spatial resolution in optical microscopy, which has permitted the study and comprehension of different physical phenomena in a broad variety of research fields by understanding the systems from atomistic approaches. In this work, we have presented a detailed characterization at the atomic scale of one-dimensional nanowire-like structures of III-V and II-VI binary compound semiconductors grown through different strategies devoted for being able to integrate them into functional devices in a scalable and reproducible way. Understanding the growth mechanisms and dynamics from an atomistic approach allows establishing how parameters as polarity or elastic and plastic deformations affect the optical and electronic behavior of the formed structures. We started by evaluating the role of polarity in the formation of defects in vertical VLS nanowires and elemental segregation in ternary and quaternary compounds. Then, we addressed the problems of integration of conventionally grown VLS nanowires to study the possible strain-mediated complications in horizontally grown nanowires: from VLS core-shell horizontal arrays to a SAG approach. In these cases, nanowire interactions with the substrate dominate the growth and strongly influence the final nanowire properties. Finally, we exploited the possibilities of using both VLS and SAG nanowires as building blocks in more complex hybrid semiconductor-superconductor systems for topological quantum computing applications. In the following, we present the main general conclusions achieved in the different parts of this study.

In Chapter 3, the effects of polarity in defining the atomic arrangement of self-catalyzed free-standing GaAs NWs were investigated from an atomistic point of

view. GaAs has been observed to spontaneously grow following B-polar {111} directions during the VLS process, but shifting the growth conditions such as growth rate and V/III ratios, conditions where {111}A and {111}B coexist can be achieved. Given the Z-contrast of HAADF technique, direct identification of atomic species in the dumbbell units was achieved by simple dipole analyses. At the same time, we could observe a preference for twinning and presence of polytypism in B-polar NWs, while A-polar NWs tend to be defect-free after few nanometers of growth. We observed that these differences in crystalline structure arise from the preference of twinning in {111}B polar planes. It was observed through HAADF imaging, proved by low-loss EELS and computed with simulations that this phenomenon arises directly inside the liquid catalyst in the nearby area to the solid growing NW. The liquid ordering behaves as a different phase that actually determines the positions where atoms deposit, determining so the ability for twinning and creating wurtzite domains. In conclusion:

- Enhancing the fraction of A-polar VLS nanowires is possible by reducing the V/III ratio during the MBE growth. A-polar nanowires are shown to preserve pristine GaAs ZB structure with very few defects, which makes them present a better optical response.
- The origin of the outstanding crystal quality of A-polar GaAs nanowires is determined at the ordered liquid phase created in the liquid catalyst nearby the solid grown NW. This ordering, which depends on material's polarity, already determines the probabilities of atom deposition at different positions and intrinsically determines the probability of twinning and polytypism formation.
- Being able to grow simultaneously A and B polar GaAs nanowires opens the possibility to grow vertical nanostructures into (001)Si substrates by promoting simultaneous bipolar growth, which results in nanostructures presenting large single crystal areas.
- Polarity has been also shown to influence the elemental segregation in ternary and quaternary alloys. This fact creates composition fluctuations in the different polar directions that might spontaneously create some quantum wires embedded along the nanowire edges.

In Chapter 4, the VLS growth was switched to an horizontal direction in a guided approach by exploiting the epitaxial and graphoepitaxial relationships with the substrate to direct the growth in specific directions. We particularly investigated the growth of ZnSe@ZnTe core-shell NWs on sapphire substrates cut in different directions. We observed that graphoepitaxial growth did not drive to morphology uniformity of the NWs due to the difficulties of ZnSe to adapt simultaneously to many different substrate facets. In the case of epitaxial growth, we observed how the substrate orientation drives to different morphologies on the core as the wetting of the catalyst varies due to the different surface energy of each orientation. The core template geometry influences the crystalline arrangement of the ZnTe shell, where we have observed and demonstrated that polar domains arise as a response to a plane bending strain minimization mechanism. In conclusion:

- Guided growth of core-shell structures was achieved by the first time, but the quality of the grown structures have been demonstrated to critically depend on the substrate orientation.
- Matching two materials with a 7.4 % mismatch in a core-shell configuration turns to be dependent of the core morphology. Presenting faceted or flat cores provides a geometry where the shell adapts by the creation of arrays of misfit dislocations, while presenting atomically stepped cylindrical cores produces a plane bending effect that improves the plane matching and thus reducing the plastic deformation.
- As the origin of plane bending relays on the atomic stepping found in cylindrical cores, the amount of bending reducing strain accumulation is also depending on it. Thanks to atomic modelling and HAADF simulations we concluded that higher bending is expected for smaller cores while it vanishes when the radius of the core gets higher.
- Plane bending spontaneously creates polar domain boundaries, which introduce an electric field inversion. This effect acts as a potential barrier for carriers that detriments the device efficiency, so reaching planar cores and/or increasing their diameter is essential for optimal device performance.
- We developed an improved VEELS-based band gap mapping methodology demonstrating that the band gap of ZnTe gets reduced in the compressively

stressed areas while we observe homogeneous distribution through the rest of the complex heterostructure. The proposed strategy opens new possibilities for band gap analyses at the nanoscale in complex binary semiconductor based systems.

In Chapter 5, we investigated one-dimensional horizontal nanostructures grown by SAG, as this strategy is presented to overcome VLS in terms of scalability. However, the technique requires a deep control of growth dynamics as multiple nucleation phenomena can create APBs destroying the electronic and optical properties. We have observed the importance of achieving single nucleation in both non-polar and polar substrates, where single spontaneous twinning in different nuclei can form polar inversion domains. At the same time, the role of strain is critical in the formation of these heterostructures, so we have performed studies on strain relaxation in different material configurations and correlated it with the electronic behavior of the NWs. In conclusion:

- GaAs nanomembranes can be grown on GaAs and Si substrates and be further used as templates for high mobility nanowire growth. In the case of growth on Si non-polar substrates, the length of the slit as well as Ga predeposition is essential for achieving a single nucleation regime. When multiple nuclei coexist, APBs and other polar defects can be formed and at the same time the morphology of the nanomembrane gets affected.
- InAs nanowires have been successfully grown on GaAs and InP substrates. The high mismatch between NW and substrate produces misfit dislocations that have been proved to act as carrier traps that produce hysteresis in conductance and decrease the carrier mobility.
- Strain nanoengineering by the addition of multiple intermediate ternary compound layers with intermediate lattice constants have successfully decreased the amount of dislocations created in the NW. This is reflected in an improvement of the electron mobility and a decrease in the measured conductance hysteresis.

In Chapter 6, we investigated tri-crystal hybrid systems for topological quantum computing applications. EuS and Al were deposited on top of VLS and SAG

grown InAs nanowires and the quality of the hybrid interfaces was evaluated. Despite the good matching of such materials in planar configurations, the appearance of different crystal phases and faceting when moving to 1D configurations strongly influences the epitaxy of materials. The difference in the crystal structure and mismatch of the materials involved gives rise to exotic epitaxial methods such as tilted epitaxy or domain match epitaxy. In conclusion:

- EuS on planar ZB InAs creates a perfect dislocation-free interface due to the low lattice mismatch and similarities between both materials. At the same time, we demonstrated the absence of intermediate phases that could add additional states to the band diagram of the system.
- In the case of growing EuS on WZ InAs NWs we observe a faceting dependence on the epitaxial quality. While $\{1\bar{1}00\}$InAs facets preserve the good matching of EuS/InAs(ZB), the high mismatch with $\{11\bar{2}0\}$InAs planes produces tilted epitaxy which creates a grainy EuS polycrystalline configuration. This is translated into a highly polycrystalline Al deposition on top of the system due to the multiple nanofacets that EuS creates.
- EuS crystallizes forming a perfectly matched single crystal on top of SAG grown InAs NWs, preserving the interface configuration of planar EuS/InAs.
- Despite the high mismatch between Al and InAs or InSb, Al can grow epitaxially on InAs and InSb SAG NWs by forming complex crystal domain matching. However, the two-fold symmetry of the Al unit cell produces two equivalent possible orientations, so single Al nucleation regime is required to uniformly cover the NW basis at large scales.

7.2 Closing remarks and outlook

The possibility of understanding physicochemical processes from an atomistic approach has allowed to understand and optimize the growth processes of nanomaterials for precise engineering of their properties. Yet, beyond the capability of 'color imaging' the atomic species of materials, the complexity of phenomena taking place as electron and matter interact is constantly opening new branches of analyses

within the framework of electron microscopy. For instance, the possibility of mapping electromagnetic fields with electron holography or iDPC, or mapping spatial variations of band gap, can allow an overall comprehension of the physical properties of complex structures from an atomistic construction, validating the performed theoretical computations. These state of the art experimental settings, if combined with in-situ growth, can provide scientists the essential tools of control over the growth mechanisms for developing the new devices that can guide the world into a more efficient technologies. Sixty years after Feynman stated the possibilities of nanostructuration, there is still plenty of room at the bottom which needs to be observed atom by atom.

Bibliography

[1]S. Nakamura, M. Senoh, N. Iwasa, and S. Nagahama, “High-brightness InGaN blue, green and yellow light-emitting diodes with quantum well structures”, Japanese Journal of Applied Physics **34**, L797–L799 (1995).

[2]Y. B. Band and Y. Avishai, “13 - low-dimensional quantum systems”, in *Quantum mechanics with applications to nanotechnology and information science*, edited by Y. B. Band and Y. Avishai (Academic Press, Amsterdam, 2013), pp. 749 –823.

[3]D. Wu, Y. Zhang, and M. Razeghi, “Room temperature operation of $In_xGa_{1-x}Sb/InAs$ type-II quantum well infrared photodetectors grown by MOCVD”, Applied Physics Letters **112**, 111103 (2018).

[4]R. Lu, C. Christianson, A. Kirkeminde, S. Ren, and J. Wu, “Extraordinary photocurrent harvesting at type-II heterojunction interfaces: toward high detectivity carbon nanotube infrared detectors”, Nano Letters **12**, 6244–6249 (2012).

[5]B. M. Borg, K. A. Dick, B. Ganjipour, M.-E. Pistol, L.-E. Wernersson, and C. Thelander, “InAs/GaSb heterostructure nanowires for tunnel field-effect transistors”, Nano Letters **10**, 4080–4085 (2010).

[6]R. Yan, S. Fathipour, Y. Han, B. Song, S. Xiao, M. Li, N. Ma, V. Protasenko, D. A. Muller, D. Jena, and H. G. Xing, “Esaki diodes in van der Waals heterojunctions with broken-gap energy band alignment”, Nano Letters **15**, 5791–5798 (2015).

[7]A Hospodková, M Zíková, J Pangrác, J Oswald, J Kubistová, K Kuldová, P Hazdra, and E Hulicius, “Type I–type II band alignment of a GaAsSb/InAs/GaAs quantum dot heterostructure influenced by dot size and strain-reducing layer composition”, Journal of Physics D: Applied Physics **46**, 095103 (2013).

[8]D. W. Palmer, (2014) http://www.semiconductors.co.uk/fndcnsts.htm.

[9]M Levinshtein, S Rumyantsev, and M Shur, *Handbook series on semiconductor parameters* (WORLD SCIENTIFIC, 1996).

[10]M. de la Mata, C. Magen, J. Gazquez, M. I. B. Utama, M. Heiss, S. Lopatin, F. Furtmayr, C. J. Fernández-Rojas, B. Peng, J. R. Morante, R. Rurali, M. Eickhoff, A. Fontcuberta i Morral, Q. Xiong, and J. Arbiol, "Polarity assignment in ZnTe, GaAs, ZnO, and GaN-AlN nanowires from direct dumbbell analysis", Nano Letters **12**, 2579–2586 (2012).

[11]M. de la Mata, R. R. Zamani, S. Martí-Sánchez, M. Eickhoff, Q. Xiong, A. Fontcuberta i Morral, P. Caroff, and J. Arbiol, "The role of polarity in nonplanar semiconductor nanostructures", Nano Letters **19**, 3396–3408 (2019).

[12]J. Arbiol, A. Fontcuberta i Morral, S. Estradé, F. Peiró, B. Kalache, P. Roca i Cabarrocas, and J. R. Morante, "Influence of the (111) twinning on the formation of diamond cubic/diamond hexagonal heterostructures in Cu-catalyzed Si nanowires", Journal of Applied Physics **104**, 064312 (2008).

[13]F. M. Davidson, D. C. Lee, D. D. Fanfair, and B. A. Korgel, "Lamellar twinning in semiconductor nanowires", The Journal of Physical Chemistry C **111**, 2929–2935 (2007).

[14]J. Arbiol, S. Estradé, J. D. Prades, A. Cirera, F. Furtmayr, C. Stark, A. Laufer, M. Stutzmann, M. Eickhoff, M. H. Gass, A. L. Bleloch, F. Peiró, and J. R. Morante, "Triple-twin domains in mg doped GaN wurtzite nanowires: structural and electronic properties of this zinc-blende-like stacking", Nanotechnology **20**, 145704 (2009).

[15]P. Hille, J. Müßener, P. Becker, M. de la Mata, N. Rosemann, C. Magén, J. Arbiol, J. Teubert, S. Chatterjee, J. Schörmann, and M. Eickhoff, "Screening of the quantum-confined Stark effect in AlN/GaN nanowire superlattices by germanium doping", Applied Physics Letters **104**, 102104 (2014).

[16]L. S. Ramsdell, "Studies on silicon carbide", American Mineralogist **32**, 64–82 (1945).

[17]A. R. Denton and N. W. Ashcroft, "Vegard's law", Physical Review A **43**, 3161–3164 (1991).

[18]S. T. Murphy, A. Chroneos, C. Jiang, U. Schwingenschlögl, and R. W. Grimes, "Deviations from Vegard's law in ternary III-V alloys", Physical Review B **82**, 073201 (2010).

[19]K. L. Kavanagh, "Misfit dislocations in nanowire heterostructures", Semiconductor Science and Technology **25**, 024006 (2010).

[20]A. M. Sanchez, J. A. Gott, H. A. Fonseka, Y. Zhang, H. Liu, and R. Beanland, "Stable defects in semiconductor nanowires", Nano Letters **18**, 3081–3087 (2018).

[21]J. Johansson, L. S. Karlsson, C. P. T. Svensson, T. Martensson, B. A. Wacaser, K. Deppert, L. Samuelson, and W. Seifert, "Structural properties of <111> B -oriented III–V nanowires", Nature Materials **5**, 574–580 (2006).

[22]R. R. Zamani, S. Gorji Ghalamestani, J. Niu, N. Sköld, and K. A. Dick, "Polarity and growth directions in Sn-seeded GaSb nanowires", Nanoscale **9**, 3159–3168 (2017).

[23]Y. A. R. Dasilva, R. Kozak, R. Erni, and M. D. Rossell, "Structural defects in cubic semiconductors characterized by aberration-corrected scanning transmission electron microscopy", Ultramicroscopy **176**, 11 –22 (2017).

[24]J. Arbiol, A. Fontcuberta i Morral, S. Estradé, F. Peiró, B. Kalache, P. Roca i Cabarrocas, and J. R. Morante, "Influence of the (111) twinning on the formation of diamond cubic/diamond hexagonal heterostructures in Cu-catalyzed Si nanowires", Journal of Applied Physics **104**, 064312 (2008).

[25]J. Bao, D. C. Bell, F. Capasso, J. B. Wagner, T. Mårtensson, J. Trägårdh, and L. Samuelson, "Optical properties of rotationally twinned InP nanowire heterostructures", Nano Letters **8**, 836–841 (2008).

[26]D. Spirkoska, J. Arbiol, A. Gustafsson, S. Conesa-Boj, F. Glas, I. Zardo, M. Heigoldt, M. H. Gass, A. L. Bleloch, S. Estrade, M. Kaniber, J. Rossler, F. Peiro, J. R. Morante, G. Abstreiter, L. Samuelson, and A. Fontcuberta i Morral, "Structural and optical properties of high quality zinc-blende/wurtzite gaas nanowire heterostructures", Phys. Rev. B **80**, 245325 (2009).

[27]O. Rubel and S. D. Baranovskii, "Formation energies of antiphase boundaries in GaAs and GaP: An ab initio study", International Journal of Molecular Sciences **10**, 5104–5114 (2009).

[28]R. Alcotte, M. Martin, J. Moeyaert, R. Cipro, S. David, F. Bassani, F. Ducroquet, Y. Bogumilowicz, E. Sanchez, Z. Ye, X. Y. Bao, J. B. Pin, and T. Baron, "Epitaxial growth of antiphase boundary free GaAs layer on 300 mm Si(001) substrate by

metalorganic chemical vapour deposition with high mobility", APL Materials **4**, 046101 (2016).

[29]T. David, J.-N. Aqua, K. Liu, L. Favre, A. Ronda, M. Abbarchi, J.-B. Claude, and I. Berbezier, "New strategies for producing defect free sige strained nanolayers", Scientific Reports **8**, 2891 (2016).

[30]T. Inaoka, T. Furukawa, R. Toma, and S. Yanagisawa, "Tensile-strain effect of inducing the indirect-to-direct band-gap transition and reducing the band-gap energy of Ge", Journal of Applied Physics **118**, 105704 (2015).

[31]J. Narayan and B. C. Larson, "Domain epitaxy: a unified paradigm for thin film growth", Journal of Applied Physics **93**, 278–285 (2003).

[32]A. Trampert and K. Ploog, "Heteroepitaxy of large-misfit systems: role of coincidence lattice", Crystal Research and Technology **35**, 793–806 (2000).

[33]R. P. Feynman, "There's plenty of room at the bottom", Engineering and Science **23**, 22–36 (1960).

[34]Y. Liu, G. García, S. Ortega, D. Cadavid, P. Palacios, J. Lu, M. Ibáñez, L. Xi, J. De Roo, A. M. López, S. Martí-Sánchez, I. Cabezas, M. d. l. Mata, Z. Luo, C. Dun, O. Dobrozhan, D. L. Carroll, W. Zhang, J. Martins, M. V. Kovalenko, J. Arbiol, G. Noriega, J. Song, P. Wahnón, and A. Cabot, "Solution-based synthesis and processing of Sn- and Bi-doped Cu3SbSe4 nanocrystals, nanomaterials and ring-shaped thermoelectric generators", J. Mater. Chem. A **5**, 2592–2602 (2017).

[35]Z Luo, E Irtem, M Ibáñez, R Nafria, S Martí-Sánchez, A Genç, M de la Mata, Y Liu, D Cadavid, J Llorca, J Arbiol, T Andreu, J. R. Morante, and A Cabot, "Mn3O4 @CoMn2O4–CoxOy nanoparticles: partial cation exchange synthesis and electrocatalytic properties toward the oxygen reduction and evolution reactions", ACS Applied Materials & Interfaces **8**, 17435–17444 (2016).

[36]Z. Luo, S. Martí-Sànchez, R. Nafria, G. Joshua, M. de la Mata, P. Guardia, C. Flox, C. Martínez-Boubeta, K. Simeonidis, J. Llorca, J. R. Morante, J. Arbiol, M. Ibáñez, and A. Cabot, "Fe3O4@NiFexOy nanoparticles with enhanced electrocatalytic properties for oxygen evolution in carbonate electrolyte", ACS Applied Materials & Interfaces **8**, 29461–29469 (2016).

[37]R. Nafria, Z. Luo, M. Ibáñez, S. Martí-Sànchez, X. Yu, M. de la Mata, J. Llorca, J. Arbiol, M. V. Kovalenko, A. Grabulosa, G. Muller, and A. Cabot, "Growth of Au–Pd2Sn nanorods via galvanic replacement and their catalytic performance on hydrogenation and sonogashira coupling reactions", Langmuir **34**, 10634–10643 (2018).

[38]Y. Fontana, P. Corfdir, B. Van Hattem, E. Russo-Averchi, M. Heiss, S. Sonderegger, C. Magen, J. Arbiol, R. T. Phillips, and A. Fontcuberta i Morral, "Exciton footprint of self-assembled AlGaAs quantum dots in core-shell nanowires", Phys. Rev. B **90**, 075307 (2014).

[39]P. Neuderth, P. Hille, J. Schörmann, A. Frank, C. Reitz, S. Martí-Sánchez, M. d. l. Mata, M. Coll, J. Arbiol, R. Marschall, and M. Eickhoff, "Passivation layers for nanostructured photoanodes: ultra-thin oxides on InGaN nanowires", J. Mater. Chem. A **6**, 565–573 (2018).

[40]J. Arbiol, C. Magen, P. Becker, G. Jacopin, A. Chernikov, S. Schäfer, F. Furtmayr, M. Tchernycheva, L. Rigutti, J. Teubert, S. Chatterjee, J. R. Morante, and M. Eickhoff, "Self-assembled GaN quantum wires on GaN/AlN nanowire templates", Nanoscale **4**, 7517–7524 (2012).

[41]J. Müßener, L. A. T. Greif, S. Kalinowski, G. Callsen, P. Hille, J. Schörmann, M. R. Wagner, A. Schliwa, S. Martí-Sánchez, J. Arbiol, A. Hoffmann, and M. Eickhoff, "Optical emission of GaN/AlN quantum-wires – the role of charge transfer from a nanowire template", Nanoscale **10**, 5591–5598 (2018).

[42]F. Schuster, M. Hetzl, S. Weiszer, J. A. Garrido, M. de la Mata, C. Magen, J. Arbiol, and M. Stutzmann, "Position-controlled growth of GaN nanowires and nanotubes on diamond by molecular beam epitaxy", Nano Letters **15**, 1773–1779 (2015).

[43]L. Bigiani, D. Barreca, A. Gasparotto, C. Sada, S. Martí-Sanchez, J. Arbiol, and C. Maccato, "Controllable vapor phase fabrication of F:Mn3O4 thin films functionalized with Ag and TiO2", CrystEngComm **20**, 3016–3024 (2018).

[44]D. Barreca, L. Bigiani, M. Monai, G. Carraro, A. Gasparotto, C. Sada, S. Martí-Sanchez, A. Grau-Carbonell, J. Arbiol, C. Maccato, and P. Fornasiero, "Supported Mn3O4 nanosystems for hydrogen production through ethanol photoreforming", Langmuir **34**, 4568–4574 (2018).

[45]Y. He, P. Tang, Z. Hu, Q. He, C. Zhu, L. Wang, Q. Zeng, P. Golani, G. Gao, W. Fu, Z. Huang, C. Gao, J. Xia, X. Wang, X. Wang, C. Zhu, Q. Ramasse, A. Zhang, B. An, Y. Zhang, S. Martí-Sánchez, J. Morante, L. Wang, B. K. Tay, B. Yakobson, A. Trampert, H. Zhang, M. Wu, Q. J. Wang, J. Arbiol, and Z. Liu, "Engineering grain boundary at 2D limit for hydrogen evolution reaction", Nature Communications **Just accepted** (2019).

[46]Y. Liu, D. Cadavid, M. Ibáñez, S. Ortega, S. Martí-Sánchez, O. Dobrozhan, M. V. Kovalenko, J. Arbiol, and A. Cabot, "Thermoelectric properties of semiconductor-metal composites produced by particle blending", APL Materials **4**, 104813 (2016).

[47]Y. Liu, Y. Zhang, K. H. Lim, M. Ibáñez, S. Ortega, M. Li, J. David, S. Martí-Sánchez, K. M. Ng, J. Arbiol, M. V. Kovalenko, D. Cadavid, and A. Cabot, "High thermoelectric performance in crystallographically textured n-type Bi2Te3–xSex produced from asymmetric colloidal nanocrystals", ACS Nano **12**, 7174–7184 (2018).

[48]Y. Liu, Y. Zhang, S. Ortega, M. Ibáñez, K. H. Lim, A. Grau-Carbonell, S. Martí-Sánchez, K. M. Ng, J. Arbiol, M. V. Kovalenko, D. Cadavid, and A. Cabot, "Crystallographically textured nanomaterials produced from the liquid phase sintering of BixSb2–xTe3 nanocrystal building blocks", Nano Letters **18**, 2557–2563 (2018).

[49]R. R. Zamani, M. Ibáñez, M. Luysberg, N. García-Castelló, L. Houben, J. D. Prades, V. Grillo, R. E. Dunin-Borkowski, J. R. Morante, A. Cabot, and J. Arbiol, "Polarity-driven polytypic branching in Cu-based quaternary chalcogenide nanostructures", ACS Nano **8**, 2290–2301 (2014).

[50]E. González, J. Arbiol, and V. F. Puntes, "Carving at the nanoscale: sequential galvanic exchange and Kirkendall growth at room temperature", Science **334**, 1377–1380 (2011).

[51]P. Tang, H. Xie, C. Ros, L. Han, M. Biset-Peiró, Y. He, W. Kramer, A. P. Rodríguez, E. Saucedo, J. R. Galán-Mascarós, T. Andreu, J. R. Morante, and J. Arbiol, "Enhanced photoelectrochemical water splitting of hematite multilayer nanowire photoanodes by tuning the surface state via bottom-up interfacial engineering", Energy Environ. Sci. **10**, 2124–2136 (2017).

[52]*ISI Web of Knowledge*, `https://apps.webofknowledge.com/`.

[53]F. Krizek, J. E. Sestoft, P. Aseev, S. Marti-Sanchez, S. Vaitiekénas, L. Casparis, S. A. Khan, Y. Liu, T. Stankevic, A. M. Whiticar, A. Fursina, F. Boekhout, R. Koops, E.

Uccelli, L. P. Kouwenhoven, C. M. Marcus, J. Arbiol, and P. Krogstrup, “Field effect enhancement in buffered quantum nanowire networks”, Phys. Rev. Materials **2**, 093401 (2018).

[54]Y. Huang, X. Duan, Y. Cui, L. J. Lauhon, K.-H. Kim, and C. M. Lieber, “Logic gates and computation from assembled nanowire building blocks”, Science **294**, 1313–1317 (2001).

[55]F. Schuster, B. Laumer, R. R. Zamani, C. Magén, J. R. Morante, J. Arbiol, and M. Stutzmann, “p-GaN/n-ZnO heterojunction nanowires: optoelectronic properties and the role of interface polarity”, ACS Nano **8**, 4376–4384 (2014).

[56]E. Oksenberg, S. Martí-Sánchez, R. Popovitz-Biro, J. Arbiol, and E. Joselevich, “Surface-guided core–shell ZnSe@ZnTe nanowires as radial p–n heterojunctions with photovoltaic behavior”, ACS Nano **11**, 6155–6166 (2017).

[57]P. Krogstrup, N. L. B. Ziino, W. Chang, S. M. Albrecht, M. H. Madsen, E. Johnson, J. Nygard, C. M. Marcus, and T. S. Jespersen, “Epitaxy of semiconductor-superconductor nanowires”, Nature Materials **14**, 400 –406 (2015).

[58]W. Chang, S. M. Albrecht, T. S. Jespersen, F. Kuemmeth, P. Krogstrup, J. Nygård, and C. M. Marcus, “Hard gap in epitaxial semiconductor-superconductor nanowires”, Nature Nanotechnology **10**, 232 –238 (2015).

[59]T. D. Stanescu and S. Das Sarma, “Superconducting proximity effect in semiconductor nanowires”, Phys. Rev. B **87**, 180504 (2013).

[60]H. Zhang, C.-X. Liu, S. Gazibegovic, D. Xu, J. A. Logan, G. Wang, N. van Loo, J. D. S. Bommer, M. W. A. de Moor, D. Car, R. L. M. Op het Veld, P. J. van Veldhoven, S. Koelling, M. A. Verheijen, M. Pendharkar, D. J. Pennachio, B. Shojaei, J. S. Lee, C. J. Palmstrøm, E. P. A. M. Bakkers, S. D. Sarma, and L. P. Kouwenhoven, “Quantized Majorana conductance”, Nature **556**, 74 –79 (2018).

[61]R. M. Lutchyn, E. P. A. M. Bakkers, L. P. Kouwenhoven, P. Krogstrup, C. M. Marcus, and Y. Oreg, “Majorana zero modes in superconductor-semiconductor heterostructures”, Nature Reviews Materials **3**, 52–68 (2018).

[62]R. R. LaPierre, M Robson, K. M. Azizur-Rahman, and P Kuyanov, “A review of III–V nanowire infrared photodetectors and sensors”, Journal of Physics D: Applied Physics **50**, 123001 (2017).

[63]M. Asad, R. Wang, Y.-H. Ra, P. Gavirneni, Z. Mi, and W. S. Wong, "Optically invariant InGaN nanowire light-emitting diodes on flexible substrates under mechanical manipulation", npj Flexible Electronics **3**, 16 (2019).

[64]P. Krogstrup, H. I. Jørgensen, M. Heiss, O. Demichel, J. V. Holm, M. Aagesen, J. Nygard, and A. Fontcuberta i Morral, "Single-nanowire solar cells beyond the Shockley-Queisser limit", Nature Photonics **7**, 306–310 (2013).

[65]G. Bemski, "Recombination properties of gold in silicon", Phys. Rev. **111**, 1515–1518 (1958).

[66]E. Koren, G. Elias, A. Boag, E. R. Hemesath, L. J. Lauhon, and Y. Rosenwaks, "Direct measurement of individual deep traps in single silicon nanowires", Nano Letters **11**, 2499–2502 (2011).

[67]A. Fontcuberta i Morral, C. Colombo, G. Abstreiter, J. Arbiol, and J. R. Morante, "Nucleation mechanism of gallium-assisted molecular beam epitaxy growth of gallium arsenide nanowires", Applied Physics Letters **92**, 063112 (2008).

[68]C. Colombo, D. Spirkoska, M. Frimmer, G. Abstreiter, and A. Fontcuberta i Morral, "Ga-assisted catalyst-free growth mechanism of GaAs nanowires by molecular beam epitaxy", Phys. Rev. B **77**, 155326 (2008).

[69]J. Vukajlovic-Plestina, W. Kim, L. Ghisalberti, G. Varnavides, G. Tütüncuoglu, H. Potts, M. Friedl, L. Güniat, W. C. Carter, V. G. Dubrovskii, and A. Fontcuberta i Morral, "Fundamental aspects to localize self-catalyzed III-V nanowires on silicon", Nature Communications **10**, 869 (2019).

[70]H. Schmid, M. Borg, K. Moselund, L. Gignac, C. M. Breslin, J. Bruley, D. Cutaia, and H. Riel, "Template-assisted selective epitaxy of III–V nanoscale devices for co-planar heterogeneous integration with Si", Applied Physics Letters **106**, 233101 (2015).

[71]M. Borg, H. Schmid, K. E. Moselund, D. Cutaia, and H. Riel, "Mechanisms of template-assisted selective epitaxy of InAs nanowires on Si", Journal of Applied Physics **117**, 144303 (2015).

[72]K. Tomioka, K. Ikejiri, T. Tanaka, J. Motohisa, S. Hara, K. Hiruma, and T. Fukui, "Selective-area growth of III-V nanowires and their applications", Journal of Materials Research **26**, 2127–2141 (2011).

[73]P. Aseev, A. Fursina, F. Boekhout, F. Krizek, J. E. Sestoft, F. Borsoi, S. Heedt, G. Wang, L. Binci, S. Martí-Sánchez, T. Swoboda, R. Koops, E. Uccelli, J. Arbiol, P. Krogstrup, L. P. Kouwenhoven, and P. Caroff, "Selectivity map for molecular beam epitaxy of advanced III–V quantum nanowire networks", Nano Letters **19**, 218–227 (2019).

[74]L. Desplanque, A. Bucamp, D. Troadec, G. Patriarche, and X. Wallart, "Selective area molecular beam epitaxy of InSb nanostructures on mismatched substrates", Journal of Crystal Growth **512**, 6 –10 (2019).

[75]P Aseev, G Wang, L Binci, A Singh, S Martí-Sánchez, M Botifoll, L. J. Stek, A Bordin, J. D. Watson, F Boekhout, D Abel, J Gamble, K Van Hoogdalem, J Arbiol, L. P. Kouwenhoven, G de Lange, and P Caroff, "Ballistic InSb nanowires and networks via metal-sown selective area growth", Nano Letters (2019).

[76]D. B. Williams and C. B. Carter, *Transmission electron microscopy*, 2nd ed. (Springer, New York, NY, 1996).

[77]E. Ruska, "The development of the electron microscope and of electron microscopy", Bioscience Reports **7**, 607–629 (1987).

[78]O. L. Krivanek, N. Dellby, and A. R. Lupini, "Towards sub-angstrom electron beams", Ultramicroscopy **78**, 1–11 (1999).

[79]O. Scherzer, "The theoretical resolution limit of the electron microscope", Journal of Applied Physics **20**, 20 (1949).

[80]A. Bleloch and Q. Ramasse, *Aberration-corrected analytical transmission electron microscopy*, 1st ed., Chapter 4 (John Wiley & Sons, Ltd., 2011).

[81]O. Scherzer, "Ueber einige fehler von elektronenlinsen", Z. Physik **101**, 593–693 (1936).

[82]O. Scherzer, "Sphaerische und chromatische korrektur von elektronenlinsen", Optik **2**, 114–132 (1947).

[83]M. Haider, H. Rose, S. Uhlemann, E. Schwan, B. Kabius, and K. Urban, "A spherical-aberration-corrected 200 kV transmission electron microscope", Ultramicroscopy **75**, 53–60 (1998).

[84]Y. Jiang, Z. Chen, Y. Han, P. Deb, H. Gao, S. Xie, P. Purohit, M. Tate, J. Park, S. M. Gruner, V. Elser, and D. A. Muller, "Electron ptychography of 2D materials to deep sub-angstrom resolution", Nature **559**, 343–349 (2018).

[85]A. V. Crewe, J. Wall, and J. Langmore, "Visibility of single atoms", Science **168**, 1338 –1340 (1970).

[86]M. M. J. Treacy, A. Howie, and S. J. Pennycook, "Z contrast of supported catalyst particles in the STEM", Ins. Phys. Conf. Ser. No. 52 (EMAG 79), 261 (1980).

[87]Z. W. Wang, Z. Y. Li, S. J. Park, A. Abdela, D. Tang, and R. E. Palmer, "Quantitative z-contrast imaging in the scanning transmission electron microscope with size-selected cluster", Physical Review B **84**, 073408 (2011).

[88]R. Ishikawa, E. Okunishi, H. Sawada, Y. Kondo, F. Hosokawa, and E. Abe, "Direct imaging of hydrogen-atom columns in a crystal by annular bright-field electron microscopy", Nature Materials **10**, 278–281 (2011).

[89]V. Grillo and F. Rossi, "A new insight on crystalline strain and defect features by STEM-ADF imaging", Journal of Crystal Growth **318**, 1151–1156 (2011).

[90]P. J. Phillips, M. D. Graef, L. Kovarik, A. Agrawal, W. Windl, and M. J. Mills, "Atomic resolution defect contrast in low angle annular dark-field stem", Ultramicroscopy **166**, 47–55 (2012).

[91]E. Oveisi, M. Spadaro, E. Rotunno, V. Grillo, and C. Hébert, "Insights into image contrast from dislocations in ADF-STEM", Ultramicroscopy **200**, 139–148 (2019).

[92]H. Yang, I. MacLaren, L. Jones, G. T. Martinez, M. Simson, M. Huth, H. Ryll, H. Soltaud, R. Sagawa, Y. Kondo, C. Ophus, P. Ercius, L. Jin, A. Kovács, and P. D. Nellist, "Electron ptychographic phase imaging of light elements in crystalline materials using wigner distribution deconvolution", Ultramicroscopy **180**, 173–179 (2017).

[93]K. Müller, F. F. Krause, A. Béché, M. Schowalter, V. Galioit, S. Löffler, J. Verbeeck, J. Zweck, P. Schattschneider, and A. Rosenauer, "Atomic electric fields revealed by a quantum mechanical approach to electron picodiffraction", Nature Communications **5**, 5653 (2014).

[94]K. Müller-Caspary, T. Grieb, J. Müßener, N. Gauquelin, P. Hille, J. Schörmann, J. Verbeeck, S. V. Aert, M. Eickhoff, and A. Rosenauer, "Electrical polarization in AlN/GaN nanodisks measured by momentum-resolved 4D scanning transmission electron microscopy", Physical Review Letters **122**, 106102 (2019).

[95]C. Jeanguillaume and C. Colliex, "Spectrum-image: the next step in EELS digital acquisition and processing", Ultramicroscopy **28**, 252–257 (1989).

[96]J. A. Hunt and D. B. Williams, "Electron energy-loss spectrum-imaging", Ultramicroscopy **38**, 47–73 (1991).

[97]B. Rafferty and L. M. Brown, "Direct and indirect transitions in the region of the band gap using electron-energy-loss spectroscopy", Physical Review B **58**, 326–337 (1998).

[98]H. Tan, J. Verbeeck, A. Abakumov, and G. V. Tendeloo, "Oxidation state and chemical shift investigation in transition metal oxides by EELS", Ultramicroscopy **116**, 24–33 (2012).

[99]P. Torruella, R. Arenal, F. de la Peña, Z. Saghi, L. Yedra, A. Eljarrat, L. Lopez-Conesa, M. Estrader, A. Lopez-Ortega, G. Salaza-Alvarez, J. Nogues, C. Ducati, P. A. Midgley, F. Peiro, and S. Estrade, "3D visualization of the iron oxidation state in FeO/Fe3O4 core-shell nanocubes from electron energy loss tomography", Nano Letters **16**, 5068–5073 (2016).

[100]T. Riedl, T. Gemming, and K. Wetzig, "Extraction of eels white-line intensities of manganese compounds: methods, accuracy, and valence sensitivity", Ultramicroscopy **106**, 284–291 (2006).

[101]L. Bigiani, M. Hassan, D. Peddis, C. Maccato, G. Varvaro, C. Sada, E. Bontempi, S. Martí-Sánchez, J. Arbiol, and D. Barreca, "High magnetic coercivity in nanostructured Mn3O4 thin films obtained by chemical vapor deposition", Applied Nano Materials **2**, 1704–1712 (2019).

[102]V. Grillo, "Advances in stem-cell. a free software for TEM and STEM analysis and simulations: probe deconvolution in STEM-HAADF", Microscopy and Microanalysis **11**, 1292–1293 (2011).

[103]P. L. Galindo, S. Kret, A. M. Sanchez, J.-Y. Laval, A Yáñez, J Pizarro, E Guerrero, T Ben, and S. I. Molina, "The peak pairs algorithm for strain mapping from hrtem images", Ultramicroscopy **107**, 1186–1193 (2007).

[104]M. J. Hÿtch, J.-L. Putaux, and J.-M. Pénisson, "Measurement of the displacement field of dislocations to 0.03 a by electron microscopy", Nature **423**, 270–273 (2003).

[105]F. Hüe, M. Hÿtch, H. Bender, F. Houdellier, and A. Claverie, "Direct mapping of strain in a strained silicon transistor by high-resolution electron microscopy", Physical Review Letters **100**, 270–273 (2008).

[106]M. de la Mata, C. Magén, P. Caroff, and J. Arbiol, "Atomic scale strain relaxation in axial semiconductor III–V nanowire heterostructures", Nano Letters **14**, 6614–6620 (2014).

[107]P. Trebbia and N. Bonnet, "EELS elemental mapping with unconventional methods i . theoretical basis: image analysis with multivariate statistics and entropy concepts", Ultramicroscopy **34**, 165–178 (1990).

[108]M. Bosman, M. Watanabe, D. T. L. Alexander, and V. J. Keast, "Mapping chemical and bonding information using multivariate analysis of electron energy-loss spectrum images", Ultramicroscopy **106**, 1024–1032 (2006).

[109]S Bernal, J. J. Calvino, C. López-Cartes, J. A. P. omil, and J. M. Rodríguez-Izquierdo, "The interpretation of HREM images of supported metal catalysts using image simulation: profile view images", Ultramicroscopy **72**, 135–164 (1998).

[110]J. Arbiol, A. Cirera, F. Peiró, A. Cornet, J. R. Morante, J. J. Delgado, and J. J. Calvino, "Optimization of tin dioxide nanosticks faceting for the improvement of palladium nanocluster epitaxy", Applied Physics Letters **80**, 329–331 (2002).

[111]P. D. Nellist and S. J. Pennycook, "Incoherent imaging using dynamically scattered coherent electrons", Ultramicroscopy **78**, 111–124 (1999).

[112]E. J. Kirkland, *Advanced computing in electron microscopy* (Plenum, New York, NY, 1998).

[113]V. Grillo and E. Rotunno, "STEM-CELL: A software tool for electron microscopy. Part 1 - Simulations", Ultramicroscopy **125**, 97–111 (2013).

[114]V. Grillo and F. Rossi, "STEM-CELL: A software tool for electron microscopy. Part 2 - Analysis of crystalline materials", Ultramicroscopy **125**, 112–129 (2013).

[115]S. Birnera, S. Hackenbuchner, M. Sabathil, G. Zandler, J. A. Majewski, T. Andlauer, T. Zibold, R. Morschl, A. Trellakis, and P. Vogl, "Modeling of semiconducto rnanostructures with nextnano^3", Acta Physica Polonica A **110**, 2137–2142 (2006).

[116]S. Birner, T. Zibold, T. Andlauer, T. Kubis, M. Sabathil, A. Trellakis, and P. Vogl, "Nextnano: general purpose 3-D simulations", IEEE Transactions on Electron Devices **50**, 2137–2142 (2007).

[117]R. S. Wagner and W. C. Ellis, "Vapor-liquid-solid mechanism of single crystal growth", Applied Physics Letters **4**, 89–90 (1964).

[118]I Zardo, L Yu, S Conesa-Boj, S Estradé, P. J. Alet, J Rössler, M Frimmer, P. R. i Cabarrocas, F Peiró, J Arbiol, J. R. Morante, and A. F. i Morral, "Gallium assisted plasma enhanced chemical vapor deposition of silicon nanowires", Nanotechnology **20**, 155602 (2009).

[119]I. Zardo, S. Conesa-Boj, S. Estradé, L. Yu, F. Peiro, P. Roca i Cabarrocas, J. R. Morante, J. Arbiol, and A. Fontcuberta i Morral, "Growth study of indium-catalyzed silicon nanowires by plasma enhanced chemical vapor deposition", Applied Physics A **100**, 287–296 (2010).

[120]J. E. Allen, E. R. Hamesath, D. E. Perea, J. L. Lensch-Falk, Z. Y. Li, F. Yin, M. H. Gass, P. Wang, A. L. Bleloch, R. E. Palmer, and L. J. Lauhon, "High-resolution detection of Au catalyst atoms in Si nanowires", Nature Nanotechnology **3**, 168–173 (2008).

[121]D. V. Beznasyuk, E. Robin, M. D. Hertog, J. Claudon, and M. Hocevar, "Dislocation-free axial InAs-on-GaAs nanowires onsilicon", Nanotechnology **28**, 365602 (2017).

[122]H. Y. Hui, M. de la Mata, J. Arbiol, and M. A. Filler, "Low-temperature growth of axial Si/Ge nanowire heterostructures enabled by trisilane", Chemistry of Materials **29**, 3397–3402 (2017).

[123]M. Beeler, C. B. Lim, P. Hille, J. Bleuse, J. Schörmann, M. de la Mata, J. Arbiol, M. Eickhoff, and E. Monroy, "Long-lived excitons in GaN/AlN nanowire heterostructures", Physical Review B **91**, 205440 (2015).

[124]J. Lähnemann, M. Den Hertog, P. Hille, M. de la Mata, T. Fournier, J. Schörmann, J. Arbiol, M. Eickhoff, and E. Monroy, "Uv photosensing characteristics of nanowire-based GaN/AlN superlattices", Nano Letters **16**, 3260–3267 (2016).

[125]V. Schmidt, S. Senz, and U. Gösele, "Diameter-dependent growth direction of epitaxial silicon nanowires", Nano Letters **5**, 931–935 (2005).

[126]S. Guillemin, L. Rapenne, H. Roussel, E. Sarigiannidou, G. Brémond, and V. Consonni, "Formation mechanisms of ZnO nanowires: the crucial role of crystal orientation and polarity", The Journal of Physical Chemistry C **117**, 20738–20745 (2013).

[127]E. Uccelli, J. Arbiol, C. Magen, P. Krogstrup, E. Russo-Averchi, M. Heiss, G. Mugny, F. Morier-Genoud, J. Nygard, J. R. Morante, and A. F. i Morral, "Three-dimensional multiple-order twinning of self-catalyzed GaAs nanowires on Si substrates", Nano Letters **11**, 3827–3832 (2011).

[128]H. Potts, Y. van Hees, G. Tütüncüoglu, M. Friedl, J.-B. Leran, and A. Fontcuberta i Morral, “Tilting catalyst-free InAs nanowires by 3D-twinning and unusual growth directions”, Crystal Growth & Design **17**, 3596–3605 (2017).

[129]M. I. B. Utama, M. de la Mata, C. Magen, J. Arbiol, and Q. Xiong, “Twinning-, polytypism-, and polarity-induced morphological modulation in nonplanar nanostructures with van der Waals epitaxy”, Advanced Functional Materials **23**, 1636–1646 (2013).

[130]S. Conesa-Boj, E. Russo-Averchi, A. Dalmau-Mallorqui, J. Trevino, E. F. Pecora, C. Forestiere, A. Handin, M. Ek, L. Zweifel, L. R. Wallenberg, D. Rüffer, M. Heiss, D. Troadec, L. Dal Negro, P. Caroff, and A. Fontcuberta i Morral, “Vertical “III–V” V-shaped nanomembranes epitaxially grown on a patterned Si[001] substrate and their enhanced light scattering”, ACS Nano **6**, 10982–10991 (2012).

[131]E. Russo-Averchi, G. Tütüncüoglu, A. Dalmau-Mallorqui, I. C. Mundet, M. de la Mata, D. Rüffer, J. Arbiol, S. Conesa-Boj, and A. F. i Morral, “Bottom-up engineering of InAs at the nanoscale: from V-shaped nanomembranes to nanowires”, Journal of Crystal Growth **420**, 47 –56 (2015).

[132]X. Yuan, P. Caroff, J. Wong-Leung, L. Fu, H. H. Tan, and C. Jagadish, “Tunable polarity in a III–V nanowire by droplet wetting and surface energy engineering”, Advanced Materials **27**, 6096–6103 (2015).

[133]M. Heiss, Y. Fontana, A. Gustafsson, G. Wust, C. Magen, D. O. Regan, J. W. Luo, B. Ketterer, S. Conesa-Boj, A. V. Kuhlmann, l J. Houe, E. Russo-Averchi, J. R. Morante, M. Cantoni, N. Marzari, J. Arbiol, A. Zunger, R. J. Warburton, and A. Fontcuberta i Morral, “Self-assembled quantum dots in a nanowire system for quantum photonics”, Nature Materials **12**, 439–444 (2013).

[134]M. Zamani, G. Tütüncüoglu, S. Martí-Sánchez, L. Francaviglia, L. Güniat, L. Ghisalberti, H. Potts, M. Friedl, E. Markov, W. Kim, J.-B. Leran, V. G. Dubrovskii, J. Arbiol, and A. Fontcuberta i Morral, “Optimizing the yield of A-polar GaAs nanowires to achieve defect-free zinc blende structure and enhanced optical functionality”, Nanoscale **10**, 17080–17091 (2018).

[135]M. Heiss, S. Conesa-Boj, J. Ren, H.-H. Tseng, A. Gali, A. Rudolph, E. Uccelli, F. Peiró, J. R. Morante, D. Schuh, E. Reiger, E. Kaxiras, J. Arbiol, and A. Fontcuberta i Morral, “Direct correlation of crystal structure and optical properties in

wurtzite/zinc-blende GaAs nanowire heterostructures", Phys. Rev. B **83**, 045303 (2011).

[136]W. Kim, V. G. Dubrovskii, J. Vukajlovic-Plestina, G. Tütüncüoglu, L. Francaviglia, L. Güniat, H. Potts, M. Friedl, J.-B. Leran, and A. Fontcuberta i Morral, "Bistability of contact angle and its role in achieving quantum-thin self-assisted GaAs nanowires", Nano Letters **18**, 49–57 (2018).

[137]M. de la Mata, R. Leturcq, S. R. Plissard, C. Rolland, C. Magén, J. Arbiol, and P. Caroff, "Twin-induced InSb nanosails: A convenient high mobility quantum system", Nano Letters **16**, 825–833 (2016).

[138]A. M. Sanchez, Y. Zhang, E. W. Tait, N. D. M. Hine, H. Liu, and R. Beanland, "Stable defects in semiconductor nanowires", Nano Letters **17**, 2454–2459 (2017).

[139]M. Murayama and T. Nakayama, "Chemical trend of band offsets at wurtzite/zinc-blende heterocrystalline semiconductor interfaces", Phys. Rev. B **49**, 4710–4724 (1994).

[140]L. Ahtapodov, H. Kauko, A. M. Munshi, B. O. Fimland, A. T. J. van Helvoort, and H. Weman, "Determination of GaAs zinc blende/wurtzite band offsets utilizing GaAs nanowires with an axial GaAsSb insert", Journal of Applied Physics **122**, 245102 (2017).

[141]S. H. Oh, Y. Kauffmann, C. Scheu, W. D. Kaplan, and M. Ruhle, "Ordered liquid aluminum at the interface with sapphire", Science **310**, 661–663 (2005).

[142]Y. Kauffmann, S. Oh, C. Koch, A. Hashibon, C. Scheu, M. Rühle, and W. Kaplan, "Quantitative analysis of layering and in-plane structural ordering at an alumina – aluminum solid–liquid interface", Acta Materialia **59**, 4378 –4386 (2011).

[143]M. Gandman, Y. Kauffmann, and W. D. Kaplan, "Quantification of ordering at a solid-liquid interface using plasmon electron energy loss spectroscopy", Applied Physics Letters **106**, 051603 (2015).

[144]S. J. Dillon, M. Tang, W. C. Carter, and M. P. Harmer, "Complexion: a new concept for kinetic engineering in materials science", Acta Materialia **55**, 6208 –6218 (2007).

[145]R. Brydson and N. Hondow, *Aberration-corrected analytical transmission electron microscopy*, 1st ed., Chapter 4 (John Wiley & Sons, Ltd., 2011).

[146]R. F. Egerton, *Electron energy-loss spectroscopy in the electron microscope*, 3rd ed. (Springer US, 2011).

[147]A. Maigné and R. D. Twesten, "Review of recent advances in spectrum imaging and its extension to reciprocal space.", Journal of electron microscopy **58 3**, 99–1091 (2009).

[148]J. Wang, S. R. Plissard, M. A. Verheijen, L.-F. Feiner, A. Cavalli, and E. P. A. M. Bakkers, "Reversible switching of InP nanowire growth direction by catalyst engineering", Nano Letters **13**, 3802–3806 (2013).

[149]A. H. Carim, K.-K. Lew, and J. M. Redwing, "Bicrystalline silicon nanowires", Advanced Materials **13**, 1489–1491 (2001).

[150]S. Conesa-Boj, I. Zardo, S. Estradé, L. Wei, P. Jean Alet, P. Roca i Cabarrocas, J. R. Morante, F. Peiró, A. F. i. Morral, and J. Arbiol, "Defect formation in Ga-catalyzed silicon nanowires", Crystal Growth & Design **10**, 1534–1543 (2010).

[151]Z. Sun, D. N. Seidman, and L. J. Lauhon, "Nanowire kinking modulates doping profiles by reshaping the liquid–solid growth interface", Nano Letters **17**, 4518–4525 (2017).

[152]L Guinat, S. Martí-Sánchez, O Garcia, M. Boschardin, D Vindice, N Tappy, Martin, M Friedl, W Kim, M Zamani, L Francavila, A Balgakashi, J.-B. Leran, J Arbiol, and A Fontcuberta i Morral, "III-V integration on Si (100) : vertical nanospades", ACS Nano **13**, 5833–5840 (2019).

[153]L. Mancini, Y. Fontana, S. Conesa-Boj, I. Blum, F. Vurpillot, L. Francaviglia, E. Russo-Averchi, M. Heiss, J. Arbiol, A. F. i. Morral, and L. Rigutti, "Three-dimensional nanoscale study of Al segregation and quantum dot formation in GaAs/AlGaAs core-shell nanowires", Applied Physics Letters **105**, 243106 (2014).

[154]G. Tutuncuoglu, M. de la Mata, D. Deiana, H. Potts, F. Matteini, J Arbiol, and A Fontcuberta i Morral, "Towards defect-free 1-D GaAs/AlGaAs heterostructures based on GaAs nanomembranes", Nanoscale **7**, 19453–19460 (2015).

[155]C. Zheng, J. Wong-Leung, Q. Gao, H. H. Tan, C. Jagadish, and J. Etheridge, "Polarity-driven 3-fold symmetry of GaAs/AlGaAs core multishell nanowires", Nano Letters **13**, 3742–3748 (2013).

[156]L. Francaviglia, G. Tütüncüoglu, S. Martí-Sánchez, E. Di Russo, S. Escobar Steinvall, J. Segura Ruiz, H. Potts, M. Friedl, L. Rigutti, J. Arbiol, and A. Fontcuberta i Morral, "Segregation scheme of indium in AlGaInAs nanowire shells", Phys. Rev. Materials **3**, 023001 (2019).

[157]K. Storm, F. Halvardsson, M. Heurlin, D. Lindgren, A. Gustafsson, P. M. Wu, B. Monemar, and L. Samuelson, "Spatially resolved Hall effect measurement in a single semiconductor nanowire", Nature Nanotechnology **7**, 718 –722 (2012).

[158]D. Tsivion, M. Schvartzman, R. Popovitz-Biro, P. von Huth, and E. Joselevich, "Guided growth of millimeter-long horizontal nanowires with controlled orientations", Science **333**, 1003–1007 (2011).

[159]Y. Zi, K. Jung, D. Zakharov, and C. Yang, "Understanding self-aligned planar growth of InAs nanowires", Nano Letters **13**, 2786–2791 (2013).

[160]D. Tsivion, M. Schvartzman, R. Popovitz-Biro, and E. Joselevich, "Guided growth of horizontal ZnO nanowires with controlled orientations on flat and faceted sapphire surfaces", ACS Nano **6**, 6433–6445 (2012).

[161]E. Shalev, E. Oksenberg, K. Rechav, R. Popovitz-Biro, and E. Joselevich, "Guided CdSe nanowires parallelly integrated into fast visible-range photodetectors", ACS Nano **11**, 213–220 (2017).

[162]E. Oksenberg, R. Popovitz-Biro, K. Rechav, and E. Joselevich, "Guided growth of horizontal ZnSe nanowires and their integration into high-performance blue–UV photodetectors", Advanced Materials **27**, 3999–4005 (2015).

[163]G. Reut, E. Oksenberg, R. Popovitz-Biro, K. Rechav, and E. Joselevich, "Guided growth of horizontal p-type ZnTe nanowires", The Journal of Physical Chemistry C **120**, 17087–17100 (2016).

[164]B. Nikoobakht, C. A. Michaels, S. J. Stranick, and M. D. Vaudin, "Horizontal growth and in situ assembly of oriented zinc oxide nanowires", Applied Physics Letters **85**, 3244–3246 (2004).

[165]H. Jeon, J. Ding, W. Patterson, A. V. Nurmikko, W. Xie, D. C. Grillo, M. Kobayashi, and R. L. Gunshor, "Blue-green injection laser diodes in (Zn,Cd)Se/ZnSe quantum wells", Applied Physics Letters **59**, 3619–3621 (1991).

[166]Q. Wu, M. Litz, and X. Zhang, "Broadband detection capability of ZnTe electro-optic field detectors", Applied Physics Letters **68**, 2924–2926 (1996).

[167]J. Bang, J. Park, J. H. Lee, N. Won, J. Nam, J. Lim, B. Y. Chang, H. J. Lee, B. Chon, J. Shin, J. B. Park, J. H. Choi, K. Cho, S. M. Park, T. Joo, and S. Kim, "ZnTe/ZnSe (core/shell) type-II quantum dots: their optical and photovoltaic properties", Chemistry of Materials **22**, 233–240 (2010).

[168]R. Peköz, "Ab initio study of structural and electronic properties of single crystal and core/shell II-VI semiconductor nanowires", Computational Materials Science **123**, 158 –163 (2016).

[169]C. Zhang, X. Miao, K. D. Chabak, and X. Li, "A review of III–V planar nanowire arrays: selective lateral VLS epitaxy and 3D transistors", Journal of Physics D: Applied Physics **50**, 393001 (2017).

[170]R. Gabai, A. Ismach, and E. Joselevich, "Nanofacet lithography: a new bottom-up approach to nanopatterning and nanofabrication by soft replication of spontaneously faceted crystal surfaces", Advanced Materials **19**, 1325–1330 (2007).

[171]E. Shalev, E. Oksenberg, K. Rechav, R. Popovitz-Biro, and E. Joselevich, "Guided cdse nanowires parallelly integrated into fast visible-range photodetectors", ACS Nano **11**, 213–220 (2017).

[172]P. A. Cherenkov, "Visible emission of clean liquids by action of γ radiation", in Dokl. akad. nauk sssr, Vol. 2, 8 (1934), pp. 451–454.

[173]S. Korneychuk, B. Partoens, G. Guzzinati, R. Ramaneti, J. Derluyn, K. Haenen, and J. Verbeeck, "Exploring possibilities of band gap measurement with off-axis EELS in TEM", Ultramicroscopy **189**, 76 –84 (2018).

[174]M. Stoger-Pollach, H. Franco, P. Schattschneider, S. Lazar, B. Schaffer, W. Grogger, and H. Zandbergen, "Cerenkov losses: a limit for bandgap determination and Kramers–Kronig analysis", Micron **37**, Proceedings of the International Workshop on Enhanced Data Generated with Electrons (EDGE), 396 –402 (2006).

[175]L. Gu, V. Srot, W. Sigle, C. Koch, P. van Aken, F. Scholz, S. B. Thapa, C. Kirchner, M. Jetter, and M. Rühle, "Band-gap measurements of direct and indirect semiconductors using monochromated electrons", Phys. Rev. B **75**, 195214 (2007).

[176]N. Brodusch, H. Demers, A. Gellé, A. Moores, and R. Gauvin, "Electron energy-loss spectroscopy (EELS) with a cold-field emission scanning electron microscope at low accelerating voltage in transmission mode", Ultramicroscopy **203**, 75th Birthday of Christian Colliex, 85th Birthday of Archie Howie, and 75th Birthday of Hannes Lichte / PICO 2019 - Fifth Conference on Frontiers of Aberration Corrected Electron Microscopy, 21 –36 (2019).

[177]M Polyanskiy, (2008) `https://refractiveindex.info/`.

[178]C. S. Granerød, W. Zhan, and Øystein Prytz, "Automated approaches for band gap mapping in STEM-EELS", Ultramicroscopy **184**, 39 –45 (2018).

[179]D. Keller, S. Buecheler, P. Reinhard, F. Pianezzi, D. Pohl, A. Surrey, B. Rellinghaus, R. Erni, and A. N. Tiwari, "Local band gap measurements by VEELS of thin film solar cells", Microscopy and Microanalysis **20**, 1246–1253 (2014).

[180]B. Rafferty, S. J. Pennycook, and L. M. Brown, "Zero loss peak deconvolution for bandgap EEL spectra", Journal of Electron Microscopy **49**, 517–524 (2000).

[181]D. R. G. Mitchell, *Savitzky-Golay spectral filter for digitalmicrograph*, http://www.dmscripting.com/savitzky-golay_spectral_filter.html.

[182]P Schattschneider, M Stöger, C Hébert, and B Jouffrey, "The separation of surface and bulk contributions in ELNES spectra", Ultramicroscopy **93**, 91 –97 (2002).

[183]F. J. García de Abajo and A. Howie, "Retarded field calculation of electron energy loss in inhomogeneous dielectrics", Phys. Rev. B **65**, 115418 (2002).

[184]F. J. García de Abajo, "Optical excitations in electron microscopy", Rev. Mod. Phys. **82**, 209–275 (2010).

[185]F. J. García de Abajo and A. Howie, "Relativistic electron energy loss and electron-induced photon emission in inhomogeneous dielectrics", Phys. Rev. Lett. **80**, 5180–5183 (1998).

[186]M. Aven, D. T. F. Marple, and B. Segall, "Some electrical and optical properties of ZnSe", Journal of Applied Physics **32**, 2261–2265 (1961).

[187]F. Kootstra, P. L. de Boeij, and J. G. Snijders, "Application of time-dependent density-functional theory to the dielectric function of various nonmetallic crystals", Phys. Rev. B **62**, 7071–7083 (2000).

[188]D. N. Talwar and P. Becla, "Polarization dependent reflectivity and transmission for Cd1-XZnxTe/GaAs(001) epifilms in the far-infrared and near-infrared to ultraviolet region", in (2016).

[189]A. K. Harman, S. Ninomiya, and S. Adachi, "Optical constants of sapphire (α-Al2O3) single crystals", Journal of Applied Physics **76**, 8032–8036 (1994).

[190]W. S. M. Werner, K. Glantschnig, and C. Ambrosch-Draxl, "Optical constants and inelastic electron-scattering data for 17 elemental metals", Journal of Physical and Chemical Reference Data **38**, 1013–1092 (2009).

[191]S. K. Yadav, V. Sharma, and R. Ramprasad, "Controlling electronic structure through epitaxial strain in ZnSe/ZnTe nano-heterostructures", Journal of Applied Physics **118**, 015701 (2015).

[192]D. Muller and J. Silcox, "Delocalization in inelastic scattering", Ultramicroscopy **59**, 195 –213 (1995).

[193]J. A. Joyce B. D.and Baldrey, "Selective epitaxial deposition of silicon", Nature **195**, 485–486 (1962).

[194]A. Y. Cho, "Recent developments in molecular beam epitaxy (MBE)", Journal of Vacuum Science and Technology **16**, 275–284 (1979).

[195]K. Ikejiri, J. Noborisaka, S. Hara, J. Motohisa, and T. Fukui, "Mechanism of catalyst-free growth of GaAs nanowires by selective area MOVPE", Journal of Crystal Growth **298**, 616 –619 (2007).

[196]K. Ikejiri, T. Sato, H. Yoshida, K. Hiruma, J. Motohisa, S. Hara, and T. Fukui, "Growth characteristics of GaAs nanowires obtained by selective area metal–organic vapour-phase epitaxy", Nanotechnology **19**, 265604 (2008).

[197]K. Tomioka, Y. Kobayashi, J. Motohisa, S. Hara, and T. Fukui, "Selective-area growth of vertically aligned GaAs and GaAs/AlGaAs core–shell nanowires on Si(111) substrate", Nanotechnology **20**, 145302 (2009).

[198]H. Yoshida, K. Ikejiri, T. Sato, S. Hara, K. Hiruma, J. Motohisa, and T. Fukui, "Analysis of twin defects in GaAs nanowires and tetrahedra and their correlation to GaAs(111)B surface reconstructions in selective-area metal organic vapour-phase epitaxy", Journal of Crystal Growth **312**, 52 –57 (2009).

[199]Z. Yang, A. Surrente, G. Tutuncuoglu, K. Galkowski, M. Cazaban-Carrazé, F. Amaduzzi, P. Leroux, D. K. Maude, A. Fontcuberta i Morral, and P. Plochocka, "Revealing large-scale homogeneity and trace impurity sensitivity of GaAs nanoscale membranes", Nano Letters **17**, 2979–2984 (2017).

[200]M. Friedl, K. Cerveny, P. Weigele, G. Tütüncüoglu, S. Martí-Sánchez, C. Huang, T. Patlatiuk, H. Potts, Z. Sun, M. O. Hill, L. Güniat, W. Kim, M. Zamani, V. G. Dubrovskii, J. Arbiol, L. J. Lauhon, D. M. Zumbühl, and A. Fontcuberta i Morral, "Template-assisted scalable nanowire networks", Nano Letters **18**, 2666–2671 (2018).

[201]F. F. Charles, v. d. M. J. H., and M. N. Francis, “One-dimensional dislocations iv. dynamics”, Proceedings of the Royal Society of London. Series A. Mathematical and Physical Sciences **201**, 261–268 (1950).

[202]M. Volmer and A. Weber, “Nucleus formation in supersaturated systems”, Zeitschrift für Physikalische Chemie **119**, 277–301 (1926).

[203]I. N. Stranski and L. Krastanov, “Zur theorie der orientierten ausscheidung von ionenkristailen aufeinander”, Monatshefte für Chemie und verwandte Teile anderer Wissenschaften **71**, 351–364 (1937).

[204]S. Arab, C.-Y. Chi, T. Shi, Y. Wang, D. P. Dapkus, H. E. Jackson, L. M. Smith, and S. B. Cronin, “Effects of surface passivation on twin-free GaAs nanosheets”, ACS Nano **9**, 1336–1340 (2015).

[205]C.-Y. Chi, C.-C. Chang, S. Hu, T.-W. Yeh, S. B. Cronin, and P. D. Dapkus, “Twin-free GaAs nanosheets by Selective Area growth: implications for defect-free nanostructures”, Nano Letters **13**, 2506–2515 (2013).

[206]M. Hetzl, M. Kraut, J. Winnerl, L. Francaviglia, M. Döblinger, S. Matich, A. Fontcuberta i Morral, and M. Stutzmann, “Strain-induced band gap engineering in selectively grown GaN–(Al,Ga)N core–shell nanowire heterostructures”, Nano Letters **16**, 7098–7106 (2016).

[207]U. Kaiser, A. Chuvilin, P. Brown, and W. Richter, “Origin of threefold periodicity in high-resolution transmission electron microscopy images of thin film cubic SiC”, Microscopy and Microanalysis **5**, 420–427 (1999).

[208]Z. Wang, H. Guo, S. Shao, M. Saghayezhian, J. Li, R. Fittipaldi, A. Vecchione, P. Siwakoti, Y. Zhu, J. Zhang, and E. W. Plummer, “Designing antiphase boundaries by atomic control of heterointerfaces”, Proceedings of the National Academy of Sciences **115**, 9485–9490 (2018).

[209]D. Car, J. Wang, M. A. Verheijen, E. P. A. M. Bakkers, and S. R. Plissard, “Rationally designed single-crystalline nanowire networks”, Advanced Materials **26**, 4875–4879 (2014).

[210]T. Rieger, D. Rosenbach, D. Vakulov, S. Heedt, T. Schäpers, D. Grützmacher, and M. I. Lepsa, “Crystal phase transformation in self-assembled InAs nanowire junctions on patterned Si substrates”, Nano Letters **16**, 1933–1941 (2016).

[211]J.-H. Kang, Y. Cohen, Y. Ronen, M. Heiblum, R. Buczko, P. Kacman, R. Popovitz-Biro, and H. Shtrikman, "Crystal structure and transport in merged InAs nanowires MBE grown on (001) InAs", Nano Letters **13**, 5190–5196 (2013).

[212]F. Krizek, T. Kanne, D. Razmadze, E. Johnson, J. Nygård, C. M. Marcus, and P. Krogstrup, "Growth of InAs wurtzite nanocrosses from hexagonal and cubic basis", Nano Letters **17**, 6090–6096 (2017).

[213]S. Gazibegovic, D. Car, H. Zhang, S. C. Balk, J. A. Logan, M. W. A. de Moor, M. C. Cassidy, R. Schmits, D Xu, G. Wang, P. Krogstrup, R. L. M. Op het Veld, K. Zuo, Y. Vos, J. Shen, D. Bouman, B. Shojaei, D. Pennachio, J. S. Lee, P. J. van Veldhoven, S. Koelling, M. A. Verheijen, L. P. Kouwenhoven, C. J. Palmstrøm, and E. P. A. M. Bakkers, "Epitaxy of advanced nanowire quantum devices", Nature **548**, 434–438 (2017).

[214]N Moll, M Scheffler, and E Pehlke, "Influence of surface stress on the equilibrium shape of strained quantum dots", Plysical Review B **58**, 4566–4571 (1998).

[215]L. Zeng, C. Gammer, B. Ozdol, T. Nordqvist, J. Nygård, P. Krogstrup, A. M. Minor, W. Jäger, and E. Olsson, "Correlation between electrical transport and nanoscale strain in InAs/In0.6Ga0.4As core–shell nanowires", Nano Letters **18**, 4949–4956 (2018).

[216]M. O. Lipinski, H. Schuler, O. G. Schmidt, K. Eberl, and N. Y. Jin-Phillipp, "Strain-induced material intermixing of InAs quantum dots in GaAs", Applied Physics Letters **77**, 1789–1791 (2000).

[217]E. Ahmad, M. R. Karim, S. B. Hafiz, C. L. Reynolds, Y. Liu, and S. Iyer, "A two-step growth pathway for high Sb incorporation in GaAsSb nanowires in the telecommunication wavelength range", Scientific Reports **7**, 10111 (2017).

[218]W. Sarney, S. Svensson, E. Anderson, A. Lundquist, C. Pearson, and J. Millunchick, "The influence of growth temperature on Sb incorporation in InAsSb, and the temperature-dependent impact of Bi surfactants", Journal of Crystal Growth **406**, 8 –11 (2014).

[219]E. A. Anyebe, M. K. Rajpalke, T. D. Veal, C. J. Jin, Z. M. Wang, and Q. D. Zhuang, "Surfactant effect of antimony addition to the morphology of self-catalyzed InAs1-xSbx nanowires", Nano Research **8**, 1309–1319 (2015).

[220]Önder Gül, D. J. van Woerkom, I. van Weperen, D. Car, S. R. Plissard, E. P. A. M. Bakkers, and L. P. Kouwenhoven, "Towards high mobility InSb nanowire devices", Nanotechnology **26**, 215202 (2015).

[221]L Desplanque, A Bucamp, D Troadec, G Patriarche, and X Wallart, "In-plane InSb nanowires grown by selective area molecular beam epitaxy on semi-insulating substrate", Nanotechnology **29**, 305705 (2018).

[222]A. Kitaev, "Fault-tolerant quantum computation by anyons", Annals of Physics **303**, 2 –30 (2003).

[223]R. M. Lutchyn, J. D. Sau, and S. D. Sarma, "Majorana fermions and a topological phase transition in semiconductor-superconductor heterostructures", Phys. Rev. Lett. **105**, 077001 (2010).

[224]C. Nayak, S. H. Simon, A. Stern, M. Freedman, and S. Das Sarma, "Non-abelian anyons and topological quantum computation", Rev. Mod. Phys. **80**, 1083–1159 (2008).

[225]S. M. Albrecht, A. P. Higginbotham, M. Madsen, F. Kuemmeth, T. S. Jespersen, J. Nygård, P. Krogstrup, and C. M. Marcus, "Exponential protection of zero modes in Majorana islands", Nature **531**, 206 –209 (2016).

[226]F. Wilczek, "Majorana returns", Nature Physics **5**, 614–618 (2009).

[227]E. Majorana, "Teoria simmetrica dell'elettrone e del positrone", Il Nuovo Cimento (1924-1942) **14**, 171 (1937).

[228]J. D. Sau, R. M. Lutchyn, S. Tewari, and S. Das Sarma, "Generic new platform for topological quantum computation using semiconductor heterostructures", Phys. Rev. Lett. **104**, 040502 (2010).

[229]A. Das, Y. Ronen, Y. Most, Y. Oreg, M. Heiblum, and H. Shtrikman, "Zero-bias peaks and splitting in an Al-InAs nanowire topological superconductor as a signature of Majorana fermions", Nature Physics **8**, 887–895 (2012).

[230]M. Deng, C. Yu, G. Huang, M. Larsson, P. Caroff, and H. Xu, "Anomalous zero-bias conductance peak in a Nb-InSb nanowire-Nb hybrid device", Nano letters **12**, 6414–6419 (2012).

[231]S. D. Sarma, J. D. Sau, and T. D. Stanescu, "Splitting of the zero-bias conductance peak as smoking gun evidence for the existence of the majorana mode in a superconductor-semiconductor nanowire", Physical Review B **86**, 220506 (2012).

[232]L. P. Rokhinson, X. Liu, and J. K. Furdyna, "The fractional ac Josephson effect in a semiconductor–superconductor nanowire as a signature of Majorana particles", Nature Physics **8**, 795 (2012).

[233]V. Mourik, K. Zuo, S. M. Frolov, S. R. Plissard, E. P. A. M. Bakkers, and L. P. Kouwenhoven, "Signatures of Majorana fermions in hybrid superconductor-semiconductor nanowire devices", Science **336**, 1003–1007 (2012).

[234]Y. Oreg, G. Refael, and F. von Oppen, "Helical liquids and Majorana bound states in quantum wires.", Physical review letters **105 17**, 177002 (2010).

[235]T. D. Stanescu and S. Das Sarma, "Superconducting proximity effect in semiconductor nanowires", Phys. Rev. B **87**, 180504 (2013).

[236]Y. Liu, A. Luchini, S. Martí-Sánchez, C. Koch, S. Schuwalow, S. A. Khan, T. Stankevič, S. Francoua, J. R. Mardegan, J. A. Krieger, et al., "Coherent epitaxial semiconductor-ferromagnetic insulator InAs/EuS interfaces: band alignment and magnetic structure", ACS Applied Materials & Interfaces (2019).

[237]S. R. Plissard, I. van Weperen, D. Car, M. A. Verheijen, G. W. G. Immink, J. Kammhuber, L. J. Cornelissen, D. B. Szombati, A. Geresdi, S. M. Frolov, L. P. Kouwenhoven, and E. P. A. M. Bakkers, "Formation and electronic properties of InSb nanocrosses", Nature Nanotechnology **8**, 859 864 (2013).

[238]S. Vaitiekénas, A. M. Whiticar, M.-T. Deng, F. Krizek, J. E. Sestoft, C. J. Palmstrom, S. Marti-Sanchez, J. Arbiol, P. Krogstrup, L. Casparis, and C. M. Marcus, "Selective-area-grown semiconductor-superconductor hybrids: a basis for topological networks", Phys. Rev. Lett. **121**, 147701 (2018).

[239]S. Takei, B. M. Fregoso, H.-Y. Hui, A. M. Lobos, and S. Das Sarma, "Soft superconducting gap in semiconductor Majorana nanowires", Phys. Rev. Lett. **110**, 186803 (2013).

[240]S. Lamari, "Zero field spin splitting in inversion layers on p-InSb: a fully numerical study", Journal of Applied Physics **91**, 1698–1700 (2002).

[241]F. Qu, J. van Veen, F. K. de Vries, A. J. A. Beukman, M. Wimmer, W. Yi, A. A. Kiselev, B.-M. Nguyen, M. Sokolich, M. J. Manfra, F. Nichele, C. M. Marcus, and L. P. Kouwenhoven, "Quantized conductance and large g-factor anisotropy in InSb quantum point contacts", Nano Letters **16**, 7509–7513 (2016).

[242]P. Caroff, M. E. Messing, B. M. Borg, K. A. Dick, K. Deppert, and L.-E. Wernersson, “InSb heterostructure nanowires: MOVPE growth under extreme lattice mismatch”, Nanotechnology **20**, 495606 (2009).

[243]L. Lugani, D. Ercolani, F. Rossi, G. Salviati, F. Beltram, and L. Sorba, “Faceting of InAs-InSb heterostructured nanowires”, Crystal Growth & Design **10**, 4038–4042 (2010).

[244]G. Allison, T. Fujita, K. Morimoto, S. Teraoka, M. Larsson, H. Kiyama, A. Oiwa, S. Haffouz, D. G. Austing, A. Ludwig, A. D. Wieck, and S. Tarucha, “Tuning the electrically evaluated electron Landé g factor in GaAs quantum dots and quantum wells of different well widths”, Phys. Rev. B **90**, 235310 (2014).

[245]I. J. Guilaran, D. E. Read, R. L. Kallaher, P. Xiong, S. von Molnár, P. A. Stampe, R. J. Kennedy, and J. Keller, “Observation of anomalous Hall effect in thin film EuS”, Phys. Rev. B **68**, 144424 (2003).

[246]O. Gül, H. Zhang, F. K. de Vries, J. van Veen, K. Zuo, V. Mourik, S. Conesa-Boj, M. P. Nowak, D. J. van Woerkom, M. Quintero-Pérez, M. C. Cassidy, A. Geresdi, S. Koelling, D. Car, S. R. Plissard, E. P. A. M. Bakkers, and L. P. Kouwenhoven, “Hard superconducting gap in InSb nanowires”, Nano Letters **17**, 2690–2696 (2017).

[247]K. A. Dick, C. Thelander, L. Samuelson, and P. Caroff, “Crystal phase engineering in single InAs nanowires”, Nano Letters **10**, 3494–3499 (2010).

[248]H. J. Joyce, J. Wong-Leung, Q. Gao, H. H. Tan, and C. Jagadish, “Phase perfection in zinc blende and wurtzite III-V nanowires using basic growth parameters”, Nano Letters **10**, 908–915 (2010).

[249]H. Potts, M. Friedl, F. Amaduzzi, K. Tang, G. Tütüncüoglu, F. Matteini, E. Alarcon Lladó, P. C. McIntyre, and A. Fontcuberta i Morral, “From twinning to pure zincblende catalyst-free InAs(Sb) nanowires”, Nano Letters **16**, 637–643 (2016).

[250]H. Shtrikman, R. Popovitz-Biro, A. Kretinin, L. Houben, M. Heiblum, M. Bukała, M. Galicka, R. Buczko, and P. Kacman, “Method for suppression of stacking faults in wurtzite III-V nanowires”, Nano Letters **9**, 1506–1510 (2009).

[251]Y. Liu, S. Vaitiekėnas, S. Martí-Sànchez, C. Koch, S. Hart, Z. Cui, T. Kanne, S. A. Khan, R. Tanta, S. Upadhyay, M. E. Cachaza, C. M. Marcus, J. Arbiol, K. A. Moler, and P. Krogstrup, “Semiconductor - ferromagnetic insulator - superconductor nanowires: stray field and exchange field”, Nano Letters **20**, 456–462 (2019).

[252]M. Ohring, "Chapter 8 - epitaxy", in *Materials science of thin films (second edition)*, edited by M. Ohring, Second Edition (Academic Press, San Diego, 2002), pp. 417 –494.

[253]D. Rainis and D. Loss, "Majorana qubit decoherence by quasiparticle poisoning", Phys. Rev. B **85**, 174533 (2012).

[254]F. Sánchez, C. Ocal, and J. Fontcuberta, "Tailored surfaces of perovskite oxide substrates for conducted growth of thin films", Chem. Soc. Rev. **43**, 2272–2285 (2014).

[255]M. Holland, M. van Dal, B. Duriez, R. Oxland, G. Vellianitis, G. Doornbos, A. Afzalian, T.-K. Chen, C.-H. Hsieh, P. Ramvall, T. Vasen, Y.-C. Yeo, and M. Passlack, "Atomically flat and uniform relaxed III-V epitaxial films on silicon substrate for heterogeneous and hybrid integration", Scientific Reports **7**, 14632 (2017).

[256]T. Zheleva, K. Jagannadham, and J. Narayan, "Epitaxial growth in large-lattice-mismatch systems", Journal of Applied Physics **75**, 860–871 (1994).

[257]M. Bjergfelt, D. J. Carrad, T. Kanne, M. Aagesen, E. M. Fiordaliso, E. Johnson, B. Shojaei, C. J. Palmstrøm, P. Krogstrup, T. S. Jespersen, and J. Nygård, "Superconducting vanadium/indium-arsenide hybrid nanowires", Nanotechnology **30**, 294005 (2019).

[258]B. T. Matthias, T. H. Geballe, and V. B. Compton, "Superconductivity", Rev. Mod. Phys. **35**, 1–22 (1963).

[259]J. Eisenstein, "Superconducting elements", Rev. Mod. Phys. **26**, 277–291 (1954).

Appendix A
List of acronyms, symbols & notation

A.1 Acronyms

ADF - Annular Dark Field

APB - Antiphase Boundary

BF - Bright Field

CL - Cathodoluminiscence

CMOS - Complementary metal–oxide–semiconductor

DF - Dark Field

EDX - Energy Dispersive X-Ray Spectroscopy

EELS - Electron Energy Loss Spectroscopy

fcc - Face Centered Cubic

FFT - Fast Fourier Transform

FE - Field Effect

FIB - Focused Ion Beam

FMI - Ferromagnetic Insulator

GG - Guided Growth

GPA - Geometric Phase Analysis

HRTEM - High Resolution Transmission Electron Microscopy

(L/M/H)AADF - (Low/Middle/High) Angular Annular Dark Field

MBE - Molecular Beam Epitaxy

NM - Nanomembrane

NW - Nanowire

PCA - Principal Component Analysis

PL - Photoluminiscence

QD - Quantum Dot

SAE - Selected Area Epitaxy

SAG - Selected Area Growth

SE - Semiconductor

SF - Stacking Fault

SEM - Scanning Electron Microscopy

STEM - Scanning Transmission Electron Microscopy

SU - Superconductor

TB - Twin Boundary

TEM - Transmission Electron Microscopy

VLS - Vapor-Liquid-Solid

VS - Vapor-Solid

WZ - Wurtzite

ZB - Zinc Blende

A.2 Symbols

Z - Atomic Weight

a - Lattice constant

d_{hkl} - Plane spacing

ε - Mismatch

ε_{ij} - Strain matrix component ij

D - Dilatation

R - Rotation

C_{ij} - Aberration coefficients

μ - Mobility

E_g - Band gap

A.3 Notation

(hk(i)l) - Crystallographic plane

{**hk(i)l**} - Crystallographic family of planes

[hk(i)l] - Zone axis or crystallographic direction hk(i)l

<hk(i)l> - Equivalent crystallographic directions

A/B/.../C - Epitaxy of A on B on ... on C substrate

A@B@C@... - Core (A) @ shell 1 (B) @ shell 2 (C) @... configuration

Appendix B
List of Publications

B.1 Publications

Publications related with the PhD

- E. Oksenberg, S. Martí-Sánchez, R. Popovitz-Biro, J. Arbiol and E. Joselevich, *"Surface-Guided Core-Shell ZnSe@ZnTe Nanowires as Radial p-n Heterojunctions with Photovoltaic Behavior"*, ACS Nano, **11**, 6155-6166 (2017).
- P. Neuderth, P. Hille, J. Schörmann, A. Frank, C. Reitz, S. Martí-Sánchez, M. de la Mata, M.Coll, J. Arbiol, R. Marschallh and M. Eickhoff, *"Passivation layers for nanostructured photoanodes: ultra-thin oxides on InGaN nanowires"*, Journal of Materials Chemistry A, **6**, 565-573 (2018).
- J. Müßener , L. A. Th. Greif, S. Kalinowski , G. Callsen , P.l Hille, J. Schörmann, M. R. Wagner , A. Schliwa , S. Martí-Sánchez, J. Arbiol , A. Hoffmann and M. Eickhoff, *"Optical Emission of GaN/AlN Quantum-Wires - The Role of Charge Transfer from the Nanowire Template "*, Nanoscale, **18**, 2557-2563 (2018).
- M. Friedl, K. Kristopher Cerveny, P. Weigele, G. Tütüncüoglu, S. Marti-Sánchez, C. Huang, T. Patlatiuk, H. Potts, Z. Sun, M. O Hill, L. Güniat, W. Kim, M. Zamani, V. G. Dubrovskii, J. Arbiol, L. J. Lauhon, D. M. Zumbühl and A. Fontcuberta i Morral, *"Template-assisted scalable nanowire networks"*, Nano Letters, **18**, 2666-2671 (2018).
- M. Zamani, G. Tütüncüoglu , S. Martí-Sánchez, L. Francaviglia, E. Markov, W. Kim, L. Güniat, L. Ghisalberti, H. Potts, M. Friedl, J-B Leran, V. G. Dubrovskii, J. Arbiol and A. Fontcuberta i Morra, *"Optimizing the yield of A-polar GaAs nanowires to achieve defect-free zinc blende structure and enhanced optical functionality"*, Nanoscale, **10**, 17080-17091 (2018).

- P. Neuderth, P. Hille, S. Martí-Sánchez, M. de la Mata, M. Coll, J. Arbiol and M. Eickhoff, *"Optical Analysis of Oxygen Self-Diffusion in Ultrathin CeO_2 Layers at Low Temperatures"*, Advanced Energy Materials, **8**, 1802120 (2018).

- F. Krizek, J.E. Sestoft, P. Aseev, S. Martí-Sánchez, S. Vaitiekėnas, L. Casparis, S. A. Khan, Y. Liu, T. Stankevič, A. M. Whiticar, A. Fursina, F. Boekhout, R. Koops, E. Uccelli, L. P. Kouwenhoven, C. M. Marcus, J.Arbiol and P. Krogstrup, *"Field effect enhancement in buffered quantum nanowire networks"*, Physical Review Materials, **2**, 093401 (2018).

- S. Vaitiekėnas, A. M. Whiticar, M.-T. Deng, F. Krizek, J. E. Sestoft, C. J.Palmstrøm, S. Martí-Sánchez, J. Arbiol, P. Krogstrup, L. Casparis and C. M. Marcus, *"Selective-Area-Grown Semiconductor-Superconductor Hybrids: A Basis for Topological Networks"*, Physical Review Letters, **121**, 147701 (2018).

- P. Aseev, A. Fursina, F. Boekhout, F. Krizek, J. E. Sestoft, F. Borsoi, S. Heedt, G. Wang, L. Binci, S. Martí-Sánchez, T. Swoboda, R. Koops, E. Uccelli, J. Arbiol, P. Krogstrup, L. P. Kouwenhoven and P. Caroff , *"Selectivity map for molecular beam epitaxy of advanced III-V quantum nanowire networks"*, Nano Letters, **19**, 218-227 (2019).

- L. Francaviglia, G. Tütüncüoglu, S. Martí-Sánchez, E. Di Russo, S. Escobar Steinvall, J. Segura Ruiz, H. Potts, M. Friedl, L. Rigutti, J. Arbiol and A. Fontcuberta i Morral, *" Segregation scheme of indium in AlGaInAs nanowire shells"*, Physical Review Materials, **3**, 023001 (2019).

- L. Bigiani, M. Hassan, D. Peddis, C. Maccato, G. Varvaro, C. Sada, E. Bontempi, S. Martí-Sánchez, J. Arbiol and D. Barreca, *"High Magnetic Coercivity in Nanostructured Mn_3O_4 Thin Films Obtained by Chemical Vapor Deposition"*, ACS Appl. Nano Mater., **2**, 1704-1712 (2019).

- L. Güniat, S. Martí-Sánchez, O. Garcia, M. Boscardin, D. Vindice, N. Tappy, M. Friedl, W. Kim, M. Zamani, L. Francaviglia, A. Balgarkashi, J-B. Leran, J. Arbiol and A. Fontcuberta i Morral, *". III-V Integration on Si(100): Vertical Nanospades"*, ACS Nano, **13**, 5833-5840 (2019).

- M. de la Mata, R. R. Zamani, S. Martí-Sánchez , M.Eickhoff, Q. Xiong, A. Fontcuberta i Morral, P. Caroff and J. Arbiol,*"The Role of Polarity in Nonplanar Semiconductor Nanostructures"*, Nano Letters, **19**, 3396-3408 (2019).

- P. Aseev, G. Wang, L. Binci, A. Singh, S. Martí-Sánchez, M. Botifoll, L. J. Stek, A. Bordin, J. D. Watson, F. Boekhout, D. Abel, J. Gamble, K. Van Hoogdalem, J. Arbiol, L. Kouwenhoven, G. de Lange, P. Caroff, *"Ballistic InSb Nanowires and Networks via Metal-Sown Selective Area Growth"*, Nano Letters, **19**, 9102-9111 (2019).

- Y. Liu, S. Vaitiekėnas, S. Martí-Sánchez, C. Koch, S. Hart, Z. Cui, T. Kanne, S. A. Khan, R. Tanta, S. Upadhyay, M. Espiñeira Cachaza, C. M. Marcus, J. Arbiol, K. A. Moler, P. Krogstrup, *"Semiconductor - Ferromagnetic Insulator - Superconductor Nanowires: Stray Field and Exchange Field"*, Nano Letters, **20**, 456-462 (2020).

- A. M. Raya*, M. Friedl*, S. Martí-Sánchez*, V. G. Dubrovskii, L. Francaviglia, B. Alén, N. Morgan, G. Tütüncüoglu, Q. M. Ramasse, D. Fuster, J. M. Llorens, J. Arbiol, and A. Fontcuberta i Morral, *"GaAs Nanoscale Membranes on silicon: Prospects for a Seamless Integration"*, Nanoscale, **12**, 815-824 (2020).

  *Contributed equally

- Y. Liu, A. Luchini, S. Martí-Sánchez, C. Koch, S. Schuwalow, S. A. Khan, T. Stankevič, S. Francoual, J. R. L. Mardegan, J. Krieger, V. N. Strocov, J. Stahn, C. A. F. Vaz, M. Ramakrishnan, U. Staub, K. Lefmann, G. Aeppli, J. Arbiol, P. Krogstrup, *Coherent Epitaxial Semiconductor - Ferromagnetic Insulator InAs/EuS Interfaces: Band Alignment and Magnetic Structure*, ACS Appl. Mater. Interfaces, **12**, 8780-8787 (2020). *Including also the **Front Cover** of the Issue 12 (7) (2020)

- M. Zamani, G. Imbalzano, N. Tappy, D.T.L. Alexander, S. Martí-Sánchez, L. Ghisalberti, Q.M. Ramasse, M. Friedl, G. Tutuncuoglu, L. Francaviglia, S. Bienvenue, C. Hebert, J. Arbiol, M. Ceriotti, A. Fontcuberta i Morral, *Three-dimensional ordering at the liquid-solid polar interface of nanowires - Submitted* (2020).

Other publications developed during the PhD period

- Z. Luo, E. Irtem, M. Ibáñez, R. Nafria, S. Martí-Sánchez, A. Genç, M. de la Mata, Y. Liu, D. Cadavid, J. Llorca, J. Arbiol, T. Andreu, J. R. Morante and A. Cabot , *"Mn_3O_4@$CoMn_2O_4$-Co_xO_y Nanoparticles: Partial Cation Exchange Synthesis and Electrocatalytic Properties toward the Oxygen Reduction and Evolution Reactions"*, ACS Appl. Mater. Interfaces, **8**, 17435–17444 (2016).

- Y. Liu, D. Cadavid, M. Ibáñez, S. Ortega, S. Martí-Sánchez, O. Dobrozhan, M. V. Kovalenko, J. Arbiol and A.Cabot, *"Thermoelectric properties of semiconductor-metal composites produced by particle blending"*, APL Materials, **4**, 104813 (2016).

- Z. Luo, S. Martí-Sánchez, R. Nafria, G. S. Joshua, M. de la Mata, P. Guardia, C. Flox, C. Martinez-Boubeta, K. Simeonidis, J. Llorca, J. R. Morante, J. Arbiol, M. Ibáñez and A. Cabot, *"Fe_3O_4@$NiFe_xO_y$ nanoparticles with enhanced electrocatalytic properties for oxygen evolution in carbonate electrolyte"*, ACS Appl. Mater. Interfaces, **8**,29461-29469 (2016).

- Y. Liu, G. García, S. Ortega, D.Cadavid, P. Palacios, J. Lu, M. Ibáñez, L. Xi, J. De Roo, A. M. Lopez, S. Martí-Sánchez, I. Cabezas, M.de la Mata, Z. Luo, C. Dun, O. Dobrozhan, D. Carroll, W. Zhang, J. C. Martins, M. Kovalenko, J. Arbiol, G. Noriega, J. Song, P. Wahnon Benarroch and A. Cabot *"Solution-Based Synthesis and Processing of Sn- and Bi-Doped Cu_3SbSe_4 Nanocrystals, Nanomaterials and Ring-Shaped Thermoelectric Generators"*, Journal of Materials Chemistry A, **5**, 2592-2602 (2017).

- Y. Liu, Y. Zhang, S. Ortega, M. Ibáñez, K. H. Lim, A. Grau-Carbonell, S. Martí-Sánchez, K. M. Ng, J. Arbiol, M. V. Kovalenko, D. Cadavid and A. Cabot, *"Crystallographically Textured Nanomaterials Produced from the Liquid Phase Sintering of $Bi_xSb_{2-x}Te_3$ Nanocrystal Building Blocks"*,Nano Letters, **18**, 2557-2563 (2018).

- D. Barreca, L. Bigiani, M. Monai, G. Carraro, A. Gasparotto, C. Sada, S. Martí-Sanchez, A. Grau-Carbonell, J. Arbiol, C. Maccato and P. Fornasiero, *"Supported Mn_3O_4 Nanosystems for Hydrogen Production through Ethanol Photoreforming"*, Langmuir, **34**, 4568–4574 (2018).

- L. Bigiani, D. Barreca, A. Gasparotto, Cinzia Sada, S. Martí-Sanchez, J. Arbiol, and C. Maccato, *"Controllable vapor phase fabrication of Mn_3O_4 thin films functionalized with Ag and TiO_2"*, CrystEngComm, **20**, 3016-3024 (2018).
  **Including the Front Cover of Issue 22 (2018).*

- Y. Liu, Y.Zhang, K. Ho Lim, M. Ibáñez, S. Ortega, M. Li, J. David, S. Martí-Sánchez, K. Ming Ng, J.Arbiol, M. V. Kovalenko, D. Cadavid and A. Cabot, *"High Thermoelectric Performance in Crystallographically Textured n type $Bi_2Te_3-xSe_x$ Produced from Asymmetric Colloidal Nanocrystals"*, ACS Nano, **12**, 7174-7184 (2018).

- P. J. Shaw, M. Meyns, Y. Zuo, A. Grau-Carbonell, P. G. Lagoudakis, M. D. B. Charlton, S. Martí-Sánchez, J. Arbiol, A. Cabot and A. G. Kanaras, *"Colloidal Synthesis of CsX Nanocrystals (X = Cl, Br, I)"*, Nanomaterials, **8**, 506 (2018).

- R. Nafria, Z. Luo, M. Ibáñez, S. Martí-Sánchez, X. Yu, M. de la Mata, J. Llorca, J.Arbiol, M. V. Kovalenko, A. Grabulosa, G. Muller and A. Cabot, *"Growth of Au-Pd_2Sn Nanorods via Galvanic Replacement and their Catalytic Performance on Hydrogenation and Sonogashira Coupling Reactions"*, Langmuir, **34**, 10634-10643 (2018).

- J. Masa, C. Andronescu, H. Antoni, I. Sinev, S. Seisel, K. Elumeeva, S. Barwe, S. Martí-Sánchez, J. Arbiol, B. Roldan Cuenya, M. Muhler and W.Schuhmann, *"Role of Boron and Phosphorus in Enhanced Electrocatalytic Oxygen Evolution by Nickel Borides and Nickel Phosphides"*, ChemElectroChem, **6**, 236-240 (2019).

- Y. He, P. Tang, Z. Hu, Q. He, C. Zhu, L. Wang, Q. Zeng, P. Golani, G. Gao, W. Fu, Z. Huang, C. Gao, J. Xia, X. Wang, X. Wang, C. Zhu, Q. M. Ramasse, A. Zhang, B. An, Y. Zhang, S. Martí-Sánchez, J. R. Morante, L. Wang, B. K. Tay, B. Yakobson, A. Trampert, H. Zhang, M. Wu, Q. J. Wang, J. Arbiol and Z. Liu, *"Engineering grain boundary at 2D limit for hydrogen evolution reaction"*, Nature Communications, **11**, 57 (2020).

B.2 Communications in conferences and workshops

2020 Winter School on Microscopy and Imaging Sciences in the Master of Multidisciplinary Research in Experimental Sciences-BIST, Universitat Pompeu Fabra, Barcelona, Spain - lecture

2019 NW week 2019 (NWW19), Pisa, Italy - poster *AWARDED*

2019 Microscopy at the Frontiers of Science 2019 (MFS2019), Granada, Spain - oral

2019 Winter School on Microscopy and Imaging Sciences in the Master of Multidisciplinary Research in Experimental Sciences-BIST, Universitat Pompeu Fabra, Barcelona, Spain - lecture

2018 MRS Fall Meeting 2018, Boston, USA - oral

2018 Applied Nanoscience and Nanotechnology International Conference (ANNIC2018), Berlin, Germany - oral

2018 International Microscopy Congress 2018 (IMC19), Sydney, Australia - oral (On behalf of Prof. J. Arbiol)

2018 International Microscopy Congress 2018 (IMC19), Sydney, Australia - oral

2018 Winter workshop in Advanced Techniques in Multidisciplinary Science in the Master of Multidisciplinary Research in Experimental Sciences – BIST, Universitat Pompeu Fabra, Barcelona, Spain - lecture

2017 European Materials Research Society Fall Meeting (e-MRS 2017), Warsaw, Poland - oral

2017 Microscopy at the Frontiers of Science 2017 (MFS2017), Zaragoza, Spain - oral

2017 VIII International Congress on Analytical Nanoscience and Nanotechnology (NyNA 2017), Barcelona, Spain - oral

2017 NW Week 2017, Lund, Sweden - poster

2016 European Microscopy Congress 2016 (EMC2016), Lyon, France - poster

Appendix C

Resum

Els nanofils de semiconductors binaris i els seus aliatges tenen característiques per superar les tecnologies convencionals basades en semiconductors ja que presenten propietats millorades comparades amb els seus equivalents macro o microscopics. Això va intrinsecament acompanyat d'una reducció del consum dels materials emprats i la possibilitat de crear dispositius més eficients. Per aquesta raó són candidats excepcionals per millorar l'electrònica i l'optoelèctronica convencionals. Recentment s'han proposat inclús com a base per canviar el panorama de les ciències computacionals cap al nou paradigma de la computació quàntica topològica.

La tècnica principal pel creixement de nanofils durant els últims 50 anys ha sigut el mecanisme vapor-líquid-sòlid (VLS). Des que es va proposar al 1964, els incomptables esforços en entendre els mecanismes de creixement han permès un control precís dels paràmetres macroscòpics que condueixen a la formació de nanofils. No obstant, diversos factors com la formació espontània de defectes i l'escasa escalabilitat encara limiten la seva incorporació a tecnologies funcionals. Diverses estratègies revolucionàries de creixement s'han estat desenvolupant els últims anys amb el propòsit de superar aquestes limitacions. Aquestes estratègies inclouen l'inversió de la direcció típica de creixement per prevenir la formació espontània de defectes i el politipisme, el que permet el creixement de nanofils monocristal·lins. Igualment, el creixement VLS es pot guiar horitzontalment al llarg de direccions específiques del substrat, cosa que permet la creació de nanofils autoensamblats ordenadament, els quals habiliten la seva manipulació en paral·lel. Finalment, però no menys important, es poden crear patrons nanomètrics predissenyats al substrat on crèixer nanofils en forma de xarxes escalables. Aquesta metodologia es coneix com a creixement d'àrea selectiva.

Donats els requeriments de precisió i reproducibilitat de les tecnologies actuals,

el dipòsit de material s'ha de controlar a nivell atòmic, especialment quan el creixement s'expandeix a sistemes heterostructurats. En aquest sentit, la microscòpia electrònica de transmissió i les seves espectroscòpies associades són les tècniques idònies per estudiar els mecanismes de creixement a escala atòmica. Amb aquest objectiu, la present tesi doctoral proporciona una investigació atomística basada en microscòpia electrònica de transmissió dels mecanismes de creixement de nanofils en aquestes noves estratègies, tot correlacionant l'estructura cristal·lina de les nanoestructures creades amb les seves propietats (opto)electròniques i quàntiques.

Aquesta memòria consta de diversos capítols. Al capítol 1 es presenta una introducció a la física dels semiconductors des de punts de vista macro i microscòpics, seguit al capítol 2 amb una descripció teòrica i pràctica de la metodologia emprada en aquesta investigació. Els resultats d'aquesta tesi estan recollits en quatre capítols que engloben en ordre cronològic els diferents avenços en el creixement de nanofils per a una millor reproducibilitat i escalabilitat.

- El capítol 3 tracta el control de la polaritat en el creixement VLS convencional com un pas final per aconseguir nanofils monocristal·lins.
- El capítol 4 ofereix un avenç del mètode VLS al canviar el creixement cap a una direcció horitzontal per la producció de nanofils ordenats que permeten la seva manipulació en paral·lel.
- El capítol 5 engloba les tècniques de creixement horitzontal en substrats prèviament dissenyats amb patrons nanomètrics, el que proporciona rutes escalables per crear circuits i elimina la necessitat d'emprar catalitzadors durant el creixement.
- Al capítol 6 s'utilitzen els nanofils crescuts mitjançant les tècniques prèviament esmentades com a base per depositar epitaxialment aïllants ferromagnètics i/o superconductors, tot formant la propera generació de xarxes quàntiques híbrides.

Finalment, la memòria es conclou al capítol 7 amb un resum dels resultats principals i les perspectives futures.

Appendix D
Resumen

Los nanohilos de semiconductores binarios i sus aleaciones tienen características para superar las tecnologías convencionales basadas en semiconductores ya que presentan propiedades mejoradas en comparación con sus equivalentes macro o microscópicos. Esto va intrínsecamente acompañado de una reducción del consumo de los materiales utilizados y la posibilidad de crear dispositivos más eficientes. Por este motivo son candidatos excepcionales para mejorar la electrónica y la optoelectrónica convencionales. Recientemente se han propuesto incluso como base para cambiar el panorama de las ciencias computacionales hacia el nuevo paradigma de la computación cuántica topológica.

La técnica principal para el crecimiento de nanohilos durante los últimos 50 años ha sido el mecanismo vapor-líquido-sólido (VLS). Desde su propuesta en el 1964, los incontables esfuerzos en entender los mecanismos de crecimiento han permitido un control preciso de los parámetros macroscópicos que conducen a la formación de nanohilos. No obstante, varios factores como la formación espontánea de defectos y la escasa escalabilidad limitan aún su incorporación en tecnologías funcionales. Varias estrategias revolucionarias de crecimiento se han propuesto en los últimos años con el fin de superar estas limitaciones. Dichas estrategias incluyen la inversión de la dirección típica de crecimiento para prevenir la formación espontánea de defectos y el politipismo, dando lugar al crecimiento de nanohilos monocristalinos. Del mismo modo, el crecimiento VLS se puede guiar horizontalmente a lo largo de direcciones específicas del substrato, lo que permite la creación de nanohilos autoensamblados ordenadamente que habilitan su manipulación en paralelo. Finalmente, pero no menos importante, pueden crearse patrones nanométricos prediseñados en el substrato donde crecer nanohilos en forma de redes escalables. Esta metodología se conoce como crecimiento de área selectiva.

Dados los requisitos de precisión y reproducibilidad de las tecnologías actuales, el depósito de material se debe controlar a nivel atómico, especialmente cuando el crecimiento se expande a sistemas heteroestructurados. En este sentido, la microscopía electrónica de transmisión y sus espectroscopías asociadas son las técnicas idóneas para estudiar los mecanismos de crecimiento a escala atómica. Con este fin, la presente tesis doctoral proporciona una investigación atomística basada en microscopía electrónica de transmisión de los mecanismos de crecimiento de nanohilos mediante estas nuevas estrategias, incluyendo una correlación de la estructura cristalina de las nanoestructuras creadas con sus propiedades (opto)electrónicas y cuánticas.

Esta memoria consta de varios capítulos. En el capítulo 1 se presenta una introducción a la física de semiconductores desde puntos de vista macro y microscópicos, seguido en el capítulo 2 por una descripción teórica y práctica de la metodología utilizada para el desarrollo de esta investigación. Los resultados de esta tesis están recogidos en cuatro capítulos que engloban en orden cronológico los diferentes avances en el crecimiento de nanohilos para una mejor reproducibilidad y escalabilidad.

- El capítulo 3 trata del control de la polaridad en el crecimiento VLS convencional como un paso final para conseguir nanohilos monocristalinos.
- El capítulo 4 ofrece un avance del método VLS al cambiar el crecimiento hacia una dirección horizontal para la producción de nanohilos ordenados que permiten su manipulación en paralelo.
- El capítulo 5 engloba las técnicas de crecimiento horizontal en substratos previamente diseñados con patrones nanométricos, lo que proporciona rutas escalables para crear circuitos y elimina la necesidad de utilizar catalizadores durante el crecimiento.
- En el capítulo 6 se utilizan los nanohilos crecidos mediante las técnicas previamente citadas como base para el depósito epitaxial de aislantes ferromagnéticos y/o superconductores, formando así la siguiente generación de redes cuánticas hibridas.

Finalmente, la memoria concluye en el capítulo 7 con un resumen de los resultados principales y las perspectivas de futuro.

The research presented in this PhD dissertation has received funding from "la Caixa" Foundation in the framework of "Programa Internacional de Becas "la Caixa"-Severo Ochoa", the Generalitat de Catalunya 2017 SGR 327, the CSIC Research Platform on Quantum Technologies PTI-001 and the European Union's Horizon 2020 research and innovation program under grant agreement No 823717 - ESTEEM3. ICN2 is supported by the Severo Ochoa program from Spanish MINECO (Grant No. SEV-2017-0706) and is funded by the CERCA Programme / Generalitat de Catalunya.